Toward Developing Made-to-Order Metal-Organic Frameworks:
Design, Synthesis and Applications

Dissertation by

Lubna Y. Ashri

In Partial Fulfillment of the Requirements

For the Degree of

Doctor of Philosophy

King Abdullah University of Science and Technology

Thuwal, Kingdom of Saudi Arabia

The dissertation of Lubna Y. Ashri is approved by the examination committee.

Committee Chairperson: Mohamed Eddaoudi

Committee Member: Ingo Pinnau

Committee Member: Klaus-Viktor Peinemann

Committee Member: Pantelis Trikalitis

ABSTRACT

Toward Developing Made-to-Order Metal-Organic Frameworks:

Design, Synthesis and Applications

Lubna Y. Ashri

Synthesis of materials with certain properties for targeted applications is an ongoing challenge in materials science. One of the most interesting classes of solid-state materials that have been recently introduced with the potential to address this is metal-organic frameworks (MOFs). MOFs chemistry offers a higher degree of control over materials to be synthesized utilizing various new design strategies, such as the molecular building blocks (MBBs) and the supermolecular building layers (SBLs) approaches. Depending on using predetermined building blocks, these strategies permit the synthesis of MOFs with targeted topologies and enable fine tuning of their properties.

This study examines a number of aspects of the design and synthesis of MOFs while exploring their possible utilization in two diverse fields related to energy and pharmaceutical applications.

Concerning MOFs design and synthesis, the work presented here explores the rational design of various MOFs with predicted topologies and tunable cavities constructed by pillaring pre-targeted 2-periodic SBLs using the ligand-to-axial and six-connected axial-to-axial pillaring strategies. The effect of expanding the confined spaces in prepared MOFs or modifying their functionalities, while preserving the underlying network topology, was investigated.

Additionally, The MBBs approach was employed to discover new modular polynuclear rare earth (RE)-MBBs in the presence of different angular polytopic

ligands containing carboxylate and nitrogen moieties with the aid of a modulator. The goal was to assess the diverse possible coordination modes and construct highly-connected nets for utility in the design of new MOFs and enhance the predictability of structural outcomes. The effect of adjusting ligands' length-to-width ratio on the prepared MOFs was also evaluated. As a result, the reaction conditions amenable for reliable formation of the unprecedented octadecanuclear, octanuclear and double tetranuclear RE-MBBs were isolated, and their corresponding MOFs were successfully synthesized and characterized.

Regarding the applications of MOFs, gas sorption behavior of the novel prepared MOFs was studied to establish structure-property relationships that elucidate the effect of using different metals and/or ligands on tuning various properties of the prepared compounds. Furthermore, the magnetic properties of selected MOFs were investigated. Besides, as a proof-of-concept, known neutral and anionic MOFs were considered as potential drug delivery carriers.

ACKNOWLEDGMENTS

In the name of *Allah*, the Most Gracious and the Most Merciful

Foremost, all praises to *Allah* for His blessing in successfully completing my Ph.D. journey. This degree is now a reality because of *Allah's* blessing and the support of many exceptional people whom I am fortunate to know and have in my life.

Firstly, special appreciation goes to my advisor Prof. Mohamed Eddaoudi for his infinite support since the day I joined his lab. His deep knowledge, valuable guidance, and sincere encouragement and motivation kept me going - even when it was difficult to continue. Dr. Eddaoudi, thank you for being my mentor. It has been an immense honor to work under your leadership and to be a member of your research group.

I am grateful to the research scientists and posts doctoral researchers who patiently and expertly introduced me to field of MOFs. I am thankful to Dr. Youssef Belmabkhout and Dr. Dong-Xu Xue for their valuable support, stimulating remarks, and challenging questions. I am also especially grateful to Dr. Amy Cairns, Dr. Mohamed Alkordi, Dr. Yunling Liu and Dr. Osama Shekhah for sharing their immense knowledge and sincere motivation.

Words cannot express my gratitude to my close friends and colleagues for their encouragement, patience, and long fruitful discussions of my work. I am grateful to Dalal Alezi who volunteered to help in proofreading my dissertation, to Rasha AbdulHalim for being there when most needed, and to Ryan Luebke for always being ready to share his knowledge and help with all lab-related issues.

I would like to acknowledge others I collaborated with, including Dr. Xianrong Guo for his support in running the NMR drug loading and release experiments, as well as Qiang Zhang for supporting in studying the magnetic properties of my compounds.

Sincere gratitude to my committee members: Prof. Ingo Pinnau, Prof. Klaus-Viktor Peinemann and Prof. Pantelis Trikalitis for their inspirational comments and stimulating questions.

My sincerest appreciation also goes to The Executive Vice President of Administration and Finance at KAUST, Mr. Nadhmi Al-Nasr and to The Dean of The College of Pharmacy at King Saud University, Prof. Yousef Asiri for providing valuable fatherly support and for helping in overcoming all administrative hurdles.

I also would like to express my appreciation to my great parents, Fatima Feda and Youssef Ashri, they taught me - by example- how to be strong and compassionate; not to allow hardships to break me, but to make me stronger. I am forever indebted to them for believing in me and for giving me the gift of being able to dream impossible dreams, the courage to pursue those dreams, and the determination to never quit. My deepest thanks and love to my siblings. Dr. Nadia, your sincere prayers continue to light up my path; Dr. Nahid, you have stood beside me and held my hand when I needed to be held; Dr. Najah, I discovered your ears and shoulders at KAUST, and they have proven to be my safe haven; Mohamed, your brave, encouraging and loving smile kept me motivated, and Ahmed, your constant inquiry about the state of my affairs pushed me forward. Thank you all for the strength you provided and helped me see in myself. I am blessed to have you in my life.

Last but not least, a special thanks and appreciation to my family: My husband Saeed Alneghaimishi, my daughter Hanadi and my sons Abdulrahman, Abdulmajeed and Khalid. I am forever grateful for all the sacrifices that you have made for me to reach this day. Your unlimited support was my drive; your unconditional love was my pillar of strength. You never turned me down and I am so proud of you. This is “our” accomplishment!

TABLE OF CONTENTS

LIST OF ABBREVIATIONS

6-c A-A	6-connected axial-to-axial
A-A	axial-to-axial
AAS	atomic absorption spectroscopy
AcOEt	ethyl acetate
API	active pharmaceutical ingredient
CCDC	The Cambridge Crystallographic Data Center
CDDS	controlled drug delivery systems
CSD	Cambridge Structural Database
DDS	drug delivery systems
DEF	diethylformamide
DI	distilled deionized
DMF	N,N'-dimethylformamide
DMSO-d_6	deuterated dimethyl sulfoxide
EA	elemental analysis
H_3ImDC	4,5 imidazole dicarboxylic acid
HP	high pressure
HPLC	high-pressure liquid chromatography
IAST	Ideal Adsorption Solution Theory
IBU	ibuprofen
ICP-OES	inductively coupled plasma optical emission spectrometry
IS	internal standard
L-A	ligand-to-axial
L-L	ligand-to-ligand
Ln	lanthanides
LP	low pressure
MOFs	metal-organic frameworks
MOPs	metal-organic polyhedra
MS	Material Studio software
n-c	n-connected where n = 1, 2, etc.
n-D	n-dimensional where n = 1, 2, etc.
NLDFT	Non-local density functional theory
NMOFs	nano-sized MOFs

NMP	N-methyl-2-pyrrolidone
n-P	n-periodic where n = 1, 2, etc.
NS	normal saline
NSAID	non-steroidal anti-inflammatory drug
PBS	phosphate buffer saline
PDDB	4,4’-(pyridine-3,5-diyl)dibenzoic acid
PIP	5-(Pyridin-4-yl)isophthalic acid
PMIP	5-(pyrimidin-5-yl)isophthalic acid
Proc	procainamide
PSD	pore size distribution
PTPDC	5'-(pyridin-4-yl)-[1,1':3',1"-terphenyl]-4,4"-dicarboxylic acid
PV_{Theo}	theoretical pore volume
PXRD	powder X-ray diffraction
Q_{st}	isosteric heat of adsorption
RCSR	Reticular Chemistry Structure Resource database
RT	room temperature
SA	surface area
SA_{BET}	surface area determined using Brunauer, Emmett and Teller model
SA_{Lang}	surface area determined using Langmuir model
SBF	simulated body fluid
SBLs	supermolecular building layers
SC	single crystal
SC-CO_2	supercritical CO_2 activation
SCSC	single-crystal-to-single-crystal
SCXRD	single crystal X-ray diffraction studies
SDA	structure directing agents
TCA	tetrazole carboxylic acid
TCEE	1H-tetrazole-5-carboxylic acid ethyl ester sodium salt
TGA	thermogravimetric analysis
TMS	tetramethylsilane
TZ	tetrazole
US-DOE	U.S. Department of Energy
VT-PXRD	variable temperature powder X-ray diffraction
ZMOF	zeolite-like metal-organic framework

LIST OF FIGURES

LIST OF TABLES

Chapter 1: General Introduction to Metal-Organic Frameworks: Classification, Properties and Selected Applications

This chapter reviews the field of metal-organic frameworks (MOFs), beginning with the advancements in X-ray technology, the crystallography field and the self-assembly process, which allowed the development of a degree of control over the construction of materials at the nanoscale. In addition, it provides a brief historical review of the field and is followed by summarizing the key characteristics and advantages of MOFs. The main section of this chapter discusses design strategies and principles for the construction of made-to-order MOFs, including the molecular building blocks (MBBs), supermolecular building blocks (SBBs) and the supermolecular building layers (SBLs) approaches. Finally, potential applications of MOFs are reviewed with particular emphases on the field of clean energy and drug delivery.

1.1. Manipulation of materials at the nanoscale

Nanotechnology, or nanoscience, is the branch of science concerned with structures, materials or devices within the nanometer range.[1] These microscopic particles or objects have at least one dimension in the range of 1-100 nanometer (nm), where one nm is equal to a billionth (10^{-9}) of a meter. The early beginnings of the actual scientific exploration into nanoscience and nanomaterials began in the mid-1900s as a consequence of the development of new techniques that fostered a better understanding of how atoms are arranged.[2] These methods include X-rays along with the advances in crystallography, which made detecting chemical structures of different materials possible. In addition, modern techniques, such as the atomic force microscopy and the scanning tunneling microscopy, as well as understanding the self-assembly process, granted some degree of control over matter at the molecular and atomic levels. This level of control, where atoms can be imaged and positioned according to requirements, enabled the design and fabrication of nanostructures with fine-tunable properties, which in turn permitted the fabrication of made-to-order materials targeted toward specific demanding applications, such as drug delivery and gas storage or separation.

1.2. Crystal formation and self-assembly

Self-assembly is a powerful strategy that has helped scientists to enrich various methods for the synthesis of new and fascinating materials with higher complexity and functionality from simpler precursors.[3] In self-assembly, a spontaneous one-pot process is employed where specific local interactions of simple building blocks that contain certain functional groups at a particular relative geometry, facilitating molecular recognition, results in the formation of organized structures where atoms, molecules or ions are aligned and arranged in a periodic fashion.[4] This strategy allows the creation of and control over large, sophisticated structures and provides a measure of control over their properties at the molecular and atomic levels. It is worth mentioning that self-assembly is adopted from procedures found in nature, such as the process of assembly of DNA from basic building blocks, being nucleotides and amino acids.[3b, 5] Important examples of materials synthesized utilizing the self-assembly strategy are the coordination polymers.

1.3. Coordination compounds and coordination polymers

As mentioned earlier, coordination polymers are a class of materials that are synthesized via the self-assembly strategy and involve coordinate covalent bond formation. They are composed of well-defined repeating units that result from the coordination between functional organic ligands and metal ions or clusters.[6] In its infancy, not enough information was available on coordination materials chemistry to advance the creation of reliable design strategies; instead, only random trials that resulted in the formation of discrete or extended units were performed.[7]

The *discrete coordination compounds* are zero periodic (0-P) structures that were initially realized with the pioneering work of Alfred Warner, who introduced a family of compounds now known as the Warner clathrates.[8] These complexes represented the first category of coordination compounds and are mainly transition metal ions that are octahedrally coordinated to neutral amine donor ligands and anionic ligands, like CN^-, I^- or NO_3^-. Later, many discrete coordination compounds were synthesized based on either single metal ions, polynuclear metal clusters (e.g., paddlewheel clusters) or metal-organic polyhedra (MOPs)[7b, 9] where polytopic ligands are connected to multiple metal clusters to form supermolecular assemblies (Figure 1.1).

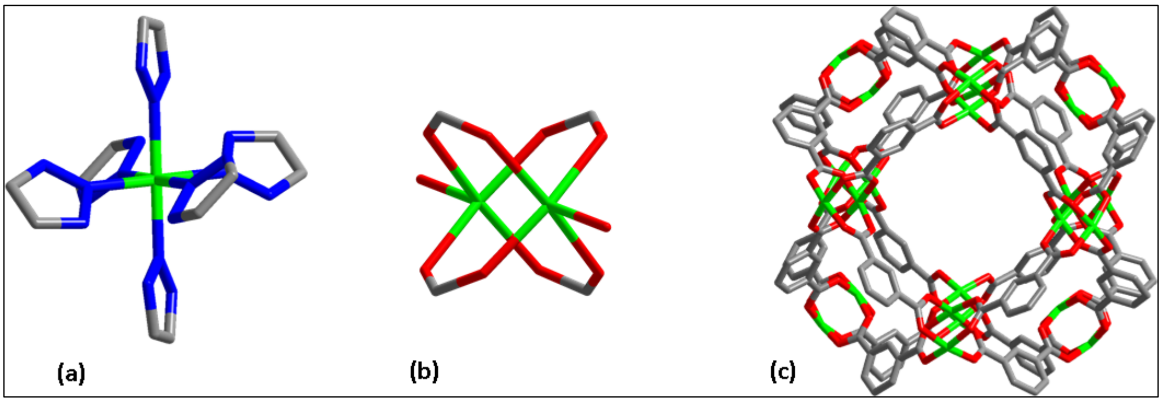

Figure 1.1 Different 0-P discrete coordination compounds: (a) single metal-ion based cluster, (b) polynuclear metal-ion cluster (paddlewheel) and (c) metal-organic polyhedra (MOP)[10].

On the other hand, the *extended coordination polymers* can be divided into two categories - the 1-P coordination polymers and the 2-P and 3-P coordination polymers. In 1-P structures, metal ions or clusters coordinate to ligands and extend indefinitely or continuously in one dimension, e.g., the 1-P chains (Figure 1.2 a). The introduction of the 2-P and 3-P structures took coordination polymers to a more sophisticated level whereby 2-P structures signified layers that extend in two dimensions (Figure 1.2 b). 3-P structures are even more complex and extend in three dimensions (Figure 1.2 c). The construction of 3-P coordination polymers in the late 1980s marked the beginning of the new and interesting class of metal-organic frameworks (MOFs), possessing open frameworks that contained potential voids.[11,12]

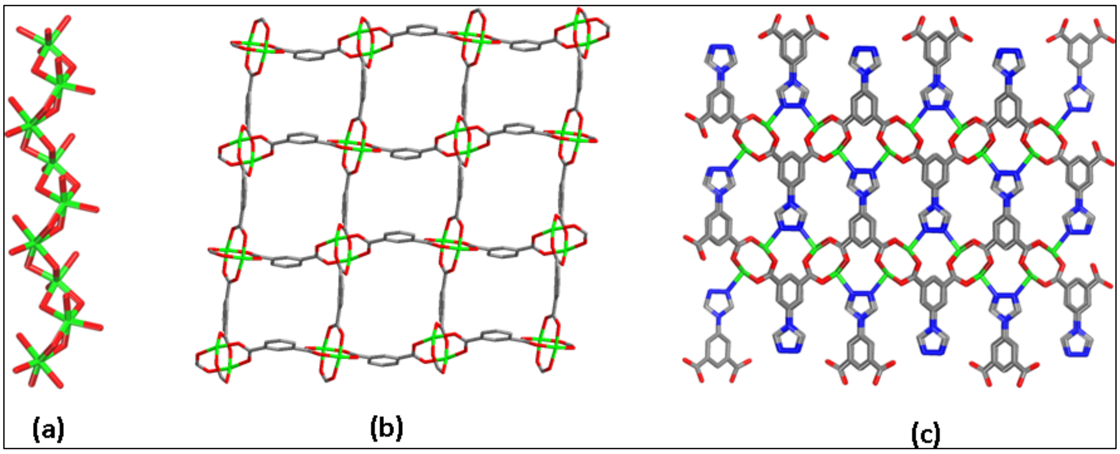

Figure 1.2 Different extended coordination polymers: (a) 1-P chain, (b) 2-P layer and (c) 3-P MOF[13].

1.4. Metal-organic frameworks

Metal–organic frameworks (MOFs), the focus of the research in this dissertation, are an emerging class of solid-state crystalline porous materials that are fabricated by the association of metal ions or clusters and a wide range of polytopic polyfunctional organic linkers.[14] MOFs are considered a subclass of coordination polymers with new topologies or with topologies similar to those of inorganic salts/minerals or zeolites.[15]

In the late 1980s, MOFs emerged as an attractive field of research based upon the fundamental work of Hoskins and Robson who reported the first three-dimensional (3-D) coordination polymer with a diamond-like network and a formula of $(Cu^1[C(C_6H_4.CN)_4])_n^{n+}$.[16] Since then, this field has experienced accelerated and prominent growth and a large number of MOFs have been described in the literature.[11, 17]

The earliest examples of 3-P MOFs were constructed from neutral nitrogen-donor polytopic ligands, such as pyrazine, pyrimidine, triazine, 4,4'–bipyridine and others similar (Figure 1.3). These MOFs were not stable upon activation (i.e. removal of solvent guest molecules from cavities) as a result of the relative flexibility of the N-M (nitrogen-metal) bond; consequently, they were not porous to gas.[18] Alternatively, many of these compounds showed promise in various applications, like anion exchange or solution phase guest exchange.[19]

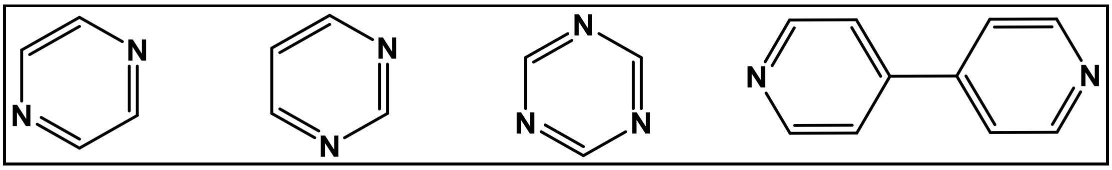

Figure 1.3 Examples of nitrogen-based ligands used in early MOFs studies.

On the other hand, anionic nitrogen-donor polytopic ligands, such as tetrazole-based ligands, were used later together with metal ions to create new MOFs with improved stability upon guest molecules removal.[20]

The second generation of MOFs used carboxylate-based ligands (Figure 1.4),[14b, 21] and thus more robust MOFs with permeant microporosity were synthesized.

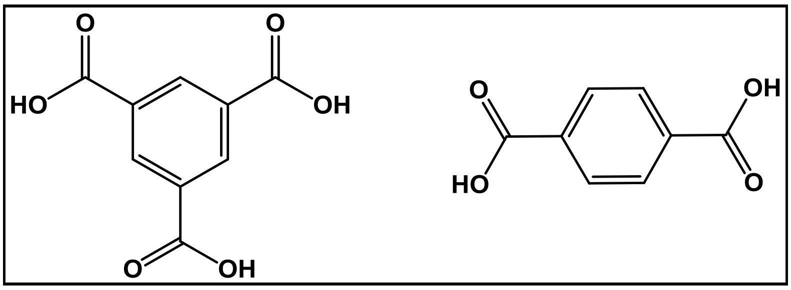

Figure 1.4 Examples of carboxylate-based ligands used to construct MOFs.

One of the first examples of these types of MOFs is MOF-5, introduced by Eddaoudi et al. in 1998, and from that point, a large number of new structures that were stable and had a higher degrees of rigidity were synthesized and reported.[21a, 22] The improved stability of these compounds is attributed to many factors, including the electrostatic interaction between the negatively-charged carboxylate moiety and the positively-charged metal ions or clusters.[23] Besides, carboxylate-based ligands can coordinate to metal ions through different modes, such as monodentate, bidentate and bis-monodentate, leading to increased stability of the final structures (Figure 1.5).[24]

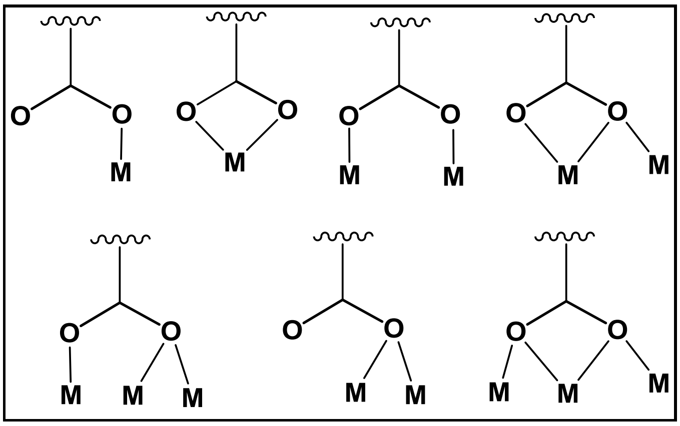

Figure 1.5 Coordination modes between metal ions and carboxylate groups.

Finally, because of the presence of carboxylate moieties, these MOFs are based on more complex building units that were later referred to as "molecular building blocks" (MBBs) (Figure 1.6). One notable example is the 4-connected (4-c) paddlewheel MBB, within which binuclear metal centers are connected through four bis-monodendate carboxylate moieties from several ligands (Figure 1.6 a).[14a, 22a, 25]

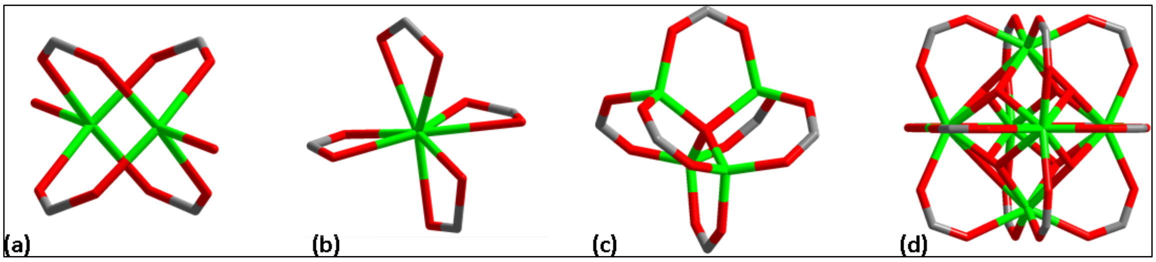

Figure 1.6 Examples of carboxylate-based MBBs: (a) the 4-c paddlewheel, (b) the 4-c single metal ion MBB, (c) the 6-c basic zinc acetate cluster and (d) the 12-c hexanuclear MBB.

Recently, hetero-functional ligands have been employed to yield new MOFs where the ligands contain both nitrogen donors and carboxylate moieties (Figure 1.7).[13, 26]

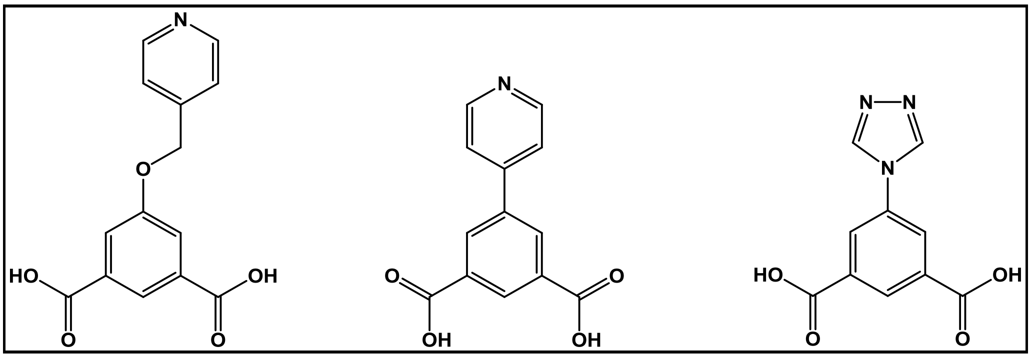

Figure 1.7 Examples of hetero-functional ligands used in the synthesis of MOFs.

Theoretically, the different functional groups in these ligands offer the potential to form unique coordination environments and building units and therefore allow isolation of new complex structures with divergent geometries and shapes. For example, hetero-functional ligands possessing both carboxylate and nitrogen groups can be used to construct 3-P MOFs that are based on pillared 2-P layers. Here, the carboxylate groups of the ligands chelate metal ions and form specific metal clusters, creating 2-P layers. Moreover, the nitrogen donor moieties of the ligands that form one layer chelate open metal sites of the metal clusters of adjacent layers, which leads to the construction of a pillared 3-P MOF. This is a particularly intriguing class of pillared MOFs that are constructed utilizing the ligand-to-axial (L-A) pillaring technique, recently introduced by Eddaoudi et al. in 2011.[13] It is worth noting that MOF pillaring is the focus of Chapter 3 in this dissertation.

1.4.1. Characteristics and advantages of MOFs

Over the last two decades, MOFs have received considerable attention in both academia and industry because of the numerous attributes that make them suitable candidates for a wide range of potential applications in presently demanding technologies.[14d, 17b] These salient features originate from their unique physical and chemical properties in addition to their topologies and architectures, which engenders them with the ability to overcome many of the limitations of existing porous materials, like the zeolites, mesoporous silica and activated carbon.[14b, 27]

One of the most unique properties of MOFs is their chemical versatility with the possibility of synthesizing an infinite number of rigid or flexible structures. These structures can be formed based on the inherent hybrid nature of MOFs, consisting of interchangeable organic and inorganic moieties. In addition, these structures are characterized by topologies that can be predicted or targeted using the aforementioned newly introduced design strategies, like the supermolecular building approach.[28]

Moreover, MOFs are characterized by their permanent well-ordered porosity and the exceptionally controllable functionalities in their pores.[29] Another prime feature that is unique to MOFs is the high degree of structural and functional tunability and modularity (reticular chemistry, use of different metal ions, post-synthetic modification, etc.).[14c, 30, 31, 32] Therefore, tuning of porosity, affinity towards gases and many other characteristics can be easily adjusted by an assortment of methods, such as modifying the ligands, metal ions or counter ions, if present.[11b, 33] Ligands can be modulated either by extending, contracting or introducing/removing functional groups, which may enhance the surface area

(SA) or provide functional sites for guest interactions.[13, 14c, 31, 34] Whereas metal ions can be modified with different metal ions that can form similar clusters or can introduce open or unsaturated metal sites as guest substrate interaction sites to improve the properties of prepared MOFs.[35] Finally, counter ions in charged frameworks can have a significant effect on MOF properties and can be manipulated with metal salts or through ion exchange.[36, 37]

Depending on the ligands and metal ions used, certain MOFs may have large and unprecedented pore sizes[14c, 38] and shapes with low densities (as low as 0.13 g/cm^3 for MOF-399)[39] as well as ultra-high internal SAs.[40] It is notable that chemical structures with ultra-high SAs are of great importance in a number of applications, including gas storage, but their design and construction has always been a challenge.[41] Recently, several MOFs have been demonstrated to possess ultra-high SAs (Table 1.1) that can be considered among the highest values ever reported for any class of porous material to date.[40a]

Table 1.1 BET surface areas and pore volumes of selected highly porous MOFs.

MOF	BET surface area (m^2/g)	Pore Volume (cm^3/g)	Ref.
NU-110E	7140	4.40	40a
NU-109E	7010	3.75	40a
MOF-210	6240	3.6	40b
NU-100	6140	2.82	42
Al-**soc**-MOF-1	5585	2.3	43
UMCM-2	5200	2.32	44
DUT-23-Co	4850	2.03	45
MOF-200	4530	3.59	40b
MOF-177	4500	1.89	46
MOF-205	4460	2.16	40b
Bio-MOF-100	4300	4.30	47
Cr-MIL-101	4230	2.15	48
UMCM-1	4160		49
PCN-66	4000	1.36	50
UMCM-1-NH_2	3920		51
MOF-5	3800	1.55	52
SNU-77	3670	1.52	53
PCN-61	3000	1.36	50
NOTT-102	2940	1.14	54
MFU-4 L	2750	1.26	55

Furthermore, these mostly chemically and thermally stable compounds[27, 44] are extremely crystalline, facilitating unambiguous structural characterization using techniques that include X-ray and synchrotron diffractometers,[56] permitting a greater understanding of the structure-function relationship and consequently, improving control of targeted properties.[57]

These properties, in addition to many others, have led to MOFs being applied in a myriad of ways, including, but not limited to, gas storage/separation,[58] heterogeneous catalysis,[59] chemical sensing,[60] magnetization,[61] proton conductivity,[62] drug delivery[63], imaging[60b, 64] and photoluminescence[65].

With the goal of preparing MOFs tailor-made for specific applications, i.e., made-to-order MOFs, a variety of design strategies were implemented here. Even though they are fairly novel and still in their infancy, they provide an unprecedented amount of control over the properties and functionality of the prepared materials. In this regard, different MOF design strategies and principles will be introduced later, followed by the integration of those that were selected in the following chapters.

1.4.2. MOFs classification and identification

1.4.2.1. MOFs topologies and nets

In MOFs, the coordination or connectivity between metal ions/clusters and organic ligands is what identifies their periodic nature and underlying nets. Therefore, it is highly recommended to employ topology to improve MOF crystal structures description.[12, 66] Hence, MOFs are categorized according to their network topology, which is identified and described using descriptors and notations, such as the point symbol, the vertex symbol and the coordination sequence.[67]

Consequently, MOFs topology is used to define the structural relationship between different MOFs. For example, topological analysis can aid in determining whether a 4-c network has a diamond (**dia**), lonsdaleite (**lon**) or niobium oxide (**nbo**) topology (Figure 1.8).

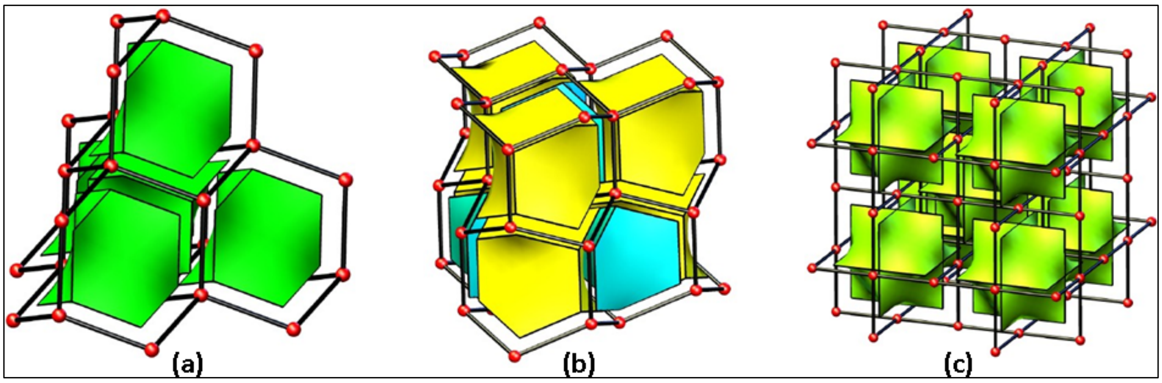

Figure 1.8 (a) Part of the **dia,** (b) **lon** and (c) **nbo** nets. Natural tiles are shown.[68]

In addition, and based on the introduction of new design strategies (Section 1.4.3), topological tools (connectivity, net, edge-transitive, minimal transitivity)[28] are now used for predicting topologies and to facilitate the design of novel MOFs with attractive properties. For example, when considering pillaring of 2-D **sql** layers having octahedral nodes (6-c) with 3-c ligands, a (3,6)-connected net with pyrite (**pyr**) topology is the most logical target.[13] Then, a survey of the Reticular Chemistry Structure Resource (RCSR) database[69] (Section 1.4.2.2) could reveal other possible nets for such a combination.

Finally, it is worthwhile to remember that topological analysis can be accomplished with several tools, including SYSTRE[70] and TOPOS[71], software packages specifically for computing these calculations.

1.4.2.2. Reticular Chemistry Structure Resource (RCSR) Database

RCSR is a comprehensive database that provides valuable crystallographic information and topological details on a vast number of crystal structures and chemical compounds.[69] It was developed by O'Keeffe and coworkers to deal with the fast growing reticular chemistry field. Similar to the zeolite database, the nomenclature codes adopted in RCSR follows a three-letter system where the only difference is using lower case letters rather than the uppercase letters in zeolites. Symbol assignments in RCSR relating to different nets might be the result of their association with minerals, e.g., diamond (**dia**), or, when applicable, based on their relationship to zeolites, e.g., LTA is **lta**. Furthermore, for nets with new topologies, the net symbol can be assigned based on a person, e.g., the **med** net that is named after Prof. Mohamed Eddaoudi.[15d]

1.4.2.3. The Cambridge Structural Database (CSD)

Introduced by The Cambridge Crystallographic Data Center (CCDC), CSD[72] is a database and software package that contains several programs including, in addition to others, *ConQuest* for structural database search, *Mercury* for structures visualization and *Vista* for numerical analysis. CSD is an important comprehensive resource for scientists and crystal engineers as it has an inventory of all currently published crystal structures and is linked to all known related chemical, crystallographic and bibliographic information. The database is very useful in that it provides users with an immense amount of data. For example, it supplies insights into the preferred metal-ligand coordination environment and the different reaction conditions that may govern various intermolecular interactions, which could assist formulating new reactions with specific targets in mind.

1.4.3. Toward made-to-order MOFs: Design strategies and principles

One of the features that distinguish MOFs from other similar systems, e.g., zeolites, is that the reaction conditions used for their construction are relatively mild, preserving the integrity of the building blocks (the built-in rigidity, functionality and directionality) that are formed *in situ* from metal ions and/or organic linkers. This feature allows the implementation of rational design strategies with the goal of constructing made-to-order MOFs that are appropriate for targeted applications. This is true because being able to deal with a combination of certain predesigned building blocks grants a modicum of control and predictability over the composition and topology of resulting products.

One of the most common guiding principles for MOFs construction is the *node-and-spacer* approach, considered the basis for today's activity in coordination compounds.[73] It was first introduced in 1977 by Wells[74] to understand zeolites; then, in the early 1990s, Robson and colleagues employed this approach for the design and synthesis of coordination polymers.[16] Here, the inorganic building units (metal clusters) and the organic ones (ligands) are considered *nodes* and *spacers* connected to create extended frameworks with well-defined void spaces (Figure 1.9). Using this approach, novel materials were designed and constructed founded upon formerly known topologies of naturally-occurring minerals.[73]

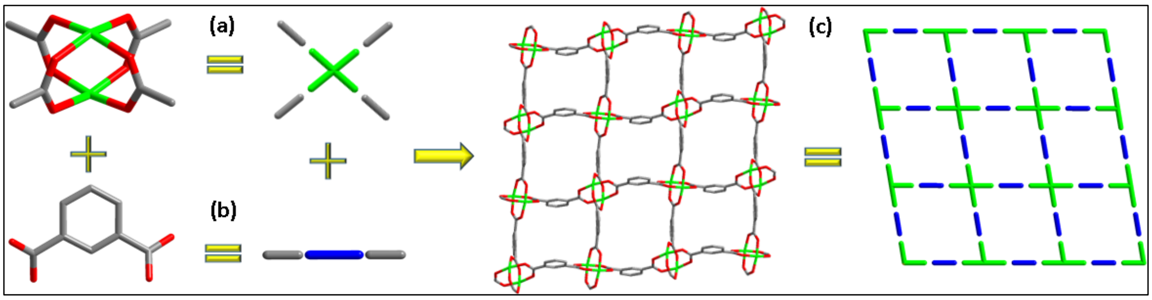

Figure 1.9 Schematic illustration showing the node-and-spacer representation of the (a) 4-c paddlewheel MBB, (b) 2-c ligand and (c) 2-P square grid layer.

This marked the dawn of the conventional molecular building blocks (MBBs) design strategy that depends on identifying the simplest repeating building unit in these materials. The MBBs approach is now considered a powerful design strategy for the construction of novel MOFs with predicted topology and targeted functionality.[75]

1.4.3.1. Molecular building blocks (MBBs) approach

The last two decades have witnessed the great success of the MBBs approach as it became a powerful tool for designing, discovering/exploring and developing diverse MOF platforms with predicted/targeted topologies.[75a, 75c] The MBBs approach relies on *in situ* metal-ligand self-assembly into predesigned rigid MBBs (simplest repeating building unit), of which the desired functionality and directionality can be introduced at the molecular level. This can be established through utilizing the different coordination modes and geometries of the judiciously-designed and selected molecular precursors (metal ions and organic ligands).

In other words, to construct a MOF with a given underlying net, this approach enables the introduction of anticipated properties and functionalities before the actual synthesis of the material by preselecting building units that are encoded with the required structure and geometry information.[28]

It is worth mentioning that in crystal chemistry, highly-connected uninodal and binodal nets that have at least one node with $n \geq 8$ connectivity are appropriate targets as they offer just a limited number of nets that are suitable for highly-connected MBBs assembly.[69]

For the MBBs approach to be carried out successfully, the reaction conditions, under which the consistent *in situ* assembly of the pre-programmed inorganic MBBs occurs, must be discerned.[76] Despite its importance, to date, not enough work on the effects of the widely ranging reaction variables that may affect the nature of the products have been performed.

Furthermore, fine tuning of the resulting structures can be achieved by replacing the single metal ion-based MBBs with more rigid 3-, 4- and/or 6-c metal clusters, i.e., multi-nuclear metal cluster-based MBBs, while keeping the intrinsic modularity and geometrical properties required for building targeted network.[69] An example of such multi-nuclear MBBs is the rigid binuclear paddlewheel MBB that acquired great importance because of its role in driving the field of MOFs forward. One of the first examples of MOFs with permanent porosity that was stable and enclosed a significant amount of void space is MOF-2, reported by Eddaoudi et al. in 1998, and is based on Zn paddlewheel MBBs.[14a, 21a, 22a]

A paddlewheel MBB is carboxylate based where two transition metal ions (metals that are susceptible to form paddlewheels, e.g., Cu, Zn, Ni, Fe, etc.) are coordinated to four carboxylate moieties of the organic ligand in a bis-monodentate fashion (Figure 1.10 a). Geometrically, these clusters can function as 4-c squares or slightly rectangular when their axial positions are occupied by terminal ligands, like water or N,N'-dimethylformamide (DMF), that are not involved in the connectivity of the MOF (Figure 1.10 b). In addition, this cluster can function as 6-c octahedral units when the axial positions are occupied by the ligand and are engaged in the connectivity of the prepared MOF (Figure 1.10 c).[13]

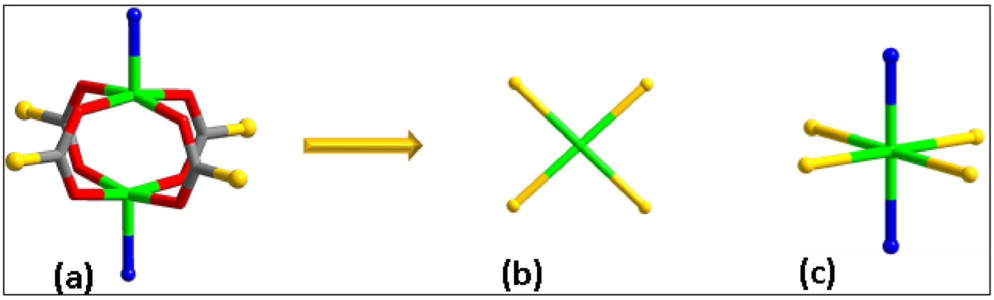

Figure 1.10 (a) The paddlewheel MBB can function as a (b) 4-c square or (c) 6-c octahedral MBB depending on its coordination.

Generally, targeting multi-nuclear highly-connected MBBs (n-c where $n \geq 12$) as building units reduces the number of possible resultant networks, which in turn facilitates MOFs design and synthesis. Furthermore, more stable structures are expected to be built.[10, 76-77] At present, very few highly-connected MBBs have been reported in the literature,[76, 77b, 78] possibly attributed to the complications and difficulties in attaining polynuclear metal clusters.[76] For example, in RE metal ion chemistry, and because of RE hard sphere behavior, the dominant building units are the inorganic infinite chains that limit the potential of controlling the coordinated ligands' directionality.[76, 79]

Our group is actively pursuing the investigation of coordination chemistries between various metals, such as RE metal ions, and functional ligands with the intent of discovering new modular highly-connected polynuclear metal clusters or MBBs. As a result, we initiated the use of fluorinated ligands and/or modulators, such as 2-fluorobenzoic acid (2-FBA), to support in controlling the directionality of RE-based MBBs.[77b] This process, under suitable reaction conditions and in the presence of functional ligands, provides consistent *in situ* formation of multinuclear RE-based MOFs (RE-MOFs) and precludes the formation of RE default MBBs (e.g., infinite chains). Consequently, our group has discovered, designed and isolated a series of unique materials, namely RE-**fcu**-MOFs that are based on electron-rich RE hexanuclear clusters $[RE_6(\mu_3\text{-}OH)_8(O_2C\text{–})_6(N_4C\text{–})_6]$ and linear hetero-functional ligands containing both carboxylate and tetrazolate moieties. RE-**fcu**-MOFs are characterized by their highly-localized charge density and tunable pore size with enhanced carbon dioxide (CO_2) energetics at very low CO_2 loading applicable specifically for trace CO_2 removal (Figure 1.11 A).[77b] Later, a 12-c RE hexanuclear MBB was present in a (4,12)-connected RE-**ftw**-MOF upon the use of square tetracarboxylate-based linkers (Figure 1.11 A).[80]

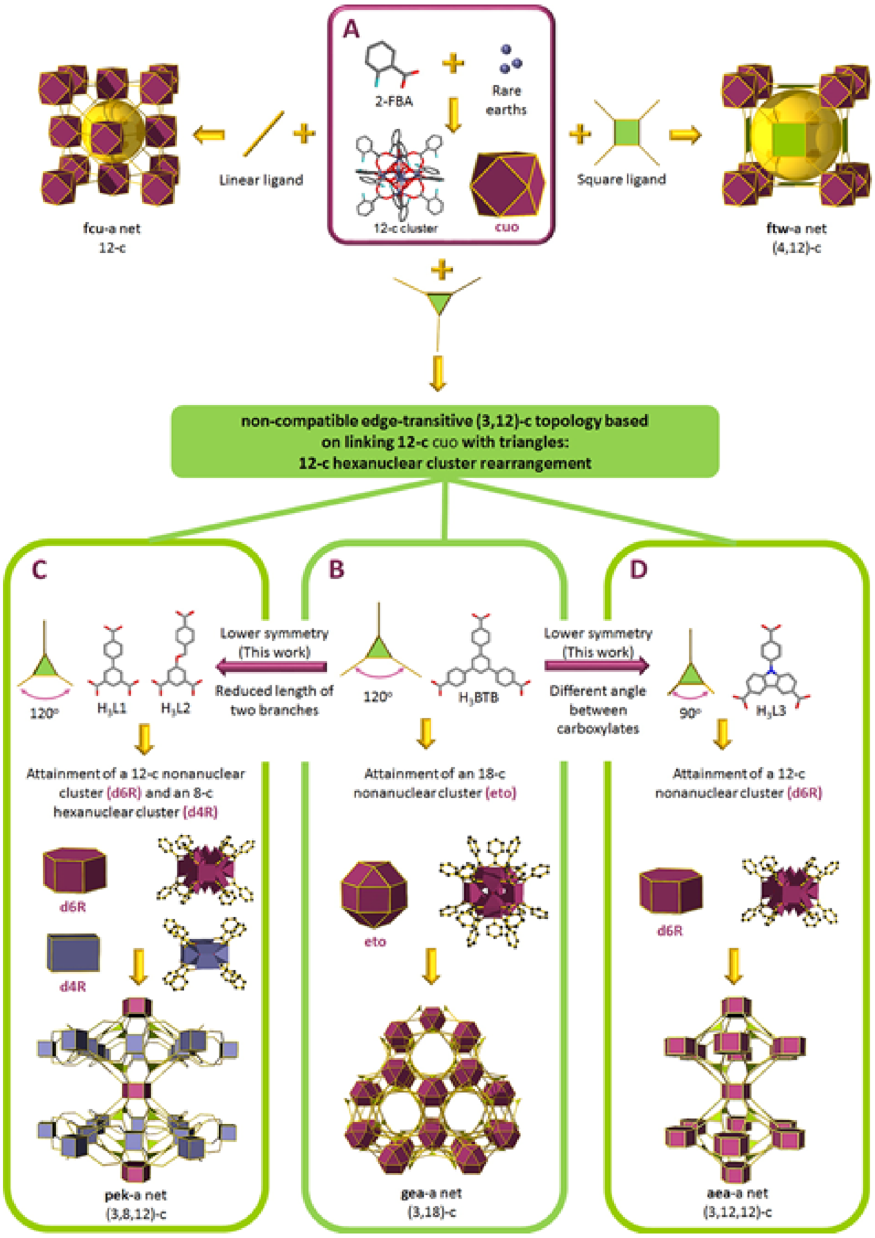

Figure 1.11 Summary of our laboratory's recent discoveries of new RE-MBBs. (A) The 12-c RE hexanuclear cluster and the resulting **fcu-** and **ftw**-MOFs when using linear and square ligands, respectively. (B) The 18-c nonanuclear cluster and **gea-**MOF resulting when using a 3-c symmetrical ligand. (C & D) The 3,8,12-c and 3,12,12-c **pek** and **aea** MOFs are produced by using less symmetric ligands. Figure adapted with permission from Alezi, et al., 2015.[76]

Encouraged and inspired by our initial discovery of the RE hexanuclear cluster, which can be consistently formed *in situ* with the assistance of 2-FBA, we continued our efforts with the objective of isolating new modular highly-connected inorganic MBBs in the presence of distinctive organic linkers. Accordingly, several new platforms were designed and developed in our laboratory. For instance, with the use of a symmetric tritopic ligand (Figure 1.11 B), a novel RE nonanuclear cluster $[RE_9(\mu_3\text{-}OH)_8(\mu_2\text{-}OH)_3(O_2C\text{–})_{18}]$ was further isolated to serve as an 18-c MBB for the assembly of a (3,18)-c **gea**-MOF.[77a] Interestingly, when less symmetric tritopic ligands (Figure 1.11 C and D) were utilized, a 12-c RE nonanuclear MBB (d6R or hexagonal prism building unit) was observed in a (3,8,12)-c **pek**-MOF and a (3,12,12)-c **aea**-MOF.[76] Certainly, a 12-c nonanuclear MBB (d6R building unit) was present in the **shp**-MOF upon the use of rectangular/square tetracarboxylate-based linkers.

To further survey the effect of using unique ligands, in the presence of 2-FBA, on the adaptability of RE polynuclear clusters, a portion of the work put forth in this dissertation (Chapter 4) was the continuing discovery of new highly-connected RE-MBBs and their corresponding nets. Here, the fact that it is possible to identify new frameworks and network topologies by subtly changing the geometry of the employed ligands, e.g., adjusting their length-to-width ratio, was utilized with different trigonal hetero-functional ligands that contained both carboxylate and nitrogen donor moieties.

Worth mentioning is that with increased complexity in MOFs along with the discovery of advanced MBBs that are composed of more than a single atom, new methods to simplify, describe and help in the design of new structures were required. Resultantly, the secondary building units (SBUs) approach was instituted where the points of extension of the MBBs define the SBUs (Figure 1.12).[75a] Therefore, for a given net, the SBU is the vertex figure of the original vertex where the vertices are the augmented nodes. In other words, the SBU is where a single metal ion at a network vertex is decorated or replaced by a group of vertices that can be connected to the ligands to form the extended framework.[75a] The geometric representations offered by the SBUs (the vertex figures, e.g., triangles, octahedral or squares) simplify complex structures and yield additional structural and geometric information.

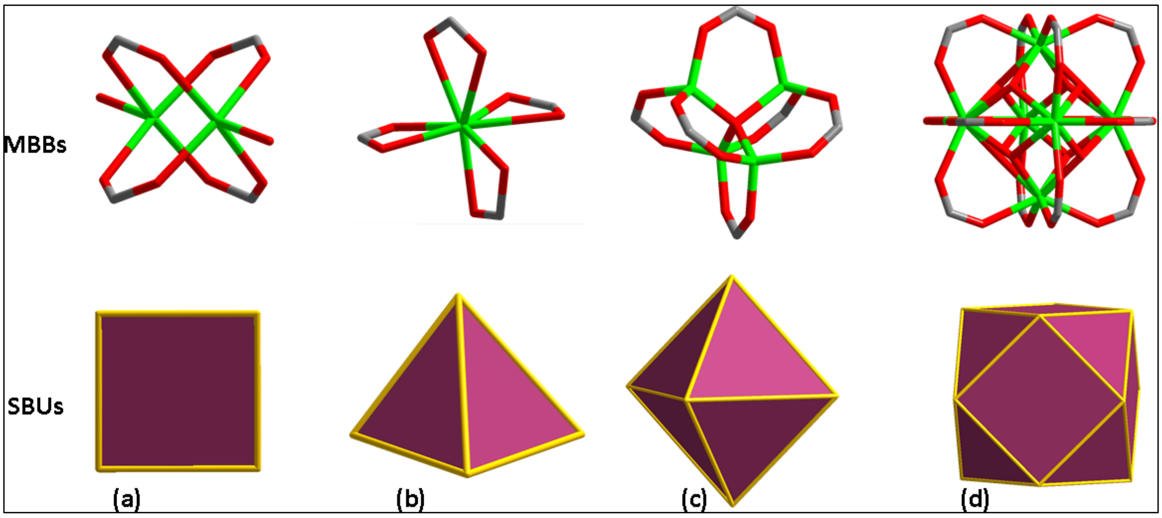

Figure 1.12 Examples of SBUs (geometrical shapes) based on rigid metal-carboxylate MBBs. (a) The 4-c paddlewheel MBB can be viewed as square SBU; (b) the 4-c single metal ion can be rationalized as a tetrahedral SBU; (c) the basic Zn acetate cluster can be considered an octahedral SBU; and (d) the hexanuclear RE-MBB can be regarded as a cuboctahedron SBU.

In practical terms, to synthesize MOFs with particular underlying networks and targeted applications, a judicious choice of metal ions and organic ligands is crucial. First of all, it is critical to carefully select the ligands and metal clusters that resemble the geometry and directionality of the augmented basic building units (vertex figures) and form the required MBBs for the targeted net. Further, it is imperative to determine the range of solvothermal reaction conditions that will enable consistent and reliable *in situ* generation of the desired inorganic MBBs. Additionally, the metal ion should exhibit specific activity relevant to the targeted application, e.g., guest sensing, gas sorption, drug delivery or catalysis. Similarly, for the organic ligand, one can choose/synthesize analogues of organic linkers used in prototypal MOFs in order to fine-tune (expand or decorate) them or enhance their stability.

It is noteworthy that fine-tuning prepared MOFs can be achieved by either pre-design or post-synthetic modification strategies.[81, 82] This may improve MOFs stability and/or boost their performance in targeted applications.[35a]

1.4.3.2. Supermolecular building entities

Supermolecular building layers (SBLs) and supermolecular building blocks (SBBs) are new conceptual approaches that were recently introduced by our group to enhance control over the targeted framework and provide a higher degree of predictability that is not the case with the MBBs approach.[28] These approaches facilitate the prediction, design and construction of new unique made-to-order MOFs using supermolecular entities with larger dimensions and higher complex connectivity as building blocks.[28, 77c]

Highly-connected polynuclear metal clusters can be utilized as MBBs, but the building blocks that have connectivity of ≥ 8 are too complicated to obtain with simple ligands or polynuclear clusters. Therefore, the SBBs approach can be employed by the *in situ* assembly of relatively simple and easily accessible 3-, 4- or 6-c MBBs (e.g., the paddlewheel MBB (Figure 1.13 a) to form more complex 0-P metal-organic polyhedra (MOPs) (Figure 1.13 b).[28, 77a] Here, the peripheral points of extension outline a geometric building unit that corresponds to the net vertex figure (Figure 1.13 c).[10, 83]

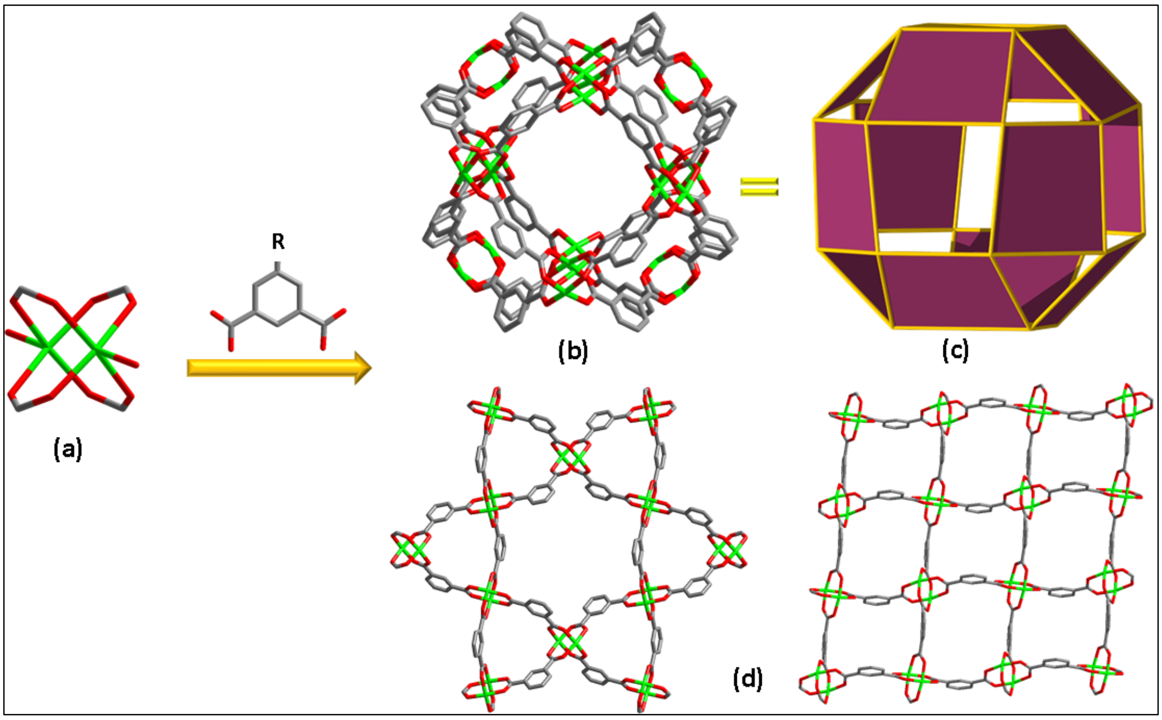

Figure 1.13 (a) The paddlewheel MBB, (b) the 0-P polyhedral SBB, (c) its corresponding SBU and d) different 2-P SBLs constructed through the association of paddlewheel MBBs.[10, 13]

For successful implementation of the SBBs and SBLs strategies, the organic ligands have to be designed or chosen wisely with appropriate geometry to associate different MBBs and create the targeted supermolecular entities, being the 0-P MOPs and 2-P metal-organic layers (Figure 1.13 d) for SBBs and SBLs, respectively, with peripheral functionalities.[28] Furthermore, the ligands used have to have additional functional groups that will complete the coordination of the constructed building blocks to form an extended framework.

In general, the combination of supermolecular entities in addition to their encoding with the required information will make possible the construction of targeted frameworks and exclude the formation of default or easy to attain ones.[84] It is significant that when these approaches are applied, the targeted products are not guaranteed to be constructed, but, rather, these approaches simply limit the number of expected outcomes.

Recently, our research group has developed and successfully put into action the SBBs approach, constructing non-default n-c nets (n ≥ 8) with improved control over the resulting topology.[10, 83] For example, 24-, 18-, or 12-c MOPs were used as SBBs for the intended formation of highly-connected **rht**-MOFs (Figure 1.14),[10, 77c, 85] **gea**-MOFs,[77a] and **fcu**-MOFs,[77b, 86] respectively.[83]

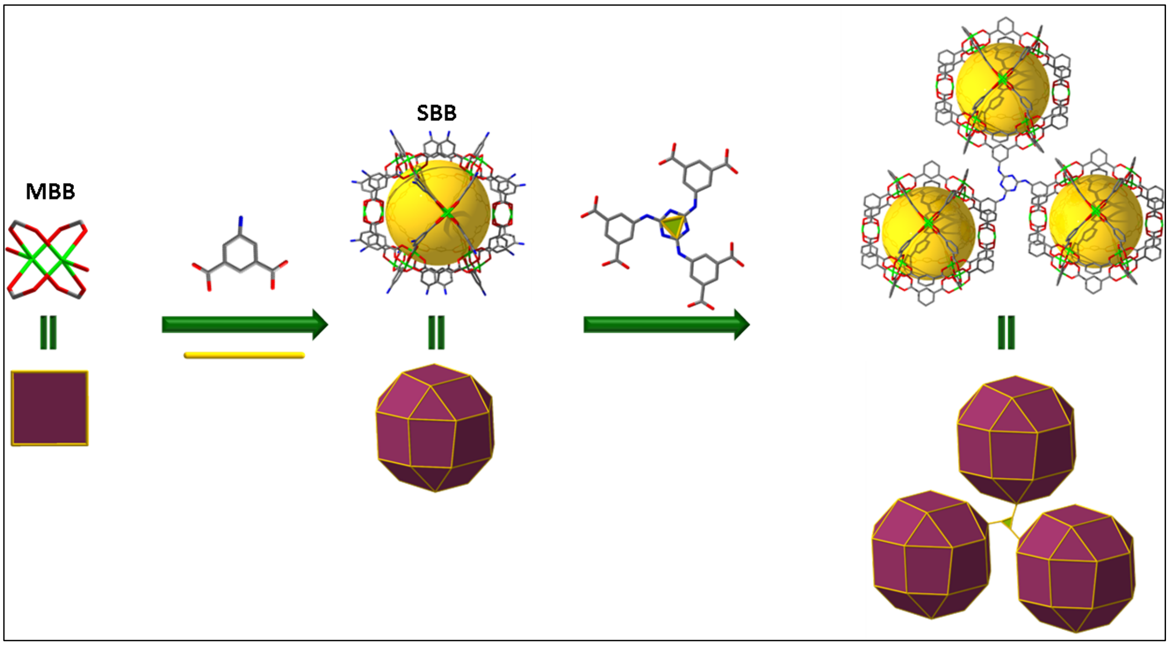

Figure 1.14 An example on the successful implementation of the SBBs approach where the highly-connected **rht**-MOF-7 was built utilizing 24-c MOPs as SBBs.[85a]

Now, the SBLs approach will be considered in more detail as, as described in this dissertation, it was implemented and led to the formation of novel interesting frameworks that will be discussed in Chapter 3.

1.4.3.2.1. Supermolecular building layers

As mentioned earlier, the SBLs approach is a powerful design strategy that was introduced by Eddaoudi et al. in 2011 to aid the discovery and construction of more complex 3-P MOFs. Here, cross-linking or pillaring of 2-P sheets (the building units or SBLs) occurs through available bridging sites in the layers, such as open-metal sites and/or the ligands' functional groups.[13, 87]

To better understand this approach, it is important to remember that one of the ideal targets in crystal chemistry is the minimal edge-transitive 3-P nets (with one or two kinds of edges). These nets use edge-transitive 2-P layers (or 0-P MOPs when the SBBs strategy is applied), which have specific coding for the targeted net, as building units.

As far as 2-P nets are concerned, there are only five edge-transitive sheets that exist where targeting them and their corresponding pillared versions can significantly assist the rational design of unique MOFs.[28] These five edge-transitive sheets are the square lattice (**sql**), Kagome´ (**kgm**), honeycomb (**hcb**), Kagome´ dual (**kgd**) and hexagonal lattice (**hex**) (Figure 1.15 a).

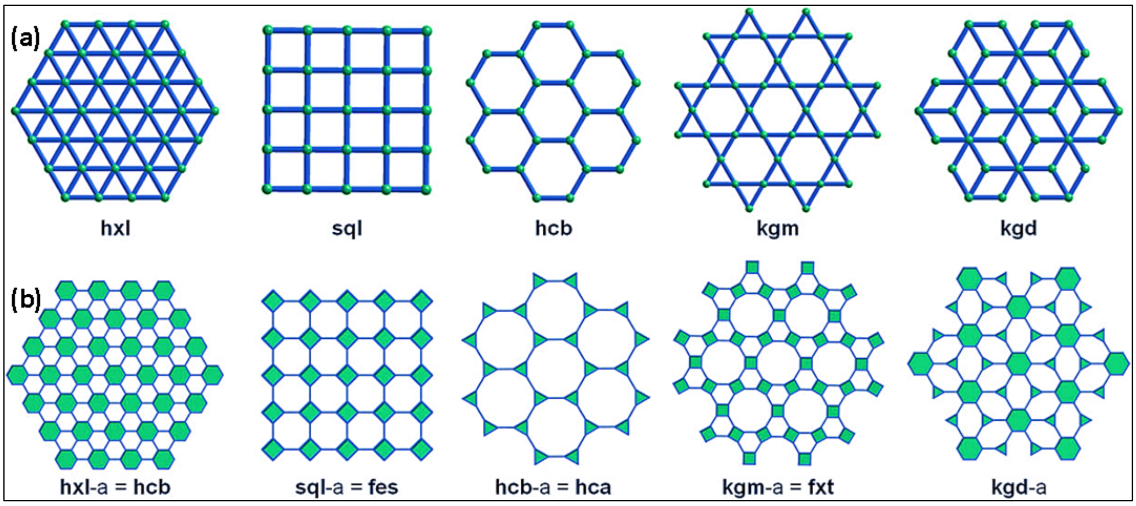

Figure 1.15 (a) The five 2-P edge-transitive sheets and (b) their augmented nets. Figure adapted with permission from Guillerm et al., 2014.[28]

Furthermore, when considered augmented, the **sql** and **kgm** can be viewed as solely composed of squares or 4-c vertices (Figure 1.15 b). Therefore, they can be targeted using metals that are known to form the 4-c dinuclear paddlewheel MBB, such as Cu, Zn, Ni, Fe, etc.[25, 87] Consequently, countless examples of 3-P pillared MOFs that have certain underlying network topologies constructed with designs utilizing pre-targeted SBLs can be found in the CSD.[72b]

There are many advantages to designing and constructing MOFs using the SBLs approach. For example, as the frameworks depend on the pillaring of constant 2-P layers, they can be endlessly modified through expanding their confined spaces (channels, cages or cavities) or altering their functionalities while their network topologies remain invariable. Besides this, based on the inherent modularity of the SBLs approach, specific applications can be targeted through introducing additional functional groups, e.g., introduction of free carboxylic acid groups to target CO_2 capture.[87]

Indeed, there are a variety of pillaring techniques to assist cross-linking the 2-P layers into sophisticated 3-P MOFs. These techniques are mainly ligand-to-ligand (L-L), axial-to-axial (A-A) and ligand-to-axial (L-A) in addition to a few others, such as the six-connected axial-to-axial pillars of **kgm** layers (6-c A-A).[28]

The **L-L** pillaring technique is contingent on the choice of ligands used. These ligands need to have two functional groups that, when combined with the appropriate metal within proper reaction conditions, will foster the formation of the 2-P layers and bridge them at the same time to form 3-P MOFs. One case in point is the use of di-isophthalates (containing tetracarboxylate groups, (Figure 1.16)) with the proper metal ions to form the 4-c paddlewheel MBBs that are the base of the **sql** or **kgm** layers, in turn simultaneously becoming pillared by the ligand to form a 3-P MOF with (4,4)-connected topology.[88]

The second technique is **A-A** pillaring that takes advantage of the open-metal sites, usually occupied by terminal ligands like water or DMF, in the already constructed 2-P layers. Therefore, ditopic-bridging ligands are used to replace the terminal ligands on adjacent layers, causing their pillaring into 3-P MOFs. The employed pillaring ligands are usually based on nitrogen donor moieties, such as bipyridine that can connect to the axial position of the paddlewheels (or other metal clusters) in adjacent 2-P layers bringing about the construction of 3-P MOFs that are based on the 6-c octahedral SBU (Figure 1.16).[89]

A new technique that was introduced by Eddaoudi et al. in 2011[13] is the **L-A** pillaring, combining the two previously known A-A and L-L pillaring strategies and utilizing trigonal multifunctional ligands that contain ditopic-bridging moieties – it is meant to pillar pre-targeted SBLs and grant access to higher dimensional MOFs (Figure 1.16).

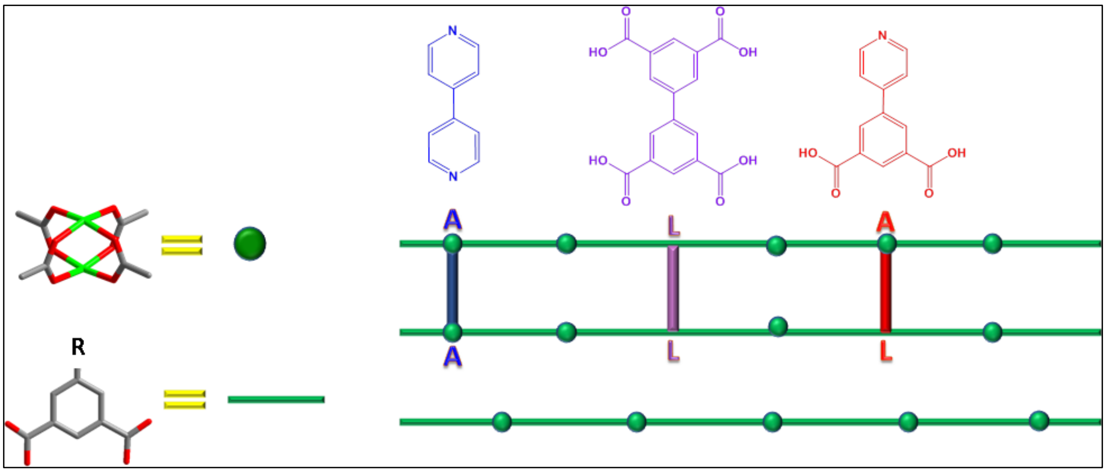

Figure 1.16 Schematic representation of the different MOFs pillaring techniques using demonstrative ligands; (blue) axial-to-axial, (purple) ligand-to-ligand and (red) ligand-to-axial pillaring.

In their study, Eddaoudi et al. made use of particular ligands with isophthalic acid cores that are functionalized at the 5-position with nitrogen donor moieties, such as pyridyl (Figure 1.17).[13]

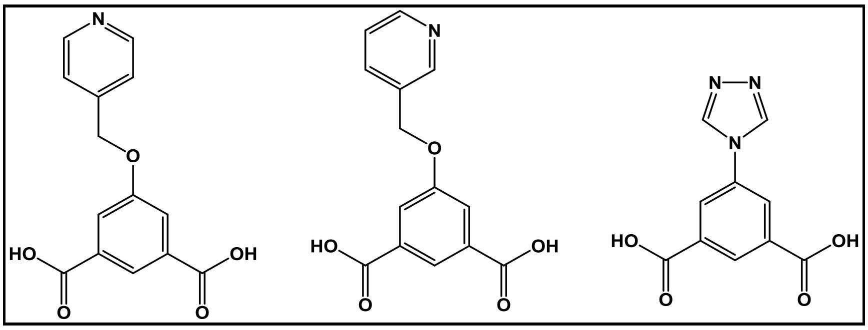

Figure 1.17 Ligands used by our group to build L-A pillared MOFs.

As expected, the carboxylate moieties, combined with appropriate metal ions in a favorable environment, formed the paddlewheel MBBs that are the basis of edge-transitive **kgm** or **sql** SBLs. Concurrently, the nitrogen donor moieties of the ligands coordinated to the axial positions of the paddlewheels in adjacent neighboring layers, inducing their pillaring and the formation of predicted (3,6)-connected 3-P MOFs. Here, the 3-connectivity is from the trigonal ligand and the 6-connecitvitiy is because of the formation of the octahedral SBUs after nitrogen coordination to the axial position of the paddlewheel.[75a] Therefore, this study paved the way for the utility of the unlimited number of trigonal ligands to design and synthesize an infinite number of new MOFs with tunable cavities that have different sizes and functionalities.[13]

Eddaoudi et al.'s groundbreaking approach was next utilized by our group to synthesize a variety of novel MOFs based on the pillaring of **kgm** or **sql** SBLs. The effect of functionalizing the pores with moieties that can impact prepared MOF behavior toward probe molecules, as well as the effect of altering the nitrogen donor position, were examined (Figure 1.18). These factors had an impact on gas uptake by the prepared frameworks - it was found that an increase in the associated CO_2 uptake occurred by simply modifying the nitrogen donor position of the ligands.[26b]

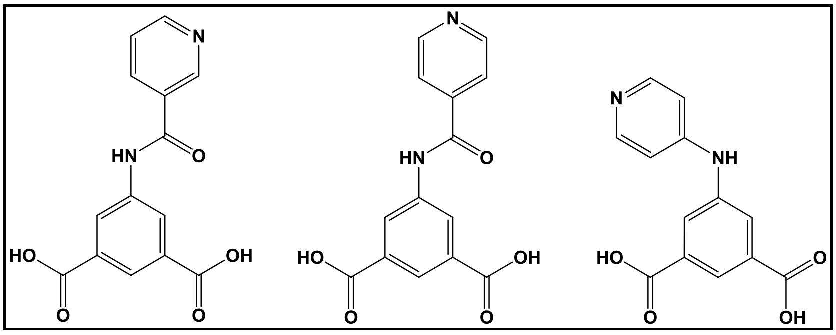

Figure 1.18 Ligands used to construct the L-A pillared MOFs and study the effect of altering the nitrogen position and the functionality of the ligands on gas uptake behavior of the constructed MOFs.

In general, to demonstrate how this technique can be used to target MOFs with specific underlying network topology, a survey of the RCSR database,[69] as conducted by Eddaoudi et al.[13, 28] showed that there are fifty one possible nets when targeting

(3,6)-connected frameworks. This number drops to six when the 2-P layers have **sql** topology and are constructed from octahedral SBUs linked by triangles. These six most plausible topologies are **pyr**, **rtl**, **anh**, **apo**, **ant** and **brk**. If the 2-P layers have **kgm** topology and are constructed from octahedral SBUs that are connected by triangles, the expected topology of the 3-P framework is **eea**.

In addition to the aforementioned pillaring techniques, several others were reported in the literature. These include the six-connected L-L (6-c L-L) or A-A (6-c A-A) pillars of **kgm** layers. These special types of pillaring emanate from the nature of **kgm** layers that have triangular and hexagonal pores and may need 6-c pillars between layers. In 2013, Zawarotko et al. developed trinuclear trigonal prism discrete clusters made from Cr salts decorated by six pyridyl moieties. These clusters were used as 6-c A-A pillars for the *in situ*-formed **kgm** SBLs to construct a series of functional pillared 3-P MOFs with **lon**-e topology and various functional groups (Figure 1.19).[90]

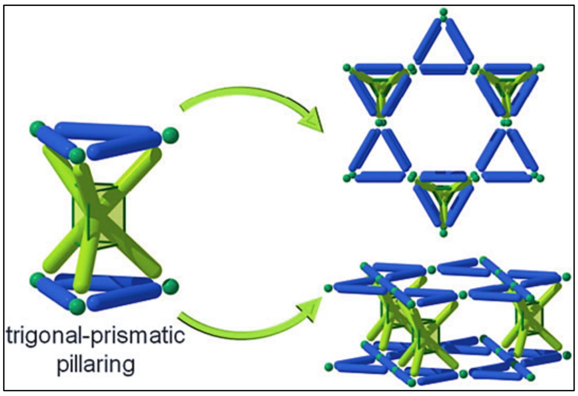

Figure 1.19 A representation of the 6-c A-A pillaring of kgm layers through trigonal prism pillars. Figure adapted with permission from Guillerm et al, 2014.[28]

Overall, by employing the introduced SBBs and SBLs approaches in combination with an ideal blueprint, designing MOFs with desired functionality is nearly a reality restricted only by imagination.[28]

In Chapter 3 of this dissertation, the L-A pillaring strategy was implemented and novel MOFs with interesting structures and properties were prepared and fully studied, to demonstrate the significance of this design strategy. In addition, the 6-c A-A pillaring approach was followed to create a functional 3-P MOF where the trigonal prism pillars are built solely from ligands rather than from metal clusters.

1.4.4. Potential applications of MOFs

As mentioned earlier, MOFs, with their unique properties, have a number of candidate applications, including gas storage and/or separation. Hence, one of the main objectives of this dissertation was to study gas sorption behavior of important pollutants and commodities, including CO_2, hydrogen (H_2) and methane (CH_4), in selected MOFs. Therefore, gas storage and separation in MOFs will be emphasized in the next section.

As well, over the course of the last decade, MOFs, with their unique chemical and physical properties in addition to their biochemical stability, became promising candidates for biomedical applications, like sensing and imaging. Moreover, and as a result of their homogenously distributed void spaces and windows, MOFs garnered interest as candidates for applications that require the encapsulation and/or release of functional guest molecules, such as, again, chemical sensing, in addition to catalysis, drug delivery, etc. Using MOFs as drug delivery vehicles is a distinct possibility and this dissertation will be highlighting this later.

Other applications of MOFs include magnetism, enantiomer separation and fabrication of luminescent and fluorescent materials.[91]

1.4.4.1. Energy-related applications

In recent years, the rapid increase in the global population, economic growth and industrial development have led to the rise in global energy demands and consumption.[92] These factors have created many environmental challenges with serious consequences for the planet, like global warming and ocean acidification.[93] Additionally, greenhouse gas emissions, such as CO_2, is responsible for 60% of global warming and mostly arises from the combustion of conventional carbon-based fossil fuels along with industrial chemical processes.[93a] So, in a means to maintain environmental sustainability, global efforts have been dedicated to improving current methods, and to develop new ones related to the capture and storage of CO_2 from various sources, including vehicle emissions and stationary post-combustion effluents, e.g., flue gas.[14d]

Currently, despite its many drawbacks, amine-scrubbing technology or the use of aqueous alkanolamine absorbents are still considered the state-of-the-art methods for post-combustion capture of CO_2.[94] The limitations of these approaches include the high regeneration energy costs because of the need for large amounts of heat during the regeneration process in addition to their liquid nature that is hard to handle and corrosive to their containers. Moreover, these materials suffer from diminishing performance over time from amine decomposition and have relative chemical instability upon heating with the generation of toxic by-products.[95]

These drawbacks necessitated the search for novel alternatives, such as traditional adsorbents that included activated carbons and zeolites, which have been the main constituents of porous materials with potential applications for gas storage and separation until relatively recently.[96] These methods have been widely studied as potential materials for CO_2 capture, but each has been demonstrated to possess many disadvantages, like low selectivity and low capacity.[42, 93a, 97] Consequently, the last two decades have witnessed the introduction of new classes of porous materials - polymers, covalent organic frameworks (COFs) and MOFs.[92b]

Generally, an optimal material for gas capture, storage and separation should have permanent porosity with an optimal SA, have a high degree of tunability and adjustable exposed internal surfaces and chemical functionalization to optimize uptake capacity. Also, it should possess a large capacity and selectivity for targeted gases at given pressures and temperatures, incur less energetic costs in its regeneration and be environmentally benign. Furthermore, the material should have unsaturated metal sites, highly-localized charge density or different functional groups on the ligand to enhance gas sorption energetics and increased selectivity at relatively low pressure (LP).[97-98]

These features are some of the characteristics of MOFs that make them promising candidates for targeted physisorption applications related to gases (gas capture, storage and/or separation) and strong competitors to activated carbon, chemical and zeolite-based sorbents.[8, 11b, 27, 58a]

It is worth mentioning that, over the past decade, MOFs were extensively explored as potential materials for the storage and separation of different gases.[14d, 42, 98c] Many studies have shown that MOFs with multifunctional groups, e.g., open metal sites and Lewis basic sites, like amino groups, have a tunable affinity toward CO_2 and could potentially lead to effective materials for its capture, storage and separation from binary mixtures.[99] Moreover, numerous reports have indicated that, to date, MOFs show superior performance concerning CO_2 and H_2 physisorption,[96b, 100] and a large number of MOFs were synthesized with the ability to reversibly adsorb and store CO_2 (Table 1.2).[95]

Table 1.2 CO_2 sorption capacities for selected MOFs

Material	SA (m^2/g)		CO_2 Adsorption		**Pressure**	**Temp**	**Ref**
	BET	**Lang.**	**wt%**	**mmol/g**	**(bar)**	**(K)**	
MOF-200	4530	10400	70.9		50	298	40b
MOF-177	4500	5340	60.8	33.5	50	298	40b
HKUST-1	1781		32		35	298	96b
PCN-61	3000	3500	50.8		35	298	101
Mg-MOF-74	1542		68.9		36	278	102
IR-MOF-11	2096		39.3		35	298	96b
IR-MOF-3	2160		45.1		35	298	96b
IR-MOF-6	2516		46.2		35	298	96b
IR-MOF-1	2833		48.8		35	298	96b
Cr-MIL-101	4230	5900	56.9	40	50	304	103
MOF-2	345		12.3		35	298	96b

In general, CO_2 capture, storage and separation are still challenging processes and the development of more efficient materials for these purposes is required, especially if fossil fuels will remain the primary energy supply in the decades to come.[92a]

Equally, global efforts have been invested in developing clean energy alternative fuels, such as H_2 and CH_4 (natural gas), for stationary and mobile applications, and finding ways for their storage and transportation with the goal of replacing the current carbon-based energy sources.[98a, 100b, 104] Additional efforts are being allocated to upgrading these fuels through reducing their impurities to a certain level before use, e.g., purify CH_4 from N_2, CO_2 and higher order hydrocarbons.[105] As their name implies, clean energy fuels do not cause environmental pollution as they significantly diminish the emissions of pollutants, such as CO_2.[106]

Further, it was found that H_2 energy is considered one of the most promising candidates in the present context based on its greater energy density among other chemical fuels.[100a, 107] However, at the present moment, no developed material for H_2 storage has satisfied the challenging U.S. Department of Energy (DOE) targets for on-board H_2 storage systems.[99c, 108] Therefore, further development of current systems and the search for novel materials that possess a large potential for H_2 storage, such as MOFs, are needed.[46, 108] To date, Al-**soc**-MOF is considered one of the best performing MOFs with an H_2 capacity of 11 wt% at a cryogenic temperature of 77 K and high pressure (HP) of 30 bar. In contrast, under ambient temperature conditions, MOFs typically have storage capacities that are not more than 1 wt%.[42-43, 109]

In the past, CH_4 storage in MOFs did not receive as much attention as that of H_2 and CO_2, though recently, many studies have shown that several MOFs have robust volumetric capacities for CH_4.[43, 110] The previous US-DOE volumetric working capacity target for CH_4 storage was 180 cm^3(STP)/cm^3, but it has since been increased to 263 cm^3 (STP: 273.15 K, 1 atm)/cm^3.[110a, 111] In addition, in the case of various earlier works in the literature, the upper limit boundary was usually 35 bar, a typical pipeline pressure, but more studies have been conducted at 65 bar, which is approximately the upper limit that can be reached with comparatively inexpensive two-stage compressors.[110a]

The deliverable or the working capacity of materials intended for energy storage in automotives should be evaluated between 5 bar (the lower limit for vehicle engine delivery of natural gas) and 35 bar (the optimal maximum pressure), but can go up to 50, 65 bar or even higher values.[110a]

In this dissertation, an exploratory synthesis that is based on electron-rich RE metal ions or transition metal ions and different polytopic hetero-functional ligands was initiated to study gas sorption behavior of CO_2, H_2 and CH_4 in selected MOFs.

1.4.4.2. Magnetism

Recently, magnetism was introduced within MOFs by using paramagnetic 3d transition metals (e.g., Cu, Fe, etc.) or lanthanides (Ln) nodes together with suitable organic linkers.[112] These MOFs have attracted a great deal of attention and are considered multifunctional materials because of the additional properties of the metal itself, including magnetism.[113]

In general, as a consequence of the interesting magnetic features from the single-ion anisotropy of Ln ions, Ln-based compounds are regarded as superb molecule-based magnetic materials.[79a] This can be attributed to the large ground-state spin of Ln ions as well as the related significant magnetic anisotropy.[114]

One of the interesting applications for Ln-based materials is magnetic refrigeration, where the magnetocaloric effect is utilized.[61b, 113] When compared to traditional coolant systems, such as gas-compression refrigeration, Ln-based coolants are safer and more environmentally friendly.

In this dissertation, an exploratory synthesis founded upon electron-rich Ln metal ions and different polytopic hetero-functional ligands was performed, and the magnetic behavior of selected MOFs evaluated.

1.4.4.3. Drug delivery

The methods of administering pharmaceutically-active compounds in humans or animals to achieve therapeutic effects are referred to as drug delivery systems (DDS).[115] There are many routes of drug administration to the body - some are invasive, like those involving intramuscular, subcutaneous, intravenous, etc. means, while others are non-invasive, such as transmucosal, transdermal, peroral, etc. methods.

In general, most conventional DDS are not always the most efficient for particular therapies because they have non-specific distribution when administered to the body, which happens to be the primary cause of mild, moderate or severe side effects. In addition, the rapid clearance of certain drugs necessities the administration of higher doses or the increase of the frequency of their administration, usually the main source of patient compliance reduction during treatment.[116] Furthermore, plasma concentrations of drugs delivered via conventional DDS show saw-tooth curves, i.e., the concentration of drug in the plasma is not constant.[117]

Therefore, better methods are necessary to address the aforementioned limitations, and the development of new DDS is required. This need is becoming even more acute because of the introduction of new biologic drugs, such as proteins and nucleic acids, to treat genetically-based diseases.[118] Additionally, when reformulating known drugs, their side effects may be minimized, and the frequency of drug administration can be reduced, ultimately leading to better patient compliance.[119]

Controlled drug delivery systems (CDDS) were developed to address an assortment of these known problems and to control the drug release profile, its absorption, distribution and elimination. Furthermore, CDDS assists in targeting specific areas of the body, e.g., cancer cells, while sparing healthy ones. Moreover, CDDS maintain therapeutic levels of the drug, improving product efficacy and safety as well as patient compliance.[117]

Specific examples of current CDDS include polymers, which are nonporous and come in different forms, including nanoparticles, micelles and dendrimers.[120] Various polymers have many advantages when used as drug delivery vehicles, like biocompatibility, biodegradability and the ease to functionalize and manipulate their structures. Besides these reasons, polymers also allow greater control of the pharmacokinetics and are demonstrated to be more stable drug carriers.[121] Conversely, polymers have many distinct disadvantages, such as premature degradation and subsequent release of active agents and heterogeneity of samples emanating from the difficulty in ensuring homogeneous distribution of the drug through the matrix, affecting the release differentially between samples.[122] Some known polymers used in drug delivery include stealth liposomes with polyethylene glycol (PEG), chitosan and polycaprolactone.[121a, 123]

Further well-known examples of CDDS are silica- and silicon-based, the most commonly investigated being mesoporous silica and porous silicon nanoparticles.[124] Silica mesoporous matrices are highly-ordered structures with large pore size, high pore volume (PV) and large SA; therefore, they exhibit more favorable properties, such as higher drug loading, when compared to that of amorphous colloidal and porous silica.[125] In addition, they are characterized by their chemical and thermal stability with excellent compatibilities with other materials. Moreover, a silanol (Si-O-H)-containing surface can be functionalized to foster better control over drug loading and release. However, these additional functional groups will result in pore size reduction as they occupy the walls, leading to decreasing drug loading capacity of the material. In addition, more efforts should be attempted to optimize the bioactivity and controlled drug delivery kinetics of the material.[125] Compared to silica-based systems, silicon-based ones have many advantages, but they also have several key disadvantages, including the wider pore size distribution.[124a] It is worth mentioning that the evaluation of aforementioned drug delivery systems was performed with various model drugs, such as erythromycin, ibuprofen (IBU), naproxen and captopril.[117, 126]

In summary, current CDDS are generally unsatisfactory and mostly demonstrate poor drug loading (usually < 5 wt%) with burst effect, the rapid release of a large initial dose of the drug upon administration. These drawbacks can specifically be seen in nonporous materials where the absence of well-defined pores makes it difficult to achieve satisfactory control over drug release. In addition, and as mentioned earlier, attempts to functionalize or graft organic molecules onto the walls of porous materials to elevate the amount of loaded drug may imply a decrease in drug-loading capacity.[127]

For efficient therapy, optimal CDDS should be biocompatible (non-toxic) and biodegradable with a controlled matrix degradation. In addition, they should efficiently entrap drugs with high payloads (high drug-loading capacity), provide controlled release and avoid “burst effect”. Furthermore, CDDS should allow easy surface engineering to preferentially associate with therapeutics and diagnostics. Likewise, these systems should be stable with reproducible formulations when preparing patches, pellets, tablets, etc., Moreover, for certain drug administration methods, such as the intravenous (IV), subcutaneous, intranasal, etc. the control over particle size of the delivery system is essential - nanoparticles are often necessary to circumvent tissue damage.[63a, 63b, 127]

During the last decade, MOFs, with their unique chemical and physical properties in addition to their biochemical stability, became promising candidates for medical applications - assortments of MOFs have emerged as potentially suitable materials for drug delivery.[128] These properties include, in addition to their intrinsic biodegradability, exceptionally large tunable pore sizes with high SAs for high drug-loading capacities, i.e., only very small amounts of material are required for the administration of high doses of drugs. Furthermore, MOFs are very modular -

biocompatible metals (e.g., Cu, Fe, Zn, Ni and Mg), ligands and/or solvents can be used for their preparation.[63a, 129] In this case, MOFs can either be exclusively drug carriers where drug molecules are loaded into the cavities of the framework or, when the ligand and/or metal of choice have pharmaceutical activity, the MOF itself can become the active ingredient with pharmaceutical effect.[127, 130]

MOFs are also characterized by their versatile functionality for post-synthetic grafting of drug molecules or changing the chemical properties of the framework.[131] As well, the pores of MOFs can be either hydrophobic, appropriate for drug molecules with poor aqueous solubility, or hydrophilically cationic or anionic in nature to encapsulate charged drugs.[63e] Moreover, the high structural flexibility of certain MOFs enables the adaptation of their porosity to the shape of the hosted molecule, which influences their drug release profile.[132]

Additionally, MOFs are well suited to serve as nanocarriers (NMOFs) for delivery and imaging applications, and in this case, their surface modification can result in stabilization of NMOFs suspensions, provide attractive “stealth” properties, ensure NMOFs reach the active sites and/or induce bioadhesive properties.[133]

The first MOFs that were studied as drug delivery vehicles are of the MIL (Material of Institute Lavoisier) Family. The particular study involving them was pioneered by Férey et al. in 2006, where they studied the loading/release of IBU (Figure 1.20), a non-steroidal anti-inflammatory drug (NSAID), into/from Cr-MIL-100 and MIL-101 (Figure 1.20). Even though Cr is a toxic metal, this investigation served as a proof-of-concept for the ability of MOFs, with their excellent crystallinity, to act as drug delivery vehicles.[128]

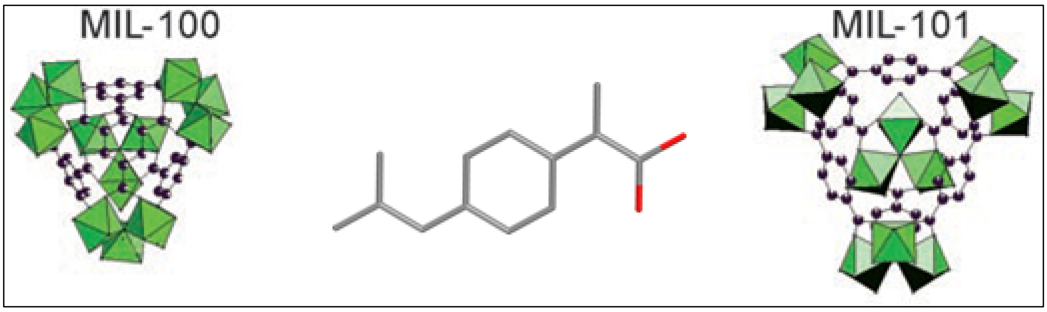

Figure 1.20 (Middle) The structure of IBU, (left) a MIL-100 cage and (right) a MIL-101 cage.[128]

Overall, Férey et al.'s work demonstrated that MIL-101 can adsorb unprecedentedly large amounts of IBU - a volume greater than the initial matrix weight (1.4 g IBU/g MIL-101) without losing the framework's crystallinity, much higher than any material previously studied for drug encapsulation. In addition, controlled drug release from this material was decidedly achieved.

Another study by Rosi et al. in 2009, where they assessed bio-MOF-1, an anionic framework, as a drug delivery vehicle for procainamide (Proc), a cationic antiarrhythmic drug (Figure 1.21).[134] Drug loading and release was accomplished through a cation exchange process. The maximum amount of drug loading was reached after 15 days of exchange and found to be 0.22 g/g material. Furthermore, drug release was complete after 72 h of soaking in simulated body fluid (SBF).

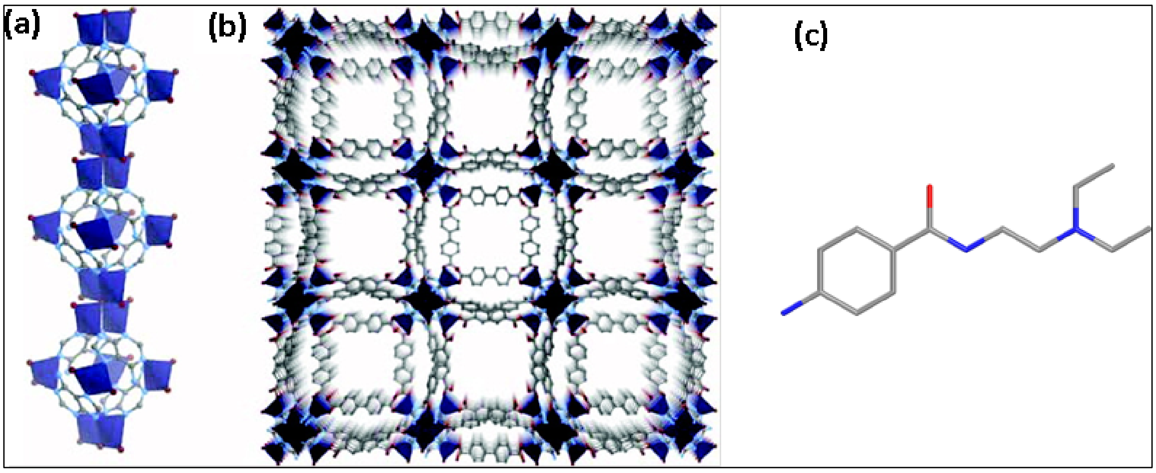

Figure 1.21 (a) Zinc-adeninate columns connected through biphenyldicarboxylate linkers to form (b) the 3-P framework of bio-MOF-1. (c) Proc structure. Zn = dark blue, C = dark gray, N = light blue and O = red. H atoms omitted for clarity. Figure adapted with permission from An et al., 2009.[134]

Later on, a biodegradable MOF was prepared with which the ligand used to construct the MOF is the active pharmaceutical ingredient (API). Therefore, drug release occurs as a result of framework degradation upon administration to the body.[130] Table 1.3 summarizes the results of some early examples of MOFs studied as drug delivery vehicles.

Table 1.3 A selection of the first trials where MOFs were studied as drug delivery vehicles.

MOF	Drug	Loading (%)	MOF properties	Drug release fast /complete	Ref
MIL-100-Cr	IBU	35	windows = 4.8 x 5.8 Å and 8.6 Å	2h/3d	128
MIL-101-Cr	IBU	140	windows = 12 Å and 14.7 x 16 Å	8h/6d	128
MIL-53-Cr and Fe	IBU	20	Flexible	3w	132
Bio-MOF-1-Zn	Proc	22	Anionic	20h/3d	134
BioMIL-1-Fe	Vit. B3 (ligand)	71.5	Biodegradable	Degradation/ 1h	130

Recently, certain MOFs have been demonstrated to possess the ability to encapsulate large biomolecules, like proteins, in their relatively small nanopores, a phenomenon that can be credited to the significant conformational changes of the protein during translocation into framework interior.[135] With this, Deng et al. in 2012 were able to expand the pore aperture of the well-known MOF-74 and to synthesize its isoreticular series (IRMOF-74-II to XI) with pore apertures ranging from 20 to 98 Å.[38] The SA of some members of this series, e.g., IRMOF-74-IX, was much higher than that reported for other crystalline materials known at the time, and they had the largest-ever reported pore apertures that were adequate for encapsulation of many natural proteins. This discovered ability to encapsulate proteins meant that MOFs may have additional significant biological applications, such as tissue engineering.

Since then, many other examples of using MOFs in biomedicine are seen in the literature for a range of drug molecules, including metronidazole, cidofovir, busulfan, azidothymidine triphosphate, doxorubicin, urea and others.[63e, 127, 136]

However, the field is still in its infancy and more remarkable results are expected, possibly resulting in an unlimited number of biomedical applications.

In general, with porous materials, drug loading into pores takes place via "soaking", where porous material particles are immersed in a concentrated solution of the model drug (provided they are stable in that solution).[137] This process is reversible and is driven by the charge or concentration gradient depending on the nature of both the drug and the framework. Therefore, the diffusion and adsorption equilibrium of the drug inside the pores are affected by the chemical properties of the porous material, its cavities and windows structures and sizes and its surface heterogeneity. In addition, the properties of drug molecules, such as structure, solubility, polarity, hydrophilic/hydrophobic nature and size and molecular weight, have a significant effect on drug loading.[63a, 129b, 136e]

In this dissertation, two different MOFs previously introduced by our group were investigated as potential drug delivery vehicles. The first was a zeolite-like MOF (ZMOF), namely In **rho**-ZMOF, an anionic framework that is prepared using 4,5-imidazoledicarboxylic acid (H_3ImDC).[75c] This framework was investigated as a delivery vehicle for the cationic antiarrhythmic drug, Proc. The second MOF was Cu **rht**-MOF-7,[85a] a neutral framework studied as a delivery carrier for the neutrally charged NSAID, IBU.

1.5. Dissertation structure and goals

This dissertation is structured into six chapters in which details of the main observations of our studies are discussed. Here, different design strategies used to target and construct novel MOF materials that are characterized and investigated for various applications, such as gas storage and separation as well as magnetization, were introduced. Moreover, neutral and anionic known MOFs were investigated as potential drug delivery vehicles. In general, various results will be introduced and considered in light of structure-function relationships.

Chapter 2 will cover the materials, methods and characterization techniques used and developed to construct novel MOFs and investigate their chemical structures and structure-function relationships concerning their application to gas storage or separation. In addition, the experimental techniques employed to study selected known MOFs as drug delivery vehicles are detailed. In other words, all experimental procedures, apparatus and standard operating procedures, including the synthesis of organic ligands, will be described.

In Chapter 3, a complete characterization of novel MOFs that were targeted and prepared using the SBLs design approach is put forth. As a continuation of our group's previous work,[13] we studied the effects of expanding the confined spaces (isoreticular chemistry), modifying their functionalities or introducing additional functional groups on the structure of prepared MOFs and their structure-function relationship. In addition, as gas storage/separation applications are in demand, gas sorption behavior of all the prepared structures and their isostructures and/or isoreticular structures was examined.

In Chapter 4, the synthesis of a variety of novel MOFs that are based on unprecedented RE-MBBs is reported, introducing the reaction conditions under which consistent *in situ* formation of these MBBs occurs and show the importance of using 2-FBA as a modulator during their synthesis. In addition, full characterization of the prepared MOFs was conducted, including their gas sorption behavior and magnetic properties.

In Chapter 5, the selected MOFs that were previously reported by our group, namely In **rho**-ZMOF and Cu **rht**-MOF-7, were evaluated as potential drug delivery vehicles. It is worth noting that even though In is regarded for its toxicity, the investigation of this framework served as a proof-of-concept as the study was conducted at a time when MOFs were newly introduced as drug delivery carriers.

Chapter 6 concludes this dissertation and outlines the main principles hypothesized for the rational design of novel MOFs targeted for a number of critical applications. Recommendations are provided for new MOFs development that leverages the various conclusions drawn from this dissertation.

1.6. REFERENCES

1. Eric Drexler, K., *Engines of Creation: The Coming Era of Nanotechnology*. Anchor Press/Doubleday: Garden City, New York, **1986**.

2. Shew, A., *B. Sci. Technol. Soc.* **2008,** *28*, 390-399.

3. (a) Whitesides, G. M.; Grzybowski, B., *Science* **2002,** *295*, 2418-2421.(b) Alkordi, M. H., *Glob. Cardiol. Sci. Pract.* **2013,** *2013*, 37-43.

4. (a) Lindsey, J. S., *New J. Chem.* **1991,** *15*, 153-179.(b) Whitesides, G. M.; Mathias, J. P.; Seto, C. T., *Science* **1991,** *254*, 1312-1319.

5. (a) Hosseini, M. W., *Accts. Chem. Res.* **2005,** *38*, 313-323.(b) Hosseini, M. W., *Chem. Commun.* **2005**, 5825-5829.

6. Bailar, J. C., *The chemistry of the coordination compounds*. Reinhold Pub. Corp.: New York, **1956**.

7. (a) Bourne, S. A.; Lu, J. J.; Mondal, A.; Moulton, B.; Zaworotko, M. J., *Angew. Chem. Int. Ed. Engl.* **2001,** *40*, 2111-2113.(b) Moulton, B.; Lu, J. J.; Mondal, A.; Zaworotko, M. J., *Chem. Commun.* **2001**, 863-864.

8. Cook, T. R.; Zheng, Y. R.; Stang, P. J., *Chem. Rev.* **2013,** *113*, 734-777.

9. (a) Eddaoudi, M.; Kim, J.; Wachter, J. B.; Chae, H. K.; O'Keeffe, M.; Yaghi, O. M., *J. Am. Chem. Soc.* **2001,** *123*, 4368-4369.(b) Prakash, M. J.; Lah, M. S., *Chem. Commun.* **2009**, 3326-3341.

10. Nouar, F.; Eubank, J. F.; Bousquet, T.; Wojtas, L.; Zaworotko, M. J.; Eddaoudi, M., *J. Am. Chem. Soc.* **2008,** *130*, 1833-1835.

11. (a) Allendorf, M. D.; Stavila, V., *CrystEngComm* **2015,** *17*, 229-246.(b) Ferey, G., *Chem. Soc. Rev.* **2008,** *37*, 191-214.

12. Batten, S. R.; Champness, N. R.; Chen, X. M.; Garcia-Martinez, J.; Kitagawa, S.; Ohrstrom, L.; O'Keeffe, M.; Suh, M. P.; Reedijk, J., *Pure Appl. Chem.* **2013,** *85*, 1715-1724.

13. Eubank, J. F.; Wojtas, L.; Hight, M. R.; Bousquet, T.; Kravtsov, V.; Eddaoudi, M., *J. Am. Chem. Soc.* **2011,** *133*, 17532-17535.

14. (a) Eddaoudi, M.; Li, H. L.; Reineke, T.; Fehr, M.; Kelley, D.; Groy, T. L.; Yaghi, O. M., *Top. Catal.* **1999,** *9*, 105-111.(b) Li, H.; Eddaoudi, M.; O'Keeffe, M.; Yaghi, O. M., *Nature* **1999,** *402*, 276-279.(c) Eddaoudi, M.; Kim, J.; Rosi, N.; Vodak,

D.; Wachter, J.; O'Keeffe, M.; Yaghi, O. M., *Science* **2002,** *295*, 469-472.(d) Zhou, H. C.; Long, J. R.; Yaghi, O. M., *Chem. Rev.* **2012,** *112*, 673-674.(e) Farha, O. K.; Hupp, J. T., *Accts. Chem. Res.* **2010,** *43*, 1166-1175.

15. (a) O'Keeffe, M.; Eddaoudi, M.; Li, H. L.; Reineke, T.; Yaghi, O. M., *J. Solid State Chem.* **2000,** *152*, 3-20.(b) Grunker, R.; Senkovska, I.; Biedermann, R.; Klein, N.; Lohe, M. R.; Muller, P.; Kaskel, S., *Chem. Commun.* **2011,** *47*, 490-492.(c) Li, H.; Shi, W.; Zhao, K.; Niu, Z.; Chen, X.; Cheng, P., *Chemistry* **2012,** *18*, 5715-5723.(d) Eddaoudi, M.; Sava, D. F.; Eubank, J. F.; Adil, K.; Guillerm, V., *Chem. Soc. Rev.* **2015,** *44*, 228-249.

16. (a) Hoskins, B. F.; Robson, R., *J. Am. Chem. Soc.* **1989,** *111*, 5962-5964.(b) Hoskins, B. F.; Robson, R., *J. Am. Chem. Soc.* **1990,** *112*, 1546-1554.

17. (a) James, S. L., *Chem. Soc. Rev.* **2003,** *32*, 276-288.(b) Long, J. R.; Yaghi, O. M., *Chem. Soc. Rev.* **2009,** *38*, 1213-1214.

18. (a) Alkordi, M. H.; Eddaoudi, M., Zeolitelike Metal–Organic Frameworks (ZMOFs): Design, Structure, and Properties. In *Supramol. Chem.*, John Wiley & Sons, Ltd: **2012**.(b) Luebke, R. Metal-Organic Frameworks: Building Block Design Strategies for the Synthesis of MOFs. King Abdullah University of Science and Technology, Thuwal, Kingdom of Saudi Arabia, **2014**.

19. Gardner, G. B.; Venkataraman, D.; Moore, J. S.; Lee, S., *Nature* **1995,** *374*, 792-795.

20. (a) Dinca, M.; Yu, A. F.; Long, J. R., *J. Am. Chem. Soc.* **2006,** *128*, 8904-8913.(b) Dinca, M.; Dailly, A.; Liu, Y.; Brown, C. M.; Neumann, D. A.; Long, J. R., *J. Am. Chem. Soc.* **2006,** *128*, 16876-16883.

21. (a) Li, H.; Eddaoudi, M.; Groy, T. L.; Yaghi, O. M., *J. Am. Chem. Soc.* **1998,** *120*, 8571-8572.(b) Yaghi, O. M.; Davis, C. E.; Li, G. M.; Li, H. L., *J. Am. Chem. Soc.* **1997,** *119*, 2861-2868.

22. (a) Eddaoudi, M.; Li, H. L.; Yaghi, O. M., *J. Am. Chem. Soc.* **2000,** *122*, 1391-1397.(b) Eddaoudi, M.; Li, H. L.; Reineke, T. M.; Yaghi, O. M., *Abstr. Pap. Am. Chem. Soc.* **1999,** *217*, U1048-U1049.

23. bosch, M., Zhang, M., Zhou, H., *Adv. Chem.* **2014**, Article ID 182327.

24. (a) Sun, D. F.; Collins, D. J.; Ke, Y. X.; Zuo, J. L.; Zhou, H. C., *Chem. Eur. J.* **2006,** *12*, 3768-3776.(b) Gao, J. K.; Ye, K. Q.; He, M.; Xiong, W. W.; Cao, W. F.; Lee, Z. Y.; Wang, Y.; Wu, T.; Huo, F. W.; Liu, X. G.; Zhang, Q. C., *J. Solid State Chem.* **2013,** *206*, 27-31.

25. Eddaoudi, M.; Kim, J.; Vodak, D.; Sudik, A.; Wachter, J.; O'Keeffe, M.; Yaghi, O. M., *Proc. Natl. Acad. Sci. USA* **2002,** *99*, 4900-4904.

26. (a) Du, L. T.; Lu, Z. Y.; Zheng, K. Y.; Wang, J. Y.; Zheng, X.; Pan, Y.; You, X. Z.; Bai, J. F., *J. Am. Chem. Soc.* **2013,** *135*, 562-565.(b) Chen, Z. J.; Adil, K.; Weselinski, L. J.; Belmabkhout, Y.; Eddaoudi, M., *J. Mater. Chem.* **2015,** *3*, 6276-6281.

27. Furukawa, H.; Cordova, K. E.; O'Keeffe, M.; Yaghi, O. M., *Science* **2013,** *341*, 1230444.

28. Guillerm, V.; Kim, D.; Eubank, J. F.; Luebke, R.; Liu, X.; Adil, K.; Lah, M. S.; Eddaoudi, M., *Chem. Soc. Rev.* **2014,** *43*, 6141-6172.

29. (a) MacGillivray, L., *Metal-organic frameworks: design and application*. Wiley: Hoboken, New Jersey, **2010**.(b) Rowsell, J. L.; Millward, A. R.; Park, K. S.; Yaghi, O. M., *J. Am. Chem. Soc.* **2004,** *126*, 5666-5667.

30. Yaghi, O. M.; O'Keeffe, M.; Ockwig, N. W.; Chae, H. K.; Eddaoudi, M.; Kim, J., *Nature* **2003,** *423*, 705-14.

31. Cohen, S. M., *Chem. Rev.* **2012,** *112*, 970-1000.

32. (a) Wang, C.; Liu, D. M.; Lin, W. B., *J. Am. Chem. Soc.* **2013,** *135*, 13222-13234.(b) Rowsell, J. L. C.; Yaghi, O. M., *Micropor. Mesopor. Mat.* **2004,** *73*, 3-14.

33. (a) Cohen, S. M., *Chem. Sci.* **2010,** *1*, 32-36.(b) Han, Y.; Li, J.-R.; Xie, Y.; Guo, G., *Chem. Soc. Rev.* **2014,** *43*, 5952-5981.(c) Lu, W.; Wei, Z.; Gu, Z.-Y.; Liu, T.-F.; Park, J.; Park, J.; Tian, J.; Zhang, M.; Zhang, Q.; Gentle Iii, T.; Bosch, M.; Zhou, H.-C., *Chem. Soc. Rev.* **2014,** *43*, 5561-5593.

34. Dinca, M.; Dailly, A.; Tsay, C.; Long, J. R., *Inorg. Chem.* **2008,** *47*, 11-13.

35. (a) Wang, X. J.; Li, P. Z.; Liu, L.; Zhang, Q.; Borah, P.; Wong, J. D.; Chan, X. X.; Rakesh, G.; Li, Y.; Zhao, Y., *Chem. Commun.* **2012,** *48*, 10286-10288.(b) Jhung, S. H.; Khan, N. A.; Hasan, Z., *CrystEngComm* **2012,** *14*, 7099-7109.

36. Chandrasekhar, V.; Das, S.; Dey, A.; Hossain, S.; Sutter, J. P., *Inorg. Chem.* **2013,** *52*, 11956-11965.

37. Nouar, F.; Eckert, J.; Eubank, J. F.; Forster, P.; Eddaoudi, M., *J. Am. Chem. Soc.* **2009,** *131*, 2864-2870.

38. Deng, H. X.; Grunder, S.; Cordova, K. E.; Valente, C.; Furukawa, H.; Hmadeh, M.; Gandara, F.; Whalley, A. C.; Liu, Z.; Asahina, S.; Kazumori, H.; O'Keeffe, M.; Terasaki, O.; Stoddart, J. F.; Yaghi, O. M., *Science* **2012,** *336*, 1018-1023.

39. Furukawa, H.; Go, Y. B.; Ko, N.; Park, Y. K.; Uribe-Romo, F. J.; Kim, J.; O’Keeffe, M.; Yaghi, O. M., *Inorg. Chem.* **2011,** *50*, 9147-9152.

40. (a) Farha, O. K.; Eryazici, I.; Jeong, N. C.; Hauser, B. G.; Wilmer, C. E.; Sarjeant, A. A.; Snurr, R. Q.; Nguyen, S. T.; Yazaydin, A. O.; Hupp, J. T., *J. Am. Chem. Soc.* **2012,** *134*, 15016-15021.(b) Furukawa, H.; Ko, N.; Go, Y. B.; Aratani, N.; Choi, S. B.; Choi, E.; Yazaydin, A. O.; Snurr, R. Q.; O'Keeffe, M.; Kim, J.; Yaghi, O. M., *Science* **2010,** *329*, 424-428.

41. Chae, H. K.; Siberio-Perez, D. Y.; Kim, J.; Go, Y.; Eddaoudi, M.; Matzger, A. J.; O'Keeffe, M.; Yaghi, O. M., *Nature* **2004,** *427*, 523-527.

42. Farha, O. K.; Yazaydin, A. O.; Eryazici, I.; Malliakas, C. D.; Hauser, B. G.; Kanatzidis, M. G.; Nguyen, S. T.; Snurr, R. Q.; Hupp, J. T., *Nat. Chem.* **2010,** *2*, 944-948.

43. Alezi, D.; Belmabkhout, Y.; Suyetin, M.; Bhatt, P. M.; Weselinski, L. J.; Solovyeva, V.; Adil, K.; Spanopoulos, I.; Trikalitis, P. N.; Emwas, A. H.; Eddaoudi, M., *J. Am. Chem. Soc.* **2015,** *137*, 13308-13318.

44. Koh, K.; Wong-Foy, A. G.; Matzger, A. J., *J. Am. Chem. Soc.* **2009,** *131*, 4184-4185.

45. Klein, N.; Senkovska, I.; Baburin, I. A.; Grunker, R.; Stoeck, U.; Schlichtenmayer, M.; Streppel, B.; Mueller, U.; Leoni, S.; Hirscher, M.; Kaskel, S., *Chemistry* **2011,** *17*, 13007-13016.

46. Furukawa, H., miller, M., Yaghi, O., *J. Mater. Chem.* **2007,** *17*, 3197-3204.

47. An, J.; Farha, O. K.; Hupp, J. T.; Pohl, E.; Yeh, J. I.; Rosi, N. L., *Nat. Commun.* **2012,** *3*, 604.

48. Ferey, G.; Mellot-Draznieks, C.; Serre, C.; Millange, F.; Dutour, J.; Surble, S.; Margiolaki, I., *Science* **2005,** *309*, 2040-2042.

49. Koh, K.; Wong-Foy, A. G.; Matzger, A. J., *Angew. Chem. Int. Ed. Engl.* **2008,** *47*, 677-680.

50. Zhao, D.; Yuan, D.; Sun, D.; Zhou, H. C., *J. Am. Chem. Soc.* **2009,** *131*, 9186-9188.

51. Wang, Z.; Tanabe, K. K.; Cohen, S. M., *Chemistry* **2010,** *16*, 212-217.

52. Kaye, S. S.; Dailly, A.; Yaghi, O. M.; Long, J. R., *J. Am. Chem. Soc.* **2007,** *129*, 14176-14177.

53. Park, H. J.; Lim, D. W.; Yang, W. S.; Oh, T. R.; Suh, M. P., *Chemistry* **2011,** *17*, 7251-7260.

54. Lin, X.; Telepeni, I.; Blake, A. J.; Dailly, A.; Brown, C. M.; Simmons, J. M.; Zoppi, M.; Walker, G. S.; Thomas, K. M.; Mays, T. J.; Hubberstey, P.; Champness, N. R.; Schroder, M., *J. Am. Chem. Soc.* **2009,** *131*, 2159-2171.

55. Denysenko, D.; Grzywa, M.; Tonigold, M.; Streppel, B.; Krkljus, I.; Hirscher, M.; Mugnaioli, E.; Kolb, U.; Hanss, J.; Volkmer, D., *Chemistry* **2011,** *17*, 1837-1848.

56. Leach, A. R., *Molecular modelling: principles and applications*. Pearson education: New Jersey, **2001**.

57. Zhang, J.-P.; Liao, P.-Q.; Zhou, H.-L.; Lin, R.-B.; Chen, X.-M., *Chem. Soc. Rev.* **2014,** *43*, 5789-5814.

58. (a) Li, J. R.; Sculley, J.; Zhou, H. C., *Chem. Rev.* **2012,** *112*, 869-932.(b) Herm, Z. R., Bolch, E.D, Long, J.R., *Chem. Mater.* **2013,** *26*, 323-338.(c) Herm, Z. R.; Wiers, B. M.; Mason, J. A.; van Baten, J. M.; Hudson, M. R.; Zajdel, P.; Brown, C. M.; Masciocchi, N.; Krishna, R.; Long, J. R., *Science* **2013,** *340*, 960-964.(d) First, E. L.; Gounaris, C. E.; Floudas, C. A., *Langmuir* **2013,** *29*, 5599-5608.(e) Zou, R. Q.; Abdel-Fattah, A. I.; Xu, H. W.; Zhao, Y. S.; Hickmott, D. D., *CrystEngComm* **2010,** *12*, 1337-1353.

59. (a) Zhang, Z.; Zhang, L.; Wojtas, L.; Nugent, P.; Eddaoudi, M.; Zaworotko, M. J., *J. Am. Chem. Soc.* **2012,** *134*, 924-927.(b) Alkordi, M. H.; Liu, Y.; Larsen, R. W.; Eubank, J. F.; Eddaoudi, M., *J. Am. Chem. Soc.* **2008,** *130*, 12639-12641.(c) Liu, J.; Chen, L.; Cui, H.; Zhang, J.; Zhang, L.; Su, C.-Y., *Chem. Soc. Rev.* **2014,** *43*, 6011-6061.(d) Zhang, Z.; Zhang, L.; Wojtas, L.; Eddaoudi, M.; Zaworotko, M. J., *J. Am. Chem. Soc.* **2012,** *134*, 928-933.

60. (a) Li, H. W.; Feng, X.; Guo, Y. X.; Chen, D. D.; Li, R.; Ren, X. Q.; Jiang, X.; Dong, Y. P.; Wang, B., *Sci. Rep.* **2014,** *4*.(b) Liu, D. M.; Lu, K. D.; Poon, C.; Lin, W. B., *Inorg. Chem.* **2014,** *53*, 1916-1924.

61. (a) Biswas, S.; Jena, H. S.; Adhikary, A.; Konar, S., *Inorg. Chem.* **2014,** *53*, 3926-3928.(b) Lorusso, G.; Sharples, J. W.; Palacios, E.; Roubeau, O.; Brechin, E. K.; Sessoli, R.; Rossin, A.; Tuna, F.; McInnes, E. J.; Collison, D., *Adv. Mater.* **2013,** *25*, 4653-4656.(c) Coronado, E.; Mínguez Espallargas, G., *Chem. Soc. Rev.* **2013,** *42*, 1525-1539.(d) Hu, H.-C.; Kang, X.-M.; Cao, C.-S.; Cheng, P.; Zhao, B., *Chem. Commun.* **2015,** *51*, 10850-10853.(e) Wang, R. Y.; Zhang, C. Y.; Wang, S. P.; Zhou, Y. Y., *Prog. Chem.* **2015,** *27*, 945-952.(f) Wu, Y. N.; Zhou, M. M.; Li, S.; Li, Z. H.; Li, J.; Wu, A. Z.; Li, G. T.; Li, F. T.; Guan, X. H., *Small* **2014,** *10*, 2927-2936.

62. (a) Jeong, N. C.; Samanta, B.; Lee, C. Y.; Farha, O. K.; Hupp, J. T., *J. Am. Chem. Soc.* **2012,** *134*, 51-54.(b) Sadakiyo, M.; Yamada, T.; Kitagawa, H., *J. Am. Chem. Soc.* **2009,** *131*, 9906-9907.(c) Shigematsu, A.; Yamada, T.; Kitagawa, H., *J. Am. Chem. Soc.* **2011,** *133*, 2034-2036.

63. (a) Huxford, R. C.; Della Rocca, J.; Lin, W. B., *Curr. Opin. Chem. Biol.* **2010,** *14*, 262-268.(b) Della Rocca, J.; Liu, D. M.; Lin, W. B., *Accts. Chem. Res.* **2011,** *44*, 957-968.(c) Bellido, E.; Hidalgo, T.; Lozano, M. V.; Guillevic, M.; Simon-Vazquez, R.; Santander-Ortega, M. J.; Gonzalez-Fernandez, A.; Serre, C.; Alonso, M. J.; Horcajada, P., *Adv. Healthc. Mater.* **2015,** *4*, 1246-1257.(d) Zhuang, J.; Kuo, C. H.; Chou, L. Y.; Liu, D. Y.; Weerapana, E.; Tsung, C. K., *ACS Nano* **2014,** *8*, 2812-2819.(e) Ma, D. Y.; Li, Z.; Xiao, J. X.; Deng, R.; Lin, P. F.; Chen, R. Q.; Liang, Y. Q.; Guo, H. F.; Liu, B.; Liu, J. Q., *Inorg. Chem.* **2015,** *54*, 6719-6726.

64. Foucault-Collet, A.; Gogick, K. A.; White, K. A.; Villette, S.; Pallier, A.; Collet, G.; Kieda, C.; Li, T.; Geib, S. J.; Rosi, N. L.; Petoud, S., *Proc. Natl. Acad. Sci. USA* **2013,** *110*, 17199-17204.

65. (a) Blight, B. A.; Guillet-Nicolas, R.; Kleitz, F.; Wang, R. Y.; Wang, S. N., *Inorg. Chem.* **2013,** *52*, 1673-1675.(b) Wang, X. W.; Chen, J.-Z.; Liu, J.-H., *Cryst. Growth Des.* **2007,** *7*, 1227-1229.

66. O'Keeffe, M.; Yaghi, O. M., *Chem. Rev.* **2012,** *112*, 675-702.

67. (a) O'Keeffe, M.; Hyde, S. T., *Zeolites* **1997,** *19*, 370-374.(b) Ohrstrom, L., *Crystals* **2015,** *5*, 154-162.

68. O’Keeffe, M., Reticular Chemistry Structure Resource, http://rcsr.anu.edu.au/.

69. O'Keeffe, M.; Peskov, M. A.; Ramsden, S. J.; Yaghi, O. M., *Accts. Chem. Res.* **2008,** *41*, 1782-1789.

70. *SYSTRE* (1.2). http://gavrog.org/Systre-Help.html

71. (a) Blatov, V. A.; Shevchenko, A. P.; Serezhkin, V. N., *J. Appl. Crystallogr.* **2000,** *33*, 1193.(b) Blatov, V. A., *Struct. Chem.* **2012,** *23*, 955-963.

72. (a) Cambridge Structural Database (CSD), http://www.ccdc.cam.ac.uk/products/csd/statistics/. (b) Allen, F. H., *Acta Crystallogr., Sect. B: Struct. Sci.* **2002,** *58*, 380-388.

73. Perry, J. J.; Perman, J. A.; Zaworotko, M. J., *Chem. Soc. Rev.* **2009,** *38*, 1400-1417.

74. Wells, A. F., *Three dimensional nets and polyhedra*. Wiley: New York, **1977**.

75. (a) Eddaoudi, M.; Moler, D. B.; Li, H.; Chen, B.; Reineke, T. M.; O'Keeffe, M.; Yaghi, O. M., *Accts. Chem. Res.* **2001,** *34*, 319-330.(b) Moulton, B.; Zaworotko, M. J., *Chem. Rev.* **2001,** *101*, 1629-1658.(c) Liu, Y.; Kravtsov, V.; Larsen, R.; Eddaoudi, M., *Chem. Commun.* **2006**, 1488-1490.

76. Alezi, D.; Peedikakkal, A. M.; Weselinski, L. J.; Guillerm, V.; Belmabkhout, Y.; Cairns, A. J.; Chen, Z.; Wojtas, L.; Eddaoudi, M., *J. Am. Chem. Soc.* **2015,** *137*, 5421-5430.

77. (a) Guillerm, V.; Weselinski, L.; Belmabkhout, Y.; Cairns, A. J.; D'Elia, V.; Wojtas, L.; Adil, K.; Eddaoudi, M., *Nat. Chem.* **2014,** *6*, 673-680.(b) Xue, D. X.; Cairns, A. J.; Belmabkhout, Y.; Wojtas, L.; Liu, Y.; Alkordi, M. H.; Eddaoudi, M., *J. Am. Chem. Soc.* **2013,** *135*, 7660-7667.(c) Eubank, J. F.; Nouar, F.; Luebke, R.; Cairns, A. J.; Wojtas, L.; Alkordi, M.; Bousquet, T.; Hight, M. R.; Eckert, J.; Embs, J. P.; Georgiev, P. A.; Eddaoudi, M., *Angew. Chem. Int. Ed. Engl.* **2012,** *51*, 10099-10103.

78. (a) Morris, W.; Volosskiy, B.; Demir, S.; Gandara, F.; McGrier, P. L.; Furukawa, H.; Cascio, D.; Stoddart, J. F.; Yaghi, O. M., *Inorg. Chem.* **2012,** *51*, 6443-6445.(b) Guillerm, V.; Ragon, F.; Dan-Hardi, M.; Devic, T.; Vishnuvarthan, M.; Campo, B.; Vimont, A.; Clet, G.; Yang, Q.; Maurin, G.; Ferey, G.; Vittadini, A.; Gross, S.; Serre, C., *Angew. Chem. Int. Ed. Engl.* **2012,** *51*, 9267-9271.(c) Cavka, J. H.; Jakobsen, S.; Olsbye, U.; Guillou, N.; Lamberti, C.; Bordiga, S.; Lillerud, K. P., *J. Am. Chem. Soc.* **2008,** *130*, 13850-13851.(d) Dan-Hardi, M.; Serre, C.; Frot, T.; Rozes, L.; Maurin, G.; Sanchez, C.; Ferey, G., *J. Am. Chem. Soc.* **2009,** *131*, 10857-10859.(e) Guillerm, V.; Gross, S.; Serre, C.; Devic, T.; Bauer, M.; Ferey, G., *Chem. Commun.* **2010,** *46*, 767-769.

79. (a) Roy, S.; Chakraborty, A.; Maji, T. K., *Coordin. Chem. Rev.* **2014,** *273*, 139-164.(b) Devic, T.; Serre, C.; Audebrand, N.; Marrot, J.; Ferey, G., *J. Am. Chem. Soc.* **2005,** *127*, 12788-12789.(c) Park, Y. K.; Choi, S. B.; Kim, H.; Kim, K.; Won, B. H.; Choi, K.; Choi, J. S.; Ahn, W. S.; Won, N.; Kim, S.; Jung, D. H.; Choi, S. H.; Kim, G. H.; Cha, S. S.; Jhon, Y. H.; Yang, J. K.; Kim, J., *Angew. Chem. Int. Ed. Engl.* **2007,** *46*, 8230-8233.(d) Luo, J. H.; Xu, H. W.; Liu, Y.; Zhao, Y. S.; Daemen, L. L.; Brown, C.; Timofeeva, T. V.; Ma, S. Q.; Zhou, H. C., *J. Am. Chem. Soc.* **2008,** *130*, 9626.

80. Luebke, R.; Belmabkhout, Y.; Weselinski, L. J.; Cairns, A. J.; Alkordi, M.; Norton, G.; Wojtas, L.; Adil, K.; Eddaoudi, M., *Chem. Sci.* **2015,** *6*, 4095-4102.

81. Guillerm, V.; Weselinski, L. J.; Alkordi, M.; Mohideen, M. I.; Belmabkhout, Y.; Cairns, A. J.; Eddaoudi, M., *Chem. Commun.* **2014,** *50*, 1937-1940.

82. (a) Evans, J. D.; Sumby, C. J.; Doonan, C. J., *Chem. Soc. Rev.* **2014,** *43*, 5933-5951.(b) Li, J.; Huang, P.; Wu, X. R.; Tao, J.; Huang, R. B.; Zheng, L. S., *Chem. Sci.* **2013,** *4*, 3232-3238.

83. Cairns, A. J.; Perman, J. A.; Wojtas, L.; Kravtsov, V.; Alkordi, M. H.; Eddaoudi, M.; Zaworotko, M. J., *J. Am. Chem. Soc.* **2008,** *130*, 1560-1561.

84. (a) Liu, Y.; Kravtsov, V.; Walsh, R. D.; Poddar, P.; Srikanth, H.; Eddaoudi, M., *Chem. Commun.* **2004**, 2806-2807.(b) Alkordi, M. H.; Brant, J. A.; Wojtas, L.; Kravtsov, V.; Cairns, A. J.; Eddaoudi, M., *J. Am. Chem. Soc.* **2009,** *131*, 17753-17755.

85. (a) Luebke, R.; Eubank, J. F.; Cairns, A. J.; Belmabkhout, Y.; Wojtas, L.; Eddaoudi, M., *Chem. Commun.* **2012,** *48*, 1455-1457.(b) Luebke, R.; Weselinski, L. J.; Belmabkhout, Y.; Chen, Z. J.; Wojtas, L.; Eddaoudi, M., *Cryst. Growth Des.* **2014,** *14*, 414-418.

86. Xue, D. X.; Belmabkhout, Y.; Shekhah, O.; Jiang, H.; Adil, K.; Cairns, A. J.; Eddaoudi, M., *J. Am. Chem. Soc.* **2015,** *137*, 5034-5040.

87. Eubank, J. F.; Mouttaki, H.; Cairns, A. J.; Belmabkhout, Y.; Wojtas, L.; Luebke, R.; Alkordi, M.; Eddaoudi, M., *J. Am. Chem. Soc.* **2011,** *133*, 14204-14207.

88. (a) Chen, B.; Ockwig, N. W.; Millward, A. R.; Contreras, D. S.; Yaghi, O. M., *Angew. Chem. Int. Ed. Engl.* **2005,** *44*, 4745-4749.(b) Lin, X.; Jia, J. H.; Zhao, X. B.; Thomas, K. M.; Blake, A. J.; Walker, G. S.; Champness, N. R.; Hubberstey, P.; Schroder, M., *Angew. Chem. Int. Ed. Engl.* **2006,** *45*, 7358-7364.

89. (a) Chang, Z.; Zhang, D. S.; Chen, Q.; Li, R. F.; Hu, T. L.; Bu, X. H., *Inorg. Chem.* **2011,** *50*, 7555-7562.(b) Tan, Y. X.; He, Y. P.; Zhang, J., *Inorg. Chem.* **2012,** *51*, 9649-9654.

90. Schoedel, A.; Boyette, W.; Wojtas, L.; Eddaoudi, M.; Zaworotko, M. J., *J. Am. Chem. Soc.* **2013,** *135*, 14016-14019.

91. Kuppler, R. J.; Timmons, D. J.; Fang, Q.-R.; Li, J.-R.; Makal, T. A.; Young, M. D.; Yuan, D.; Zhao, D.; Zhuang, W.; Zhou, H.-C., *Coordin. Chem. Rev.* **2009,** *253*, 3042-3066.

92. (a) Baba, U. M.; Kamarudin, K. S. N.; Alias, N., *IJCEE* **2010,** *1*, 40-46.(b) Eddaoudi, M.; Barbour, L. J., *Chem. Commun.* **2015,** *51*, 5554-5555.(c) Mikkelsen, M.; Jorgensen, M.; Krebs, F. C., *Energy Environ. Sci.* **2010,** *3*, 43-81.

93. (a) Sumida, K.; Rogow, D. L.; Mason, J. A.; McDonald, T. M.; Bloch, E. D.; Herm, Z. R.; Bae, T. H.; Long, J. R., *Chem. Rev.* **2012,** *112*, 724-781.(b) Pearson, P. N.; Palmer, M. R., *Nature* **2000,** *406*, 695-699.

94. Rochelle, G. T., *Science* **2009,** *325*, 1652-1654.

95. Liu, Y. Y.; Wang, Z. Y. U.; Zhou, H. C., *GHG* **2012,** *2*, 239-259.

96. (a) Yong, Z.; Mata, V.; Rodrigues, A. E., *Sep. Purif. Technol.* **2002,** *26*, 195-205.(b) Millward, A. R.; Yaghi, O. M., *J. Am. Chem. Soc.* **2005,** *127*, 17998-17999.

97. Liu, Y., Wang, Z. U., Zhou, H-C., *GHG* **2012,** *2*, 239-259.

98. (a) Duren, T.; Sarkisov, L.; Yaghi, O. M.; Snurr, R. Q., *Langmuir* **2004,** *20*, 2683-2689.(b) Menon, V. C.; Komarneni, S., *J. Porous Mat.* **1998,** *5*, 43-58.(c) Li, J.

R.; Ma, Y. G.; McCarthy, M. C.; Sculley, J.; Yu, J. M.; Jeong, H. K.; Balbuena, P. B.; Zhou, H. C., *Coordin. Chem. Rev.* **2011,** *255*, 1791-1823.(d) Wang, Q.; Zhong, Z., *Energy Environ. Sci.* **2014,** *7,* 3478-3518.

99. (a) Zhang, Z.; Zhao, Y.; Gong, Q.; Li, Z.; Li, J., *Chem. Commun.* **2013,** *49*, 653-661.(b) Poloni, R.; Lee, K.; Berger, R. F.; Smit, B.; Neaton, J. B., *J. Phys. Chem. Lett.* **2014,** *5*, 861-865.(c) Guo, Z.; Wu, H.; Srinivas, G.; Zhou, Y.; Xiang, S.; Chen, Z.; Yang, Y.; Zhou, W.; O'Keeffe, M.; Chen, B., *Angew. Chem. Int. Ed. Engl.* **2011,** *50*, 3178-3181.(d) Caskey, S. R.; Wong-Foy, A. G.; Matzger, A. J., *J. Am. Chem. Soc.* **2008,** *130*, 10870-10871.

100.(a) Queen, W. L.; Bloch, E. D.; Brown, C. M.; Hudson, M. R.; Mason, J. A.; Murray, L. J.; Ramirez-Cuesta, A. J.; Peterson, V. K.; Long, J. R., *Dalton Trans.* **2012,** *41*, 4180-4187.(b) Suh, M. P.; Park, H. J.; Prasad, T. K.; Lim, D. W., *Chem. Rev.* **2012,** *112*, 782-835.(c) Wong-Foy, A. G.; Matzger, A. J.; Yaghi, O. M., *J. Am. Chem. Soc.* **2006,** *128*, 3494-3495.

101.Yuan, D. Q.; Zhao, D.; Sun, D. F.; Zhou, H. C., *Angew. Chem. Int. Edit.* **2010,** *49*, 5357-5361.

102.Dietzel, P. D. C.; Besikiotis, V.; Blom, R., *J. Mat. Chem.* **2009,** *19*, 7362-7370.

103.Llewellyn, P. L.; Bourrelly, S.; Serre, C.; Vimont, A.; Daturi, M.; Hamon, L.; De Weireld, G.; Chang, J. S.; Hong, D. Y.; Hwang, Y. K.; Jhung, S. H.; Ferey, G., *Langmuir* **2008,** *24*, 7245-7250.

104.(a) Liu, Y.; Eubank, J. F.; Cairns, A. J.; Eckert, J.; Kravtsov, V.; Luebke, R.; Eddaoudi, M., *Angew. Chem. Int. Ed. Engl.* **2007,** *46*, 3278-3283.(b) Liu, D. M.; Wu, H. H.; Wang, S. Z.; Xie, Z. G.; Li, J.; Lin, W. B., *Chem. Sci.* **2012,** *3*, 3032-3037.

105.Chaemchuen, S.; Kabir, N. A.; Zhou, K.; Verpoort, F., *Chem. Soc. Rev.* **2013,** *42*, 9304-9332.

106.Li, S. L.; Xu, Q., *Energy Environ. Sci.* **2013,** *6*, 1656-1683.

107.(a) Murray, L. J.; Dinca, M.; Long, J. R., *Chem. Soc. Rev.* **2009,** *38*, 1294-1314.(b) Fang, Q. R.; Yuan, D. Q.; Sculley, J.; Lu, W. G.; Zhou, H. C., *Chem. Commun.* **2012,** *48*, 254-256.

108.Sculley, J.; Yuan, D.; Zhou, H.-C., *Energy Environ. Sci.* **2011,** *4*, 2721-2735.

109.Langmi, H. W.; Ren, J. W.; North, B.; Mathe, M.; Bessarabov, D., *Electrochim. Acta* **2014,** *128*, 368-392.

110.(a) Peng, Y.; Krungleviciute, V.; Eryazici, I.; Hupp, J. T.; Farha, O. K.; Yildirim, T., *J. Am. Chem. Soc.* **2013,** *135*, 11887-11894.(b) He, Y.; Zhou, W.; Qian, G.; Chen, B., *Chem. Soc. Rev.* **2014,** *43*, 5657-5678.

111.Burchell, T.; Rogers, M., *SAE Technical Paper* **2000**, 2000-01-2205.

112.Dey, C.; Kundu, T.; Biswal, B. P.; Mallick, A.; Banerjee, R., *Acta Crystallogr. Sect. B-Struct. Sci.* **2014,** *70*, 3-10.

113.Biswas, S.; Jena, H. S.; Goswami, S.; Sanda, S.; Konar, S., *Cryst. Growth Des.* **2014,** *14*, 1287-1295.

114.(a) Gatteschi, D.; Sessoli, R.; Villain, J., *Molecular Nanomagnets*. Oxford University Press: U.K., **2006**.(b) Aromí, G.; Brechin, E. K., Synthesis of 3d Metallic Single-Molecule Magnets. In *Single-Molecule Magnets and Related Phenomena*, Winpenny, R., Ed. Struct Bond: Berlin, **2006**; Vol. 122, pp 1-69.(c) Das, S.; Hossain, S.; Dey, A.; Biswas, S.; Sutter, J. P.; Chandrasekhar, V., *Inorg. Chem.* **2014,** *53*, 5020-5028.

115.Ma, Z.; Moulton, B., *Coordin. Chem. Rev.* **2011,** *255*, 1623-1641.

116.Paes, A. H.; Bakker, A.; Soe-Agnie, C. J., *Diabetes Care* **1997,** *20*, 1512-1517.

117.Vallet-Regí, M.; Balas, F.; Arcos, D., *Angew. Chem. Int. Ed. Engl.* **2007,** *46*, 7548-7558.

118.Vallet-Regi, M., *Chemistry* **2006,** *12*, 5934-5943.

119.Domingos, S.; Andre, V.; Quaresma, S.; Martins, I. C.; Minas da Piedade, M. F.; Duarte, M. T., *J. Pharm. Pharmacol.* **2015,** *67*, 830-846.

120.(a) Saito, N.; Takaoka, K., *Biomaterials* **2003,** *24*, 2287-2293.(b) Qiu, L. Y.; Bae, Y. H., *Pharm. Res.* **2006,** *23*, 1-30.

121.(a) Lim, E. K.; Kim, T.; Paik, S.; Haam, S.; Huh, Y. M.; Lee, K., *Chem. Rev.* **2015,** *115*, 327-394.(b) Li, Y.; Maciel, D.; Rodrigues, J.; Shi, X.; Tomás, H., *Chem. Rev.* **2015,** *115*, 8564-8608.

122.Vallet-Regi, M.; Ramila, A.; Del Real, R.; Pérez-Pariente, J., *Chem. Mater.* **2001,** *13*, 308-311.

123.(a) Sastry, S. V.; Nyshadham, J. R.; Fix, J. A., *Pharm. Sci. Technol. Today* **2000,** *3*, 138-145.(b) El-Kamel, A. H.; Ashri, L. Y.; Alsarra, I. A., *AAPS PharmSciTech* **2007,** *8*, E75.

124.(a) Salonen, J.; Kaukonen, A. M.; Hirvonen, J.; Lehto, V. P., *J. Pharm. Sci.* **2008,** *97*, 632-653.(b) Hughes, G. A., *DM-DIS. MON.* **2005,** *51*, 342-361.

125.Wang, S. B., *Micropor. Mesopor. Mat.* **2009,** *117*, 1-9.

126.(a) Zhu, Y. F.; Shi, J. L.; Li, Y. S.; Chen, H. R.; Shen, W. H.; Dong, X. P., *Micropor. Mesopor. Mat.* **2005,** *85*, 75-81.(b) Siepmann, J.; Peppas, N., *Adv. Drug Deliv. Rev.* **2012,** *64*, 163-174.(c) Davies, O. R.; Lewis, A. L.; Whitaker, M. J.; Tai, H.; Shakesheff, K. M.; Howdle, S. M., *Adv. Drug Deliv. Rev.* **2008,** *60*, 373-387.

127.Horcajada, P.; Chalati, T.; Serre, C.; Gillet, B.; Sebrie, C.; Baati, T.; Eubank, J. F.; Heurtaux, D.; Clayette, P.; Kreuz, C.; Chang, J. S.; Hwang, Y. K.; Marsaud, V.; Bories, P. N.; Cynober, L.; Gil, S.; Ferey, G.; Couvreur, P.; Gref, R., *Nat. Mater.* **2010,** *9*, 172-178.

128.Horcajada, P.; Serre, C.; Vallet-Regi, M.; Sebban, M.; Taulelle, F.; Ferey, G., *Angew. Chem. Int. Ed. Engl.* **2006,** *45*, 5974-5978.

129.(a) Keskin, S.; Kizilel, S., *Ind. Eng. Chem. Res.* **2011,** *50*, 1799-1812.(b) Horcajada, P.; Gref, R.; Baati, T.; Allan, P. K.; Maurin, G.; Couvreur, P.; Ferey, G.; Morris, R. E.; Serre, C., *Chem. Rev.* **2012,** *112*, 1232-1368.

130.Miller, S. R.; Heurtaux, D.; Baati, T.; Horcajada, P.; Grenèche, J. M.; Serre, C., *Chem. Commun.* **2010,** *46*, 4526-4528.

131.Rieter, W. J.; Taylor, K. M.; Lin, W., *J. Am. Chem. Soc.* **2007,** *129*, 9852-9853.

132.Horcajada, P.; Serre, C.; Maurin, G.; Ramsahye, N. A.; Balas, F.; Vallet-Regi, M.; Sebban, M.; Taulelle, F.; Ferey, G., *J. Am. Chem. Soc.* **2008,** *130*, 6774-6780.

133.Taylor-Pashow, K. M.; Rocca, J. D.; Xie, Z.; Tran, S.; Lin, W., *J. Am. Chem. Soc.* **2009,** *131*, 14261-14263.

134.An, J.; Geib, S. J.; Rosi, N. L., *J. Am. Chem. Soc.* **2009,** *131*, 8376-8377.

135.Chen, Y.; Lykourinou, V.; Vetromile, C.; Hoang, T.; Ming, L. J.; Larsen, R. W.; Ma, S., *J. Am. Chem. Soc.* **2012,** *134*, 13188-13191.

136.(a) McKinlay, A. C.; Allan, P. K.; Renouf, C. L.; Duncan, M. J.; Wheatley, P. S.; Warrender, S. J.; Dawson, D.; Ashbrook, S. E.; Gil, B.; Marszalek, B.; Duren, T.; Williams, J. J.; Charrier, C.; Mercer, D. K.; Teat, S. J.; Morris, R. E., *Apl. Mat.* **2014,** *2*, 124108.(b) McKinlay, A. C.; Morris, R. E.; Horcajada, P.; Ferey, G.; Gref, R.; Couvreur, P.; Serre, C., *Angew. Chem. Int. Ed. Engl.* **2010,** *49*, 6260-6266.(c) Guo, S. J.; Li, D.; Zhang, L. M.; Li, J.; Wang, E. K., *Biomaterials* **2009,** *30*, 1881-1889.(d) Kundu, T.; Mitra, S.; Patra, P.; Goswami, A.; Diaz, D. D.; Banerjee, R., *Chem. Eur. J.*

2014, *20*, 10514-10518.(e) Sun, C. Y.; Qin, C.; Wang, X. L.; Su, Z. M., *Expert Opin. Drug Deliv.* **2013,** *10*, 89-101.

137. Cavallaro, G.; Pierro, P.; Palumbo, F. S.; Testa, F.; Pasqua, L.; Aiello, R., *Drug Deliv.* **2004,** *11*, 41-46.

Chapter 2: Materials and Methods

This dissertation is based on the design, synthesis and characterization of novel MOF materials together with the study of their potential applications, particularly gas sorption application. Therefore, different synthesis methods and characterization techniques used here, including the measurement of gas sorption of pure and mixed gases, are discussed in this chapter. In addition, experimental techniques employed to investigate selected known MOFs as drug delivery vehicles are detailed.

2.1. Materials

All chemicals and solvents were obtained from commercial vendors and used as received unless noted otherwise. The drugs used in Chapter 5 of this dissertation were used without further purification and their purity was confirmed using ^{1}H NMR.

2.2. Synthesis of MOFs

As mentioned earlier, to synthesize targeted MOFs, the initial components (MBBs) must be programmed at the molecular level with the required information to form the building blocks necessary to construct frameworks with the desired topologies and functionalities. This was achieved by determining the reaction conditions that best permit the *in situ* formation of the targeted inorganic MBBs. These building units were made to undergo self-assembly, in the presence of the organic linkers, into the desired MOFs. Suitable reaction conditions are vital and can be determined either experimentally and/or through a literature search in the CSD.[1]

Experimentally, when preparing MOFs using solvothermal synthesis, various parameters can be modified and adjusted, including the solvent system which must be optimized to provide free mobility of the building blocks in order to fall into the lowest energy level with respect to each other.[2, 3] The optimal solvent system of a certain reaction can be a single solvent or multi-component solvent system. Several of the suitable solvents that are known in MOF chemistry are DMF, diethylformamide (DEF) and N, methyl-2-pyrrolidone (NMP).

In addition, the presence of secondary solvents, e.g., CH_3OH, C_2H_5OH, etc. is necessary in certain cases. Other important parameters include the molar ratio of the reactants, their total concentrations and the pH of the solution, which can be adjusted by adding specific amounts of acid, like HNO_3 or HCl. Furthermore, reaction temperatures and durations have a dramatic effect on the reaction products. The temperatures used in this work were 65, 85, 105 and/or 115 °C depending on the targeted building units and the final products. Likewise, the reaction duration ranged from few hours to few days. Moreover, the use of a variety of metal salts with various counter ions, as well as structure directing agents (SDA) have a drastic effect on guiding the reaction, especially with MOFs that are based on charged metal clusters.[4] Finally, modulators and their ratio to metal ions are crucial, particularly when targeting novel highly-connected RE polynuclear clusters.[5]

2.3. Physical and thermal characterization of MOFs

2.3.1. Microscopy

Simple optical microscopes were used as a primary brief check of sample formation, morphology and visible (visual) homogeneity. This step was followed by powder X-ray diffraction (PXRD) to verify crystallinity and phase purity of the prepared sample. Optical microscopes were also used to assist in selecting high-quality crystals for single crystal X-ray diffraction (SCXRD).

2.3.2. Single crystal X-ray diffraction (SCXRD)

In this work, SCXRD was employed to solve crystal structures of the novel synthesized MOFs.[6] Here, a high-quality crystal was chosen with the aid of an optical microscope, then single crystal (SC) data were collected using a Bruker X8 Prospector APEX II CCD diffractometer system equipped with a Cu Kα INCOATEC Imus micro-focus source ($\lambda = 1.54178$ Å) and a Kryoflex Low Temperature Cryostat. The difference vectors method was utilized for indexing using APEX2[7] and SaintPlus 6.01[8] was used for data integration and reduction. Then, multi-scan method in SADABS[9] was applied to perform absorption correction and XPREP implemented in APEX2 was used to determine the space group of the structure. Finally, the structures were solved and refined using SHELXS-97 (direct methods) and SHELXL-2013 (Full-matrix least-squares on F^2), respectively, contained in the APEX2[7, 10] and WinGX V1.70.014-7[11] and OLEX2 [10, 12] program packages. The solved structures were visualized, and their calculated powder patterns were simulated using CCDC Mercury v3.5 or Accelrys Materials Studio (MS) v7 software. In addition, theoretical pore volume (PV_{Theo}) and % accessible volume were calculated by creating a Connolly surface of solvent free crystal structures using the “Atom Volume and Surfaces” module in the MS software with a Connolly radius of 1.2 Å and fine grid resolution.

2.3.3. Topological analysis

In this work, the Topos40 software package was used to determine the topology, coordination sequencing and point symbols of the crystal structures of all constructed MOFs.[13]

2.3.4. Powder X-ray diffraction (PXRD)

Measurements were carried out at room temperature (RT) on a PANalytical X′Pert Pro diffractometer with Cu Kα radiation ($\lambda = 1.5418$ Å) at 45 kV, 40 mA with a scan speed of 1.0°/min and a step size of 0.02° in 2θ. The PXRD patterns were used to verify crystallinity and purity of the prepared MOFs by comparing experimental powder patterns with those that were calculated created from the SC structure using MS or Mercury software.[14]

2.3.5. Variable temperature powder X-ray diffraction (VT-PXRD)

VT-PXRD measurements were employed to confirm the stability and behavior of prepared MOFs under vacuum and at different (elevated) temperatures.[3] Here, the PXRD diffractometer was equipped with an Anton-Paar CHC$^+$ variable-temperature stage where the samples were subjected to vacuum and held for at least 15 min at each designated temperature between the PXRD scans.

2.3.6. Thermogravimetric analysis (TGA)

TGA is usually conducted to determine the thermal stability of samples (decomposition temperature) and the percentage of adsorbed guest molecules. In this work, high resolution dynamic TGA was carried out in a N_2 atmosphere with balance and sample purge flow rates of 10 mL/min and 25 mL/min, respectively. The resolution index was set to 3 and the sensitivity index was set at 5. Approximately 5-10 mg of samples were loaded onto a 100 μL high temperature-platinum pan and heated between RT and 700 °C with a heating rate of 5 or 20 °C per minute, depending on the sample being analyzed, and recorded on a TA Instruments hi-res TGA Q-5000-IR thermogravimetric analyzer.

2.3.7. Elemental analysis of C, H and N (EA)

EA of C, H and N is usually incorporated into an experimental paradigm to determine the mass fraction of carbon, nitrogen and hydrogen in prepared MOFs and assist molecular formulas elucidation. In addition, this test ascertains MOFs structures and aids finding the ratio of adsorbed solvents or materials, such as drug molecules, in MOFs under investigation. In this work's experiments, combustion of samples using a highly efficient Thermo Finnigan elemental analyzer was performed.

2.3.8. Fourier-transformation infrared (FT-IR) spectroscopy

FT-IR spectroscopy is used to determine specific functional groups in organic ligands and compare them to those in the resultant prepared MOFs. In addition, FT-IR can be utilized to assure post-synthetic modification of the frameworks by observing the loss or appearance of bands corresponding to certain functional groups. Here, FT-IR spectra were recorded in the solid state within the 600-4000 cm^{-1} region on a Nicolet 6700 FT-IR spectrometer.

2.3.9. Solution nuclear magnetic resonance spectroscopy (NMR)

NMR spectroscopy is an important chemical technique that is quite frequently used for structural characterization.

In this work, NMR was employed to confirm the preparation of organic ligands and their purity. In addition, when characterizing a MOF where a mixed-ligands approach was used, NMR verified the presence of and the ratio between different ligands.

All ^{1}H and ^{13}C NMR spectra were acquired on Bruker Avance III 600 MHz spectrometer equipped with a variable temperature controller. The ^{1}H and ^{13}C

chemical shifts are reported in ppm relative to that of tetramethylsilane (TMS) and referenced to corresponding residual solvent peaks.[15]

2.4. Porosity screening and characterization using physical adsorption methods

Screening and characterization of prepared MOFs porosity were performed with volumetric (manometric) and/or gravimetric methods at low and high pressures in a large range of temperatures. These tests were performed after optimal samples activation, i.e., full evacuation of the framework cavities from solvent molecules. In the following sections, the activation methods, as well as the LP and the HP adsorption protocols, are described.

2.4.1. Samples activation protocols

After MOFs synthesis, their cavities are usually occupied by guest molecules that have higher boiling points, i.e., solvents used during synthesis like DMF. A prerequisite for porosity determination is their optimal activation, which is the process by which guest molecules are fully removed to free the pores or channels and make them accessible to other guests. Of note is the fact that there are different methods of activation and for each particular material, a proper procedure needs to be identified.

2.4.1.1. Conventional activation method

In general, the traditional activation method is solvent exchange,[16] where solvents used during MOFs synthesis that occupy the voids in the cavities are exchanged with volatile ones that have low affinity to the frameworks, such as CH_3CN, CH_3OH, etc. Typically, 20-100 mg of homogenous as-synthesized MOF samples were washed several times with DMF to remove unreacted material then soaked in the volatile solvent of choice (usually at RT) for a few days (1-7 days) while refreshing the solution frequently a number of times per day. After full solvent exchange (confirmed by TGA and/or IR), samples were transferred to glass sorption cells; the excess surface solvent was removed with a syringe and samples were subjected to a flow of N_2 to dry the surface solvent. The samples were then evacuated using a turbo molecular vacuum pump, starting at RT with a gradual increase in temperature at a rate of 1 °C/min, while maintaining vacuum, till having reached the optimum activation temperature. The optimal temperature is defined as the lowest temperature that permits the full removal of guest (highly volatile) solvents from the pores and was verified by adsorption of N_2 at 77 K, the standard. Finally, the samples were held at the optimum temperature for approximately 12-24 h and afterwards cooled to RT. A Quantachrome Autosorb 6 Degasser was made use of in this work and the evacuation conditions (temperature and duration) were controlled and recorded to ensure reproducible isotherms.

2.4.1.2. Supercritical-CO_2 activation method (SC-CO_2)

Another activation approach is the SC-CO_2 method[17, 18] using a Tousimis supercritical CO_2 dryer. This method can be performed either by first exchanging the sample with a conventional solvent and then transferring it to the SC-CO_2 dryer or by using a DMF-washed sample directly without any solvent exchange.

In this work, DMF-washed samples were first briefly rinsed with a volatile solvent to remove surface DMF and transferred to the SC-CO_2 dryer chamber, which was cooled until -7 °C and then pressurized by injecting CO_2. The samples were next subjected to liquid CO_2 for two days while being refreshed several times per day by repeated injection and ventilation of the liquid CO_2. The temperature and pressure were then elevated above the CO_2 critical point, i.e., 31 °C and 74 bar, respectively, and the samples were kept in SC-CO_2 for one more day. Bleeding or removal of SC-CO_2 was performed slowly over a period of roughly 6 h, after which the samples became totally dry. Similar to the traditional activation method, before LP gas sorption experiments, samples were transferred to sorption cells under a N_2 environment (in a glove box) and then subjected to a dynamic vacuum at RT for 12-24 h.

This method is mainly useful when the conventional activation method fails, e.g., when activating less robust MOFs that are susceptible to collapse if not carefully activated, like MOFs built using expanded ligands, having large pores and ultra-high SAs. Generally, SC-CO_2 activation is mild and preserves the framework because the solvent can be removed by reducing the surface tension of the materials.[18-19] CO_2 is the gas of choice in this process because it is readily available, cheap and becomes supercritical under mild conditions.

2.4.2. MOFs porosity: sorption isotherms

Porous materials are classified based on pore diameter into microporous (2 nm), mesoporous (2-50 nm) and macroporous (> 50 nm).[20] The properties of these materials depend on many factors, including pore architectures (size, shape and connectivity), nature of the pore size distribution and chemical characteristics of the pore walls.

The permanent porosity of MOFs can be confirmed, quantified and studied using gas sorption techniques that were formerly established for other porous materials, like the zeolites.[21, 22] Therefore, after activating the samples under dynamic vacuum at RT or different relatively moderate temperatures, until all volatile solvents are removed, they are subjected to an adsorbate (e.g., N_2 or Ar) at a constant temperature (boiling point of the adsorbate). Physisorption or sorption isotherms, which illustrate the relationship between equilibrium amounts of gas adsorbed by the material in a specific range of pressures, are then plotted.[23]

Depending on pore diameter of the materials, and according to IUPAC classification,[24] the majority of sorption isotherms can have one of six characteristic types (Figure 2.1). All the following isotherms demonstrate a relationship between the amount of gas adsorbed and the relative pressure (P/P_0) approaching a limit value of 1 where P is the pressure of the adsorbate at any given point, or the experimental pressure, and P_0 is its saturation pressure at the bath temperature wherein the experiment is conducted.

A fully-reversible **Type I** isotherm is typical for microporous materials and can be used to determine their SA and PV because the adsorption process is limited to just a few molecular layers.[25] In these materials, the external SA can be neglected when compared to that inside the pores and the uptake is limited by PV. This type of isotherm has a concave shape with respect to the relative pressure axis and reaches a plateau or limiting value as P/P_0 approaches 1. Another piece of information that can be obtained from Type I isotherms, depending on the gas, is the interaction strength and the affinity between the adsorbate and the adsorbent, where the steepness and high gas uptake at LP indicate stronger interactions. Examples of materials that show Type I isotherms are MOFs, zeolites and activated carbons.

A **Type II** reversible isotherm is characteristic of macroporous or non-porous materials. With respect to the P/P_0 axis, the isotherm is concave in shape at LP, but as the pressure is elevated, it exhibits an inflection point (point B) with continued uptake, indicating the completeness of monolayer coverage and the beginning of multilayer adsorption. In this situation, no plateau is reached as P/P_0 approaches 1 because of the large pores that do not restrict the multilayer sorption.[24]

Type III Isotherms are rarely seen in the literature and have a convex shape with respect to the relative pressure axis. Unlike Type I, this type of isotherm is seen when the adsorbate-adsorbent interaction is weak.

Type IV isotherms are expected for mesoporous materials. At LP, it resembles Type II isotherms in that it exhibits monolayer formation. Nonetheless, at higher pressure, a distinct hysteresis loop is observed as a result of capillary condensation of the adsorbate. Furthermore, near the end of the isotherm, the uptake becomes limited by PV (similar to Type I isotherms).

Type V isotherms are similar to Type III as they are rarely seen for porous materials and their behavior at LP indicates a weak adsorbate-adsorbent interaction. In addition, at higher pressure, it is similar to Type IV isotherms vis a vis the existence of a hysteresis loop and the pore condensation effect based on the presence of mesopores within the adsorbent.[24]

Type VI isotherms are characteristic of uniform non-porous adsorbents where multilayer adsorption takes place in a stepwise fashion, i.e., a stepwise multilayer adsorption where each step represents an adsorbed monolayer.

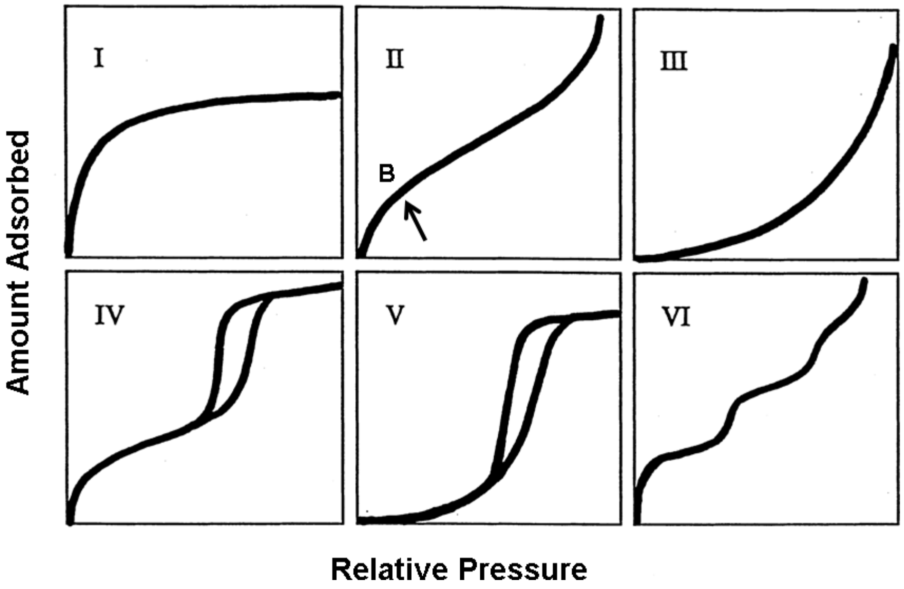

Figure 2.1 IUPAC classification of sorption isotherms. Copyright© 2016 International Union of Pure Applied Chemistry.[24]

2.4.3. Low pressure (LP) gas sorption studies: MOFs porosity measurements

In this work, LP gas sorption studies were employed to determine the actual porosity of synthesized MOFs where N_2 and/or Ar gases were utilized as probe molecules at their boiling temperatures, i.e. 77 K and 87 K, respectively. The resulting sorption isotherms were used to calculate the SA, PV, total gas uptake (cm^3(STP)/g) and pore size distribution (PSD) of the samples.[26] In addition, LP CO_2 and H_2 sorption studies were conducted at various temperatures to discern the storage capacities of the prepared MOFs for these specific gases, as well as their corresponding isosteric heat of adsorption (Q_{st}). A fully-automated Autosorb-iQ gas adsorption analyzer by Quantachrome Instruments or a fully automated 3Flex gas analyzer by Micromeritics Instruments were used at a relative pressure up to 1 atm where liquid N_2 and Ar baths were made use of to control the cryogenic temperatures at 77 K and 87 K, respectively.

For porous materials, in general, the standard adsorbate for pore characterization and porosity measurements is N_2 gas at its normal boiling point, i.e., 77 K. Other adsorbates have been proposed, including Ar gas at 87 K, which may yield more reliable quantitative results, particularly when assessing ultra-microporous materials having a pore width of < 0.7 nm.[26] This can be ascribed to the nature of the diatomic N_2 gas and its permanent quadrupole moment with the potential to interact with polarized functional groups on the adsorbent walls (e.g., hydroxyl groups), if present, leading to unsatisfactory quantitative results.[27] On the contrary, when employing Ar gas, high resolution data is collected because Ar is monatomic gas with similar kinetic diameter to that of N_2 but lacking quadrupole moment.[26]

A property calculated using the obtained N_2 and/or Ar sorption isotherms is the apparent SA of a framework, which can be determined using a variety of models, such as that of Brunauer, Emmett and Teller (BET) and Langmuir (Lang). BET SA (SA_{BET} in m^2/g) is calculated by assuming that during the adsorption process, a monolayer of adsorbate is first formed followed by the formation of the subsequent layers.[25] For this method to be successful when calculating the SA of microporous materials, at least three appropriate relative pressure points in a range below 0.04 should be chosen in order to be able to apply the BET equation and generate a linear BET plot strictly related to single layer adsorption in the pores.[26] Here, PSD was also calculated from N_2 and/or Ar sorption isotherms using the available models by assuming an oxidic (zeolitic) surface with the cylindrical/spherical non-local density functional theory (NLDFT) pore model system.[28, 29]

Additionally, H_2 and CO_2 sorption isotherms were collected to investigate the storage capacities of the prepared MOFs for specific gases. Further, to evaluate the interaction between the frameworks and adsorbed gases, Q_{st}, which is the energy (strength) of the interaction between the adsorption sites of the adsorbent and the molecular gas or a given probe molecule, was calculated from the corresponding isotherms.[26] Q_{st} was estimated using the Clausius-Clapeyron expression of multiple gas isotherms.[30, 31] Therefore, for H_2, at least two isotherms at two different temperatures (77 K and 87 K, which are controlled by liquid N_2 and liquid Ar baths, respectively) and under 1 atmospheric pressure were required to estimate the Q_{st}. The same is true when determining the CO_2 storage capacity of a framework, but in this case, multiple gas sorption isotherms were necessary to calculate the Q_{st}, i.e., 258, 273, 288 and 298 K, unless otherwise noted.[26, 31] In these experiments, a re-circulating ethylene glycol/water bath was employed to control the bath temperature for sorption measurements.

In summary, for the assessments of the prepared MOFs porosity, LP sorption measurements were performed after activating the samples using the appropriate activation method. N_2 and/or Ar sorption isotherms, at 77 and 87 K, respectively, were collected for pore characterization, i.e., finding SA, PV and PSD. This was followed by assessing the uptake capacity of the prepared frameworks for H_2 (at 77 K and 87 K) and CO_2 (at 258, 273, 288 and 298 K) and calculating their corresponding Q_{st}.

2.4.4. High pressure (HP) gas sorption studies

In this work, HP gas sorption studies were carried out to determine the adsorption capacity, kinetics and selectivity of the prepared MOFs with respect to CO_2, CH_4, N_2, C_2H_6, C_3H_8 and C_4H_{10}, as well as mixtures thereof. These experiments were performed to examine the suitability of the prepared MOFs for applications related to gas storage and/or separation of gas mixtures at elevated pressures.

Therefore, to measure the adsorption equilibrium of the pure gases, a Rubotherm gravimetric-densimetric apparatus (Bochum, Germany) was used. This instrument is principally composed of a magnetic suspension balance with a set of valves, mass flow meters and sensors to detect temperature and pressure (Scheme 1).[32] When compared to other gravimetric instruments, this device has distinct advantages, such as isolating the sample and its measurement atmosphere from the sensitive microbalance that leads to more accurate results. In addition, it can control the temperature between 77 to 423 K and measure adsorption across a multitude of pressure levels (0-20 MPa). Measurements of pressure were performed using two Drucks HP transmitters and a single LP one. The two HP transmitters ranged from 0.5 to 34 bar and from 1 to 200 bar and the LP one ranged from 0 to 1 bar.[33]

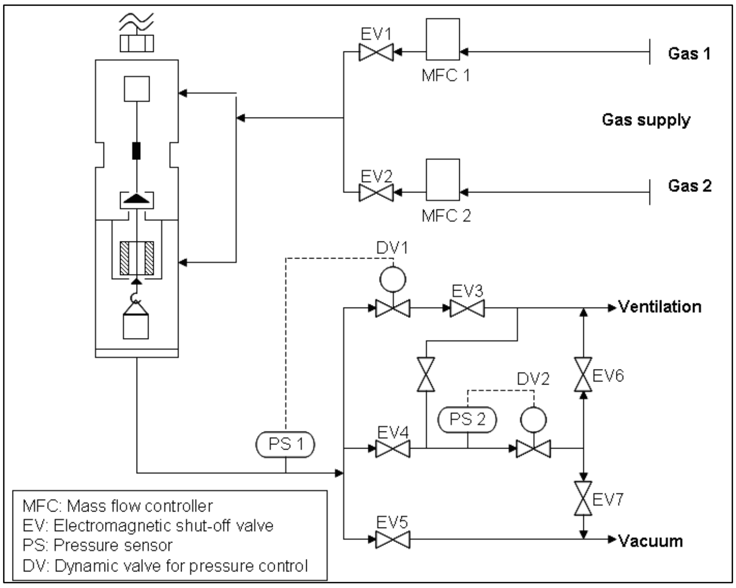

Scheme 1 Schematic representation of the Rubotherm gravimetric-densimetric device.[33]

In a typical HP adsorption experiment, the sample (adsorbent) is first appropriately activated, accurately weighed and placed in a special container, which is then suspended in the cell by an electromagnet. Vacuum or HP is then applied to the cell after it is tightly closed. The amount of the reduced gas adsorbed (Ω) is directly measured and the excess and absolute amounts are determined using equations (1) and (2), where $V_{adsorbent}$, V_{ss} and $V_{adsorbed}$ refer to the adsorbent, suspension system and adsorbed phase volumes, respectively.

$$\Omega = m_{absolute} - \rho_{gas} (V_{adsorbent} + V_{ss} + V_{adsorbed\text{-}phase}) \qquad \textbf{Eq. 1}$$

$$\Omega = m_{excess} - \rho_{gas} (V_{adsorbent} + V_{ss}) \qquad \textbf{Eq. 2}$$

These volumes can be determined using the He isotherm method, where it is assumed that He enters all the open pores of the material without being adsorbed. The correction of the buoyancy effect, resulting from the adsorbed phase, is required, and it is taken into account by correlation with the calculated sample density or its PV.[33]

The gas density is theoretically determined using the REFPROP equation of state (EOS) database and a volume-calibrated titanium cylinder is used to experimentally confirm this value. Therefore, the local gas density can be determined by weighing this calibrated cylinder in the gas atmosphere. This enables the concurrent measurement of adsorption capacity and gas-phase density as a function of pressure and temperature.[33]

In summary, prior to each HP gas adsorption experiment, around 100-200 mg of homogeneous microcrystalline samples of as-synthesized MOFs were washed with DMF several times, activated using the suitable activation method and subjected to HP or vacuum to obtain guest-free samples. Samples were then exposed to increasing pressure increments of the intended gases at given temperatures that are kept constant by using a thermostat-controlled circulating fluid. Finally, and at equilibrium, the weight change was recorded and plotted against pressure.

2.4.4.1. Prediction of gas mixture equilibria and selectivity using the Ideal Adsorption Solution Theory (IAST):

The adsorption equilibrium of a gas mixture at the temperature of interest in porous materials can be predicted using pure gas sorption isotherms through utilizing the IAST as proposed by Myers and Prausnitz.[34] IAST can be applied only if high quality sorption data for each single component of the studied gases is available in addition to a perfect curve fitting model for such data.[35] Various groups have reported that when using the IAST, the simulated mixture behavior matches well with that which is calculated from single-component isotherms.[34-36]

In the current work, the Toth model was employed to fit the pure gas isotherms because of its suitable behavior at both LP and HP and its simple formulation as expressed by equation (3).[37]

$$\boldsymbol{n = n_s \frac{KP}{(1+(KP)^m)^{\frac{1}{m}}}} \qquad \textbf{Eq. 3}$$

where n is the amount adsorbed, n_s is the amount adsorbed at saturation, P is the equilibrium pressure, K is the equilibrium constant and m is a parameter indicating the heterogeneity of the adsorbent.

The most important equations used in the IAST calculation are listed hereafter:

$$\boldsymbol{f_i = x_i f_i^0(\pi)} \qquad \textbf{Eq. 4}$$

$$\boldsymbol{\frac{\pi A}{RT} = \int_0^{f_i^0} n_i \, d \ln f_i} \qquad \textbf{Eq. 5}$$

$$\frac{1}{n_t} = \sum_i \frac{x_i}{n_i^0} \qquad \textbf{Eq. 6}$$

$$S_{CO_2-i} = \frac{x_{CO_2} / x_i}{y_{CO_2} / y_i} \qquad \textbf{Eq. 7}$$

where f_i is the fugacity of component, i, in the gas phase; f_i^0 is the standard-state fugacity (the fugacity of pure component, i, at the equilibrium spreading pressure of the mixture), π; x_i and y_i are the mole fractions of component, i, in the adsorbed and gas phase, respectively; A is the SA of the adsorbent; n_i is the number of moles adsorbed of pure component, i, (the pure-component isotherm); and n_i^0 is the number of moles adsorbed of pure component, i, at the standard-state pressure.[38]

Equation (4) is the central equation of the IAST and specifies the equality of the chemical potential of component, i, in the gas and adsorbed phases (which are assumed to be ideal in the context of Raoult's law). Equation (5) allows the calculation of the spreading pressure from the pure-component adsorption isotherm. The total amount adsorbed of the mixture, $\mathrm{n_t}$, and the selectivity of CO_2 with respect to i, S_{CO_2-i}, are yielded by equations (6) and (7), respectively. The selectivity, S_{CO_2-i}, reflects the efficiency of CO_2 separation.[38-39]

2.5. Evaluation of the magnetic properties of prepared MOFs

In Chapter 4 of this work, the magnetic properties of lanthanides-based MOFs were measured by a superconducting quantum interference device (MPMS® 3, Quantum Design). To obtain the intrinsic magnetic properties of these MOFs, low-field magnetization as a function of temperature was measured in the temperature range of 1.8-300 K under a magnetic field of 100 Oe with a zero-field-cooling (ZFC) and field-cooling (FC) process. Additionally, field-dependent magnetization was measured in a temperature range of 1.8-30 K. A number of the equations that were used in this work include the following:

The Curie-Weiss law

$$\chi = \frac{C}{T\text{-}T_c} \qquad \textbf{Eq. 8}$$

Where χ is the magnetic susceptibility, C is the material specific Curie constant, T is the absolute temperature in K and T_c is the Curie temperature.

The Langevin function was also applied to provide the relationship between magnetization, $M\ (H, T)$, and the applied field, $H/(T - T_c)$:

$$\boldsymbol{M}(\boldsymbol{H}, \boldsymbol{T}) = \frac{\boldsymbol{N}}{\boldsymbol{A}} \boldsymbol{\mu_B \mu_{eff} L} \left[\frac{\boldsymbol{\mu_B \mu_{eff} H}}{\boldsymbol{k_B (T - T_c)}} \right] \qquad \textbf{Eq. 9}$$

where N is Avogadro constant, A is the molar mass, μ_B is the Bohr magneton, μ_{eff} is the effective magnetic moment - a number - and k_B is Boltzmann constant. The Langevin function may be written as $\boldsymbol{L}(\boldsymbol{x}) = \frac{\boldsymbol{1}}{\boldsymbol{3}} \boldsymbol{x}$ when $\boldsymbol{x}$ is very small. In this case, if the field, H, is low enough and T is high enough, this equation could be written as follows:

$$\boldsymbol{M}(\boldsymbol{H}, \boldsymbol{T}) = \frac{\boldsymbol{N}}{\boldsymbol{A}} \frac{\boldsymbol{\mu_B^2 \mu_{eff}^2 H}}{\boldsymbol{3 k_B (T - T_c)}} \qquad \textbf{Eq. 10}$$

The effective magnetic moment can also be calculated by applying this equation using the low field magnetization, molecular formula and molecular mass of the compounds.

2.6. MOFs evaluation as potential drug carriers

Chapter 5 of this work deals with studying selected MOFs as potential platforms for drug delivery. Therefore, In **rho**-ZMOF, an anionic framework that was previously reported by our group,[4] was evaluated as a potential carrier for Proc, which is a cationic antiarrhythmic drug. In addition, the neutrally-charged Cu **rht**-MOF-7[40] was also assessed as a potential delivery vehicle for IBU, a neutrally charged NSAID. The methods used to assess each framework are generally similar with several key differences depending on their nature.

2.6.1. Stability of studied MOFs in different loading and release solvents

Samples of MOFs under investigation were suspended in various loading solvents, such as water and CH_3OH, as well as in the release media, like phosphate buffer saline (PBS), and kept under bi-dimensional shaking for varied time intervals. PXRD was used to assess crystallinity and confirm the stability of the frameworks by comparing their calculated patterns with those collected after each treatment. In addition, structural integrity and crystallinity after drying and complete drug loading were also evaluated using the same technique.

2.6.2. Evaluation of anionic MOFs as delivery vehicles for cationic drugs

2.6.2.1. Proc loading into In rho-ZMOF

Proc was loaded into In **rho**-ZMOF cages via the cation exchange process where drug cations replaced dimethylammonium (DMA^+) ions that were balancing the charge of the anionic framework and were the result of DMF dissociation during MOF preparation. This was achieved through two methods: 1) exchange DMA^+ ions with

Na^+ and then exchange Na^+ ions with Proc cations. This method was used to help predict the amount of drug loaded indirectly using a number of techniques, such as atomic absorption spectroscopy (AAS) and inductively-coupled plasma optical emission spectrometry (ICP-OES); and 2) the direct exchange of the extra-framework DMA^+ ions with Proc cations where drug uptake was followed by direct techniques, like UV-Vis spectroscopy.

Overall, the exchange procedure involves soaking solvent-exchanged dried framework crystals in sodium nitrate solution while refreshing the solution frequently for up to 24 h. Sodium-exchanged crystals are then soaked in a solution containing Proc in Nanopure water that is also refreshed repeatedly for another 24 h to obtain drug-loaded crystals. Alternatively, drug loading into the framework can be accomplished by directly soaking the solvent-exchanged dried crystals into Proc in Nanopure water solution while refreshing the solution for 24 h. After complete drug loading, the crystals were collected, washed with C_2H_5OH and dried to be prepared for characterization experiments.

2.6.2.2. Determination of the amount of Proc loaded into In rho-ZMOF

Several methods were used to estimate the amount of drug adsorbed into the framework. These methods included ICP-OES, AAS, EA of C, H and N, TGA and UV-Vis spectroscopy.

2.6.2.2.1. ICP-OES

The ICP-OES analysis was conducted on a Varian ICP-OES spectrometer (720-ES) to determine the amount of metal in different samples. This test enabled the determination of the loaded drug ratio by first finding the Na:In ratio in sodium-exchanged samples and then calculating the ratio of Na^+ that was replaced by drug cations in the drug-loaded samples.

2.6.2.2.2. AAS

This is a spectroanalytical procedure that was conducted on a Varian AA 240FS atomic absorption spectrometer. AAS helps determine the quantities of different elements in a sample. It resembles ICP-OES in that it determines the amount of loaded drug by first finding the Na:In ratio in sodium-exchanged samples and then calculating the ratio of Na^+ that was replaced by the drug cations in the drug-loaded samples.

2.6.2.2.3. EA

This procedure estimates the amount of loaded drug inside the pores by calculating the mass fractions of C, N and H contents in the loaded framework samples (Section 2.3.7).

2.6.2.2.4. TGA

In order to estimate the amount of loaded drug in the framework, TGA was performed on the loaded samples under a N_2 atmosphere (Section 2.3.6). The tests were carried out between RT and 700 °C at an increasing heating rate of 5 °C/min in high resolution dynamic mode. For comparison, TGA of pure drug powder and that of solvent-exchanged MOF samples were collected under similar conditions.

2.6.2.2.5. FT-IR

In drug delivery experiments, FT-IR indicates the loading of drugs into the frameworks by comparing the spectra of parent MOFs, those that were loaded and pure drug samples (Section 2.3.8).

2.6.2.2.6. Drug contents determination by mechanical destruction of the framework

Drug contents were estimated by mechanical destruction of the framework while initiating cation-triggered drug release. Here, the crystals were immersed in PBS, subjected to grinding, shaking in a water bath followed by sonication. This was intended to produce complete release of the drug loaded inside the pores. The amount of drug was quantified by reverse-phase high-pressure liquid chromatography (HPLC).

2.6.2.3. Proc release from the loaded In rho-ZMOF

In a typical *in vitro* drug release experiment, a certain amount of loaded crystals are placed in 0.1 M PBS (pH = 7.4) in stoppered conical flasks. Here, the experiment was performed under sink condition, and the flasks were shaken in a thermostat-controlled horizontal shaker at 37 ± 0.5 °C and 100 rpm. At predetermined time intervals, aliquots of the release media were withdrawn with a syringe for analysis and replaced by an equal volume of fresh pre-warmed media. Extracted samples were diluted with PBS, filtered through 0.45 µm syringe filters and analyzed for Proc contents by HPLC. The amount of drug released at each time interval was calculated using a same-day constructed calibration curve of Proc in PBS.

To confirm that drug release was indeed facilitated by the buffer cations, a control experiment was performed under the same conditions while using Nanopure water as the release media and extracted samples were diluted with water.

The Hayton and Chen equation (11)[41] was applied to correct the concentration of released Proc in each sample from the dilution effects of adding the fresh release media:

$$\boldsymbol{C'_n} = \boldsymbol{C_n}\ \left(\frac{\boldsymbol{V_t}}{\boldsymbol{V_t - V_s}}\right)\left(\frac{\boldsymbol{C'_{n-1}}}{\boldsymbol{C_{n-1}}}\right) \qquad \textbf{Eq. 11}$$

Where $\boldsymbol{C'_n}$ is the corrected concentration in the nth sample, $\boldsymbol{C_n}$ is the measured concentration of Proc in the nth sample, $\boldsymbol{C'_{n-1}}$ is the corrected concentration of the (n-1)th sample, $\boldsymbol{C_{n-1}}$ is the measured concentration of Proc in the (n-1)th sample, $\boldsymbol{V_t}$ is the total volume of the release medium and $\boldsymbol{V_s}$ is the sampling volume.

2.6.3. Evaluation of neutral MOFs as delivery vehicles for neutrally-charged drugs

2.6.3.1. IBU loading into Cu rht-MOF-7

This experiment depends on mixing a known concentration of IBU with solvent-exchanged dried framework powder in the presence of an internal standard (IS) that cannot diffuse into the pores. The amount of drug loaded into the pores is indirectly calculated from the changes in the ratio between the drug and the IS, followed by ^{1}H NMR spectroscopy.

Here, the IS of choice was tetrabutylammonium bromide (TBAB) (Figure 2.2), which has larger molecular dimensions (8.4 * 10.5 Å) than the windows of the framework being studied (6.4 Å and 6.8 Å), and consequently, it remained in solution. In addition, it exhibited no chemical shifting in the ^{1}H NMR spectra (Figure 2.3 a) that may overlap with those of the studied aromatic drug, IBU (Figure 2.3 b).

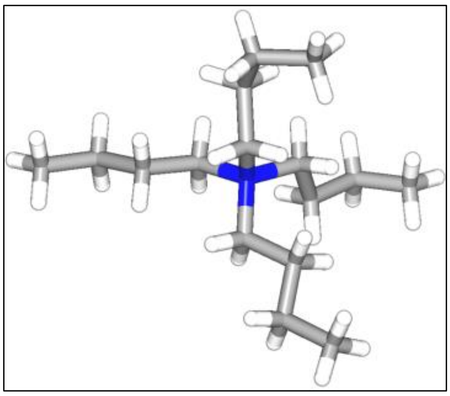

Figure 2.2 Structure of TBAB, the IS used in this study.

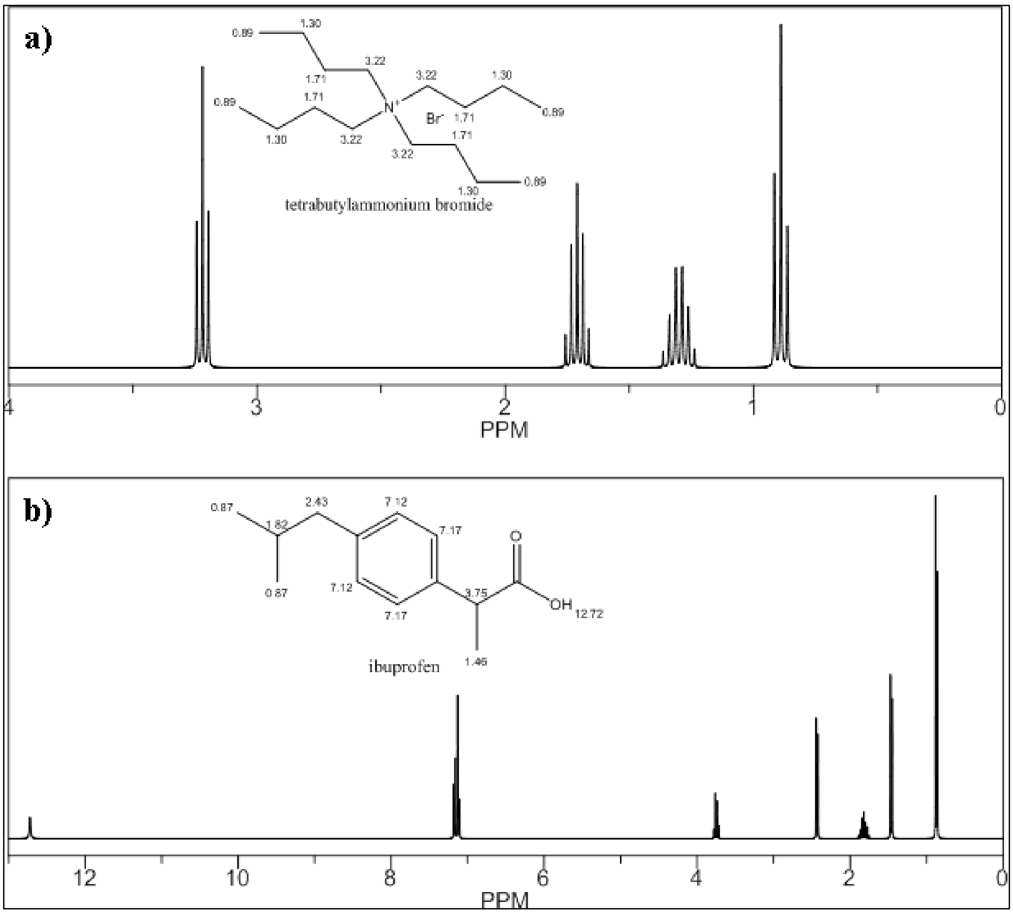

Figure 2.3 Estimated ^{1}H NMR spectra of (a) the IS, TBAB, and (b) IBU.

Experimentally, the IS solution had a concentration that was only 10% of the drug solution and the ^{1}H NMR spectra of each solution (drug and IS) and their mixture were collected first. Dehydrated framework powder was then added to the mixture followed by observing the change in the drug-to-IS ratio by collecting ^{1}H NMR spectra at each time interval. When the drug loading process was complete, the loading solution was decanted; the framework was washed once with CD_4O and dried in an oven at 65 °C before performing the release study. Here, drug loading was achieved by diffusion[42] and followed using a Bruker 500M SB liquid NMR spectrometer.

2.6.3.2. Determination of the amount of IBU loaded into Cu rht-MOF-7

Different methods were employed to estimate the amount of adsorbed drug into the framework. These methods include ^{1}H NMR during drug loading and after complete digestion of loaded crystals, TGA and EA of C, H and N. The procedures of the TGA and EA of C, H and N experiments are similar to those followed to determine the amount of loaded Proc into In **rho**-ZMOF (Section 2.6.2.2).

2.6.3.2.1. ^{1}H NMR spectroscopy of digested samples

In this case, the amount of drug loaded was calculated by finding the ratio between the drug and the ligand by acquiring the ^{1}H NMR spectrum of the loaded crystals that were fully digested with the aid of NaOH and sonication.

2.6.3.3. IBU release from loaded Cu rht-MOF-7

Drug release from the loaded framework was followed by NMR assessment with a Bruker 500MHz SB liquid NMR spectrometer using TBAB as an IS and 0.9 % NaCl or normal saline (NS) as the release media. Drug release studies were performed in a screw-capped NMR tube and kept at 37 °C at all times in the NMR spectrometer and a ^{1}H NMR spectrum was collected at each time interval. The amount of drug released was indirectly calculated from the ratio between released drug and IS in solution.

2.7. Synthesis of organic ligands

The different ligands used in the research of this dissertation were synthesized by the organic chemists in our group according to the following synthetic procedures.

2.7.1. Preparation of 5'-(pyridin-4-yl)-[1,1':3',1''-terphenyl]-4,4''-dicarboxylic acid

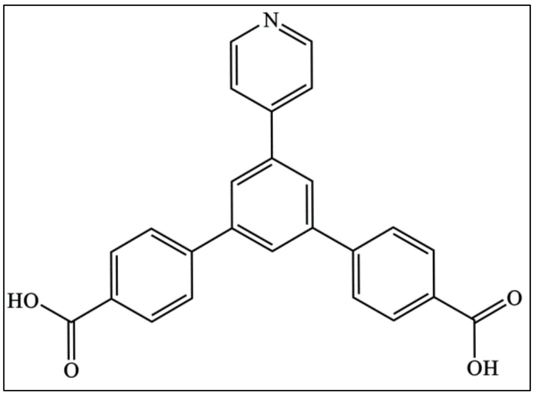

Figure 2.4 Chemical structure of 5'-(pyridin-4-yl)-[1,1':3',1"-terphenyl]-4,4"-dicarboxylic acid (PTPDC).

PTPDC was synthesized using the following Suzuki coupling reaction: In a Schlenk tube under Ar atmosphere, a mixture of diethyl 5'-iodo-1,1':3',1"-terphenyl-4,4"-dicarboxylate (0.76 mmol, 0.38 g), pyridine-4-boronic acid (2 mmol, 0.268 g), [1,1'-bis(diphenylphosphino) ferrocene] dichloropalladium(II) (0.1 mmol, 0.073 g), 2-dicyclohexylphosphino-2',6'-dimethoxybiphenyl (0.2 mmol, 0.084 g), finely ground

$K_3(PO_4)$ (5 mmol, 1.06 g), and 18-crown-6 ether (1 mmol, 0.264 g) in a mixture of degassed THF (10 mL) and C_2H_5OH (5 mL) was prepared and reacted at 90 ºC for 24 h. The reaction mixture was then filtered through a Celite® pad, volatiles removed under reduced pressure and the residual solid loaded on silica gel and subjected to column chromatography (hexanes to 50% ethyl acetate (AcOEt) in hexanes) to yield off-white solid (0.2 g, 0.44 mmol, 59% yield). To hydrolyze the product, a RB flask was utilized where a mixture of NaOH (2 mmol in 10 mL H_2O) and the ester (0.2 g in 10 mL THF and 5 mL C_2H_5OH) was prepared and held at 80 °C for 12 h. The volatiles were removed under reduced pressure and water (40 mL) was added. The solution was acidified by 1N HCl to pH 4 and the precipitate filtered and dried at 80 °C to produce white solid quantitatively.

2.7.2. Preparation of 5-(pyrimidin-5-yl)isophthalic acid

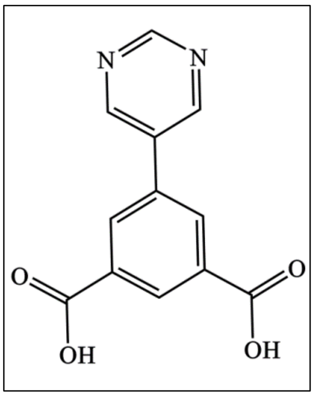

Figure 2.5 Chemical structure of 5-(pyrimidin-5-yl)isophthalic acid (PMIP).

A literature procedure was adapted.[43] At first, a mixture of CH_3CN (40 mL) and aq. K_2CO_3 (6.9 g, 50 mmol, 5 eq. in 40 mL of distilled deionized (DI) water) were placed in a 250 mL Schlenk tube and evacuated/backfilled with Ar three times. Subsequently, 5-bromopyrimidine (1.75 g, 11 mmol, 1.1 eq.), 3,5-

dicarboxyphenylboronic acid (2.1 g, 10 mmol, 1 eq.) and bis(triphenylphosphine) palladium(II) dichloride (0.4 g, 0.57 mmol, 0.06 eq.) were added in one portion, the tube was evacuated/backfilled with Ar three times, sealed and the mixture stirred vigorously at 100 °C for 24 h. Then it was cooled, diluted with 100 mL water, filtered through Celite®, and the filtrate was washed with AcOEt (2 x 70 mL, discarded). The aqueous phase was acidified with 2N HCl, and the yellow precipitate was centrifuged, after which the centrifugation was repeated with DI water (2 x), and then C_2H_5OH (1 x). Finally, the compound was concentrated from C_2H_5OH and dried further at 65 °C to yield 1.38 g (57 %) of a dark yellow solid. ^1H NMR (600 MHz, DMSO-d_6): δ = 13.5 (br s, 2 H), 9.25 (s, 1H), 9.21 (s, 2H), 8.54 (t, J=1.5, 1 H), 8.48 (d, J=1.5, 2H). ^{13}C NMR (150 MHz, DMSO-d_6): δ = 166.2 (Cq), 157.9, 155.2, 135.1 (Cq), 132.4 (Cq), 132.0 (Cq), 131.8, 130.0.

2.7.3. Preparation of 5-(pyridin-4-yl)isophthalic acid

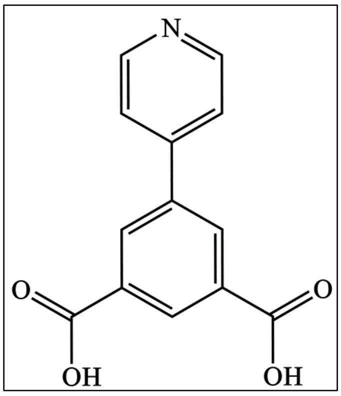

Figure 2.6 Chemical structure of 5-(Pyridin-4-yl)isophthalic acid (PIP).

This product was synthesized according to the previously reported procedure.[44] In a typical reaction, a solution of 18-crown-6 (0.66 g, 2.5 mmol) in THF (60 mL) and C_2H_5OH (30 mL) was placed in 250 mL Schlenk tube and evacuated/backfilled with

Ar three times. Then, dimethyl 5-bromoisophthalate (1.36 g, 5 mmol), 4-pyridineboronic acid (1.845 g, 15 mmol), [1,1'-bis(diphenylphosphino)ferrocene]dichloropalladium(II) (0.183 g, 0.26 mmol), 2-dicyclohexylphosphino-2',6'-dimethoxybiphenyl (SPhos, 0.205 g, 0.5 mmol) and finely ground K_3PO_4 (4.24 g, 20 mmol) were added in one portion, the tube was evacuated/backfilled with Ar three times, sealed and the mixture stirred vigorously at 90 °C for 73 h. The reaction mixture was then filtered through Celite® and the solvent evaporated. The residue was subjected to column chromatography (100% hexane to 100% ethyl acetate) to yield the product as a yellow solid (2.3 g), consisting of a mixture of ethyl/methyl esters. It was taken to the next step without further purification.

The intermediate ester (2.3 g) was dissolved in 1:1 THF/ CH_3OH mixture (100 mL). An aqueous NaOH solution (1.9 g in 50 mL H_2O, 47 mmol) was added to this mixture and then heated at 50 °C for 20 h. The solution was concentrated, residue diluted with water (100 mL), washed with ethyl acetate (2 x 50 mL, discarded), then diluted further with water to 500 mL vol. and acidified to pH 4 using 2N HCl. The precipitate was separated by filtration, washed thoroughly with water and air dried. ^1H NMR (600 MHz, DMSO-d_6): δ = 13.4 (br s, 2 H), 8.69 (d, J=5.9, 2H), 8.53 (m, ^1H), 8.47 (d, J=1.4, 2H), 7.79 (dd, J = 1.4, 4.6 Hz, 2 H). ^{13}C NMR (150 MHz, DMSO-d_6): δ = 166.3 (Cq), 150.5, 145.4 (Cq), 138.4 (Cq), 132.4 (Cq), 131.5, 130.3, 121.6.

2.7.4. Preparation of 4,4’-(pyridine-3,5-diyl)dibenzoic acid

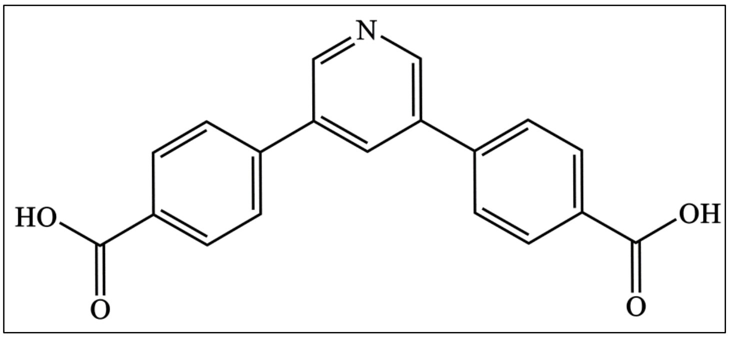

Figure 2.7 Chemical structure of 4,4’-(pyridine-3,5-diyl)dibenzoic acid.

An existing literature procedure was adapted to prepare 4,4’-(pyridine-3,5-diyl)dibenzoic acid (PDDB).[45] Here, a mixture of CH_3CN (40 mL) and aq. K_2CO_3 (5.52 g, 40 mmol, 8 eq. in 40 mL of DI water) were placed in a 500 mL Schlenk tube and evacuated/backfilled with Ar three times. Next, 3,5-dibromopyridine (1.18 g, 5 mmol, 1 eq.), 4-carboxyphenylboronic acid (1.83 g, 11 mmol, 2.2 eq.) and bis(triphenylphosphine)palladium(II) dichloride (0.4 g, 0.57 mmol, 0.11 eq.) were added in one portion, the tube was evacuated/backfilled with Ar three times, closed and the mixture stirred vigorously at 100 °C for 47 h. It was then cooled, diluted with 100 mL water, filtered through paper, and the filtrate was washed with AcOEt (50 mL, 2 x, discarded). The aqueous phase was acidified with 2N HCl and the gray precipitate was filtered, washed thoroughly with DI water and dried briefly in air with suction. The solid was redissolved in hot DMSO (150 mL) and after cooling, was reprecipitated by pouring the solution into DI water (700 mL) with stirring. The compound was filtered on paper, washed thoroughly with DI water and dried in air with suction to yield the product as a gray solid, 1.345 g (85%). ^1H NMR (600 MHz, DMSO-d_6): $\delta = 13.1$ (bs, 2H), 9.00 (d, J=1.8 Hz, 2H), 8.46 (t, J=1.8, 1H), 8.07 (d, J=8.3Hz, 4H), 8.01 (d, J=8.3Hz, 4H). 13C NMR (150 MHz, DMSO-d_6): δ = 167.0 (Cq), 147.4, 141.0 (Cq), 134.7 (Cq), 132.8, 130.5 (Cq), 130.0, 127.4.

2.7.5. Preparation of disodium tetrazole-5-carboxylate

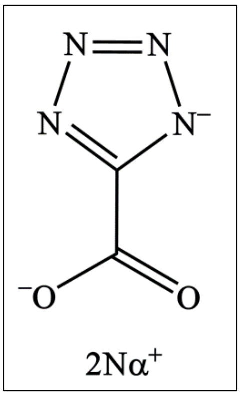

Figure 2.8 Chemical structure of disodium tetrazole-5-carboxylate.

A procedure from the literature was adapted.[46] 1H-Tetrazole-5-carboxylic acid ethyl ester sodium salt (5 g, 30 mmol) was dissolved in CH_3OH (75 mL) and an aqueous NaOH solution (3.7 g in 150 mL H_2O, 92 mmol) was added and the suspension stirred for 24 h. It was then concentrated into a small volume to generate a clear solution and poured on C_2H_5OH (200 mL) to produce a white precipitate. This was collected by filtration, washed with C_2H_5OH, dried in air at 65 °C to yield 4.68 g (97 %) of a white solid. ^{13}C NMR (150 MHz, D_2O): δ = 168.1, 160.8.

2.8. REFERENCES

1. (a) Cambridge Structural Database (CSD), http://www.ccdc.cam.ac.uk/products/csd/statistics/. (b) Allen, F. H., *Acta Crystallogr., Sect. B: Struct. Sci.* **2002,** *58*, 380-388.

2. (a) Stock, N.; Biswas, S., *Chem. Rev.* **2012,** *112*, 933-969.(b) Lee, Y.-R.; Kim, J.; Ahn, W.-S., *Korean J. Chem. Eng.* **2013,** *30*, 1667-1680.

3. Rowsell, J. L. C.; Yaghi, O. M., *Micropor. Mesopor. Mat.* **2004,** *73*, 3-14.

4. Liu, Y.; Kravtsov, V.; Larsen, R.; Eddaoudi, M., *Chem. Commun.* **2006**, 1488-1490.

5. Xue, D. X.; Cairns, A. J.; Belmabkhout, Y.; Wojtas, L.; Liu, Y.; Alkordi, M. H.; Eddaoudi, M., *J. Am. Chem. Soc.* **2013,** *135*, 7660-7667.

6. Bae, Y.-S.; Dubbeldam, D.; Nelson, A.; Walton, K. S.; Hupp, J. T.; Snurr, R. Q., *Chem. Mater.* **2009,** *21*, 4768-4777.

7. Bruker (**2013**). *APEX2* (Version 2013.6-2). Bruker AXS Inc., Madison, Wisconsin, USA.

8. Bruker (**2013**). *SAINT-V8.32A,*

9. Sheldrick, G. M. (**1996**). *SADABS*, University of Gottingen, Germany.

10. Sheldrick, G. M., *Acta Crystallogr. Sect. A* **2008,** *64*, 112-122.

11. (a) Sheldrick, G. M. (**1997**). *SHELXL-97*, University of Göttingen, Germany.(b) Farrugia, L. J., *J. Appl. Crystallogr.* **1999,** *32*, 837-838.(c) Sheldrick, G. M., *Acta Crystallogr. Sect. A* **1990,** *46*, 467-473.

12. Dolomanov, O. V.; Bourhis, L. J.; Gildea, R. J.; Howard, J. A. K.; Puschmann, H., *J. Appl. Crystallogr.* **2009,** *42*, 339-341.

13. (a) Blatov, V. A., *Struct. Chem.* **2012,** *23*, 955-963.(b) Blatov, V. A.; Carlucci, L.; Ciani, G.; Proserpio, D. M., *CrystEngComm* **2004,** *6*, 377-395.

14. Hafizovic, J.; Bjorgen, M.; Olsbye, U.; Dietzel, P. D. C.; Bordiga, S.; Prestipino, C.; Lamberti, C.; Lillerud, K. P., *J. Am. Chem. Soc.* **2007,** *129*, 3612-3620.

15. Gottlieb, H. E.; Kotlyar, V.; Nudelman, A., *J. Org. Chem.* **1997,** *62*, 7512-7515.

16. Farha, O. K.; Hupp, J. T., *Accts. Chem. Res.* **2010,** *43*, 1166-1175.

17. Liu, B.; Wong-Foy, A. G.; Matzger, A. J., *Chem. Commun.* **2013,** *49*, 1419-1421.

18. Nelson, A. P.; Farha, O. K.; Mulfort, K. L.; Hupp, J. T., *J. Am. Chem. Soc.* **2009,** *131*, 458-460.

19. Farha, O. K.; Eryazici, I.; Jeong, N. C.; Hauser, B. G.; Wilmer, C. E.; Sarjeant, A. A.; Snurr, R. Q.; Nguyen, S. T.; Yazaydin, A. O.; Hupp, J. T., *J. Am. Chem. Soc.* **2012,** *134*, 15016-15021.

20. Groen, J. C.; Peffer, L. A. A.; Pérez-Ramírez, J., *Micropor. Mesopor. Mat.* **2003,** *60*, 1-17.

21. Rouquerol, J.; Rouquerol, F.; Llewellyn, P.; Maurin, G.; Sing, K. S., *Adsorption by powders and porous solids: principles, methodology and applications*. Academic press: **2013**.

22. Barton, T. J.; Bull, L. M.; Klemperer, W. G.; Loy, D. A.; McEnaney, B.; Misono, M.; Monson, P. A.; Pez, G.; Scherer, G. W.; Vartuli, J. C.; Yaghi, O. M., *Chem. Mater.* **1999,** *11*, 2633-2656.

23. Evans, R.; Marconi, U. M. B.; Tarazona, P., *J. Chem. Soc. Faraday Trans.* **1986,** *82*, 1763-1787.

24. Sing, K.; Everett, D.; Haul, R.; Moscou, L.; Pierotti, R.; Rouquerol, J.; Siemieniewska, T., *Pure Appl. Chem.* **1982,** *54*, 2201-2218.

25. Brunauer, S.; Emmett, P. H.; Teller, E., *J. Am. Chem. Soc.* **1938,** *60*, 309-319.

26. Moellmer, J.; Celer, E. B.; Luebke, R.; Cairns, A. J.; Staudt, R.; Eddaoudi, M.; Thommes, M., *Micropor. Mesopor. Mat.* **2010,** *129*, 345-353.

27. Galarneau, A.; Desplantier, D.; Dutartre, R.; Di Renzo, F., *Micropor. Mesopor. Mat.* **1999,** *27*, 297-308.

28. Ravikovitch, P. I.; Neimark, A. V., *J. Phys. Chem. B* **2001,** *105*, 6817-6823.

29. Neimark, A. V.; Ravikovitch, P. I., *Micropor. Mesopor. Mat.* **2001,** *44*, 697-707.

30. Bhatia, S. K.; Myers, A. L., *Langmuir* **2006,** *22*, 1688-1700.

31. Vuong, T.; Monson, P. A., *Langmuir* **1996,** *12*, 5425-5432.

32. Belmabkhout, Y.; Frere, M.; De Weireld, G., *Meas. Sci. Tech.* **2004,** *15*, 848-858.

33. Alezi, D.; Belmabkhout, Y.; Suyetin, M.; Bhatt, P. M.; Weselinski, L. J.; Solovyeva, V.; Adil, K.; Spanopoulos, I.; Trikalitis, P. N.; Emwas, A. H.; Eddaoudi, M., *J. Am. Chem. Soc.* **2015,** *137*, 13308-13318.

34. Myers, A. L.; Prausnitz, J. M., *AlChE J.* **1965,** *11*, 121.

35. Bae, Y. S.; Mulfort, K. L.; Frost, H.; Ryan, P.; Punnathanam, S.; Broadbelt, L. J.; Hupp, J. T.; Snurr, R. Q., *Langmuir* **2008,** *24*, 8592-8598.

36. Yang, Q.; Zhong, C., *J. Phys. Chem. B* **2006,** *110*, 17776-17783.

37. Toth, J., *Uniform and thermodynamically consistent interpretation of adsorption isotherms*. **2002**; Vol. 107.

38. Guillerm, V.; Weselinski, L. J.; Alkordi, M.; Mohideen, M. I. H.; Belmabkhout, Y.; Cairns, A. J.; Eddaoudi, M., *Chemical Communications* **2014,** *50*, 1937-1940.

39. Van Heest, T.; Teich-McGoldrick, S. L.; Greathouse, J. A.; Allendorf, M. D.; Sholl, D. S., *J. Phys. Chem. C* **2012,** *116*, 13183-13195.

40. Luebke, R.; Eubank, J. F.; Cairns, A. J.; Belmabkhout, Y.; Wojtas, L.; Eddaoudi, M., *Chem. Commun.* **2012,** *48*, 1455-1457.

41. Hayton, W. L.; Chen, T., *J. Pharm. Sci.* **1982,** *71*, 820-821.

42. Horcajada, P.; Serre, C.; Vallet-Regi, M.; Sebban, M.; Taulelle, F.; Ferey, G., *Angew. Chem. Int. Ed. Engl.* **2006,** *45*, 5974-5978.

43. (a) Du, L. T.; Lu, Z. Y.; Zheng, K. Y.; Wang, J. Y.; Zheng, X.; Pan, Y.; You, X. Z.; Bai, J. F., *J. Am. Chem. Soc.* **2013,** *135*, 562-565.(b) Du, L. T.; Lu, Z. Y.; Ma, M. T.; Su, F.; Xu, L., *Rsc Advances* **2015,** *5*, 29505-29508.

44. (a) Jia, J. H.; Athwal, H. S.; Blake, A. J.; Champness, N. R.; Hubberstey, P.; Schroder, M., *Dalton Trans.* **2011,** *40*, 12342-12349.(b) Yun, R.; Jiang, Y.; Xu, G., *Inorg. Chim. Acta.* **2014,** *414*, 141-144.

45. Jia, J. H.; Lin, X.; Wilson, C.; Blake, A. J.; Champness, N. R.; Hubberstey, P.; Walker, G.; Cussen, E. J.; Schroder, M., *Chem. Commun.* **2007**, 840-842.

46. Smith, C.; Fleury, M.; Gendron, R.; Hudson, R.; Hughes, A. D., Neprilysin inhibitors US 20120157386 A1, **2012**.

Chapter 3: Pillaring in MOFs as a Design Strategy: The Supermolecular Building Layers (SBLs) Approach to MOFs Synthesis

3.1. Abstract

The ligand-to-axial (L-A) pillaring technique was implemented successfully in designing and synthesizing novel MOFs with targeted/predicted topologies and interesting properties. This powerful design strategy was utilized to construct a new MOF, Cu-**pyr**-MOF, with ultra-high SA, one of the highest values reported to date. An extended trigonal hetero-functional ligand, along with Cu ions, was employed to target the *in situ* formation of the necessary SBLs and pillar them into the 3-P MOF with predicted **pyr** topology, extra-large cavities and ultra-high SA.

In addition, three **eea**-MOFs were also targeted and prepared using the same strategy but starting with a shorter ligand that had an additional functional site (not involved in the coordination), permitting the introduction of additional functionalities, including different halide ions in the three isostructures.

Finally, the six-connected axial-to-axial (6-c A-A) pillaring technique was used, allowing the construction of two isoreticular MOFs with the rare **lon** topology and enabling the modification of their properties without changing their underlying network topology.

3.2. General introduction

Recently, as illustrated in Chapter 1, the SBLs approach was introduced by Eddaoudi et al. to aid in the design and rational construction of made-to-order MOFs.[1] This method depends on the construction of pre-targeted 2-P layers (SBLs) as building units that are pillared, with various pillaring techniques (Chapter 1), into predicted 3-P

MOFs possessing tunable cavities and specific underlying network topologies.[2] This approach has many distinctive advantages, including the ability to endlessly expand the confined spaces (e.g., cages, channels) or modify their functionalities without changing the underlying network topology that can help in targeting specific applications.[1]

In the first and second parts of this chapter, as an extension of our group's earlier work (Chapter 1),[2-3] the L-A pillaring technique was implemented where different trigonal hetero-functional ligands that are composed of bent dicarboxylate and N-donor moieties were used to serve as 3-connected nodes (3-c). As expected, when mixed with Cu or Zn, the carboxylate moieties of the ligands formed four connected paddlewheel MBBs that, in turn, built the SBLs (**kgm** or **sql** edge-transitive nets). The N-donor moieties connected to the axial position of the paddlewheels of adjacent layers and caused their pillaring into 3-P MOFs. The influence of using an extended ligand or a ligand with an additional functional group (Figure 3.1) was investigated and resulted in the synthesis of **pyr**-MOFs and **eea**-MOFs, respectively.

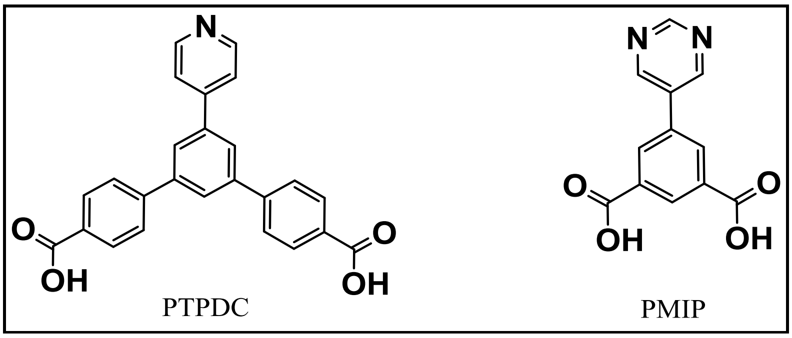

Figure 3.1 The bifunctional angular ligands used in the current study to construct pillared MOFs utilizing the L-A pillaring technique.

In the third part of this chapter is described the **kgm** layers that were formed and pillared using tetrazole-5-carboxylate ethyl ester (TCEE) (Figure 3.2) utilizing the 6-c A-A pillaring technique and resulting in the synthesis of Cu-**lon**-MOF.[1, 4] The effect of changing ligand functionalities, without modifying the underlying network topology, was examined and produced the isoreticular structure, H-Cu-**lon**-MOF.[5, 6]

Figure 3.2 The ligands used in current study to construct pillared MOFs utilizing the 6-c A-A pillaring technique.

The structural and gas sorption properties of the three prepared platforms, their isostructures and/or isoreticular structures were studied, and the compounds were fully characterized to establish the structure-property relationship that elucidated the effect of using varied ligands on tuning structure properties, including gas sorption behavior.

3.3. Experimental section part I: L-A pillaring technique to construct 3-P MOFs: The effect of ligand expansion

3.3.1. Introduction

As mentioned before, the work presented here is a continuation of our group's previous work based on the recently introduced L-A pillaring technique.[2] This strategy depends on using trigonal hetero-functional ligands to pillar 2-P edge-transitive SBLs into 3-P MOFs. With this, in order to reach this goal and construct new MOFs with large tunable cavities that are suitable for gas storage studies, the 5'-(pyridin-4-yl)-[1,1':3',1''-terphenyl]-4,4''-dicarboxylic acid (PTPDC) ligand was chosen. This is an analogous version of the previously used ligands in our group's work (Figure 3.3)[2-3] where the isophthalic acid moiety is expanded by its simple substitution with [1,1':3',1''-terphenyl]-4,4''-dicarboxylic acid.

The purpose of this type of modification is to emphasize the importance of the L-A pillaring technique in the case where MOFs synthesis using pillared layers is targeted. Accordingly, this technique offers an endless tuning capacity for constructed MOFs through the use of various ligands and functional groups.

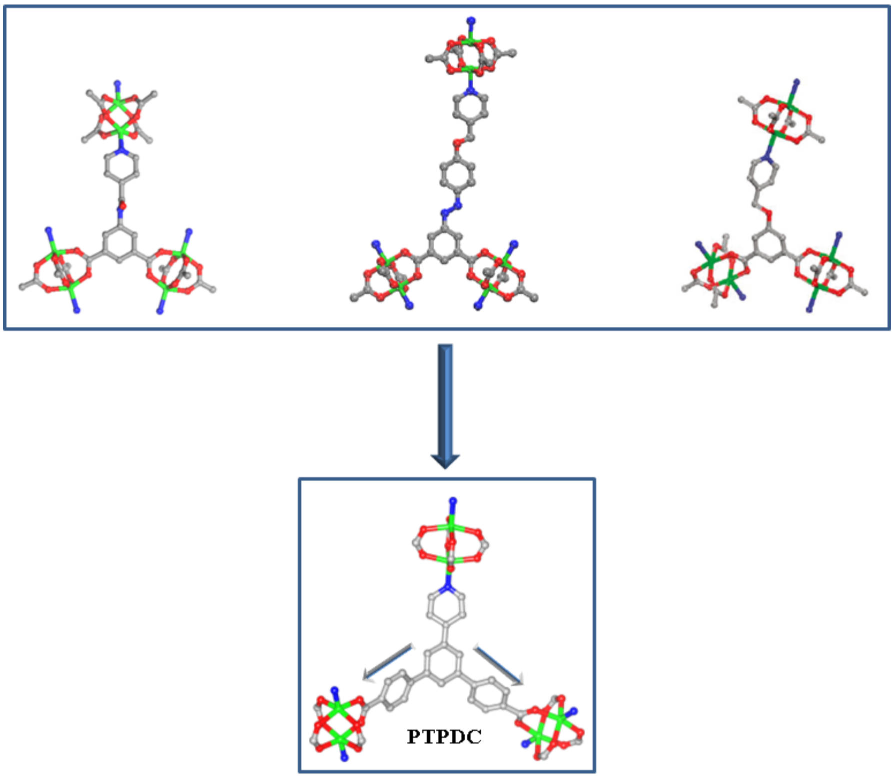

Figure 3.3 Examples of bifunctional trigonal ligands previously used by our group to construct 3-P MOFs utilizing the L-A pillaring technique compared to PTPDC with the expanded isophthalic acid moiety (indicated by arrows).

Under appropriate reaction conditions, when PTPDC is mixed with $Zn(NO_3)_2$, which can form paddlewheel MBBs, the carboxylate groups of the ligand are expected to construct 2-P **kgm** or **sql** SBLs that are pillared through the nitrogen donor moiety into a 3-P MOF with predictable underlying network topology.[7]

It is worth mentioning that, in some cases, Zn-based MOFs show lower gas uptake versus those containing Cu ions as a consequence of their lower degree of stability. As this was the case in the first isostructure of this study (Zn-**pyr**-MOF), a single-crystal-to-single-crystal (SCSC) metal ion exchange or transmetalation of Zn into Cu ions was performed, significantly inducing gas adsorption.[8]

This step was carried out because Cu is known for its higher stability in paddlewheel MBBs, which leads to the formation of a more rigid coordination environment and enhances framework stability.[9] Zn-based paddlewheel MBBs may seem structurally similar to those that are Cu-based because both have a square planar metal-O_4 conformation, though the underlying cause of this similarity is totally different. The Cu square planar arrangement is because of the orbital directing effect of the non-filled d^9 shell, whereas the Zn square planar arrangement is mainly the result of the higher coordination of the metal (d^{10} shell), causes greater repulsion effects and pushing the oxygen atoms toward the planar, i.e., steric factors with no ligand field stabilization energy.[9] In addition, Zn-based and Cu-based paddlewheel MBBs are different in terms of metal-metal distance. This can also be attributed to the orbital directing effect of the d^9 Cu(II) that leads to a shorter distance between Cu-Cu (2.71 Å) when compared to that between Zn-Zn (2.97 Å).[10, 11]

3.3.2. Materials and methods

All chemicals, unless otherwise mentioned, were used as received from Fisher Scientific, Sigma-Aldrich and/or Acros Organics and other commercial sources without further purification. For details about devices, software used and ligands syntheses, please refer to Chapter 2.

3.3.3. Synthesis and characterization

3.3.3.1. Synthesis of Zn-pyr-MOF

A solution of $Zn(NO_3)_2.6H_2O$ (7.4 mg, 0.025 mmol), PTPDC (5 mg, 0.012 mmol), 1.5 mL DMF and 0.1 mL CH_3OH was prepared in a 20-mL scintillation vial and subsequently heated to 85 °C for 12 h. Sheet-like colorless crystals of Zn-**pyr**-MOF were collected and washed with fresh DMF several times.

3.3.3.2. Activation of Zn-pyr-MOF

After different activation trials of this framework using a number of organic solvents, like CH_3OH, C_2H_5OH, CH_3CN and $CHCl_3$, two activation methods were finally adopted. The first was the conventional solvent exchange method[12] where a 50 mg DMF-washed Zn-**pyr**-MOF sample was exchanged with $CHCl_3$ over a period of 7 days while refreshing the solution frequently (3-5 times daily using approximately 15 mL of $CHCl_3$ each time). Prior to the LP gas sorption experiments, the sample was placed into a 6 mm large bulb sorption cell, the excess surface solvent was removed with a syringe and the sample was subjected to a flow of N_2 to dry the surface solvent. The sample was then subjected to dynamic vacuum at RT for 12 h, and then it was heated gradually to 105 °C and held at that temperature for 24 h while vacuum was maintained.

The second activation method was through the SC-CO_2[13] dryer, where roughly 50 mg of DMF-washed sample was first rinsed very briefly with CH_3OH and then transferred to the SC-CO_2 dryer chamber, which is cooled to -7 °C and pressurized by injecting CO_2. The sample was next soaked in liquid CO_2 that was frequently purged for two days to replace any solvent. The temperature and pressure were then raised above the CO_2 critical point, and the sample was kept in SC-CO_2 for one day. Bleeding was conducted slowly over a period of around 6 h, and the sample became completely dry. Before the LP gas sorption experiments, the sample was transferred to a 6 mm large bulb sorption cell under a N_2 environment (in a glove box) followed by being subjected to dynamic vacuum at RT for 12 h.

3.3.3.3. Preparation of Cu(e)-pyr-MOF through transmetalation

To achieve this goal, an SCSC Zn(II) to Cu(II) exchange within Zn-**pyr**-MOF was performed. Here, around 50 mg of the as-synthesized Zn-**pyr**-MOF crystals, which were initially washed with fresh DMF a few times, were soaked in 15 mL of 0.1 M $Cu(NO_3)_2$ in DMF solution at RT without stirring or disturbing for 10 days. The solution was refreshed twice during this period; by the end, the colorless crystals gradually became green, indicating exchange of Zn metal ions within the framework into Cu but they maintained their original shapes and sizes. The exchange solution was then decanted and the cation-exchanged crystals, Cu(e)-**pyr**-MOF, were washed several times and suspended in fresh DMF at RT for 7 days to remove excess Cu ions.[8]

3.3.3.4. Activation of Cu(e)-pyr-MOF

This was performed using SC-CO_2 activation following the same procedure detailed in Section 3.3.3.2.

3.3.3.5. Synthesis of Cu-pyr-MOF

A solution of $Cu(NO_3)_2.6H_2O$ (6.25mg, 0.025 mmol), PTPDC (5 mg, 0.012 mmol), 0.75 mL DMF, 0.1 mL CH_3OH and 0.02 mL 4.4 M HNO_3/DMF was prepared in a 20-mL scintillation vial and subsequently heated to 65 °C for 36 h. Polyhedral green crystals of Cu-**pyr**-MOF were collected and washed with fresh DMF several times.

3.3.3.6. Activation of (Cu-pyr-MOF)

For LP studies, SC-CO_2 was employed adhering to the same procedure detailed in Section 3.3.3.2. In addition, the same procedure was followed for activating a 100 mg sample for the HP study, though the sample was kept in liquid SC-CO_2 for 3 days with frequent purging before transferring to the SC-CO_2 state.

3.3.4. Results and discussion

In this portion of the chapter, the focus was on using the SBLs approach to develop MOF materials targeted for gas storage or separation applications. Here, a specific focus was to study the effect of using an expanded isophthalic acid-like ligand that contains bent dicarboxylate functionalities and a nitrogen donor group at the 5-position on the structure-function relationship of prepared MOFs and to specifically assess the influence of extending the ligand on gas adsorption behavior. To this end, PTPDC was employed along with $Zn(NO_3)_2$ to form a 3-P L-A pillared MOF with a predicted topology (Zn-**pyr**-MOF) where ligand extension was expected to increase the void space in the prepared MOF and consequently increase its gas storage ability.[2]

It is noteworthy that when gas sorption studies were performed, Zn-**pyr**-MOF showed substantially lower experimental PV and less gas uptake than the anticipated values. Therefore, transmetalation from Zn(II) to Cu(II) was performed to form Cu(e)-**pyr**-MOF, which allowed drastic enhancement in gas uptake, albeit with significantly diminished accessible PV compared to the theoretical one.

In light of these encouraging results, we concentrated our efforts on trying to optimize the direct synthesis of the Cu-based isostructure. To our delight, attempts to isolate Cu-**pyr**-MOF were successful. This analogue exhibited high gas uptake and the anticipated high experimental SA and PV that matched the theoretical values.

All three isostructures, Zn-**pyr**-MOF, Cu(e)-**pyr**-MOF and Cu-**pyr**-MOF, were synthesized and characterized by X-ray crystallography and gas sorption experiments.

3.3.4.1. **Zn**-pyr-**MOF**

A solvothermal reaction between $Zn(NO_3)_2.6H_2O$ and PTPDC in DMF in the presence of CH_3OH was placed at 85 °C to yield colorless sheet-like crystals of Zn-**pyr**-MOF that are insoluble in water and common organic solvents. The as-synthesized sample was purified by repeated washing with fresh DMF.

SCXRD analysis revealed that Zn-**pyr**-MOF crystallizes in the orthorhombic space group, *Pbca*, with cell parameters of a = 23.7, b = 20.7, c = 24.7 Å and $\alpha = \beta = \gamma = 90^\circ$ forming a 3-P MOF. In the crystal structure of Zn-**pyr**-MOF, four carboxylate groups from four different ligands connected a pair of zinc ions to generate paddlewheels or square SBUs. These SBUs formed edge-transitive 2-P **sql** SBLs that were pillared through the coordination of nitrogen (pyridinyl) moieties to the apical positions of the metal-carboxylate paddlewheel clusters of the adjacent layers forming a 3-P MOF (Figure 3.4).

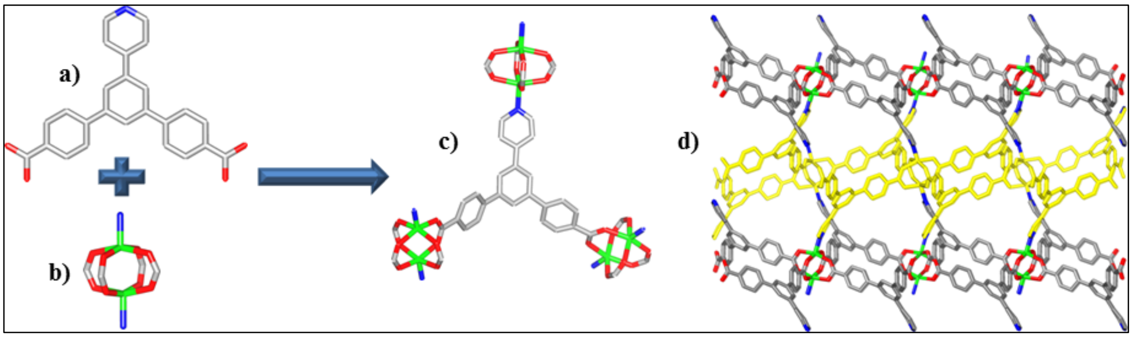

Figure 3.4 (a) PTPDC, (b) paddlewheel MBB, (c) the coordination mode of PTPDC to the MBBs and d) crystal structure of Zn-**pyr**-MOF (c-axis) showing pillared **sql** layers where one layer is highlighted in yellow. Zn = green, C = gray, O = red, and N = blue. Hydrogen atoms and solvent molecules are omitted for clarity.

Being staggered between neighboring sheets, the orientation of the 2-P layers formed 3-D intersecting zigzag-shaped channels (~10 x 12 Å) (Figure 3.5).

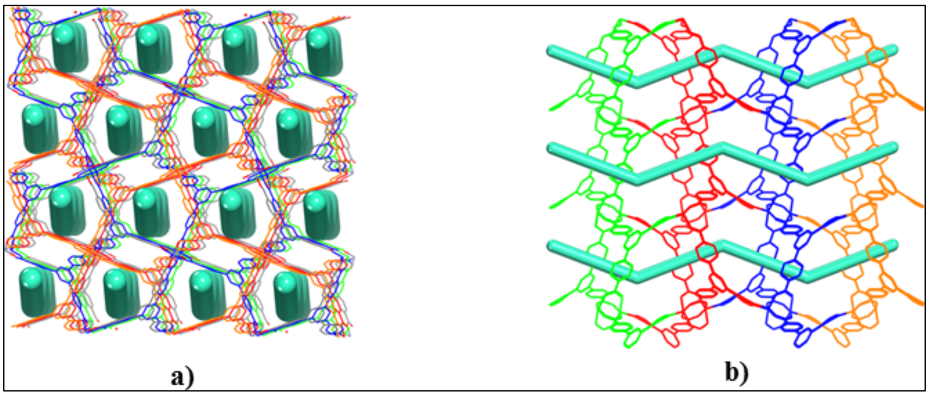

Figure 3.5 The zigzag-shaped channels (represented as turquoise cylinders) are a result of the staggered stacking of neighboring sheets; (a) overhead view, and (b) side view. Each layer is shown in a different color for clarity.

In this structure, PTPDC serves as a triangular 3-c node, and the paddlewheel cluster serves as a 6-c octahedral node leading to the formation of the anticipated (3,6)-c pyrite net (**pyr**).[2, 14] It is worth mentioning that the topological analysis of the structure was performed using TOPOS software.[15]

The evident similarities between the calculated and experimental PXRD were used to confirm the phase purity of the bulk crystalline material (Figure 3.6). This compound was stable in DMF, $CHCl_3$ and CH_3CN but demonstrated a high degree of sensitivity to water and air. Therefore, during PXRD collection, a special X-ray protective film had to be used to protect the samples.

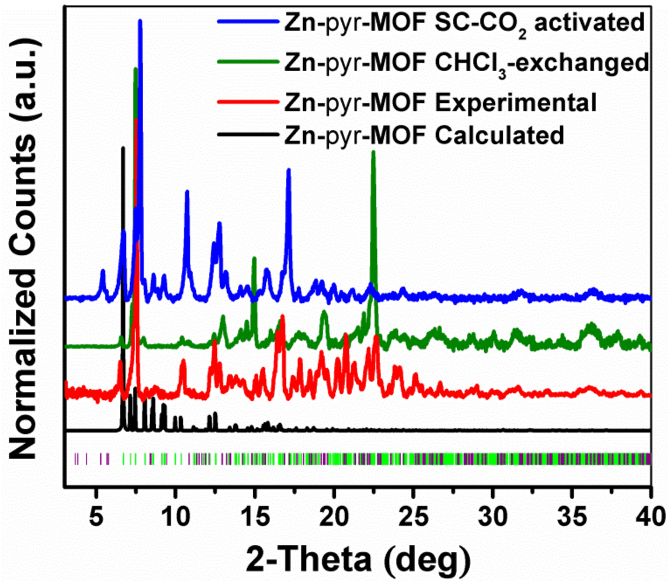

Figure 3.6 PXRD spectra of calculated Zn-**pyr**-MOF (black), experimental (red), $CHCl_3$-exchanged (olive) and SC-CO_2 activated (blue).

To investigate the thermal stability of Zn-**pyr**-MOF, TGA was performed on DMF-washed $CHCl_3$ and SC-CO_2 activated samples under a N_2 atmosphere. The tests were carried out between RT and 700 °C with an increasing heating rate of 20 °C/min in high resolution dynamic mode. The TGA plots of Zn-**pyr**-MOF indicate the framework thermal stability up to 370 °C (Figure 3.7).

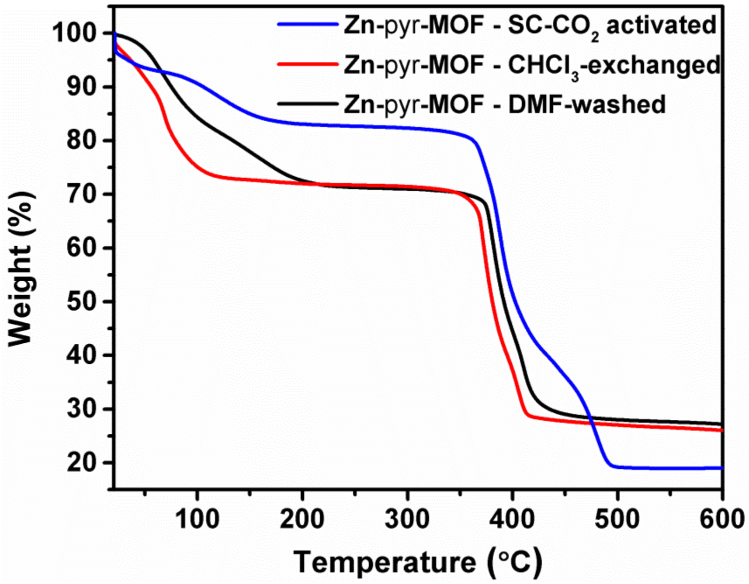

Figure 3.7 Zn-**pyr**-MOF TGA plots showing DMF-washed (black), $CHCl_3$-exchanged (red) and SC-CO_2 activated (blue) samples indicating framework stability for up to 370 °C.

The potential total solvent-accessible volume of the as-synthesized Zn-**pyr**-MOF was estimated to be 76.5% from SC structure using MS software. In addition, the PV_{Theo} of the structure was estimated to be 1.5 cm^3/g with an evacuated framework density of 0.52 g/ cm^3.

To determine the actual porosity of the framework and subsequently assay its potential for gas storage and separation applications, gas sorption experiments were performed and isotherms were collected using several probe molecules at different temperatures and pressures. The first sorption study was conducted using a $CHCl_3$-exchanged sample that was subjected to vacuum at 105 °C. This activation method was chosen after several activation attempts with various solvents at a number of different temperatures (Figure 3.8 and Figure 3.9).

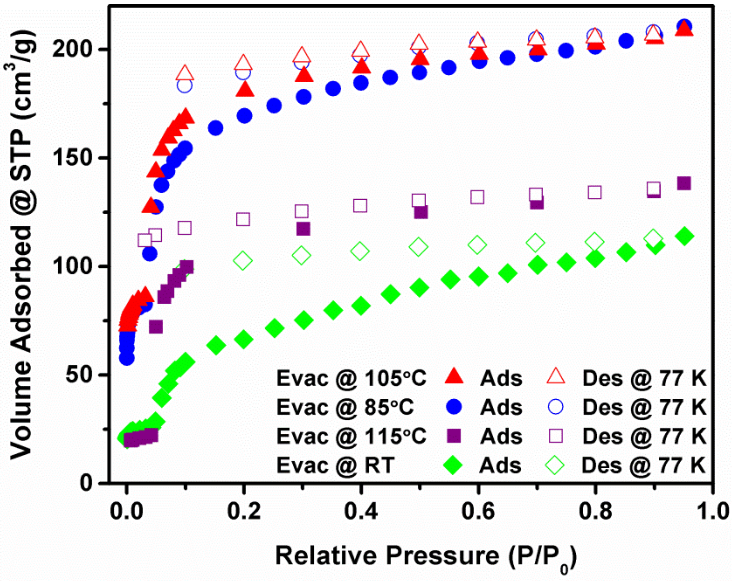

Figure 3.8 N_2 sorption isotherms at 77 K of the $CHCl_3$-exchanged Zn-**pyr**-MOF sample subjected to vacuum under different temperatures as an example of activation screening.

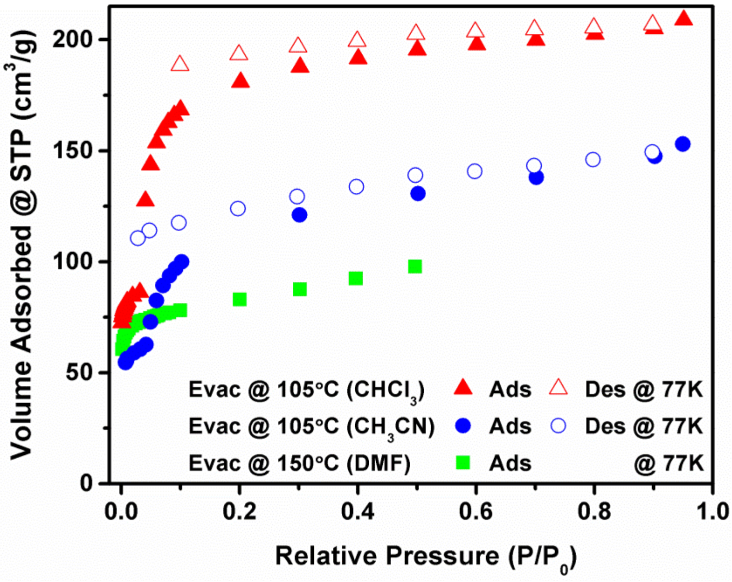

Figure 3.9 Comparing N_2 sorption isotherms at 77 K utilizing different solvents during activation screening of Zn-**pyr**-MOF.

The collected N_2 and Ar sorption isotherms of $CHCl_3$-activated Zn-**pyr**-MOF at 77 and 87 K, respectively, suggesting they were Type I, confirming the framework's permanent porosity (Figure 3.10). The step and the differences between the adsorption and desorption branches observed in both isotherms could be explained by the diffusion limitation mainly based on the flexibility of the expanded ligand.[16] As a result of the Ar isotherm, the experimental SA_{BET} and the total free PV were estimated to be 360 m^2/g and 0.3 cm^3/g, respectively.

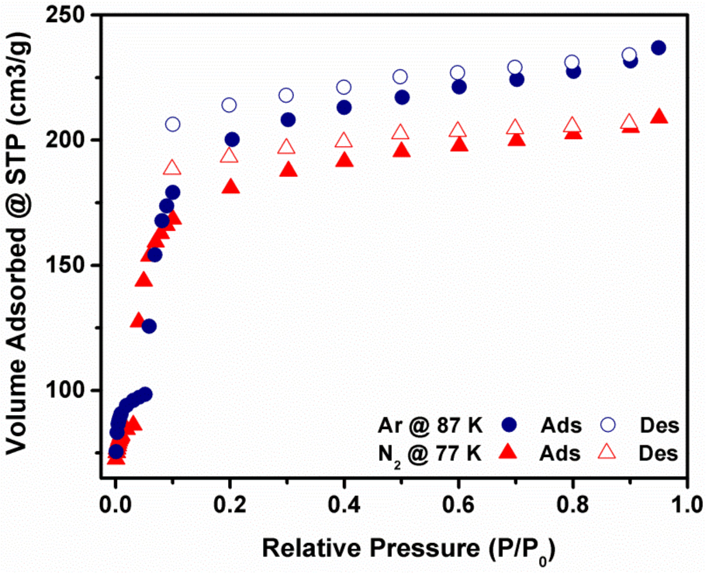

Figure 3.10 N_2 and Ar uptake of the $CHCl_3$-exchanged Zn-**pyr**-MOF sample activated at 105 °C at 77 and 87 K, respectively.

These experimental values are substantially lower than the theoretical ones estimated from SC structure, and this can be credited to the high degree of flexibility of the expanded ligand and the low stability of the Zn paddlewheel MBBs. This resulted in framework distortion and its partial collapse upon guest removal if not carefully activated, evidenced by the low intensity and broader peaks of PXRD patterns of the $CHCl_3$-activated sample (Figure 3.6).[16b, 17]

As the conventional method of activation was not effective for optimally activating Zn-**pyr**-MOF without affecting its crystallinity, i.e., its porosity toward N_2 and Ar at cryogenic temperatures, an alternative method of activation was required. Consequently, adsorption experiments were performed on SC-CO_2-activated Zn-**pyr**-MOF.[18] In this case, N_2 uptake was improved, and the isotherm showed no step or hysteresis (Figure 3.11). The experimental SA_{BET} and the total free PV were estimated to be 969 m^2/g and 0.44 cm^3/g, respectively. These experimental values are still dramatically lower than those that were theoretical; therefore, transmetalation was performed to exchange the Zn(II) in the framework with Cu(II), forming Cu(e)-**pyr**-MOF with the aim of producing a more stable MOF. Of note is that post-synthetic metal ion exchange or the transmetalation approach is considered a novel strategy to develop MOF materials for highly selective gas-related applications, including gas storage and separation.[8]

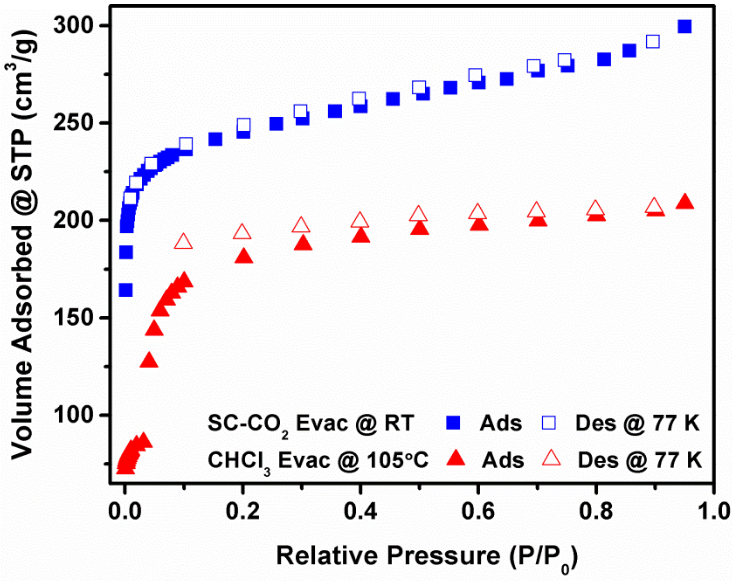

Figure 3.11 N_2 sorption isotherms at 77 K of Zn-**pyr**-MOF utilizing two different activation methods.

3.3.4.2. Cu(e)-pyr-MOF: The product of transmetalation of Zn(II) with Cu(II) within Zn-pyr-MOF

The transmetalation of Zn(II) into Cu(II) in Zn-**pyr**-MOF to produce Cu(e)-**pyr**-MOF was accomplished by soaking the colorless Zn-**pyr**-MOF crystals in $Cu(NO_3)_2$ solution for 10 days and refreshing the solution twice. The PXRD patterns of the new green crystals was identical to those of the original Zn-**pyr**-MOF, indicating that the framework was preserved during the transmetalation process (Figure 3.12).[19] ICP was employed to calculate the percentage of Zn ions exchanged with Cu ions, and it employed an exchange of approximately 75%. Further extension of exchange time caused the framework to collapse and lose its crystallinity.

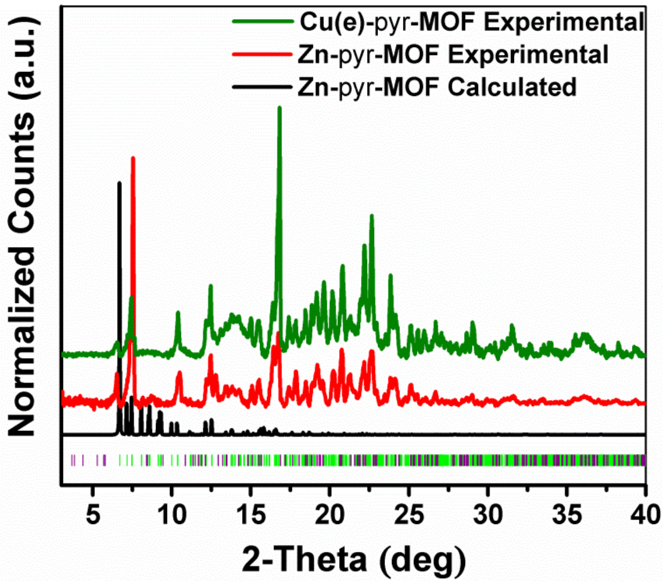

Figure 3.12 PXRD spectra of Cu(e)-**pyr**-MOF (green) compared to the calculated (black) and experimental (red) patterns of Zn-**pyr**-MOF.

The thermal stability of DMF-washed Cu(e)-**pyr**-MOF was investigated with TGA under a N_2 atmosphere. This test was performed between RT and 700 °C at an increasing heating rate of 20 °C/min in high resolution dynamic mode. The TGA plot (Figure 3.13) suggests that Cu(e)-**pyr**-MOF is thermally stable up to 280 °C.

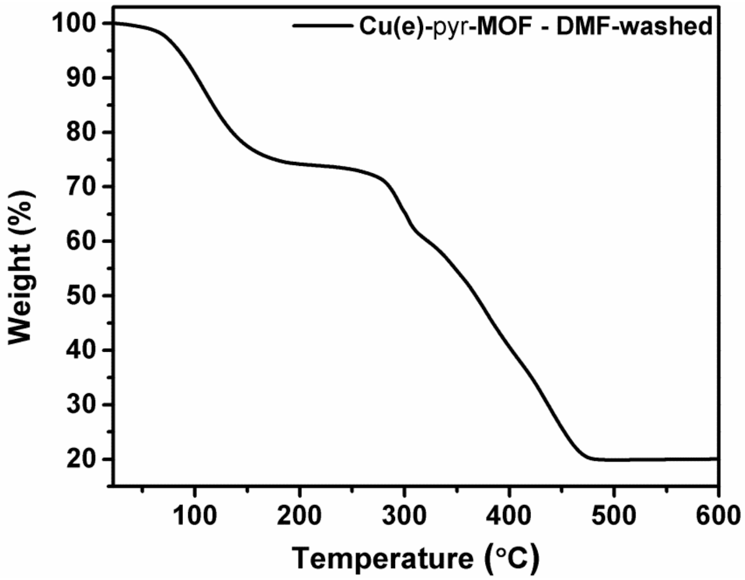

Figure 3.13 TGA plots of the DMF-washed Cu(e)-**pyr**-MOF sample showing framework decomposition at 280 °C.

Sorption studies were performed on SC-CO_2-activated Cu(e)-**pyr**-MOF and, as expected, this framework had a much higher gas uptake versus Zn-**pyr**-MOF (Figure 3.14). In this case, N_2 uptake at 77 K was enhanced, showing a typical Type I isotherm with no step or hysteresis. The experimental SA_{BET} and the total free PV were estimated to be 2151 m^2/g and 1 cm^3/g, respectively. These experimental values were still lower than what was predicted theoretically. In addition, at this stage of investigations, we were finally able to identify the reaction conditions needed to successfully prepare the Cu-**pyr**-MOF isostructure starting from $Cu(NO_3)_2$ instead of $Zn(NO_3)_2$.

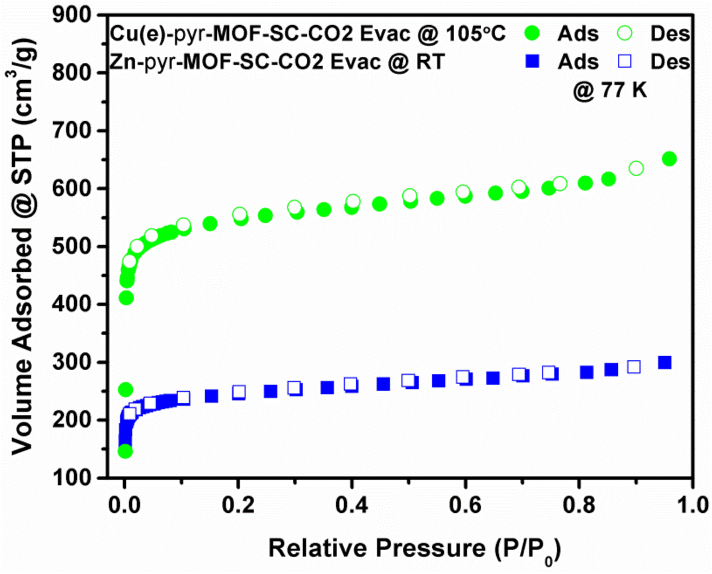

Figure 3.14 N_2 isotherms comparing gas uptake of SC-CO_2-activated Zn-**pyr**-MOF and that of Cu(e)-**pyr**-MOF.

3.3.4.3. **Cu**-pyr-**MOF**

At the beginning of this study, the direct preparation of the Cu-**pyr**-MOF isostructure, i.e., an isostructure having 100% Cu ions, was not successful. After various trials, we were finally able to establish the appropriate reaction conditions that fostered its synthesis with $Cu(NO_3)_2$ salt. Therefore, a solvothermal reaction between $Cu(NO_3)_2$ and PTPDC in DMF in the presence of CH_3OH and acid was placed at 65 °C to yield green polyhedral crystals of Cu-**pyr**-MOF that were insoluble in water and common organic solvents. The as-synthesized sample was purified by repeated washing with fresh DMF.

The crystals of Cu-**pyr**-MOF showed very weak diffraction on the SC diffractometer and synchrotron, therefore, their crystal structure determination was unsuccessful, but their PXRD patterns were identical to those of Zn-**pyr**-MOF (Figure 3.15) indicating that these two compounds were isostructural.

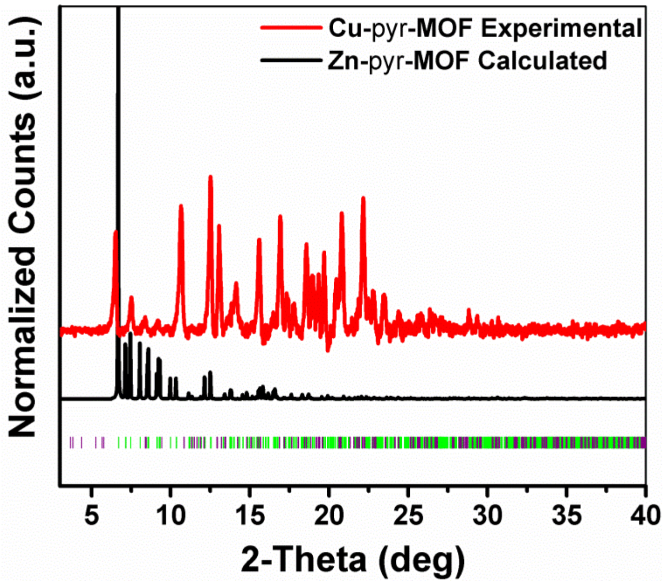

Figure 3.15 PXRD spectra of experimental Cu-**pyr**-MOF (red) compared to calculated Zn-**pyr**-MOF (black) pattern.

To investigate the thermal stability of Cu-**pyr**-MOF, TGA was carried out on DMF-washed and SC-CO_2-activated samples under a N_2 atmosphere. The tests were executed between RT and 700 °C at an increasing heating rate of 20 °C/min in high resolution dynamic mode. The TGA plots of Cu-**pyr**-MOF indicated its thermal stability up to 250 °C (Figure 3.16).

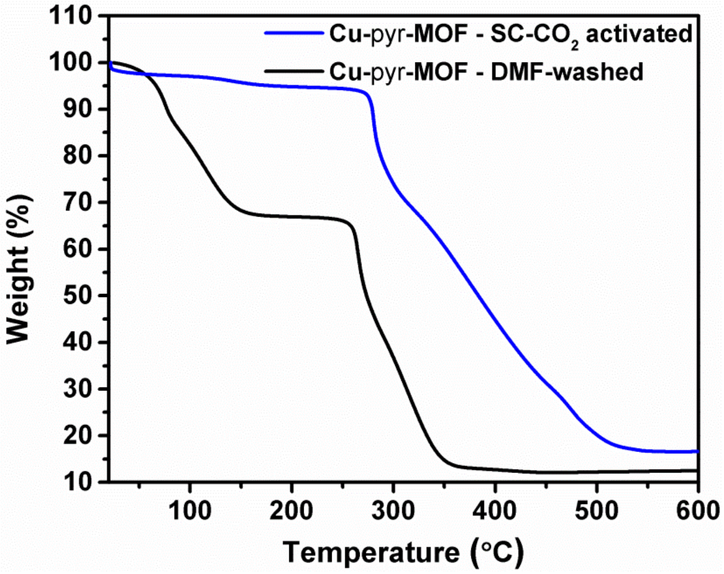

Figure 3.16 Cu-**pyr**-MOF TGA plots of DMF-washed sample (black) and SC-CO_2 activated sample (blue) indicating framework stability for up to 250 °C.

To assess the porosity of Cu-**pyr**-MOF, sorption studies were conducted on samples that were washed with DMF and directly activated using the SC-CO_2 dryer. In this situation, N_2 and Ar uptake at 77 K and 87 K, respectively (Figure 3.17), were significantly enhanced compared to those of Zn-**pyr**-MOF and Cu(e)-**pyr**-MOF (Figure 3.18), showing typical Type I reversible sorption isotherms, suggesting framework permanent microporosity. The significant enrichment in gas adsorption capacity of this isostructure could be rationalized, as mentioned earlier, by the higher stability of Cu in the paddlewheel MBB versus Zn.[8, 10]

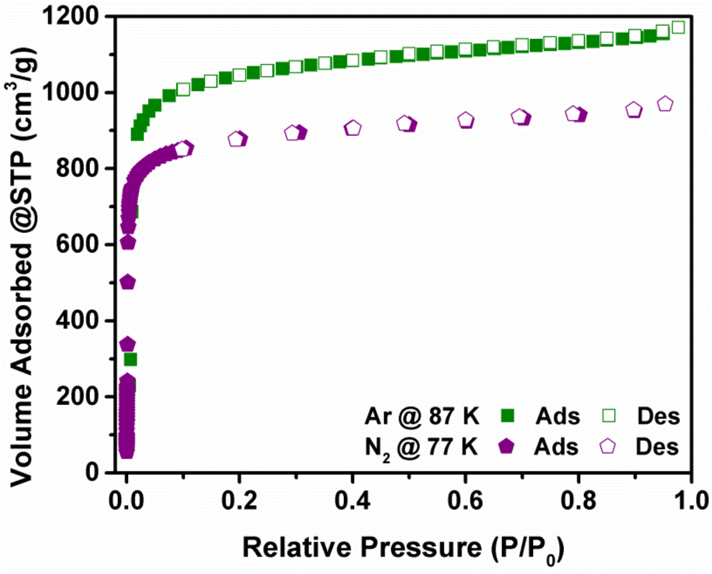

Figure 3.17 Fully-reversible LP Ar at 87 K and N_2 at 77 K sorption isotherms of SC-CO_2-activated Cu-**pyr**-MOF.

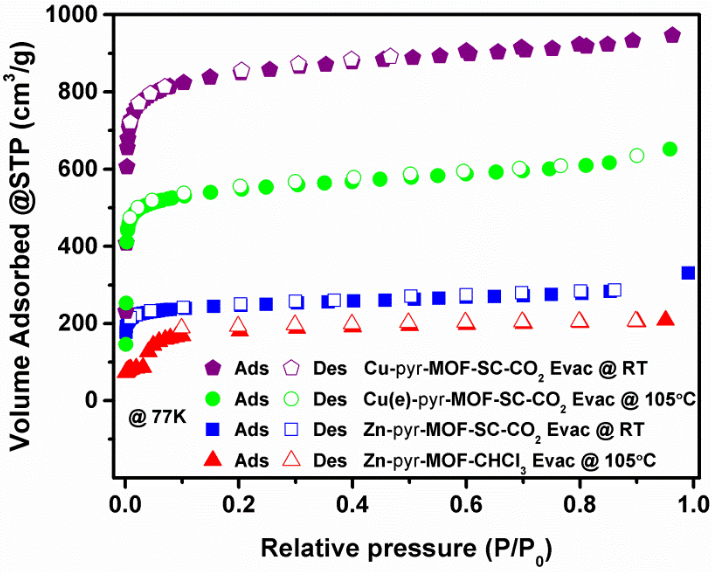

Figure 3.18 Summary of N_2 uptake at 77 K for all isostructures investigated in this study.

Here, the total experimental PV was estimated, based on the Ar isotherm, to be 1.5 cm^3/g, which is in solid agreement with the expected theoretical values estimated from the crystallographic data. Additionally, the experimental SA_{BET} was anticipated to be 4753 m^2/g, among the highest values reported to date for any porous material (Table 1.1).[13, 20] Indeed, the conformity between the experimental and theoretical values is an indication of activation method success and shows that the entire theoretical SA is accessible.[21]

It is worth noting, however, that SC-CO_2 activation is usually performed on solvent-exchanged samples[12, 22] and is very rarely used directly to activate as-synthesized samples, despite being proven successful in this study.

To further assess Cu-**pyr**-MOF as an adsorbent, LP H_2 and CO_2 sorption studies were undertaken. Adsorption isotherms of H_2 measured at 77 and 87 K and those of CO_2 measured at 258, 273, 288 and 298 K were employed to determine the Q_{st} for both gases using the Clausius-Clapeyron expression.

Based on these LP isotherms, at 760 Torr, Cu-**pyr**-MOF demonstrated a relatively high H_2 uptake of 2.99 and 1.87 wt% at 77 and 87 K, respectively. In addition, the maximum Q_{st} for H_2 was found to be 6.5 kJ/mol at zero coverage, a value that decreased to 4.5 kJ/mol with elevated loading (Figure 3.19). These values are consistent with microporous MOFs that have large cavities (> 10 Å).[23]

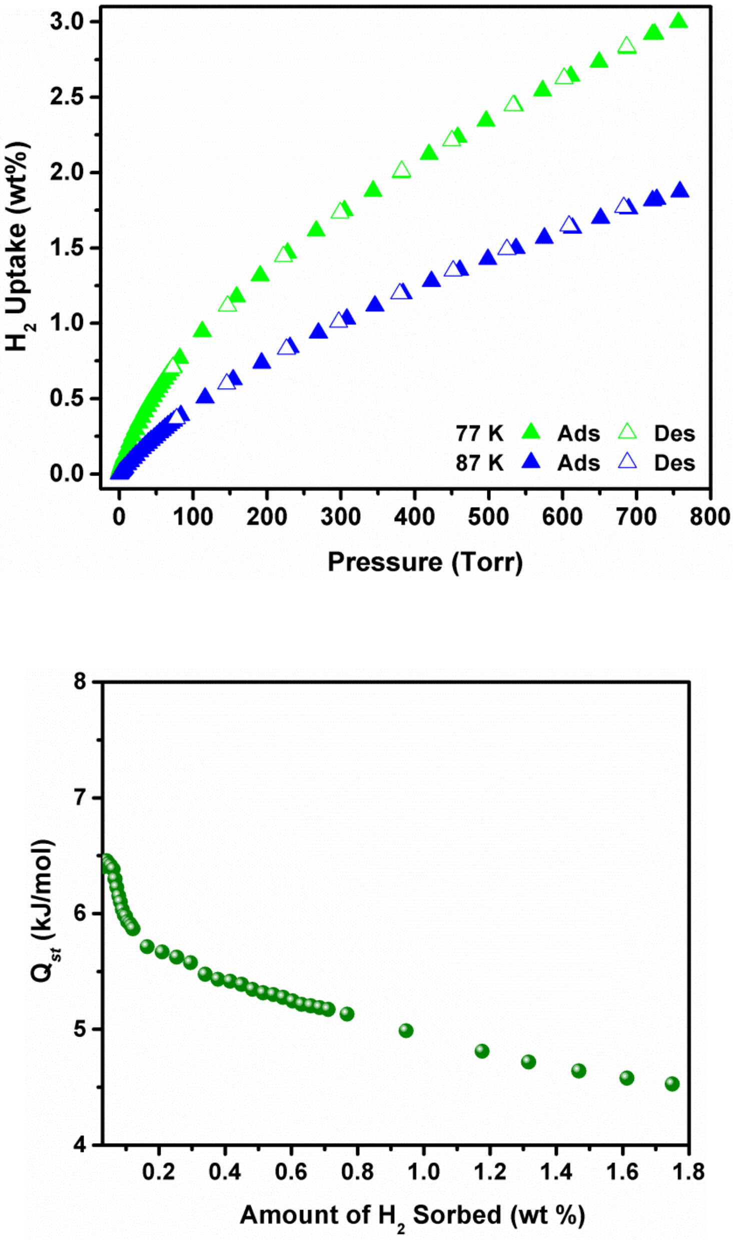

Figure 3.19 LP H_2 sorption isotherms at 77 and 87 K for Cu-**pyr**-MOF and the corresponding Q_{st}.

In addition, it was observed that Cu-**pyr**-MOF reversibly adsorbs CO_2 and the uptake was determined to be 2.17 mmol/g from the adsorption isotherm measured under ambient conditions, i.e., at 298 K and 760 Torr. Compared to the best performing MOFs, such as M-MOF-74 and bio-MOF-11,[20d, 24] the amount of CO_2 adsorbed by Cu-**pyr**-MOF under these conditions was moderate, but it still surpassed many of the well-known MOFs characterized by their functional groups and open metal sites, e.g., Cr-MIL-53.[25]

Moreover, the Q_{st} of CO_2 was determined from the variable temperature adsorption isotherms and was estimated to be 25.8 and 20.6 kJ/mol at low and high loading, respectively (Figure 3.20). These values are considered moderate when compared to values reported in the literature.[26]

Of interest is that Q_{st} is the energy of interaction between adsorption sites of the adsorbent and the molecular gases. Therefore, higher Q_{st} is observed with lower coverage as the strongest binding sites are initially occupied. However, at higher levels of loading, the sites with lower adsorption enthalpy start to become filled, leading to lower Q_{st} values.[27]

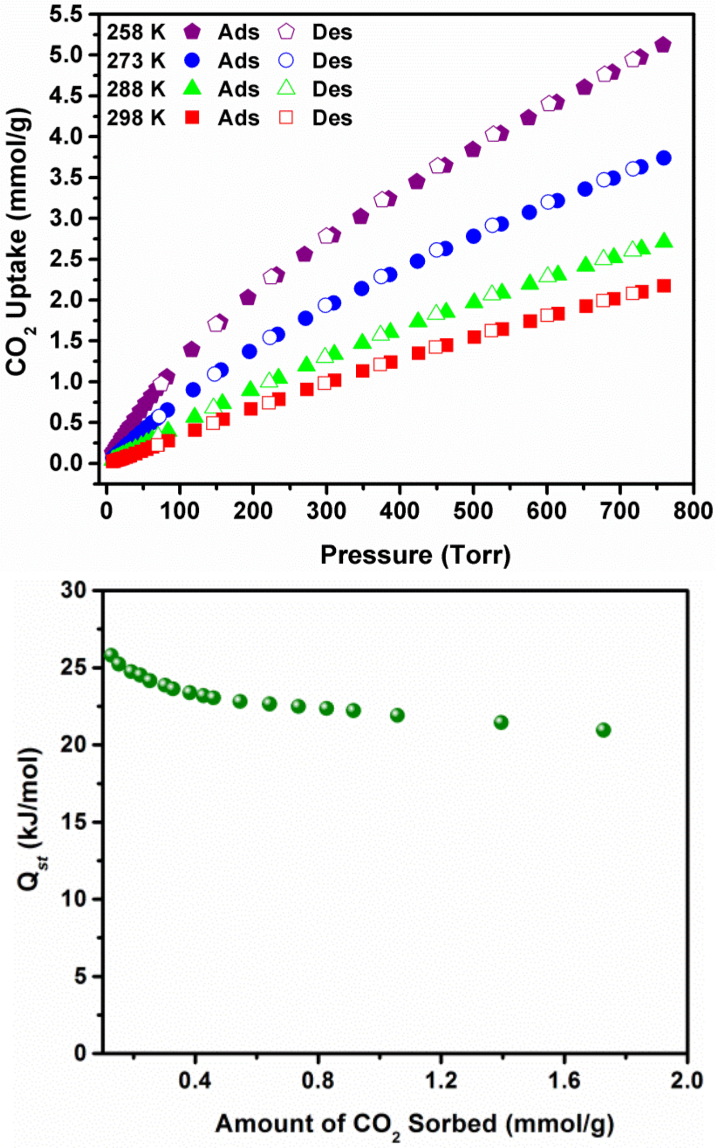

Figure 3.20 LP CO_2 variable temperature sorption isotherms at 258, 273, 288 and 298 K of Cu-**pyr**-MOF and their corresponding Q_{st}.

As Cu-**pyr**-MOF was proven to have ultra-high SA and high PV, its potential application in gas storage and separation was investigated by evaluating its selective gas uptake toward different probe molecules, such as N_2, CO_2 and CH_4. Therefore, HP sorption studies at 298 K and elevated pressure, up to 25 bar for CO_2 and N_2 and 80 bar for CH_4, were performed.

Here, Cu-**pyr**-MOF exhibited a high CO_2 adsorption capacity of 19 mmol/g or 0.84 g/g at 25 bar and 298 K (Figure 3.21), which can be considered amongst the highest CO_2 uptake per surface unit reported at this pressure.[26, 28]

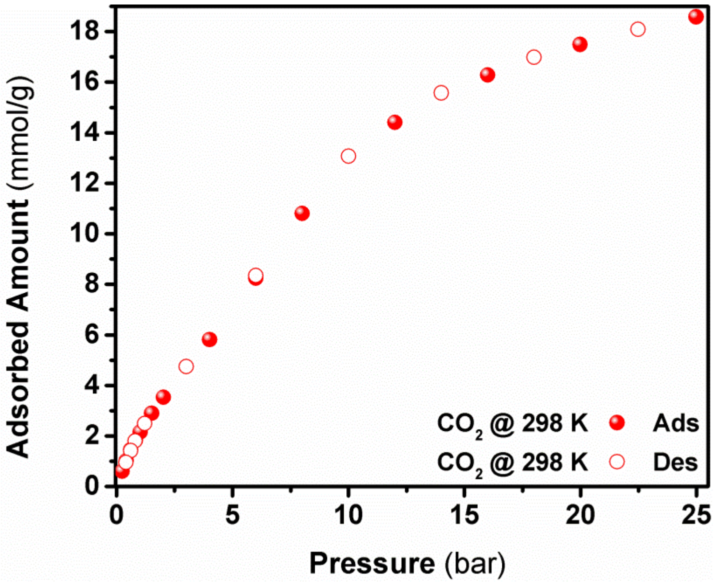

Figure 3.21 HP CO_2 adsorption and desorption isotherms of Cu-**pyr**-MOF at 298 K.

Additional HP studies were conducted at 25 °C to evaluate Cu-**pyr**-MOF adsorption behavior toward CH_4 gas and showed high CH_4 uptake of 13 mmol/g at 50 bar, 11 mmol/g at 35 bar and 3 mmol/g at 5 bar (Figure 3.22). When comparing these values to a group of high performing MOFs, Cu-**pyr**-MOF is impressive with regards to CH_4 gravimetric uptake (Table 3.1).

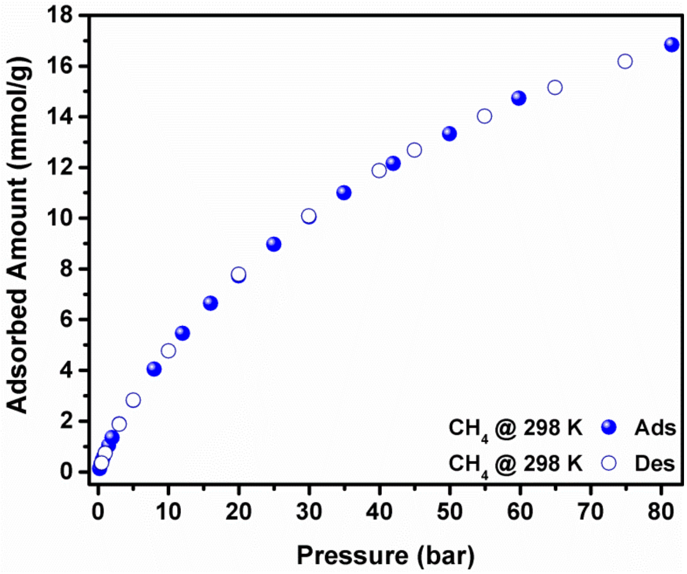

Figure 3.22 HP CH_4 sorption isotherm for Cu-**pyr**-MOF at 298 K.

Table 3-1 Total CH_4 uptake and volumetric working capacities for Cu-**pyr**-MOF at 298 K in different pressure ranges versus a selection of the most promising MOFs reported to date.

	Total uptake (cm^3(STP)/cm^3)					**Working Capacity (cm^3(STP)/cm^3)**				
Material	**5 bar**	**35 bar**	**50 bar**	**65 bar**	**80 bar**	**5-35 bar**	**5-50 bar**	**5-65 bar**	**5-80 bar**	**Ref.**
UTSA-20	60	184	178	230	--	124	80	170	--	[29]
PCN-14	73	195	--	230	250	122	--	157	--	[30]
HKUST-1	77	227	250	267	272	150	175	190	200	[18]
NU-125	49	182	220	232	--	120	170	183	--	[29b, 31]
Ni-MOF-74	--	228	--	251	--	--	--	129	--	[29b]
Al-**soc**-MOF-1	20.9	--	--	197	222	--	--	176	200.8	[28]
MOF-519	49	200	240		279	151	191	--	230	[32]
Cu-pyr-**MOF**	35	128	151	175	196	93	117	140	161	**Here**

Looking at Figure 3.22 and Table 3-1, the CH_4 volumetric working storage capacity of Cu-**pyr**-MOF was calculated and found to be about 117 cm^3(STP)/cm^3, assuming that 50 bar was the highest adsorption pressure and 5 bar the lowest (according to the requirement of the engine CH_4 injection pressure).[31] This value is much greater than that of UTSA-20, though still inferior to that of recently reported MOFs, such as NU-125. In addition, the volumetric working storage capacity of the framework was also calculated and found to be 140 cm^3(STP)/cm^3 at a pressure range of 65 to 5 bar. This value was higher than Ni-MOF-74, comparable to PCN-14 but lower than the working capacity of the best performing MOFs, like Al-**soc**-MOF-1. In this case, the density of Cu-**pyr**-MOF was assumed to be constant and equal to the theoretical value of 0.52 g/cm^3 estimated from the SC structure.[28]

For comparison's sake, CO_2, N_2 and CH_4 uptake of Cu-**pyr**-MOF under the same conditions (298 K and 25 bar) were 19, 5 and 9 mmol/g, respectively, suggesting the favorable selectivity of the framework for CO_2 over CH_4 and N_2 (Figure 3.23).

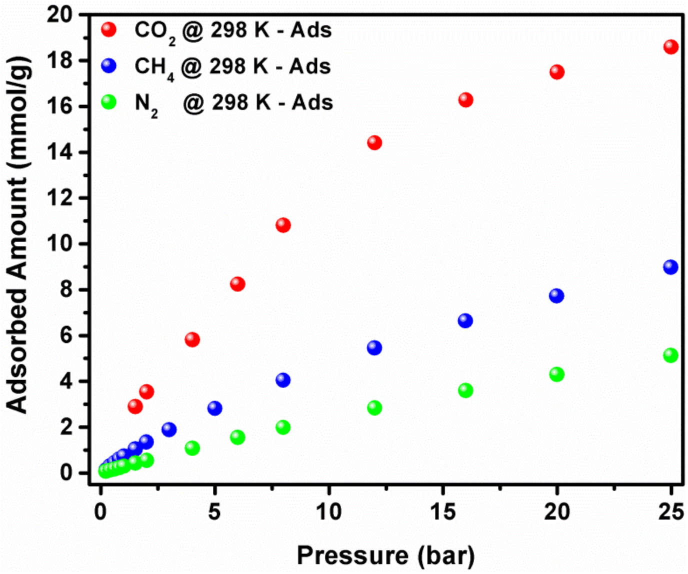

Figure 3.23 Summary of Cu-**pyr**-MOF HP adsorption isotherms at 298 K for CO_2, N_2 and CH_4.

Further HP sorption studies were undertaken to evaluate Cu-**pyr**-MOF behavior towards larger probe molecules that have relatively high polarizabilities, such as C_2H_6, C_3H_8 and n-C_4H_{10} (C2+) (Figure 3.24). Furthermore, the estimation of the Cu-**pyr**-MOF's potential use in the separation between C2+/CH_4 was performed by reviewing these results against those for the corresponding CH_4 as well as CO_2 sorption.

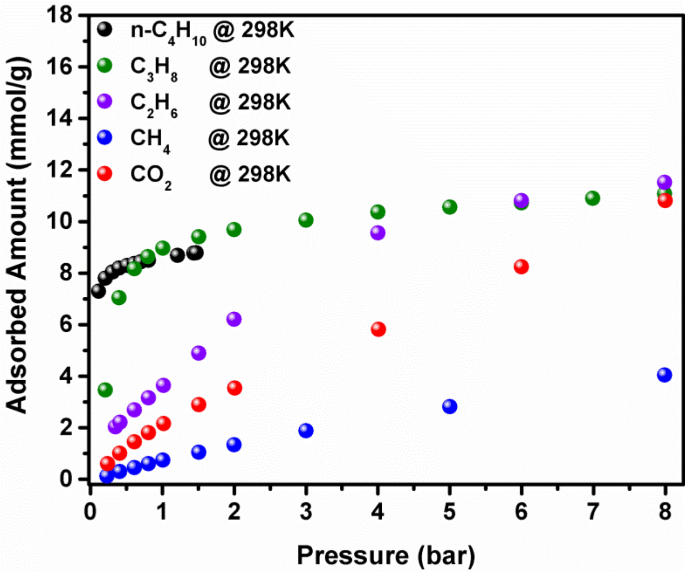

Figure 3.24 Summary of Cu-**pyr**-MOF HP adsorption isotherms at 298 K for hydrocarbons compared to those of CH_4 and CO_2.

Interestingly, C2+ showed much steeper adsorption isotherms than CO_2 and CH_4, which in turn reflects the framework's preferential adsorption of C2+.

Finally, to further this study, Cu-**pyr**-MOF behavior towards another valuable commodity, namely O_2, was also investigated. The HP O_2 adsorption data up to 60 bar (at 298 K) is presented in Figure 3.25 and shows that Cu-**pyr**-MOF exhibits higher gravimetric uptake and storage capacity when compared to HKUST-1 and NU-125 at this temperature and pressure but lower than that of Al-**soc**-MOF-1.[28, 33]

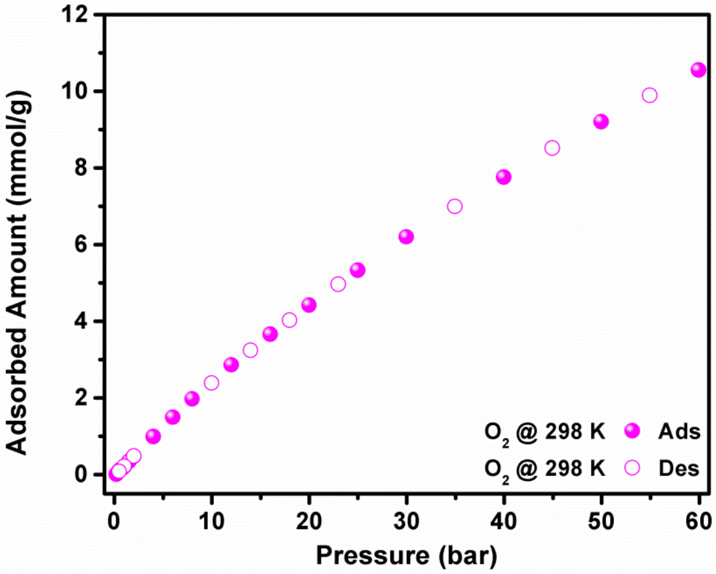

Figure 3.25 Cu-**pyr**-MOF HP O_2 sorption isotherm at 298 K.

3.3.5. Summary and conclusions

In this part of the work, we have constructed a new MOF utilizing the L-A pillaring strategy, where an extended isophthalic acid-based ligand (PTPDC) was used along with $Zn(NO_3)_2$ to build Zn-**pyr**-MOF. The framework experienced partial collapse after both conventional and SC-CO_2 activation, demonstrated in the form of low gas uptake capacity. Interestingly, post-synthetic Zn(II) ion exchange with Cu(II) in Zn-**pyr**-MOF under mild conditions led to its transformation into Cu(II)/Zn(II)-based Cu(e)-**pyr**-MOF while preserving its underlying net. This MOF demonstrated improved gas uptake capacity after SC-CO_2 activation but did not reach the expected theoretical values. Therefore, PTPDC was made use of with $Cu(NO_3)_2$ to create a new MOF (Cu-**pyr**-MOF), the Cu(II)-based isostructure. The experimental SA_{BET} of Cu-**pyr**-MOF was estimated to be among the highest values that have been reported for any porous material to date. In addition, CO_2 uptake of Cu-**pyr**-MOF under ambient conditions was found to be moderate with modest Q_{st} values versus the best performing frameworks. On the other hand, at 25 bar and 298 K, Cu-**pyr**-MOF showed high CO_2 adsorption capacity, which can be considered among the highest CO_2 uptake values per surface unit reported at this pressure. Furthermore, the framework exhibited potential for applications to separate CO_2 from N_2 and CH_4 and to separate large hydrocarbons, like C_3H_8 and n-C_4H_{10}, from CH_4.

3.4. Experimental section part II: L-A pillaring technique to construct 3-P MOFs: The effect of using a ligand with an additional functional group

3.4.1. Introduction

The work presented here is an extension of our group's previous work where the L-A pillaring technique was first introduced (Figure 3.26).[2-3] As mentioned earlier, this strategy depends on using trigonal hetero-functional ligands to pillar *in situ*-formed edge-transitive 2-P SBLs into 3-P MOFs of tunable cavities. The ligand used here was 5-(pyrimidin-5-yl)isophthalic acid (PMIP) (Figure 3.26) where the carboxylate groups were necessary to construct pre-targeted 2-P **kgm** or **sql** SBLs pillared by the L-A pillaring technique through one of the nitrogen atoms of the pyrimidine moiety into a 3-P MOF. The second nitrogen is present to allow for extra functionalization and tuning of the cavities that may direct prepared frameworks for specific applications.

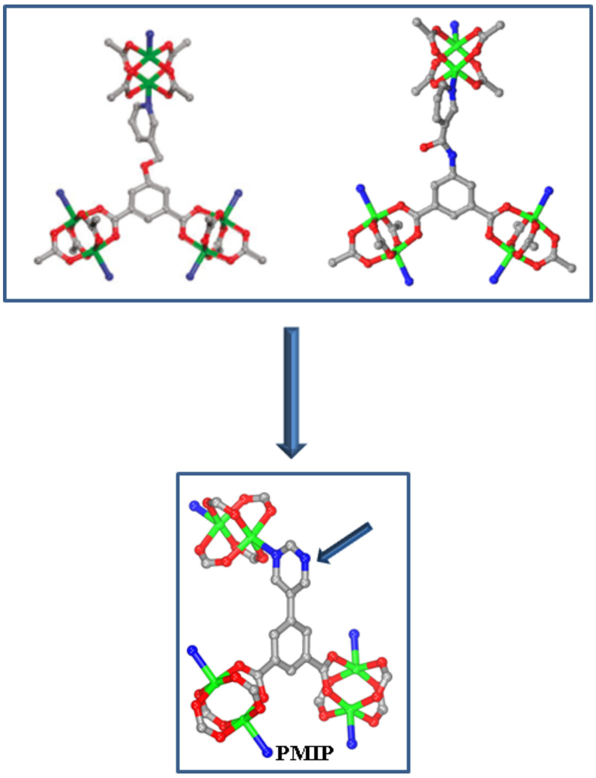

Figure 3.26 Examples of bifunctional trigonal ligands previously used by our group to construct 3-P MOFs utilizing the L-A pillaring technique compared to the ligand used here (PMIP) with its extra functionalization site (indicated by an arrow).

Three isostructural MOFs, namely Cl-**eea**-MOF, Br-**eea**-MOF and I-**eea**-MOF, containing Cl, Br and I ions, respectively, were synthesized and characterized. In addition, their properties that may be dependent on the respective halide component, such as gas sorption, were investigated. Therefore, the behavior of the frameworks toward different gases, including N_2, CO_2 and H_2, was explored.

3.4.2. Materials and methods

All chemicals, unless otherwise mentioned, were used as received from Fisher Scientific, Sigma-Aldrich or Acros Organics and other commercial sources without further purification. For ligand syntheses and details on the devices and software used, please refer to Chapter 2.

3.4.3. Synthesis and characterization

3.4.3.1. Synthesis of **Cl-**eea**-MOF**

A solution of $Cu(NO_3)_2.3H_2O$ (4.8 mg, 0.02 mmol), 1 mL NMP, CuCl (2 mg, 0.02 mmol), 0.5 mL CH_3CN, PMIP (5 mg, 0.02 mmol), 1 mL DMF, 0.1 mL CH_3OH and 0.2 mL 3.5 M HNO_3/DMF was prepared in a 20 mL scintillation vial and subsequently heated to 85 °C for 12 h. Green hexagonal sheet-like crystals of Cl-**eea**-MOF were collected and washed with fresh DMF several times.

3.4.3.2. Activation of **Cl-**eea**-MOF**

A 50-mg of DMF-washed Cl-**eea**-MOF sample was exchanged with CH_3OH over a period of 7 days while refreshing the solution frequently (3-5 times per day using approximately 15 mL of CH_3OH each time). Prior to the LP gas sorption experiments, the sample was placed into a 6 mm large bulb sorption cell; the excess surface solvent was removed with a syringe and the sample was subjected to a flow of N_2 to dry the surface solvent. The sample was then subjected to dynamic vacuum at RT for 3 h. Then, while maintaining the vacuum, the sample was heated in a gradual manner to 55 °C for another 3 h followed by heating to 85 °C for 12 h.

3.4.3.3. Synthesis of **Br-**eea**-MOF**

A solution of $Cu(NO_3)_2.3H_2O$ (4.8 mg, 0.02 mmol), 1 mL NMP, CuBr (5.74 mg, 0.04mmol), 1 mL CH_3CN, PMIP (5 mg, 0.02 mmol), 1 mL DMF, 0.1 mL CH_3OH and 0.2 mL 3.5 M HNO_3/DMF was prepared in a 20 mL scintillation vial and subsequently heated to 85 °C for 12 h. Hexagonal sheet-like green crystals of Br-**eea**-MOF were collected and washed with fresh DMF several times.

3.4.3.4. Activation of Br-eea-MOF

Br-**eea**-MOF was activated in the same manner as Cl-**eea**-MOF (Section 3.4.3.2).

3.4.3.5. Synthesis of I-eea-MOF

A solution of $Cu(NO_3)_2.3H_2O$ (4.8 mg, 0.02 mmol), 1 mL NMP, CuI (3.75 mg, 0.02mmol), 0.5 mL CH_3CN, PMIP (5 mg, 0.02 mmol), 1 mL DMF, 0.1 mL CH_3OH and 0.2 mL 3.5 M HNO_3/DMF was prepared in a 20 mL scintillation vial and subsequently heated to 85 °C for 12 h. Dark green polyhedral crystals of I-**eea**-MOF were collected and washed with fresh DMF several times.

3.4.3.6. Activation of I-eea-MOF

I-**eea**-MOF was activated in the same manner as Cl-**eea**-MOF (Section 3.4.3.2).

3.4.4. Results and discussion

In this section, concentration is directed toward using the SBLs approach to develop MOF materials targeted for gas separation applications. As an extension of our group's previous work (Chapter 1)[2], the specific focus was to study the effect of having a ligand with an additional functionalization site on the structure-function relationship of the prepared MOFs. In seeking to meet this goal, PMIP was used as the organic building unit to construct a 3-P L-A pillared MOFs where one of the nitrogen atoms of the pyrimidine moiety was intended to participate in pillaring of the *in situ*-formed 2-P layers and the second nitrogen atom would act as an additional functionalization site. Consequently, the effect of coordinating the additional functionalization site to different halides (Cl, Br and I) on gas adsorption properties of the prepared isostructures was studied. Hence, three isostructural MOFs, which are Cl-**eea**-MOF, Br-**eea**-MOF and I-**eea**-MOF containing Cl, Br and I atoms, respectively, were synthesized and characterized by X-ray crystallography and gas sorption experiments.

3.4.4.1. Cl-eea-MOF, Br-eea-MOF and I-eea-MOF

A solvothermal reaction between $Cu(NO_3)_2.3H_2O$ in NMP, CuCl in CH_3CN and PMIP (Figure 3.27 a) in DMF in the presence of CH_3OH and 3.5 M HNO_3/DMF was placed at 85 °C to yield green hexagonal sheet-like crystals of Cl-**eea**-MOF that were insoluble in water and common organic solvents. CuBr and CuI were used instead of CuCl under similar reaction conditions to prepare Br-**eea**-MOF and I-**eea**-MOF isostructures, respectively. The as-synthesized samples were purified by repeated washing with fresh DMF.

X-ray SC structure analysis revealed that both Cl-**eea**-MOF and Br-**eea**-MOF crystallized in the rhombohedral-centered hexagonal space group R-3m with cell parameters of $a = b = 18.6$, $c = 28.6$ Å, $\alpha = \beta = 90$ and $\gamma = 120^\circ$ forming 3-P MOFs with three different types of cages. The crystals of I-**eea**-MOF exhibited weak diffraction with the SC diffractometer; therefore, its SC structure determination was unsuccessful, but its PXRD patterns were identical to those of Cl- and Br-**eea**-MOF, indicating that these three compounds are isostructural (hereafter, X-**eea**-MOFs will be used to refer to the three isostructures). These compounds demonstrated high stability in air and various organic solvents.

In these structures, there are two crystallographic independent Cu atoms, Cu1 and Cu2. Cu1 exists in dinuclear clusters that are coordinated by oxygen atoms of four carboxylate groups from four independent ligands forming paddlewheel MBBs (Figure 3.27 b). These MBBs are linked together to form **kgm** edge-transitive 2-P SBLs (Figure 3.27 e). The axial positions of each paddlewheel are occupied by one of the ligands' pyrimidine nitrogen atoms from neighboring layers, leading to the formation of 6-c dimer units and pillaring of the 2-P **kgm** layers, consequently generating a 3-P MOF (Figure 3.27 f). The other independent Cu atom, Cu2, forms a tetrahedral node that connects three pyrimidine nitrogen atoms from three adjacent ligands and the fourth position is occupied by Cl, Br or I atoms in the Cl, Br and I isostructures, respectively (Figure 3.27 c). This part of the structure is the only exhibited difference between the three isostructures.

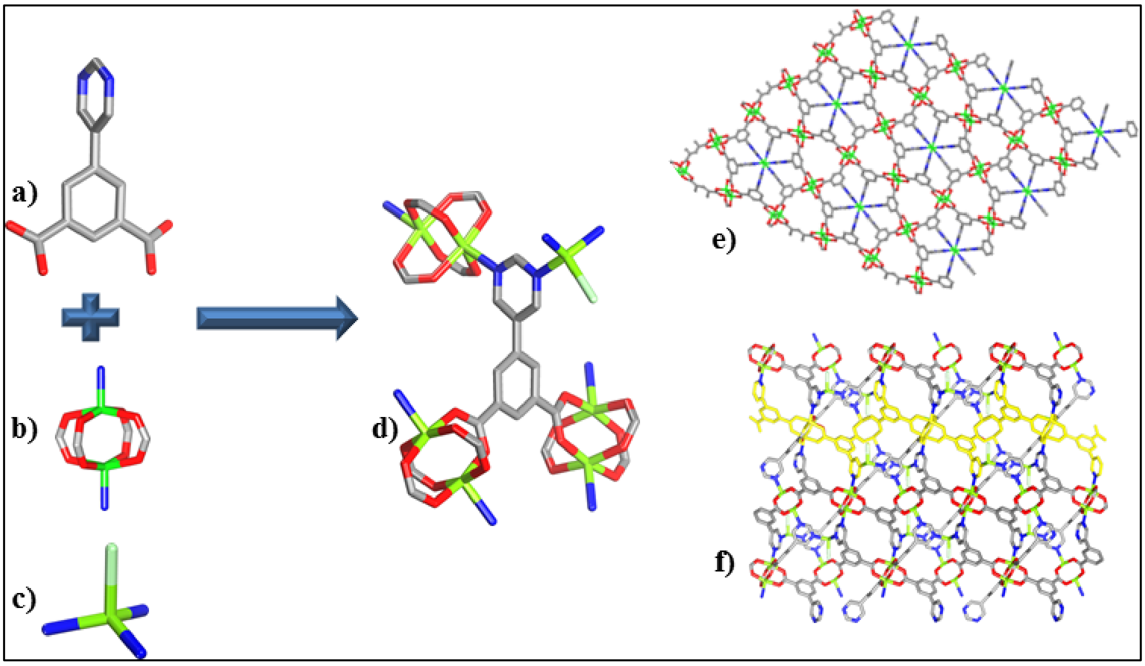

Figure 3.27 a) PMIP, (b) paddlewheel MBB, (c) tetrahedral MBB with attached halide ion, (d) the coordination mode of PMIP to the MBBs, (e) isolated **kgm** SBL and (f) the crystal structure of X-**eea**-MOF (b-axis) showing pillared **kgm** layers where one layer is highlighted in yellow. Cu = green, C = gray, O = red, N = blue and halide atoms (X = Cl, Br or I) = turquoise. Hydrogen atoms and solvent molecules are omitted for clarity.

Alternatively, the structures can be described by inspecting an individual ligand where each carboxylate group of the isophthalic acid moiety coordinates with two copper atoms (Cu1) involved in a paddlewheel MBB in a bis-monodentate fashion assisting the creation of 2-P **kgm** SBLs. One of the pyrimidine nitrogen atoms of the ligand coordinates to the Cu at the axial position of the paddlewheel in a neighboring layer leading to L-A pillaring of the layers. The other pyrimidine nitrogen coordinates to Cu2, which in turn coordinates to two other nitrogen atoms from neighboring ligands in addition to one halide atom depending on the isostructure type (Figure 3.27 d).

From the SC X-ray data, the Cu-Cl and Cu-Br bond distances in Cl-**eea**-MOF and Br-**eea**-MOF are 2.355 and 2.504 Å, respectively. This result is in line with other reported compounds where a tetrahedral Cu is coordinated to three nitrogen atoms and one halide atom (X). A search using the ConQuest CSD program version 1.17 (May 2015)[34] shows that the bond distance in Cu-X ranges from 2.125 to 2.71 Å, where X is Cl, Br or I (Figure 3.28). A more specific search shows that Cu-Cl is shorter than Cu-Br (Figure 3.29 and Figure 3.30).

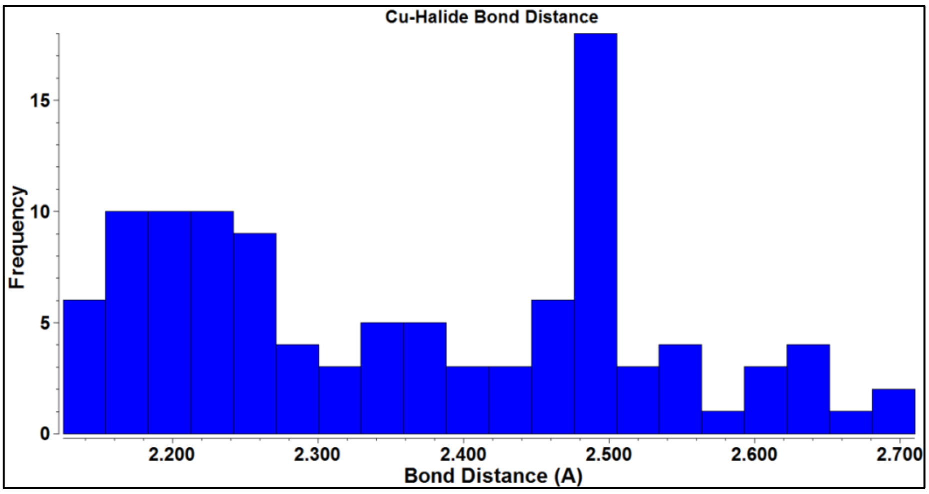

Figure 3.28 Cu-X bond distance histogram when Cu is in a tetrahedral coordination environment and is surrounded by three nitrogen atoms, X = Cl, Br or I. CSD version 1.17 (May 2015).

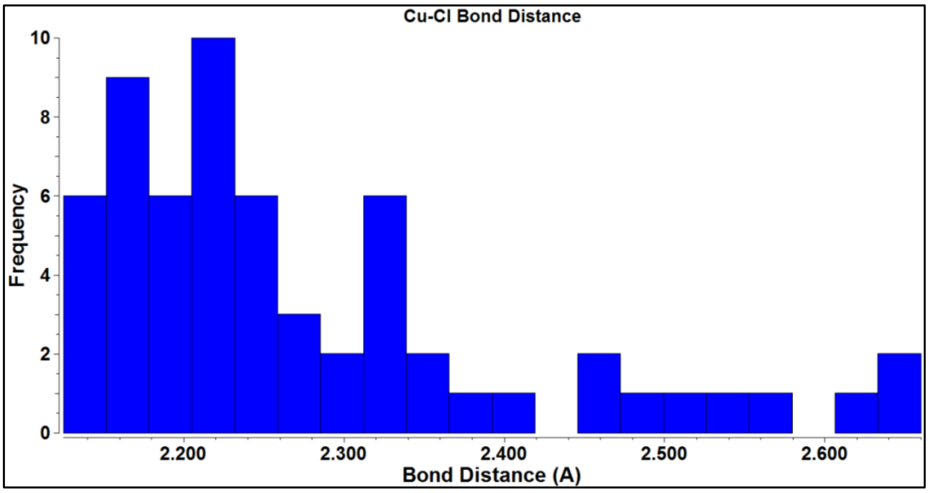

Figure 3.29 Cu-Cl bond distance histogram when Cu is in a tetrahedral coordination environment and is surrounded by three nitrogen atoms. CSD version 1.17 (May 2015).

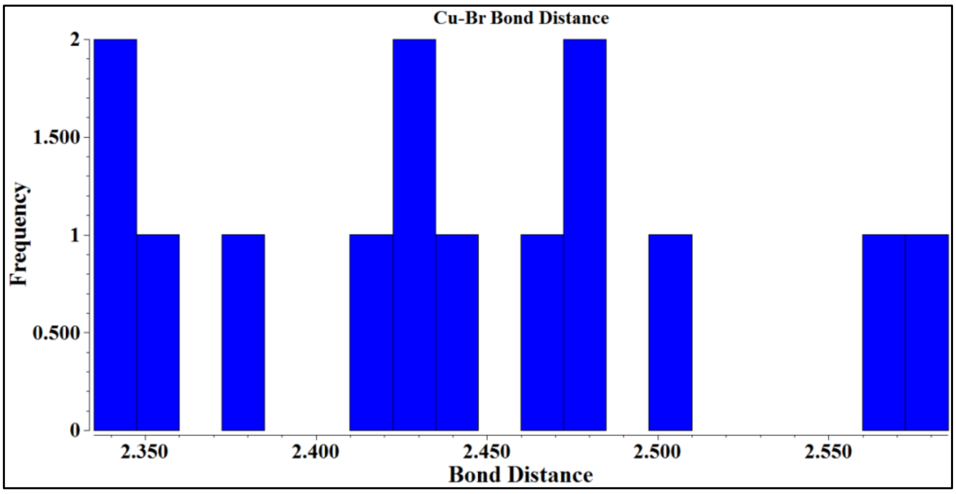

Figure 3.30 Cu-Br bond distance histogram when Cu is in a tetrahedral coordination environment and is surrounded by three nitrogen atoms. CSD version 1.17 (May 2015).

In these isostructures, there are three types of cages - A, B and C (Table 3-2). Cage A (Figure 3.31 a and b) is formed from six adjacent ligands that contribute to two 2-P **kgm** layers. These ligands are arranged in an ab fashion where each ligand forms two paddlewheel MBBs and its neighboring ligands coordinate to the axial position of these paddlewheels through one of their pyrimidine nitrogen atoms. This cage has eight windows that have aperture sizes of 4.5 x 5 and 3.6 x 1.8 Å and the diameter of the largest sphere that can fit into this cage is 6.94 Å.

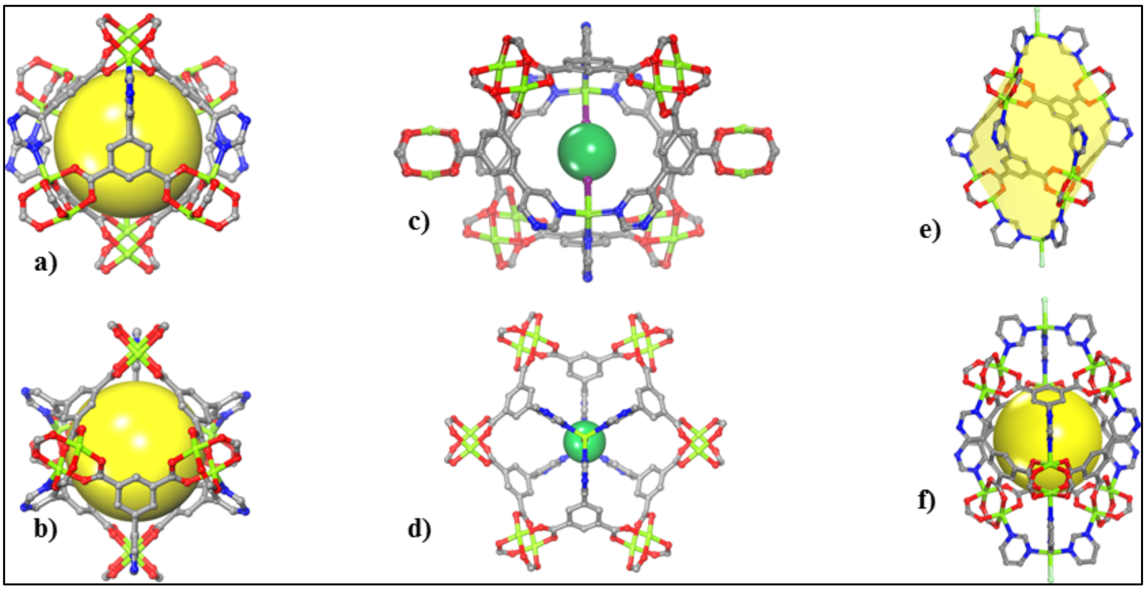

Figure 3.31 The three types of cages found in X-**eea**-MOF isostructures; type A cage (a) viewed along the a-axis and (b) c-axis; type B cage (c) viewed along the abc-plane and (d) c-axis; green sphere represents the void space between the halide atoms within the cage; and type C cage (e) viewed along the abc-plane and (f) a-axis. Yellow spheres represent the largest sphere that would fit in the cavities without touching the van der Waals atoms of the framework. Cu = green, C = gray, O = red and N = blue. Hydrogen atoms and solvent molecules omitted for clarity.

Cage B (Figure 3.31 c and d) is formed from six adjacent ligands that contribute to one 2-P **kgm** layer. These ligands are arranged in an ab fashion, and the pyrimidine nitrogen atoms of alternative ligands (3 are pointing up and 3 are pointing down) are connected to Cu2 and the halide atom at the two apexes of the cage. Therefore, two halide atoms that are opposite to each other are enclosed in each cage almost dividing its void, which is equal to 6.3 Å, into two. The distances between the two halide atoms (i.e., the narrowest point in the cage) are 0.58 and 0.38 Å in Cl and Br-**eea**-MOF, respectively. This cage has six equal triangular windows with apertures of 5.35 x 5.9 Å.

Cage C (Figure 3.31 e and f) is formed by trigonal windows of neighboring **kgm** sheets but Cu2, which is linked to a halide atom and three pyrimidine nitrogen atoms from adjacent ligands, forms the pyramid tip with the halide atom pointing outside the cage. The diameter of the largest shape that can fit in cage C is 7 x 17 Å and it has windows that are 2.6 x 4.2 and 1.8 x 6 in size.

Table 3-2 Properties of X-**eea**-MOFs cages.

	Internal diameter (Å)	**Aperture I (Å)**	**Aperture II (Å)**
Cage A	6.94	4.5 x 5	3.6 x 1.8
Cage B	6.3 (divided by halides)	5.35 x 5.9	--
Cage C	7 x 17	2.6 x 4.2	1.8 x 6

Topological analysis reveals that these isostructures fulfill the necessary criteria to form a 3,6-c net with **eea** topology. These criteria include a bi-functional trigonal ligand, which, when mixed with a suitable metal, forms the expected **kgm** 2-P layers. In addition, the ligand contains a pyrimidine N-donor group that coordinates to the accessible metal site at the axial position of the paddlewheel MBB and aids the formation of the octahedral (6-c) nodes. This in turn leads to the pillaring of the layers and the construction of (3, 6)-c 3-P MOFs with **eea** topology.

Experimental PXRD patterns were independently collected for the three compounds (Figure 3.32, Figure 3.33 and Figure 3.34). The agreement between the experimental PXRD and those calculated was validated based on the SC structure using Mercury CSD software and ultimately confirmed that the three compounds are isostructures (Figure 3.34). In addition, the PXRD patterns verified the bulk crystalline materials phase purity. These compounds are stable in air and a variety of organic solvents.

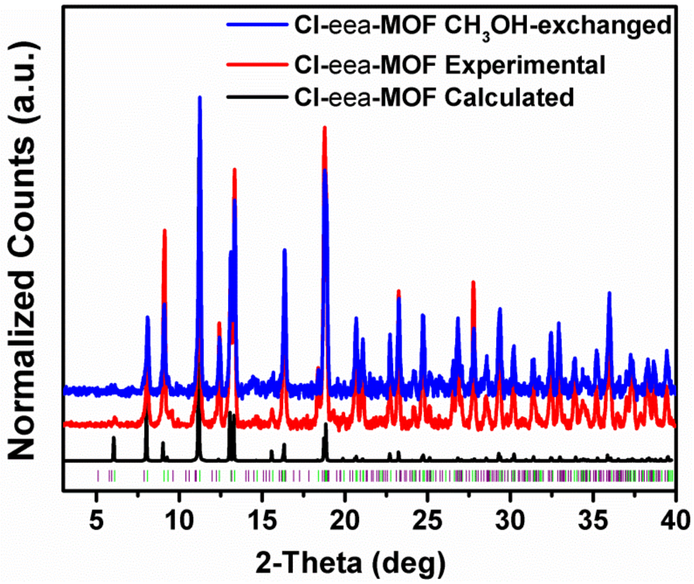

Figure 3.32 PXRD spectra of calculated (black), experimental (red) and CH_3OH-exchanged (blue) Cl-**eea**-MOF indicating its phase purity and stability in the exchange solvent.

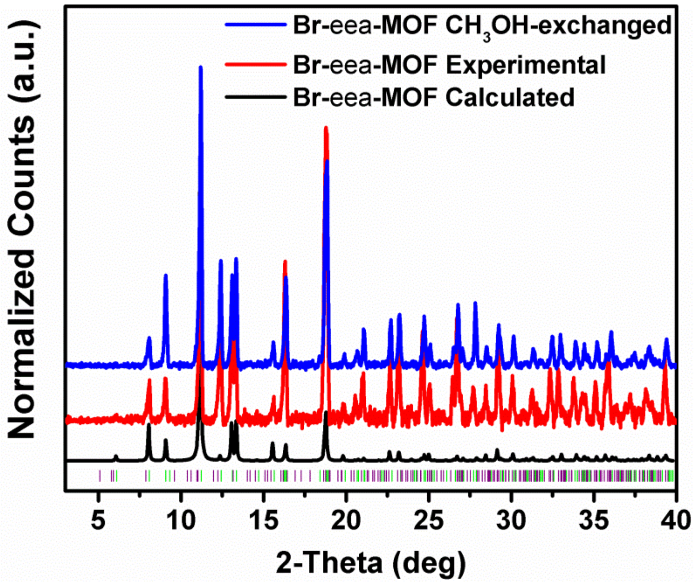

Figure 3.33 PXRD spectra of calculated (black), experimental (red) and CH_3OH-exchanged (blue) Br-**eea**-MOF indicating its phase purity and stability.

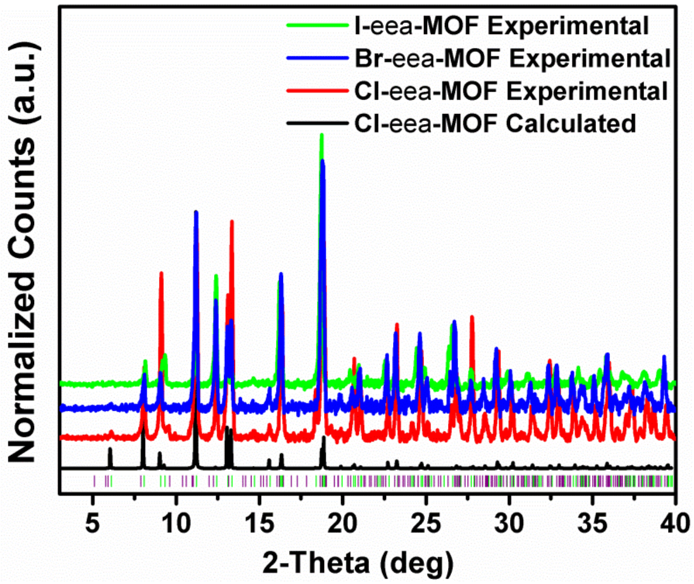

Figure 3.34 PXRD spectra of calculated (black) and experimental (red) Cl-**eea**-MOF compared to experimental Br-**eea**-MOF (blue) and that of I-**eea**-MOF (green), altogether indicating that the three frameworks are isostructural.

The thermal stability of the three isostructures was investigated by performing TGA experiments on DMF-washed and CH_3OH-exchanged samples under a N_2 atmosphere. The tests were carried out between RT and 700 °C at an increasing heating rate of 5 °C/min in high resolution dynamic mode. The TGA plots of these compounds (Figure 3.35, Figure 3.36 and Figure 3.37) suggest their thermal stability up to 255, 270 and 295 °C for the Cl-, Br- and I-isostructures, respectively.

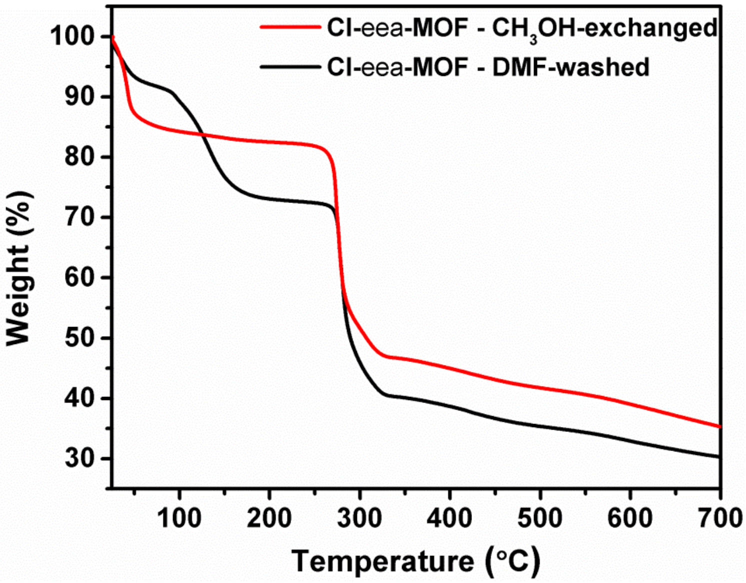

Figure 3.35 TGA plots of DMF-washed and CH_3OH-exchanged Cl-**eea**-MOF samples exhibiting framework decomposition at 255 °C.

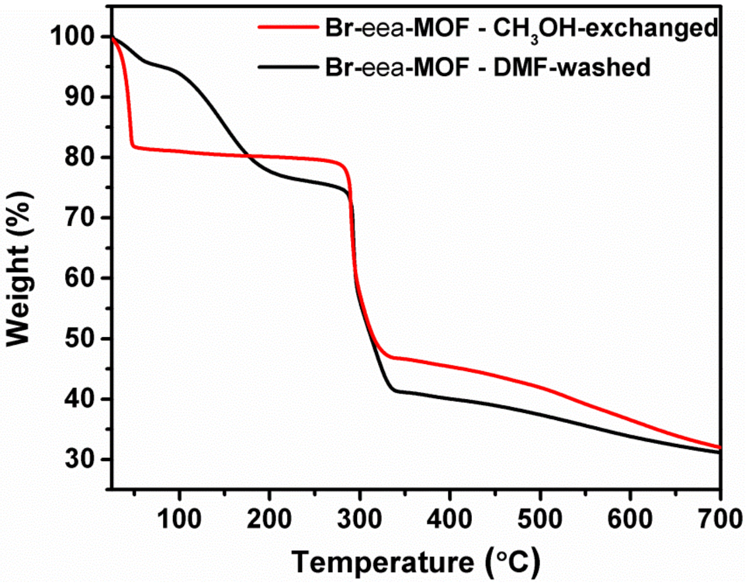

Figure 3.36 TGA plots of DMF-washed and CH_3OH-exchanged Br-**eea**-MOF samples exhibiting framework decomposition at 270 °C.

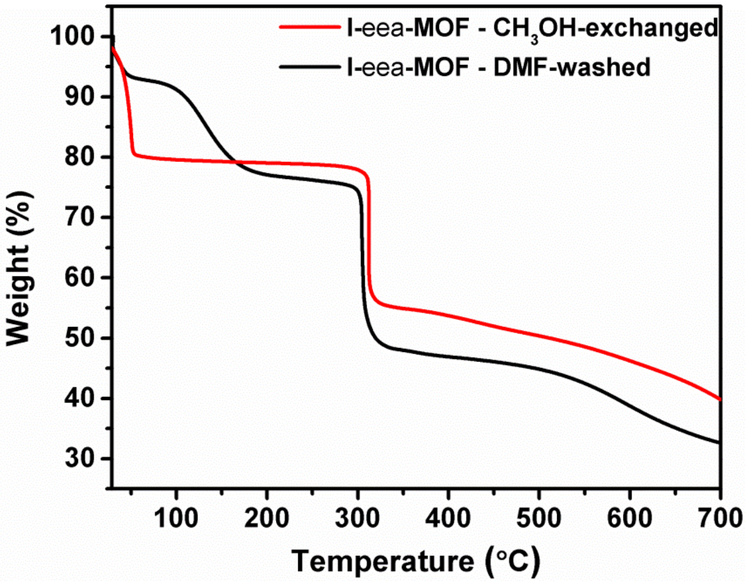

Figure 3.37 TGA plots of DMF-washed and CH_3OH-exchanged I-**eea**-MOF samples exhibiting framework decomposition at 295 °C.

The calculated total potential solvent accessible volume of the as-synthesized Cl- and Br-isostructures after removing the guest solvent molecules was estimated to be~54%

v/v with MS software. In addition, their theoretical PV based on the crystal structure was estimated to be 0.46 and 0.455 cm^3/g for the Cl- and Br-isostructures, respectively.

Permanent porosity and the available free volume of the prepared isostructures was confirmed and determined from N_2 gas adsorption studies at 77 K and based on uptake at 1 P/P_0. These studies were performed on CH_3OH-exchanged samples and demonstrated fully reversible Type I isotherms, representative of microporous materials (Figure 3.38). Here, the apparent SA_{BET} values were estimated to be 1215, 1174 and 1074 m^2/g, and the total experimental PV was estimated to be 0.48, 0.45 and 0.42 cm^3/g for the Cl-, Br- and I-isostructures, respectively. These results are consistent with the theoretical values (Table 3.3).

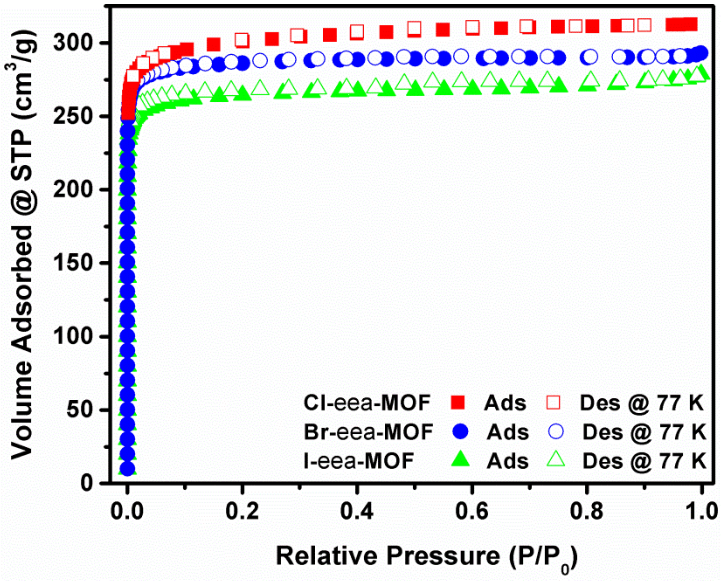

Figure 3.38 Fully-reversible LP N_2 sorption isotherms at 77 K of CH_3OH-exchanged Cl-, Br and I-isostructures.

Table 3-3 Experimental results of porosity study of the three isostructures compared to the theoretical values obtained from the corresponding SC structures.

	PV_{Theo} (cm^3/g)	**PV_{Exp} (cm^3/g)**	**SA_{BET} (m^2/g)**
Cl-**eea**-MOF	0.460	0.48	1215
Br-**eea**-MOF	0.455	0.45	1174
I-**eea**-MOF	--	0.42	1074

As the Cl- and Br-isostructures showed similar sorption results and because preparing the Cl-isostructure did not always yield pure samples in reasonable quantities, full gas sorption experiments were performed on the Br- and I-isostructures exclusively.

Therefore, initial H_2 sorption studies were performed at LP to evaluate the performance of these two isostructural compounds toward H_2. Interestingly, at 77 K and 760 Torr, Br-**eea**-MOF demonstrated higher gravimetric uptake of 1.83 wt% (Figure 3.39), Q_{st} of 6.5 kJ/mol at lower loading, and 6.2 kJ/mol at higher loading (Figure 3.40). These values are comparable to those of I-**eea**-MOF that showed H_2 uptake of 1.61 wt% at 77 K and 760 Torr (Figure 3.39) and Q_{st} of 6.73 kJ/mol at lower loading (Figure 3.40). These Q_{st} values were nearly constant as H_2 loading increased, indicative of homogenous binding sites over the full range of gas loading.

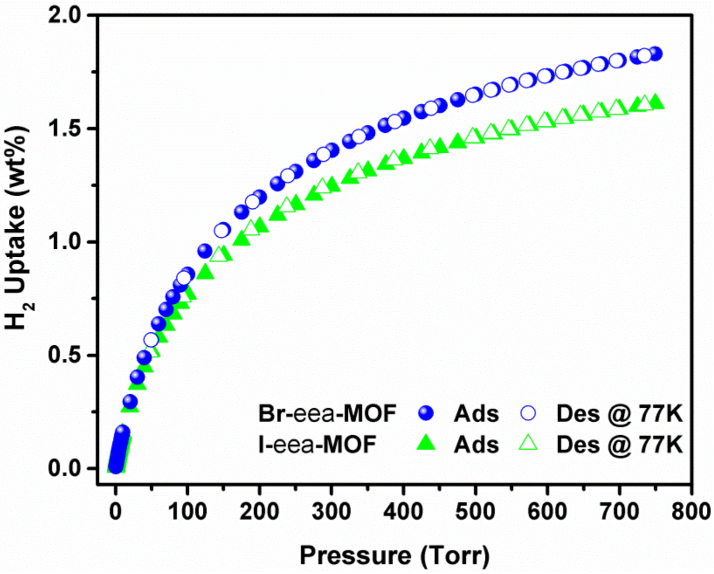

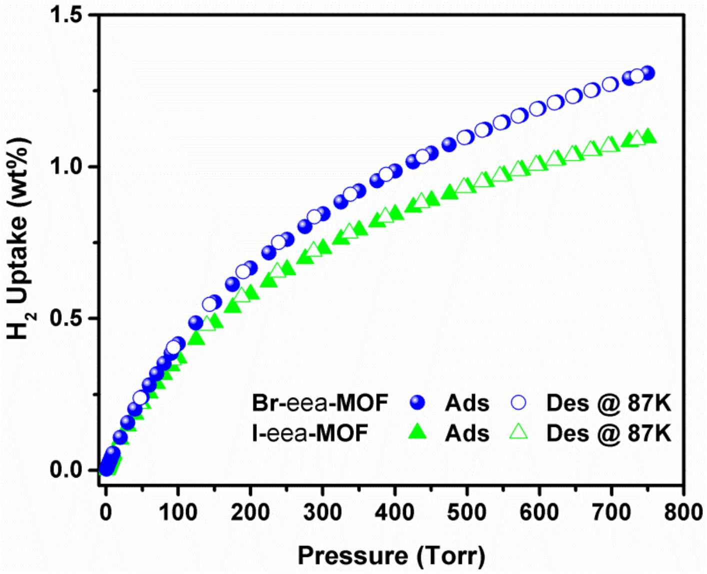

Figure 3.39 Comparing LP H_2 sorption isotherms at 77 K (up) and 87 K (down) of Br- and I-**eea**-MOF isostructures.

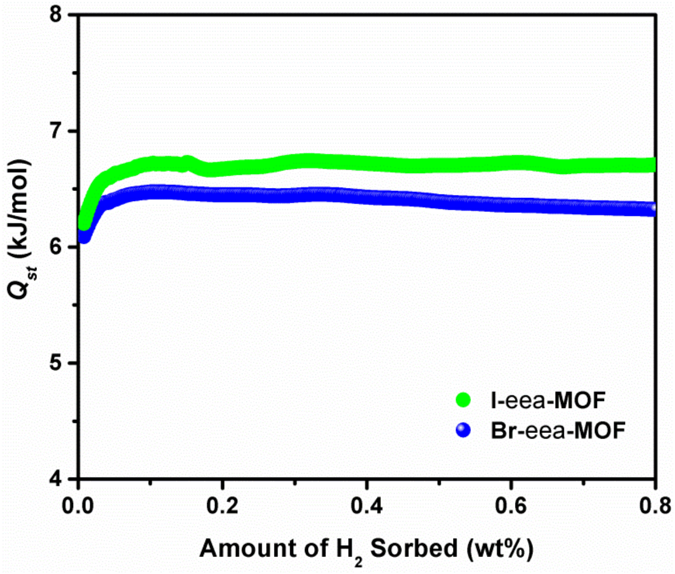

Figure 3.40 The isosteric heat of H_2 adsorption (Q_{st}) by Br- (blue) and I-**eea**-MOF (green) based on H_2 isotherms at 77 and 87 K.

To further evaluate the two isostructures as adsorbent materials, CO_2 sorption was investigated at 258, 273, 283, 288 and 298 K. It was seen that the two compounds reversibly adsorbed significant amounts of CO_2 under ambient conditions at 298 K and 760 Torr where Br-**eea**-MOF adsorbed 3.06 mmol/g and I-**eea**-MOF adsorbed 2.67 mmol/g (Figure 3.41). The Q_{st} for CO_2 calculated from the corresponding variable temperature adsorption isotherms was observed to be around 24.5 at LP for both Br- and I-isostructures, suggesting their similar affinity toward CO_2 (Figure 3.41).

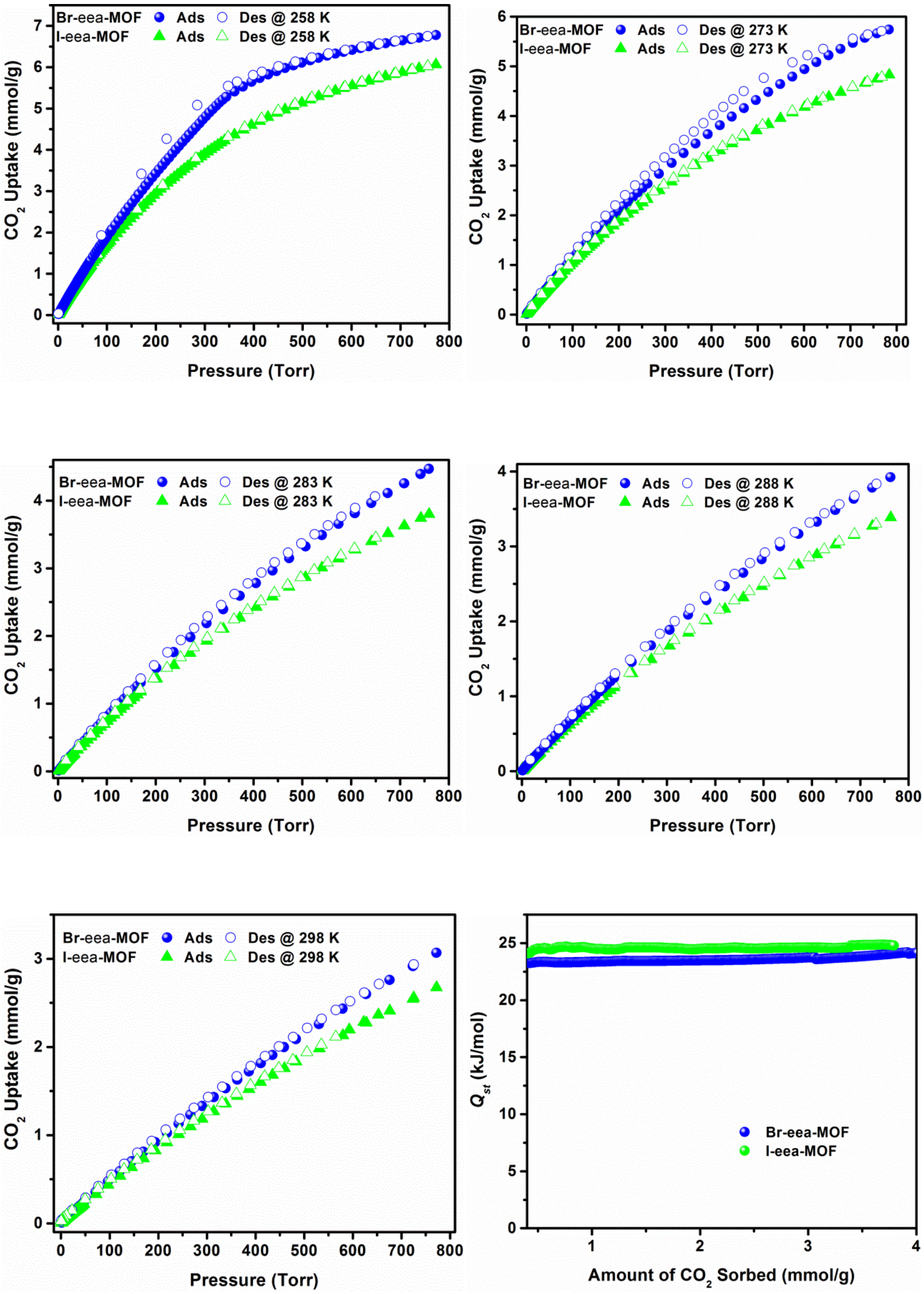

Figure 3.41 Comparing CO_2 sorption isotherms at different temperatures of Br- and I-**eea**-MOF isostructures and their corresponding Q_{st}.

3.4.5. Summary and conclusions

In this part of the work, we have successfully designed and constructed new MOFs utilizing the L-A pillaring strategy, where a ligand with an additional functionalization site (PMIP) was employed to assess the ability of constructing MOFs with tunable properties.

One intriguing finding was that by mixing PMIP with $Cu(NO_3)_2$ and Cu(X), where X is Cl, Br or I, we were able to construct three isostructural MOFs, being Cl-, Br- and I-**eea**-MOF, respectively. The only difference among these isostructures lied in the type of halide ion coordinated to the tetrahedral Cu MBB formed at the additional functionalization site of the ligand.

In this specific case, various gas sorption studies showed no obvious difference in gas uptake because of the presence of different halide ions in the various isostructures.

3.5. Experimental section part III: The construction of 3-P MOFs from SBLs utilizing the six-connected axial-to-axial pillaring technique

3.5.1. Introduction

The gas separation process plays a significant role in industry as well as daily life by providing cleaner energy and contributing to the increase in industrial procedural efficiency.[35] However, these processes are fraught with great challenges based on their high energy costs in addition to the similarities in the different gas/vapor hydrocarbon molecules structures, properties and reactivity.[35b] Therefore, the deployment of new separation agents is a still-continuing effort to overcome these issues, improve outcomes, increase selectivity and minimize costs.

MOFs are considered excellent candidates for such applications because of their unique properties, such as their chemical versatility where both inorganic and organic portions can be designed/modified either pre- or post-synthetically with a number of synthesis approaches.[36] [35b, 37] From the numerous MOFs synthesis strategies, a new approach has been recently developed in which the ligands required to prepare a targeted MOF are synthesized or modified *in situ* under specific reaction conditions.[38]

In this regard, 1H-tetrazole-5-carboxylic acid ethyl ester sodium salt (TCEE) is particular appealing candidate to explore. Depending on the reaction conditions, this ligand can itself act as a polydentate N-donor without requiring any chemical modifications (Figure 3.42 a).[38d] Furthermore, the ligand may undergo *in situ* hydrolysis to form tetrazole carboxylic acid (TCA) where the resulting $–COO^-$ group is available for chelation along with its tetrazole moiety (Figure 3.42 b).[38c] In addition, the ligand can potentially undergo decarboxylation where only the tetrazolate moiety (TZ) is left (Figure 3.42 c).[39]

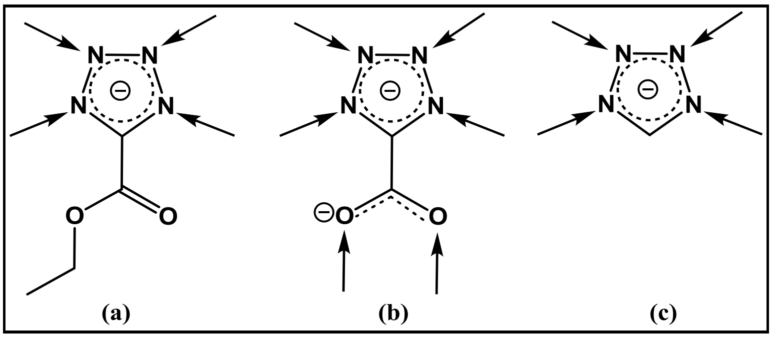

Figure 3.42 A number of the potential coordination modes of (a) TCEE and its different *in situ* hydrolysis products, (b) TCA and (c) TZ.

Consequently, in this work, this robust and versatile linker was used along with $Cu(NO_3)_2$ to construct a 3-P framework (Cu-**lon**-MOF) utilizing the 6-c A-A pillaring strategy of the *in situ*-formed 2-P **kgm** SBLs as discussed in Chapter 1. This supramolecular entity, based on TCEE and its *in situ* hydrolysis product, TZ, possess many attractive intrinsic properties.

In addition, it was of great interest to find ways to increase the space within the channels without changing the underlying topology of the framework. One feasible way to achieve this goal is to hydrolyze or to decarboxylate the ligand in the structure to TCA or TZ, respectively, in one of two ways: (I) post-synthetic modifications of the resulting framework[6] by, e.g., subjecting the framework to either acids or bases or (II) to start with a pre-hydrolyzed ligand (TCA) to target the isoreticular framework. However method (I) does not guarantee the complete hydrolysis of all ester groups. In addition, adding acid or base may affect the integrity of the framework and bring about its collapse. Thus, method (II) is relevant to us as it ensured the hydrolysis of all ester groups present in the framework, leading to the formation of larger channels.

Although the isoreticular framework containing TCA and TZ was expected to form by utilizing the hydrolyzed ligand TCA, the resulting isoreticular framework (H-Cu-**lon**-MOF) contained ligands that are totally decarboxylated, i.e., contains TZ only.

Please note that H-Cu-**lon**-MOF was synthesized using TCA and mainly characterized by Dr. Infas H. Mohideen when he was a post-doctoral fellow in Prof. Eddaoudi’s research group at KAUST.

3.5.2. Materials and methods

All chemicals, including the ligand (TCEE), were used as received from Alfa Aesar, Sigma-Aldrich or Acros without any purification or modification. TCA was prepared by the hydrolysis of TCEE, and the purity of both compounds was verified by acquiring their ^{1}H NMR spectra. For details on ligand hydrolysis or the devices and software used, please refer to Chapter 2.

3.5.3. Synthesis and characterization

3.5.3.1. Synthesis of Cu-lon-MOF

A solution of $Cu(NO_3)_2.3H_2O$ (3.624 mg, 0.015 mmol), TCEE (5 mg, 0.03 mmol), 1.5 mL DMF and 0.20 mL 3.5 M HNO_3/DMF was prepared in a 20-mL scintillation vial, sealed and placed in a preheated oven at 85 °C for 25 h to yield black hexagonal polyhedral crystals of Cu-**lon**-MOF. The as-synthesized crystals were purified by repeated washing with DMF and air-dried.

3.5.3.2. Activation of Cu-lon-MOF

A sample of approximately 100 mg of the as-synthesized Cu-**lon**-MOF was washed with aliquots of 15 mL DMF over the course of 24 h while refreshing the solution 5 times. The sample was then exchanged with C_3H_6O over a period of 7 days where approximately 15 mL of C_3H_6O was added to the sample and refreshed 3 times per day. Prior to gas sorption experiments, the sample was placed into a 6 mm large bulb glass sorption cell and dried carefully with flowing N_2 after removing the excess surface solvent with a syringe. The sample was then placed under dynamic vacuum at RT for 120 h and then backfilled with N_2 prior to sorption experiments. It is worth mentioning that no heat was applied during sample activation in order to prevent any post-synthetic hydrolysis of the ester groups.

3.5.3.3. Synthesis of H-Cu-lon-MOF

H-Cu-**lon**-MOF was prepared following the same procedure as Cu-**lon**-MOF but using TCA (3.4218 mg, 0.03 mmol) as the ligand.

3.5.3.4. Activation of H-Cu-lon-MOF

A sample of roughly 50 mg of the as-synthesized H-Cu-**lon**-MOF was washed with 15 mL DMF several times. The sample was then exchanged with CH_3CN over a period of 7 days where 15 mL of CH_3CN was added to the sample and refreshed 3 times per day. Prior to gas sorption experiments, the sample was placed into a 6 mm large bulb sorption cell; the excess surface solvent was removed with a syringe and the sample was subjected to dynamic vacuum at RT for 42 h.

3.5.4. Results and discussion

In this work presented as part of this dissertation, attention was directed toward using the SBLs approach to develop MOF materials targeted for gas separation applications. A specific focus was to study the effect of modifying the functionality of the organic building block (ligand) on the structure-function relationship in the prepared MOFs without changing the underlying network topology.

Towards this end, TCEE and its hydrolyzed version, TCA, were used to prepare Cu-**lon**-MOF and its isoreticular structure, H-Cu-**lon**-MOF, respectively, to assess the influence of the presence of ester groups on single and mixed-gas adsorption behavior of the prepared MOFs. Ester group elimination was expected to affect the characteristics of and increase the space in the cavities and ultimately change the intrinsic properties of the compound and its behavior toward different gases.

Under the reaction conditions used to prepare Cu-**lon**-MOF, a certain ratio of TCEE underwent *in situ* decarboxylation to form TZ. Similarly, when preparing H-Cu-**lon**-MOF using the same reaction conditions but replacing TCEE with its hydrolyzed version, TCA experienced complete *in situ* decarboxylation forming TZ.[38c] Both isoreticular structures were synthesized and characterized by X-ray crystallography and gas sorption experiments.

3.5.4.1. **Cu-**lon**-MOF**

A solvothermal reaction between $Cu(NO_3)_2$ and TCEE (Figure 3.43 a) in DMF in the presence of 3.5 M HNO_3/DMF was placed at 85 °C to yield black polyhedral crystals of Cu-**lon**-MOF. Using a synchrotron, Cu-**lon**-MOF was observed to crystallize in the hexagonal space group P6(3)/m with cell parameters of a = b = 13.99 Å, c = 16.24 Å and $\alpha = \beta = 90^o$, $\gamma = 120^o$ and V = 2753.69 Å^3 forming a 3-P MOF with intersecting 3-D channels.

In Cu-**lon**-MOF, each asymmetric unit contains two mixed-valence crystallographically independent Cu ions, being Cu1 and Cu2. Cu1 exhibits a 6-c octahedral coordination environment containing six nitrogen atoms from six different ligands (Figure 3.43 b). Conversely, Cu2 is surrounded by four nitrogen atoms from four different ligands to produce a 4-c node with tetrahedral geometry (Figure 3.43 c). Every two octahedral Cu1 nodes in Cu-**lon**-MOF form a trigonal prism SBU through connection to three ligands (Figure 3.43 e). Each SBU is linked, through six tetrahedral Cu2 nodes and twelve ligands, to six adjacent clusters (three above and three below) in a staggered fashion forming pillared **kgm** layers (Figure 3.43 d, f and Figure 3.44) and entrapping 3-D channels (Figure 3.43 f and g).

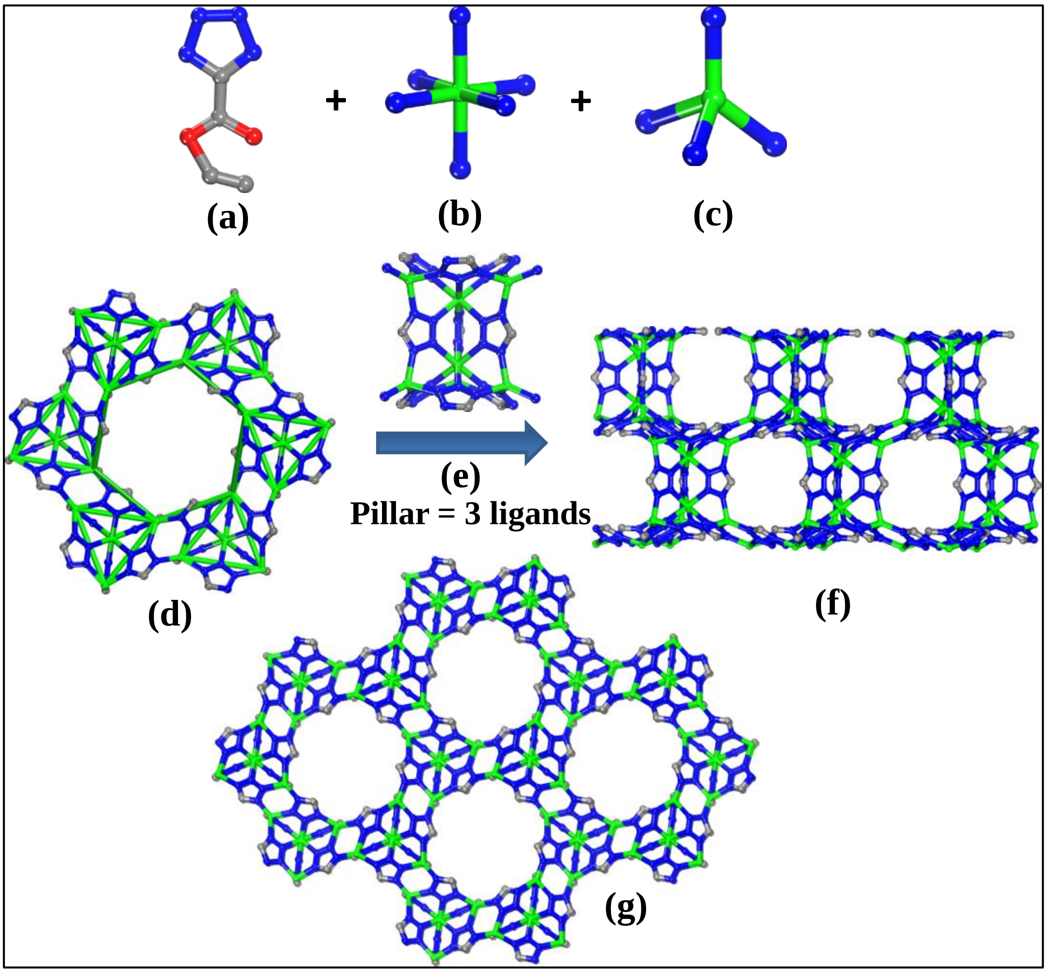

Figure 3.43 (a) TCEE, (b) the Cu1 octahedral environment, (c) the Cu2 tetrahedral environment, (d) one **kgm** layer, (e) a pillaring cluster, (f) Cu-**lon**-MOF viewed along the b-axis and (g) along the c-axis. Ester groups, solvent molecules and hydrogen atoms are omitted for clarity. Cu = green, C = gray, N = blue and O = red.

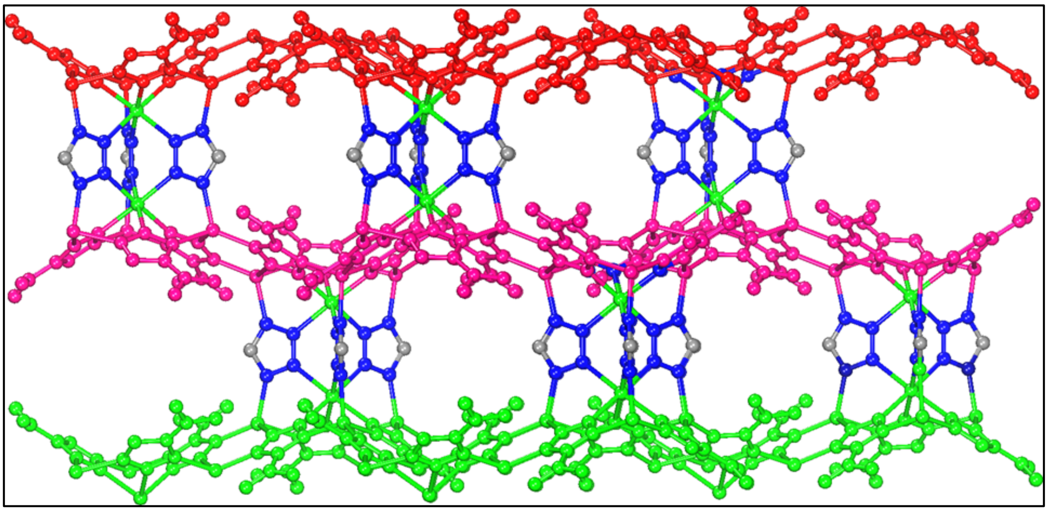

Figure 3.44 Crystal structure of Cu-**lon**-MOF reveals pillared layers with pillaring clusters stacked in a staggered fashion. Each layer is shown in a different color for clarity.

In other words, the structure can be viewed as pillared 3-P MOF where the trigonal prism SBUs (Figure 3.45 a) pillar the 2-P **kgm** layers (Figure 3.45 b) via 6-c A-A pillaring technique (Figure 3.45 c).[1] To the best of our knowledge, to date, there is only one example of this kind of pillaring. In 2013, Zawarotko et al. developed trinuclear trigonal prism discrete clusters made from Cr salts and decorated them with six pyridyl moieties for use as 6-c A-A pillars for the *in situ*-formed **kgm** SBLs to construct a series of functional pillared 3-P MOFs with **lon**-e topology.[4]

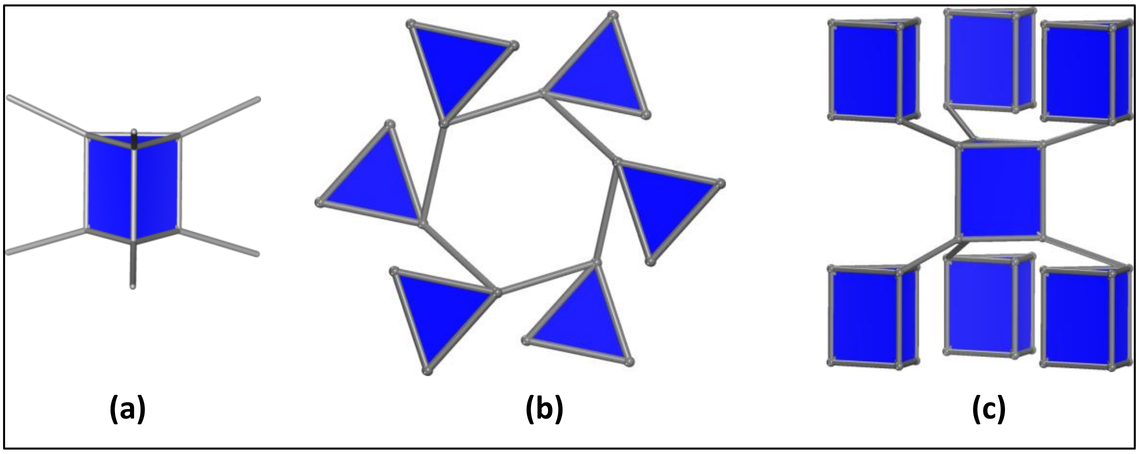

Figure 3.45 Illustration of (a) trigonal prism pillaring SBU, (b) one kagome-like arrangement in the structure and (c) six-connected axial-to-axial pillaring.

As mentioned earlier, the pillaring of **kgm** layers in Cu-**lon**-MOF entraps 3-D channels, two of which are similar and pass through the a- and b-axis (Figure 3.43 f), whereas the third channel passes through the c-axis (Figure 3.43 g) and intersects with the other two. The functional groups at the 5-position of the ligand, its hydrolysis and/or decarboxylation products (TCEE, TCA and/or TZ), when present (see Section 3.5.1), point towards the center of the channels. These functional groups, in addition to solvent molecules, are heavily disordered, making it difficult to specify the presence and the ratio of each ligand in the structure from SC data, and additional experiments were necessary to deduce their presence. Hence, IR (Figure 3.46), liquid ^{1}H NMR (Figure 3.47) and TGA (Figure 3.51) were performed to demonstrate the presence primarily of TZ and TCEE in an estimated ratio of 1:0.89. These studies also showed that the presence of TCA may be negligible.

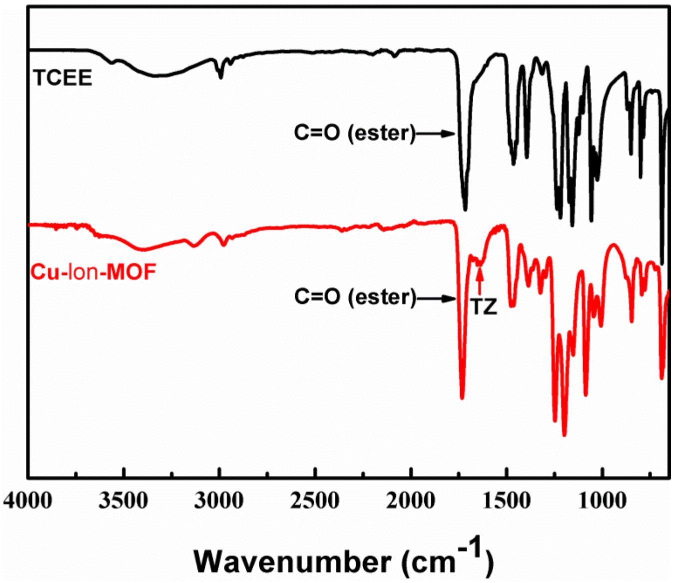

Figure 3.46 FT-IR spectrum of TCEE and C_2H_5OH-exchanged Cu-**lon**-MOF indicating the presence of TCEE and TZ.

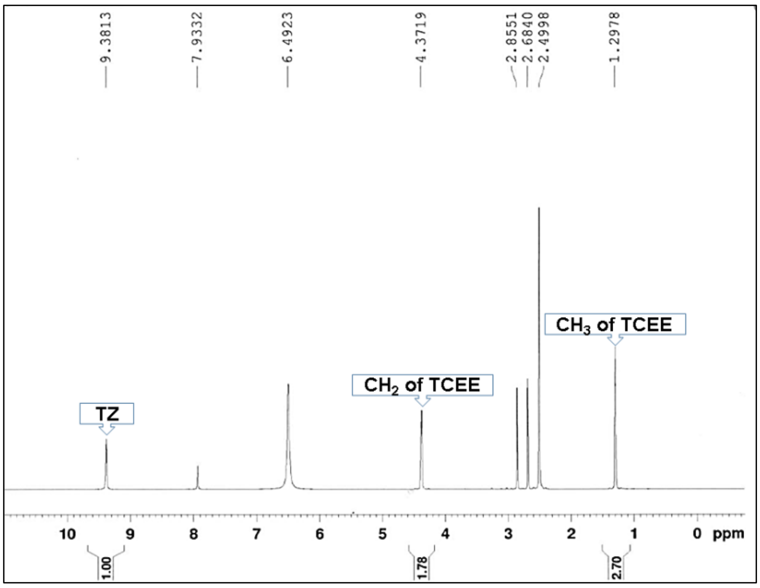

Figure 3.47 ^{1}H NMR spectra of Cu-**lon**-MOF in DMF showing the presence of TZ and TCEE in a ratio of 1:0.89.

The structural/topological analysis of the resulting crystal structure was performed using TOPOS software and revealed that Cu-**lon**-MOF is a MOF with the very uncommon **lon** topology. In this case, the two octahedral copper atoms in each pillaring cluster are replaced by two single points connecting the three pillaring ligands from top and bottom. These two points are connected and lead to the creation of a tetrahedral node at each one and, therefore, the formation of the **lon** structure (Figure 3.48 a). **lon** topology is related to diamond (**dia**) in that it is constructed from tetrahedral nodes and composed of fused 6-membered rings. These rings are in the chair conformation in **dia** but adopt both the chair and boat conformation in **lon** (Figure 3.48 b). To date, the **lon** network is very rare with only a few MOF examples in the literature.[4, 40]

Equally, Cu-**lon**-MOF can be viewed as a MOF with **kag** topology where 2-P **kgm** layers are pillared to form the 3-P structure (Figure 3.48 c). This can be achieved by reducing every two metal ions, which connect two adjacent **kgm** triangles of the pillaring clusters, to one point. Then, these reduced points are linked to adjacent ones and those above and below, leading to the formation of a structure with **kag** topology.[40]

Topologically, these two means are acceptable and are simply considered different ways to view the structure.

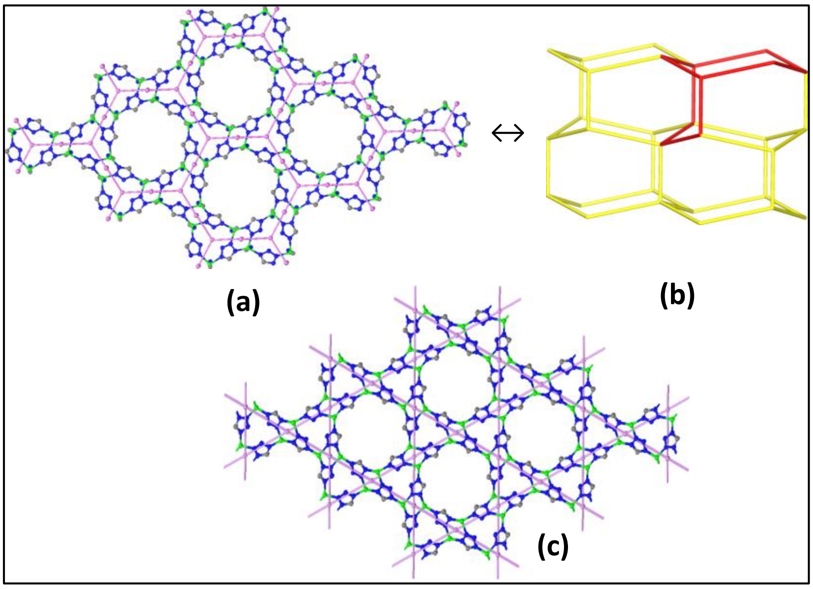

Figure 3.48 (a) Simplification of Cu-**lon**-MOF structure into its basic nodes leading to **lon** topology, (b) chair and boat conformation of **lon** topology and (c) simplification of Cu-**lon**-MOF into its basic nodes bringing about **kag** topology.

The phase purity of the bulk crystalline materials for Cu-**lon**-MOF was confirmed by similarities between simulated and experimental PXRD patterns (Figure 3.49). Further, VT-PXRD experiments were performed on C_3H_6O-exchanged samples of this compound to investigate the material stability under vacuum and heat. These experiments revealed a high degree of thermal stability of Cu-**lon**-MOF under vacuum in excess of 350 °C (Figure 3.50). Moreover, crystals of Cu-**lon**-MOF exhibited favorable stability in air and common organic solvents.

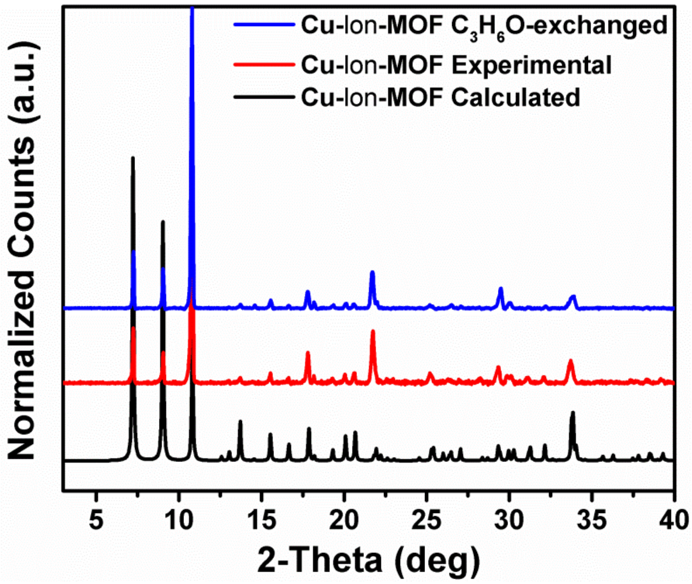

Figure 3.49 PXRD patterns of the calculated (black), experimental (red) and C_3H_6O-exchanged (blue) Cu-**lon**-MOF.

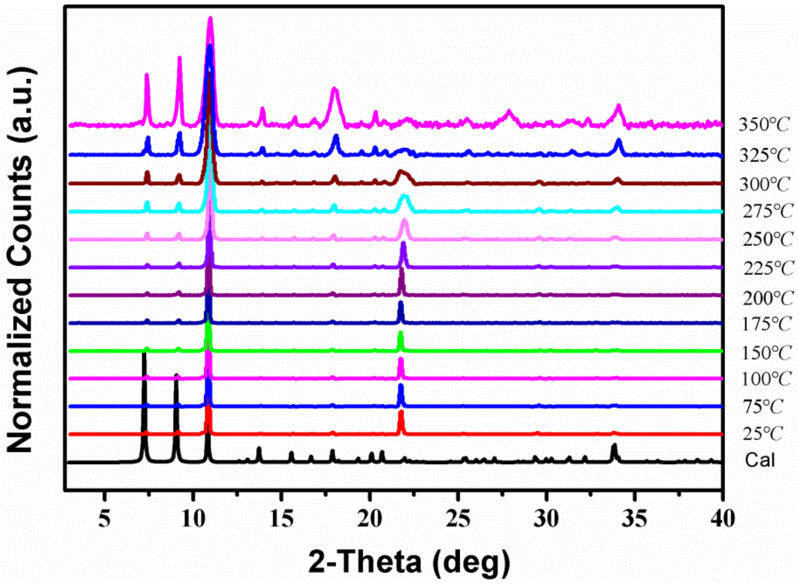

Figure 3.50 VT-PXRD of C_3H_6O-exchanged Cu-**lon**-MOF and comparison to the PXRD calculated from the SC structure (black) showing framework integrity under vacuum up to 350 °C.

To further investigate the thermal stability of Cu-**lon**-MOF, TGA was performed on both DMF-washed and C_3H_6O-exchanged samples under a N_2 atmosphere. The tests were carried out between RT and 700 °C at an increasing heating rate of 20 °C/min in high resolution dynamic mode. The TGA plots of Cu-**lon**-MOF indicate its thermal stability and show two distinct decomposition temperatures between ~180 and ~300 °C (Figure 3.51). The decomposition at the lower temperature is most likely a consequence of the scission of the ester linkage in the framework,[41] while the decomposition at roughly 300 °C and above could be attributed to the beginning of degradation followed by a total collapse of the framework at a higher temperature.

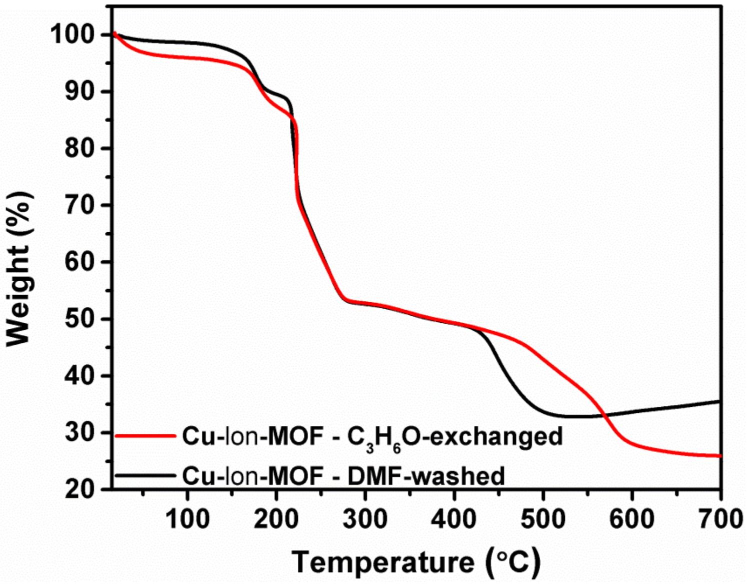

Figure 3.51 TGA plots of DMF-washed and C_3H_6O-exchanged Cu-**lon**-MOF under a N_2 atmosphere.

Furthermore, chemical stability of the material in aqueous media was examined by soaking the as-synthesized samples in water for one month while refreshing the solution regularly. The similarities between simulated and experimental PXRD patterns confirmed material stability in water (Figure 3.52). This can be ascribed to the presence of the relatively large ester groups in the small channels, rendering the framework hydrophobic and increasing its water stability. These groups protect the metal connectors within the framework, usually attacked by water and causing decomposition of the framework.[42]

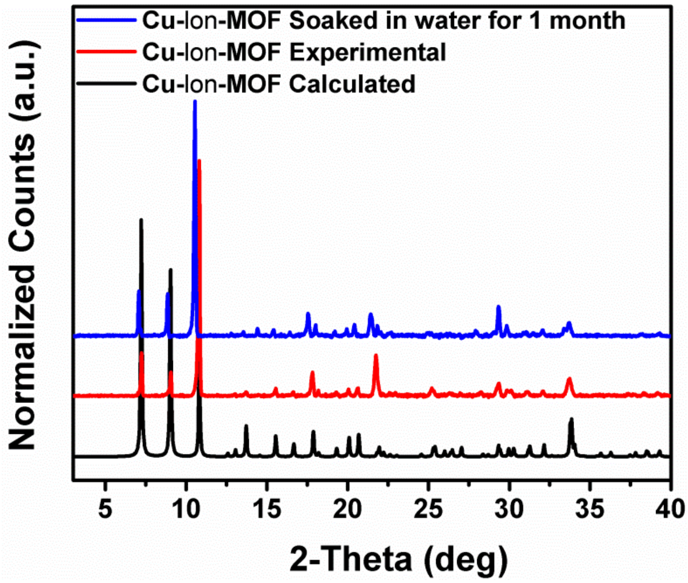

Figure 3.52 PXRD patterns of Cu-**lon**-MOF after one month of soaking in water, indicating chemical stability in aqueous media.

Looking back at the structure, one can see 3-D channels that are of great interest based on the presence of the flexible ester arms and the expected size of the channels that make the framework perfect for increasing the driving forces of passing gas/vapor molecules with different size/shapes. This was actually confirmed by performing an Ar adsorption study at 87 K (Figure 3.53). In fact, Ar gas probes the surface of Cu-**lon**-MOF as non-porous; however, LP CO_2 adsorption studies were performed and showed slight gas uptake. Sorption isotherms of CO_2 measured at 258, 273, 288 and 298 K were used to determine the Q_{st} of CO_2 gas with the Clausius-Clapeyron expression (Figure 3.54). Based on these isotherms, the Q_{st} of CO_2 was established to have moderate values of 33.6 and 29.8 kJ/mol at low and high loading, respectively.[26]

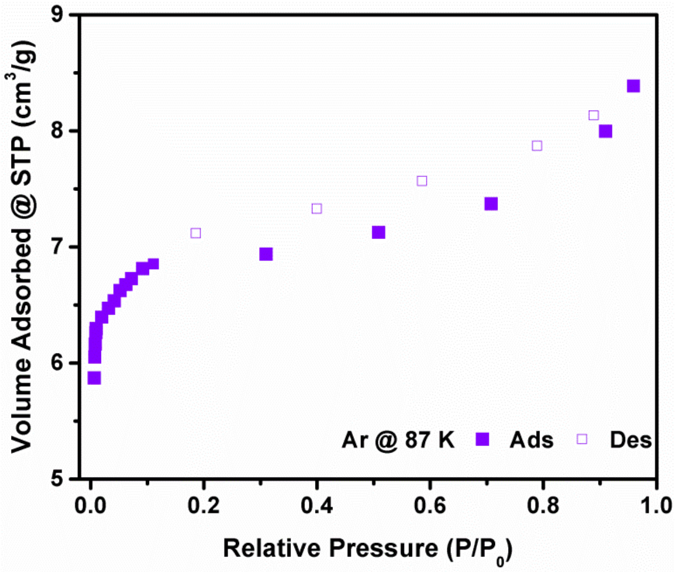

Figure 3.53 LP Ar adsorption and desorption isotherms at 87 K for C_3H_6O-exchanged Cu-**lon**-MOF probing it as non-porous.

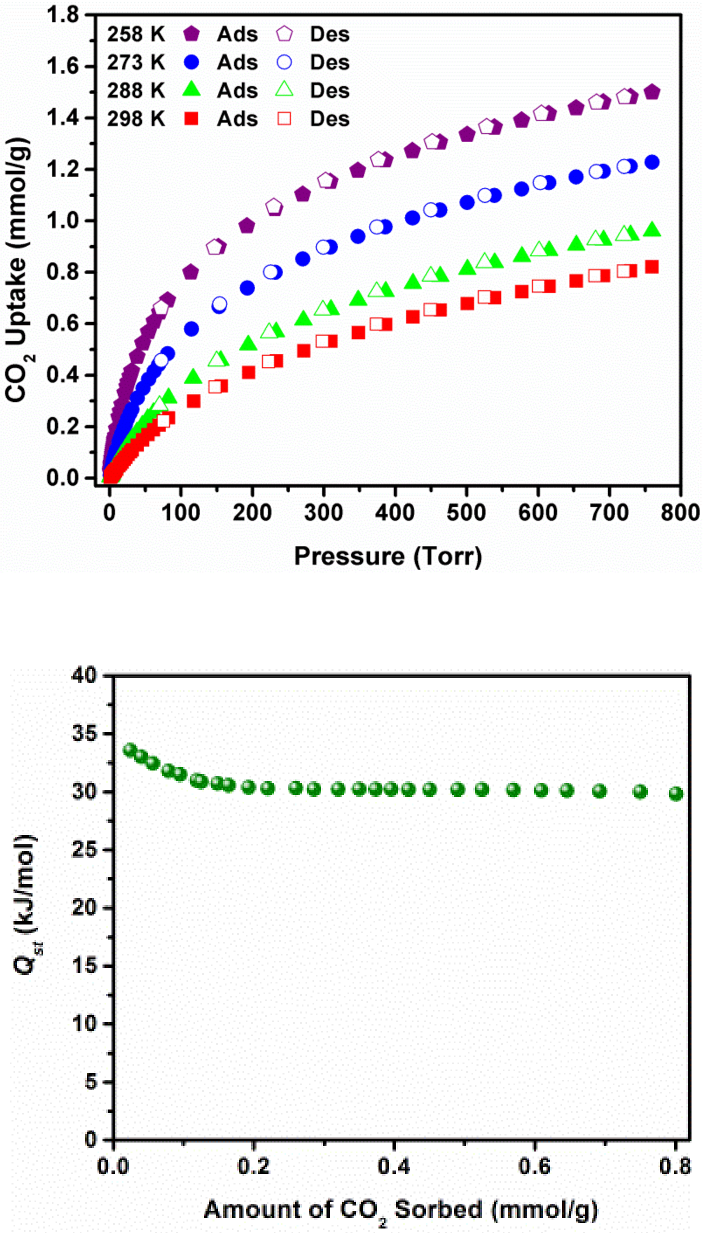

Figure 3.54 LP CO_2 variable temperature sorption isotherms at 258, 273, 288 and 298 K of Cu-**lon**-MOF and their corresponding Q_{st}.

Accordingly, it was of our interest to increase the space within the channels without altering the underlying framework topology. Therefore, the pre-hydrolyzed ligand (TCA) was used to target the isoreticular framework with more open channels, which led to the preparation of H-Cu-**lon**-MOF. Additionally, further sorption experiments were performed that compared the two isoreticular structures - all results are explained in the next section.

3.5.4.2. H-Cu-lon-MOF

The preliminary trials to prepare H-Cu-**lon**-MOF, an isoreticular structure of Cu-**lon**-MOF characterized by having larger channels, were conducted by applying the same synthesis conditions of the parent compound while varying the amount of acid added. In this case, it was seen that this procedure was responsible for building various Cu-**lon**-MOF isoreticular structures with varying TZ:TCEE ratios, where more ligand decarboxylation was observed by increasing the amount of acid (Table 3.4). Unfortunately, before reaching complete ligand decarboxylation, elevating the acid concentration above a certain level prevented the construction of any framework. In addition, a high quality crystal was obtained exclusively with the parent compound original synthesis conditions (i.e., using 0.2 mL of acid). Of note is that no TCA was observed in any of the prepared compounds.

Table 3-4 Effect of varying the amount of acid added during Cu-**lon**-MOF preparation on the produced frameworks.

3.5 M HNO_3/DMF added (mL)	Product Morphology	Product Quality	TZ:TCEE (by NMR)
0.05	Small spheres	Low intensity PXRD	1:1.15
0.1	Large spheres	Low intensity PXRD	1:1.1
0.2	Cu-**lon**-MOF	Good	1:0.89
0.4	Rods	Low intensity PXRD	1:0.63
0.8	Precipitation	Amorphous	-
1	Precipitation	Amorphous	-

Hence, TCEE was replaced by TCA in the reaction of a trial to produce the hydrolyzed isoreticular structure. As mentioned before, this method ensures the hydrolysis of all ester groups present in the framework, leading overall to the formation of larger channels. Therefore, a solvothermal reaction between $Cu(NO_3)_2$ and TCA in DMF in the presence of 3.5 M HNO_3/DMF was placed at 85 °C to yield black microcrystals that aggregated to form needle-like polycrystalline material of H-Cu-**lon**-MOF. Using PXRD studies, the powder pattern of the prepared H-Cu-**lon**-MOF was found to be identical to that calculated from the SC structure of Cu-**lon**-MOF, suggesting the preparation of the isoreticular structure and indicating its bulk phase purity (Figure 3.55).

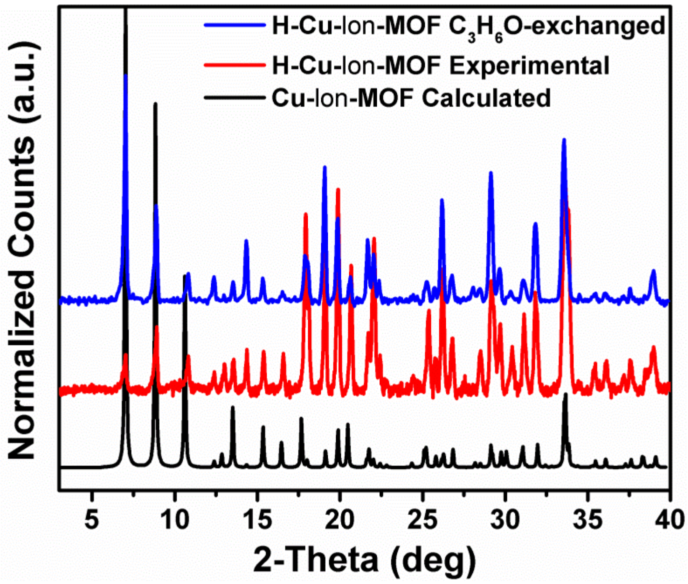

Figure 3.55 PXRD patterns of experimental H-Cu-**lon**-MOF (red) and calculated Cu-**lon**-MOF (black) indicating that the two structures are isoreticular. H-Cu-**lon**-MOF showed stability in different organic solvents, like C_3H_6O (blue).

As discussed earlier, IR (Figure 3.56 and Figure 3.57) and liquid state NMR (Figure 3.58) were required to deduce the functional groups or ligands produced in the structure (TCA and/or TZ) from the *in situ* hydrolysis of the ligand during MOF formation. Although the isoreticular framework containing both TCA and TZ was expected by utilizing the hydrolyzed ligand (TCA), the resulting isoreticular framework, H-Cu-**lon**-MOF contained ligands that were totally decarboxylated, i.e., possessing strictly TZ.

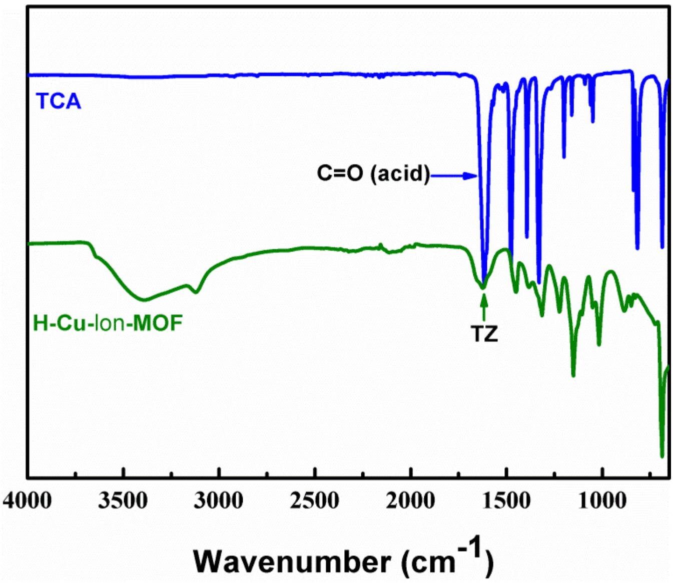

Figure 3.56 FT-IR spectrum of TCA and C_2H_5OH-exchanged H-Cu-**lon**-MOF indicating the presence of only TZ (no TCA).

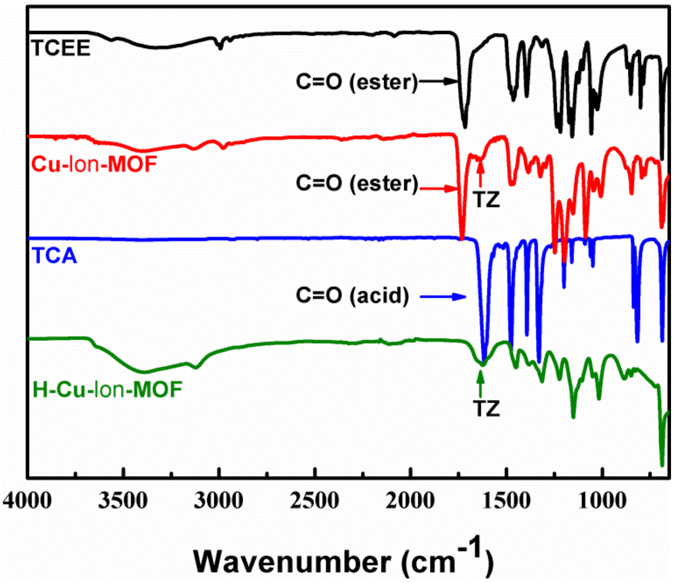

Figure 3.57 Summary of FT-IR spectra comparing the ligands used in this study and the corresponding isoreticular frameworks prepared.

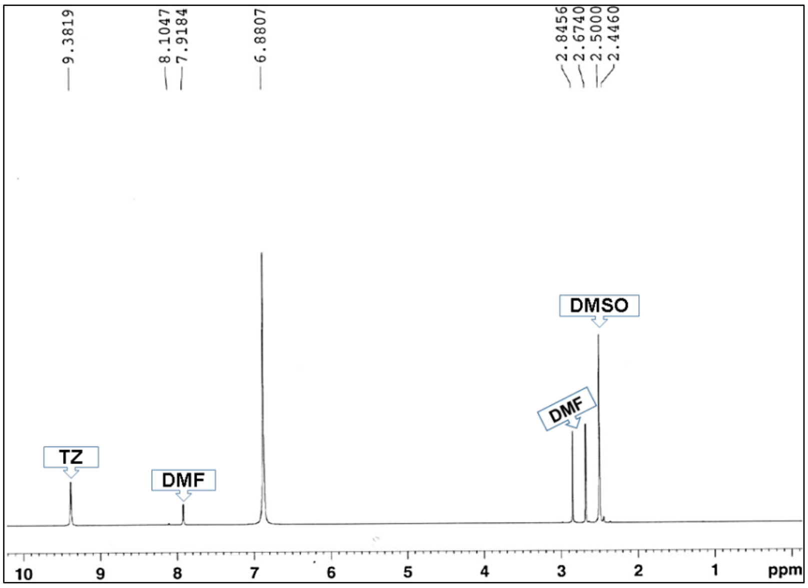

Figure 3.58 ^{1}H NMR spectra of H-Cu-**lon**-MOF in DMF showing the presence of only TZ.

VT-PXRD experiments were performed on CH_3CN-exchanged samples of this compound to investigate the material thermal stability under vacuum. These experiments revealed thermal stability of H-Cu-**lon**-MOF under vacuum up to 125 °C only (Figure 3.59). Moreover, microcrystals of H-Cu-**lon**-MOF demonstrated high sensitivity to air but favorable stability in common organic solvents, such as C_2H_5OH, CH_3OH, C_3H_6O and CH_3CN.

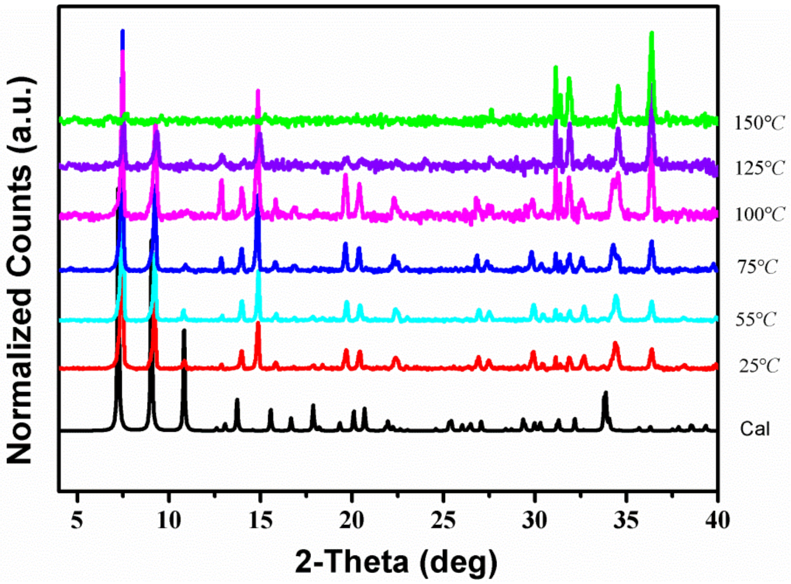

Figure 3.59 VT-PXRD of H-Cu-**lon**-MOF showing its stability under vacuum at less than 125 °C.

To further scrutinize the thermal stability of H-Cu-**lon**-MOF, TGA was performed on both DMF-washed and CH_3CN-exchanged samples under a N_2 atmosphere. The tests were carried out between RT and 700 °C at an increasing heating rate of 5 °C/min in high resolution dynamic mode. The TGA plots of H-Cu-**lon**-MOF indicated its thermal stability up to 215 °C where the degradation of the framework begins and is eventually followed by its complete collapse at around 400 °C (Figure 3.60).

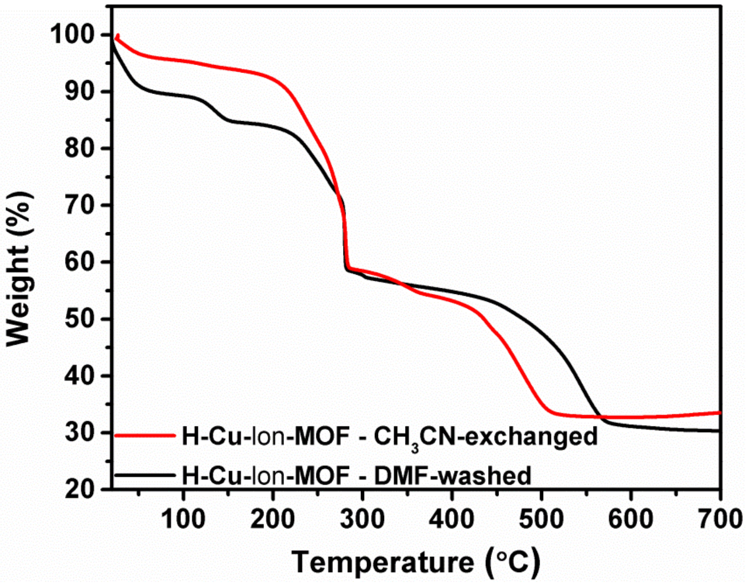

Figure 3.60 TGA plots of DMF-washed and CH_3CN-exchanged H-Cu-**lon**-MOF under a N_2 atmosphere.

Likewise, H-Cu-**lon**-MOF showed low stability in aqueous media, possibly being attributed to the absence of organic tethers in the channels (ester groups); therefore, it is more susceptible to water attacking the metal connectors and displacing ligands, leading to crystallinity loss.[42]

Moreover, to further confirm decarboxylation and to investigate the influence of larger channels, an Ar adsorption experiment at 87 K was conducted on H-Cu-**lon**-MOF and compared to the corresponding data for Cu-**lon**-MOF (Figure 3.61). As anticipated, a significant enhancement of Ar adsorption was observed for H-Cu-**lon**-MOF. Based on Ar behaving as probe molecules, H-Cu-**lon**-MOF displayed a specific SA_{BET} and PV of 449 m^2/g and 0.22 cm^3/g, respectively.

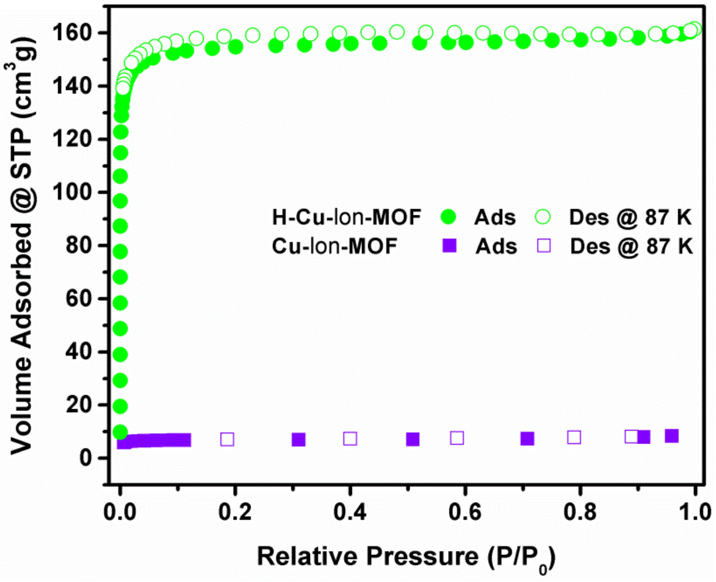

Figure 3.61 LP Ar adsorption and desorption isotherms of H-Cu-**lon**-MOF at 87 K compared to that of Cu-**lon**-MOF.

Further, analysis of CO_2 variable temperature adsorption data for H-Cu-**lon**-MOF (Figure 3.62) as compared to Cu-**lon**-MOF showed that upon complete decarboxylation of Cu-**lon**-MOF, the Q_{st} of adsorption of CO_2 decreased from 33.6 to 28 kJ/mol at low loading (Figure 3.54 and Figure 3.62). The decrease in the CO_2 heat of adsorption for H-Cu-**lon**-MOF can be understood by its less pronounced confinement versus Cu-**lon**-MOF that leads to a decrease in CO_2 interactions within the framework.

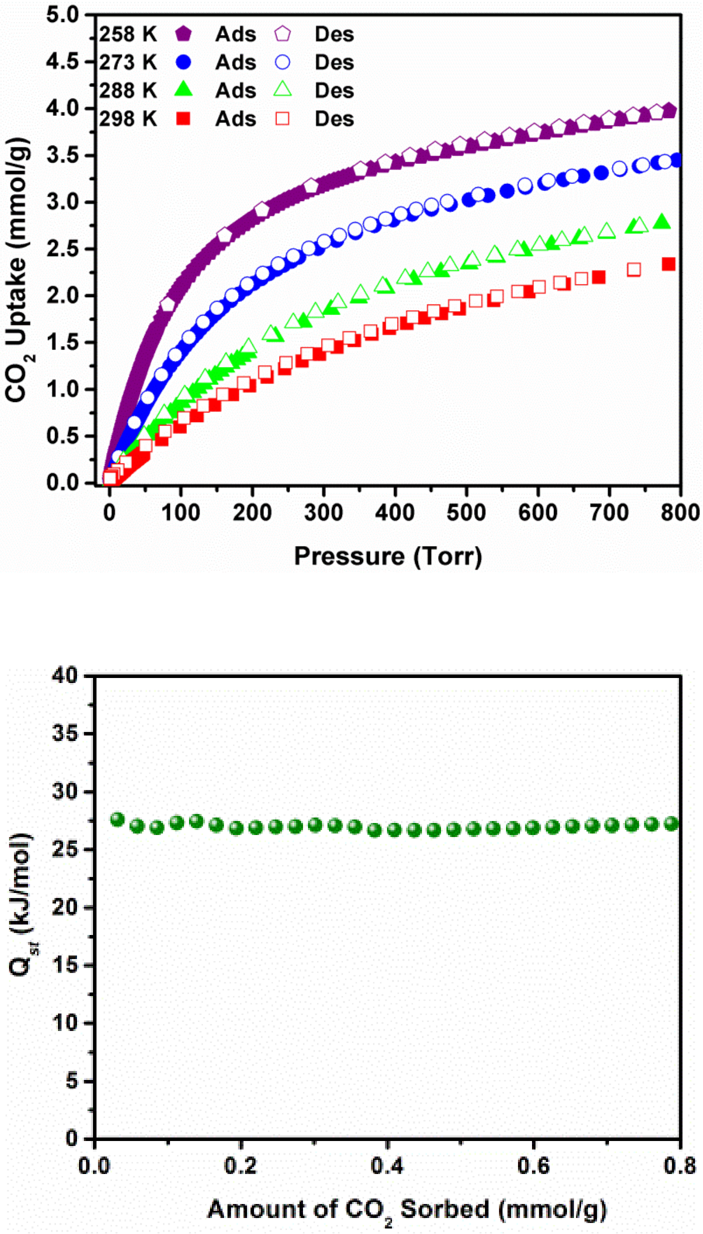

Figure 3.62 LP CO_2 variable temperature sorption isotherms at 258, 273, 288 and 298 K of H-Cu-**lon**-MOF and their corresponding Q_{st}.

Further analysis of CO_2, N_2, CH_4, C_3H_8 and n-C_4H_{10} adsorption data (Figure 3.63) at high and intermediate pressures, established the absolute decarboxylation of Cu-**lon**-MOF**.** On the whole, H-Cu-**lon**-MOF showed much higher gas uptake than Cu-**lon**-MOF.

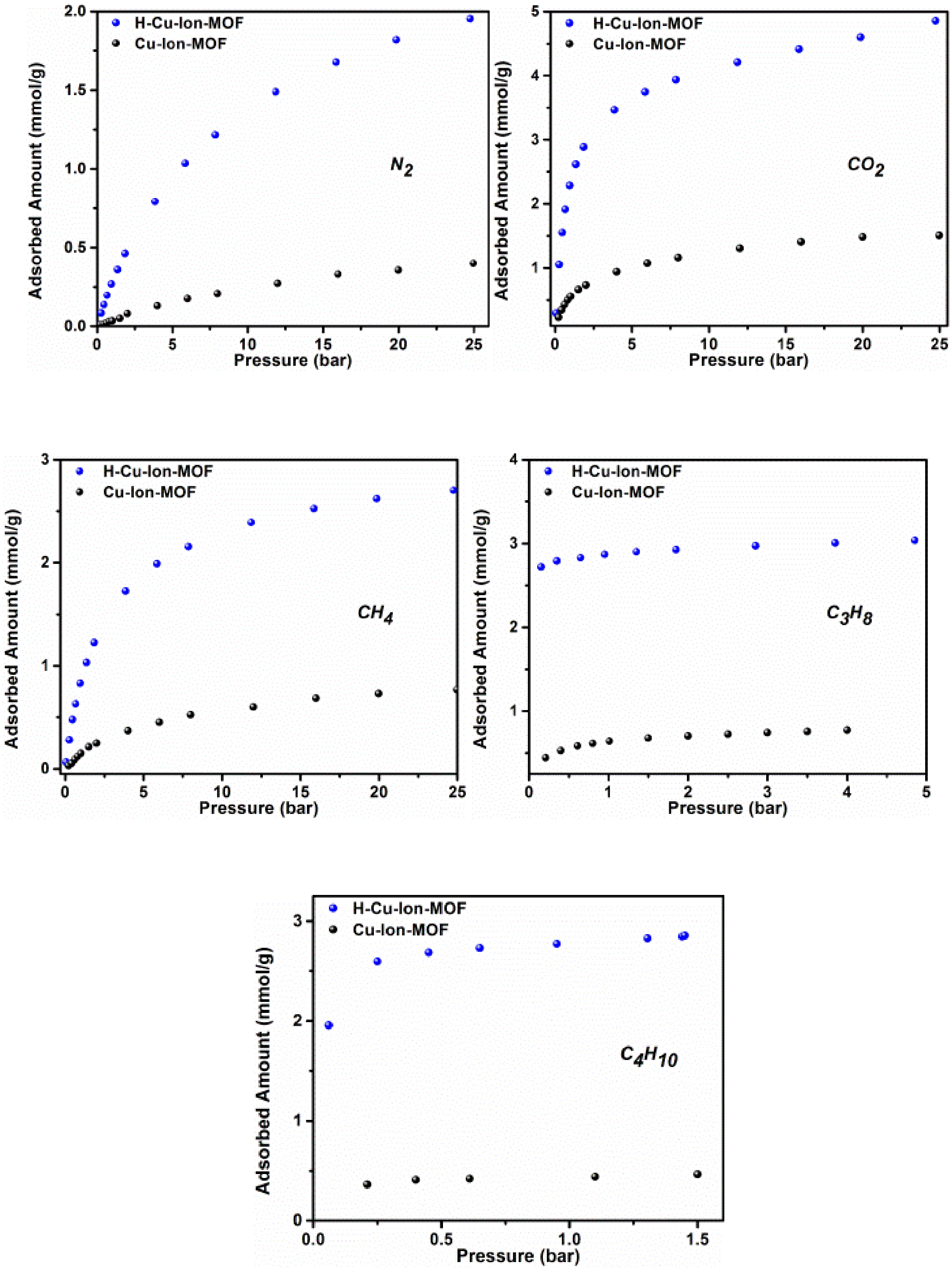

Figure 3.63 Adsorption of N_2, CO_2, CH_4, C_3H_8 and C_4H_{10} on Cu-**lon**-MOF and H-Cu-**lon**-MOF at 298 K and a wide range of pressure levels.

As seen from Table 3.5, the higher interactions of CO_2 in Cu-**lon**-MOF (because of the presence of ester groups that result in more confined spaces), as determined from the Q_{st} of CO_2 adsorption, relative to H-Cu-**lon**-MOF is apparent from the relatively higher normalized K' Toth adsorption parameter (K'= K/n_s).

The K energetic parameter is equivalent to the Henry constant while $\boldsymbol{n_s}$ is a parameter representing the CO_2 saturation uptake and determined by fitting the single adsorption isotherms to the Toth equation.

Here, the Toth model was employed to fit the pure gas isotherms (Chapter 2) and its simple formulation as expressed by equation (3).[43]

$$\boldsymbol{n = n_s \frac{KP}{(1+(KP)^m)^{\frac{1}{m}}}} \qquad \textbf{Eq. 3}$$

where $\boldsymbol{n}$ is the amount adsorbed, $\boldsymbol{n_s}$ is the amount adsorbed at saturation, $\boldsymbol{P}$ is the equilibrium pressure, K is the equilibrium constant, and $\boldsymbol{m}$ is a parameter indicating the heterogeneity of the adsorbent.

Table 3-5 Toth model parameters for adsorption on Cu-**lon**-MOF and H-Cu-**lon**-MOF.

	Parameters	**Gases**		
		N_2	**CH_4**	**CO_2**
Cu-**lon**-MOF	**n_s**	0.78	1.07	2.63
	K	0.054	0.180	1.456
	m	0.13	0.79	0.39
	K' (K/n_s)	0.07	0.17	0.55
H-Cu-**lon**-MOF	**n_s**	2.98	3.18	5.56
	K	0.110	0.439	1.89
	M	0.83	0.82	0.58
	K' (K/n_s)	0.03	0.13	0.34

Moreover, after finding considerable enhancement in gas uptake for H-Cu-**lon**-MOF vs. Cu-**lon**-MOF and the particularly steep adsorption isotherms for CO_2 vs. CH_4 and

N_2 for both isoreticular structures, the separation factors of gas pairs, such as CO_2/N_2 and CO_2/CH_4, were investigated (Figure 3.64).

CO_2 separation from N_2 and CH_4 containing streams, such as flue gas and natural gas, is of prime importance to ensure environmentally friendly energy production in fossil fuel power plants and achieve the required specifications for CH_4 transportation in pipelines.

As seen from Figure 3.64, H-Cu-**lon**-MOF display CO_2/N_2 and CO_2/CH_4 separation factors of 12 and 5 at roughly 1 bar, respectively, only slightly lower than Cu-**lon**-MOF, which has a separation factor of 24 and 9, respectively, as predicted by IAST (Chapter 2).[44] This finding indicates that hydrolysis of ester groups in Cu-**lon**-MOF permitted a rise in gas uptake in H-Cu-**lon**-MOF without a significant decrease in affinity toward CO_2.

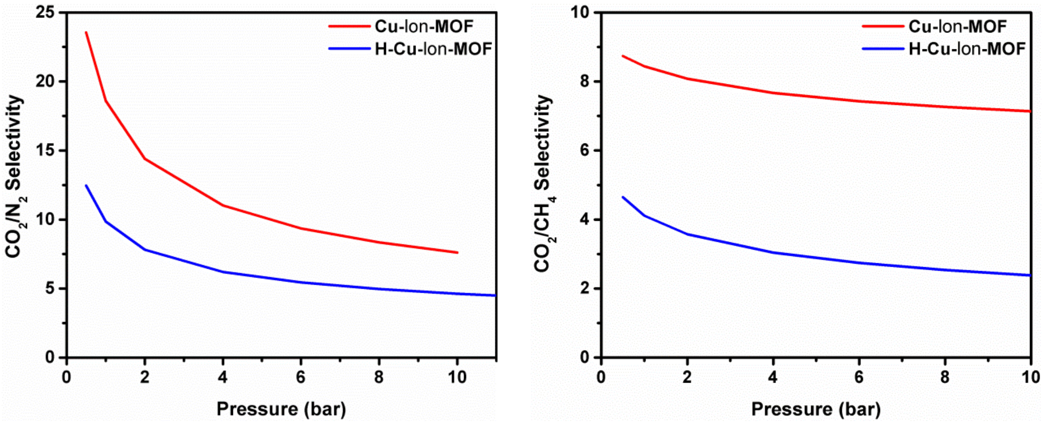

Figure 3.64 Separation factors of Cu-**lon**-MOF and H-Cu-**lon**-MOF for CO_2/N_2 and CO_2/CH_4 gas mixtures.

3.5.5. Summary and conclusions

The results presented herein are a testament to the power of the newly introduced SBLs approach for synthesizing 3-P MOFs utilizing the 6-c A-A technique to pillar *in situ*-formed 2-P SBLs. Here, the effect of modifying organic ligand functionalities on tuning different properties of the prepared MOFs, including gas sorption behavior, without changing their underlying network topology was studied.

More specifically, the effect of tetrazolate modification on the structure-function relationship of the ester-bearing and the totally decarboxylated compounds was exemplified in the case of single adsorption of Ar, CO_2, N_2, CH_4, C_3H_8 and n-C_4H_{10}, in addition to the adsorption energetics of CO_2 and CO_2/N_2, CO_2/CH_4 mixed-gas adsorption. It was found that hydrolysis of the esters in the organic building block brought about drastic enhancements in N_2, CH_4, C_3H_8 and n-C_4H_{10} adsorption uptake. Detailed analysis in the case of CO_2 adsorption demonstrated that the enhancement of CO_2 uptake occurred without altering much of the CO_2 adsorption energetics and selectivity toward CO_2.

3.6. REFERENCES

1. Guillerm, V.; Kim, D.; Eubank, J. F.; Luebke, R.; Liu, X.; Adil, K.; Lah, M. S.; Eddaoudi, M., *Chem. Soc. Rev.* **2014,** *43*, 6141-6172.

2. Eubank, J. F.; Wojtas, L.; Hight, M. R.; Bousquet, T.; Kravtsov, V.; Eddaoudi, M., *J. Am. Chem. Soc.* **2011,** *133*, 17532-17535.

3. Chen, Z. J.; Adil, K.; Weselinski, L. J.; Belmabkhout, Y.; Eddaoudi, M., *J. Mater. Chem.* **2015,** *3*, 6276-6281.

4. Schoedel, A.; Boyette, W.; Wojtas, L.; Eddaoudi, M.; Zaworotko, M. J., *J. Am. Chem. Soc.* **2013,** *135*, 14016-14019.

5. Jhung, S. H.; Khan, N. A.; Hasan, Z., *CrystEngComm* **2012,** *14*, 7099-7109.

6. (a) Cohen, S. M., *Chem. Sci.* **2010,** *1*, 32-36.(b) Cohen, S. M., *Chem. Rev.* **2012,** *112*, 970-1000.

7. Eddaoudi, M.; Kim, J.; Vodak, D.; Sudik, A.; Wachter, J.; O'Keeffe, M.; Yaghi, O. M., *Proc. Natl. Acad. Sci. USA* **2002,** *99*, 4900-4904.

8. Wang, X. J.; Li, P. Z.; Liu, L.; Zhang, Q.; Borah, P.; Wong, J. D.; Chan, X. X.; Rakesh, G.; Li, Y.; Zhao, Y., *Chem. Commun.* **2012,** *48*, 10286-10288.

9. bosch, M., Zhang, M., Zhou, H., *Adv. Chem.* **2014**, Article ID 182327.

10. Bureekaew, S., amirjalayer, S., and Schmid, R., *J. Mat. Chem.* **2012,** *22*, 10249-10254.

11. Sen, S.; Neogi, S.; Rissanen, K.; Bharadwaj, P. K., *Chem. Commun.* **2015,** *51*, 3173-3176.

12. Farha, O. K.; Hupp, J. T., *Accts. Chem. Res.* **2010,** *43*, 1166-1175.

13. Liu, B.; Wong-Foy, A. G.; Matzger, A. J., *Chem. Commun.* **2013,** *49*, 1419-1421.

14. Chae, H. K.; Kim, J.; Friedrichs, O. D.; O'Keeffe, M.; Yaghi, O. M., *Angew. Chem. Int. Ed. Engl.* **2003,** *42*, 3907-3909.

15. (a) Blatov, V. A.; Shevchenko, A. P.; Serezhkin, V. N., *J. Appl. Crystallogr.* **2000,** *33*, 1193.(b) Blatov, V. A., *Struct. Chem.* **2012,** *23*, 955-963.

16. (a) Wei, Q.; Yang, D.; Larson, T. E.; Kinnibrugh, T. L.; Zou, R.; Henson, N. J.; Timofeeva, T.; Xu, H.; Zhao, Y.; Mattes, B. R., *J. Mat. Chem.* **2012,** *22*, 10166-10171.(b) Wei, Y.-S.; Lin, R.-B.; Wang, P.; Liao, P.-Q.; He, C.-T.; Xue, W.; Hou, L.; Zhang, W.-X.; Zhang, J.-P.; Chen, X.-M., *CrystEngComm* **2014,** *16*, 6325-6330.

17. Bae, Y.-S.; Dubbeldam, D.; Nelson, A.; Walton, K. S.; Hupp, J. T.; Snurr, R. Q., *Chem. Mater.* **2009,** *21*, 4768-4777.

18. Furukawa, H.; Ko, N.; Go, Y. B.; Aratani, N.; Choi, S. B.; Choi, E.; Yazaydin, A. O.; Snurr, R. Q.; O'Keeffe, M.; Kim, J.; Yaghi, O. M., *Science* **2010,** *329*, 424-428.

19. Lalonde, M.; Bury, W.; Karagiaridi, O.; Brown, Z.; Hupp, J. T.; Farha, O. K., *J. Mater. Chem. A* **2013,** *1*, 5453-5468.

20. (a) Furukawa, H., miller, M., Yaghi, O., *J. Mater. Chem.* **2007,** *17*, 3197-3204.(b) Wong-Foy, A. G.; Matzger, A. J.; Yaghi, O. M., *J. Am. Chem. Soc.* **2006,** *128*, 3494-3495.(c) Rowsell, J. L.; Millward, A. R.; Park, K. S.; Yaghi, O. M., *J. Am. Chem. Soc.* **2004,** *126*, 5666-5667.(d) Herm, Z., Swisher, J., Smit, B., Krishna, R., and Long, J., *J. Am. Chem. Soc.* **2011,** *133*, 5664-5667.

21. Wang, T. C.; Bury, W.; Gomez-Gualdron, D. A.; Vermeulen, N. A.; Mondloch, J. E.; Deria, P.; Zhang, K.; Moghadam, P. Z.; Sarjeant, A. A.; Snurr, R. Q.; Stoddart, J. F.; Hupp, J. T.; Farha, O. K., *J. Am. Chem. Soc.* **2015,** *137*, 3585-3591.

22. Farha, O. K.; Eryazici, I.; Jeong, N. C.; Hauser, B. G.; Wilmer, C. E.; Sarjeant, A. A.; Snurr, R. Q.; Nguyen, S. T.; Yazaydin, A. O.; Hupp, J. T., *J. Am. Chem. Soc.* **2012,** *134*, 15016-15021.

23. (a) Moellmer, J.; Celer, E. B.; Luebke, R.; Cairns, A. J.; Staudt, R.; Eddaoudi, M.; Thommes, M., *Micropor. Mesopor. Mat.* **2010,** *129*, 345-353.(b) Bhatia, S. K.; Myers, A. L., *Langmuir* **2006,** *22*, 1688-1700.(c) Zhao, D.; Yuan, D. Q.; Zhou, H. C., *Energ. Environ. Sci.* **2008,** *1*, 222-235.

24. (a) Caskey, S. R.; Wong-Foy, A. G.; Matzger, A. J., *J. Am. Chem. Soc.* **2008,** *130*, 10870-10871.(b) Rosi, N. L.; Kim, J.; Eddaoudi, M.; Chen, B.; O'Keeffe, M.; Yaghi, O. M., *J. Am. Chem. Soc.* **2005,** *127*, 1504-1518.(c) An, J.; Geib, S. J.; Rosi, N. L., *J. Am. Chem. Soc.* **2010,** *132*, 38.

25. (a) Llewellyn, P. L.; Bourrelly, S.; Serre, C.; Vimont, A.; Daturi, M.; Hamon, L.; De Weireld, G.; Chang, J. S.; Hong, D. Y.; Hwang, Y. K.; Jhung, S. H.; Ferey, G., *Langmuir* **2008,** *24*, 7245-7250.(b) Du, L. T.; Lu, Z. Y.; Ma, M. T.; Su, F.; Xu, L., *Rsc Advances* **2015,** *5*, 29505-29508.

26. (a) Sumida, K.; Rogow, D. L.; Mason, J. A.; McDonald, T. M.; Bloch, E. D.; Herm, Z. R.; Bae, T. H.; Long, J. R., *Chem. Rev.* **2012,** *112*, 724-781.(b) Xue, D. X.;

Cairns, A. J.; Belmabkhout, Y.; Wojtas, L.; Liu, Y.; Alkordi, M. H.; Eddaoudi, M., *J. Am. Chem. Soc.* **2013,** *135*, 7660-7667.

27. Hirscher, M.; Panella, B.; Schmitz, B., *Micropor. Mesopor. Mat.* **2010,** *129*, 335-339.

28. Alezi, D.; Belmabkhout, Y.; Suyetin, M.; Bhatt, P. M.; Weselinski, L. J.; Solovyeva, V.; Adil, K.; Spanopoulos, I.; Trikalitis, P. N.; Emwas, A. H.; Eddaoudi, M., *J. Am. Chem. Soc.* **2015,** *137*, 13308-13318.

29. (a) Guo, Z.; Wu, H.; Srinivas, G.; Zhou, Y.; Xiang, S.; Chen, Z.; Yang, Y.; Zhou, W.; O'Keeffe, M.; Chen, B., *Angew. Chem. Int. Ed. Engl.* **2011,** *50*, 3178-3181.(b) Peng, Y.; Krungleviciute, V.; Eryazici, I.; Hupp, J. T.; Farha, O. K.; Yildirim, T., *J. Am. Chem. Soc.* **2013,** *135*, 11887-11894.

30. Ma, S.; Sun, D.; Simmons, J. M.; Collier, C. D.; Yuan, D.; Zhou, H. C., *J. Am. Chem. Soc.* **2008,** *130*, 1012-1016.

31. Wilmer, C. E.; Farha, O. K.; Yildirim, T.; Eryazici, I.; Krungleviciute, V.; Sarjeant, A. A.; Snurr, R. Q.; Hupp, J. T., *Energ. Environ. Sci.* **2013,** *6*, 1158-1163.

32. Gandara, F.; Furukawa, H.; Lee, S.; Yaghi, O. M., *J. Am. Chem. Soc.* **2014,** *136*, 5271-5274.

33. DeCoste, J. B.; Weston, M. H.; Fuller, P. E.; Tovar, T. M.; Peterson, G. W.; LeVan, M. D.; Farha, O. K., *Angew. Chem. Int. Ed. Engl.* **2014,** *53*, 14092-14095.

34. (a) Cambridge Structural Database (CSD), http://www.ccdc.cam.ac.uk/products/csd/statistics/.(b) Allen, F. H., *Acta Crystallogr., Sect. B: Struct. Sci.* **2002,** *58*, 380-388.

35. (a) Li, J. R.; Sculley, J.; Zhou, H. C., *Chem. Rev.* **2012,** *112*, 869-932.(b) Herm, Z. R., Bolch, E.D, Long, J.R., *Chem. Mater.* **2013,** *26*, 323-338.

36. (a) Eddaoudi, M.; Li, H. L.; Reineke, T.; Fehr, M.; Kelley, D.; Groy, T. L.; Yaghi, O. M., *Top. Catal.* **1999,** *9*, 105-111.(b) Eddaoudi, M.; Moler, D. B.; Li, H.; Chen, B.; Reineke, T. M.; O'Keeffe, M.; Yaghi, O. M., *Accts. Chem. Res.* **2001,** *34*, 319-330.(c) Eddaoudi, M.; Kim, J.; Rosi, N.; Vodak, D.; Wachter, J.; O'Keeffe, M.; Yaghi, O. M., *Science* **2002,** *295*, 469-472.

37. Zhou, H. C.; Long, J. R.; Yaghi, O. M., *Chem. Rev.* **2012,** *112*, 673-674.

38. (a) Sun, L.; Li, G. Z.; Xu, M. H.; Li, X. J.; Li, J. R.; Deng, H., *Z. Anorg. Allg. Chem.* **2012,** *638*, 1200-1203.(b) Sun, L.; Ma, L.; Cai, J. B.; Liang, L.; Deng, H., *CrystEngComm* **2012,** *14*, 890-898.(c) Kou, J. F.; Su, M.; Zhang, Y. H.; Huang, Z. D.;

Ng, S. W.; Yang, G. A., *Z. Anorg. Allg. Chem.* **2010,** *65*, 1467-1471.(d) Yang, W.; Lin, X.; Blake, A. J.; Wilson, C.; Hubberstey, P.; Champness, N. R.; Schroder, M., *CrystEngComm* **2009,** *11*, 67-81.

39. Zhong, D. C.; Deng, J. H.; Luo, X. Z.; Lu, T. B.; Wang, K. J., *CrystEngComm* **2012,** *14*, 1538-1541.

40. (a) kim, H., Sun, Y., Kim, Y., Kajiwara, T., Yamashita, M., Kim, K., *CrystEngComm* **2011,** *13*, 2197-2200.(b) Zou, Y., Yu, C., Li, Y., Lah, M.S., *CrystEngComm* **2012,** *14*, 7174-7177.

41. Duan, W.; Chen, C.; Jiang, L.; Li, G. H., *Carbohydr. Polym.* **2008,** *73*, 582-586.

42. Taylor, J. M.; Vaidhyanathan, R.; Iremonger, S. S.; Shimizu, G. K., *J. Am. Chem. Soc.* **2012,** *134*, 14338-14340.

43. Toth, J., *Uniform and thermodynamically consistent interpretation of adsorption isotherms*. **2002**; Vol. 107.

44. Myers, A. L.; Prausnitz, J. M., *AlChE J.* **1965,** *11*, 121.

Chapter 4: Molecular Building Blocks (MBBs)-Based Synthesis: The Pursuit of Highly-Connected MOFs Based on RE Polynuclear Clusters

4.1. Abstract

In this chapter, novel RE polynuclear clusters are introduced. The unprecedented octadecanuclear, octanuclear and double tetranuclear RE-MBBs for new MOF materials were synthesized utilizing the novel MBBs approach with 2-FBA as a modulator.

In fact, the presence of 2-FBA is essential for the production of polynuclear RE-MBBs and, consequently, the construction of their corresponding MOFs. Here, this was proven by using the same reaction conditions that led to the formation of these MOFs while excluding the modulator. As expected, only MOFs based on the dominant RE infinite-chain MBBs or simple dinuclear clusters were formed.

Various angular hetero-functional ligands that contain both carboxylate and nitrogen donor moieties were utilized in this study. It was found that nitrogen atoms are not always involved in the coordination of the frameworks, and whenever they are, they coordinate to the metal in a monodentate fashion with a relatively flexible geometry, leading to frameworks that are less stable upon guest solvent molecules removal. Therefore, the frameworks underwent partial or complete collapse as evidenced by their low or complete lack of porosity.

4.2. General introduction

As mentioned in Chapter 1, the MBBs approach introduced by Eddaoudi et al. in 2011 is considered a powerful tool to design, discover and develop diverse MOF platforms with the intrinsically peripheral geometry of the MBBs and the prerequisite of consistent *in situ* production of desirable MBBs.[1] As opposed to different transition metal-based MBBs, which are well studied and established, RE-MBBs and their corresponding networks are restricted to more simple ones, like dinuclear clusters or the dominant infinite-chain MBBs with less structural geometry information in MOFs crystal chemistry.[2] In this respect, our group has recently introduced 2-FBA as a powerful modulator that can assist in the construction of highly-connected RE polynuclear MBBs, which led to the design and discovery of unique frameworks with highly-localized charge density and tunable pore size, like RE-**fcu**-MOFs.[3]

The work presented here is a part of our group's continuous effort and ongoing exploration of various metals and functional ligands with the objective of discovering new modular inorganic RE-MBBs that are polynuclear and highly-connected.[2c, 3-4] Accordingly, in the presence of 2-FBA, RE metal ions were used with varying hetero-functional angular ligands possessing two carboxylate groups. In addition, these ligands were characterized by the presence of nitrogen donor moieties (e.g., pyridine) to evaluate the effect of their presence on the construction, connectivity and stability of new MOFs that are based on RE polynuclear clusters (Figure 4.1).

The fact that it is possible to isolate new frameworks and network topologies by subtly modifying the geometry of the ligand, e.g., adjusting its length-to-width ratio, was utilized.[5] Consequently, four different ligands were featured in this part of the study, namely, 4,4'-(pyridine-3,5-diyl)dibenzoic acid (PDDB), 5'-(pyridin-4-yl)-[1,1':3',1''-terphenyl]-4,4''-dicarboxylic acid (PTPDC), 5-(pyridin-4-yl)isophthalic acid (PIP) and 5-(pyrimidin-5-yl)isophthalic acid (PMIP). These ligands are analogous to each other, and their relationship depicted in Figure 4.1.

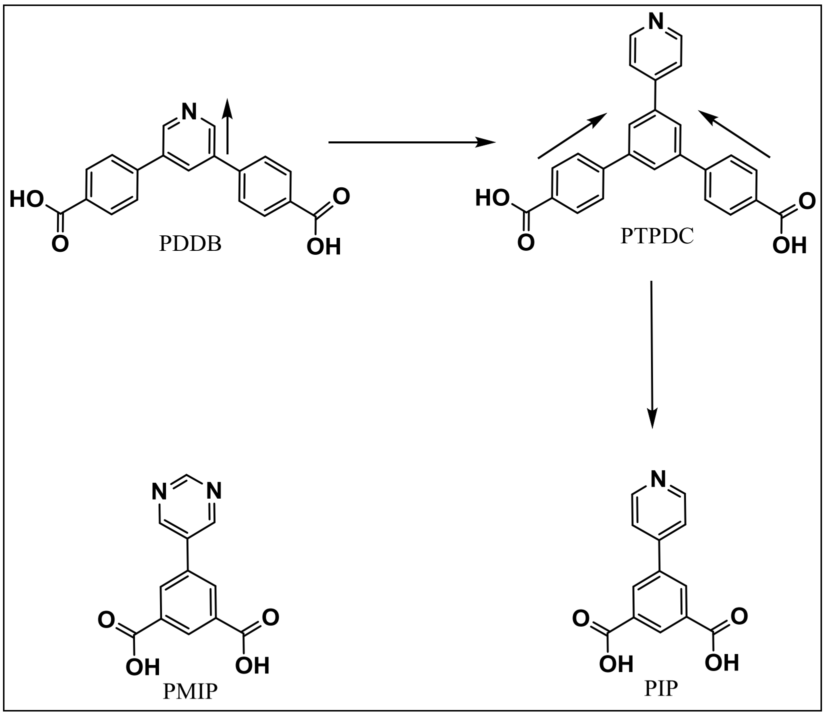

Figure 4.1 Schematic representation of the bifunctional angular ligands used in the current study. The relationship between these linkers is indicated by arrows.

As noted, PTPDC is related to 1,3,5-benzene(tris)benzoic acid (BTB) (Figure 4.2 a), previously employed by our group to prepare a novel RE nonanuclear carboxylate cluster that had been further isolated serving as an 18-connected MBB for the assembly of a (3,18)-connected MOF with **gea** topology.[6] In addition, PIP is also related to the less symmetrical tritopic biphenyl-3,4',5-tricarboxylic acid (Figure 4.2 b) used by our group to construct the 12-connected RE nonanuclear MBB (d6R or hexagonal prism building unit) and 8-connected RE hexanuclear MBB along with their related (3,8,12)-connected **pek**-MOF.[2c] In PTPDC and PIP, one of the carboxylate groups of the ligands from previous studies is replaced with a nitrogen atom from a nitrogen donor moiety, such as pyridine.

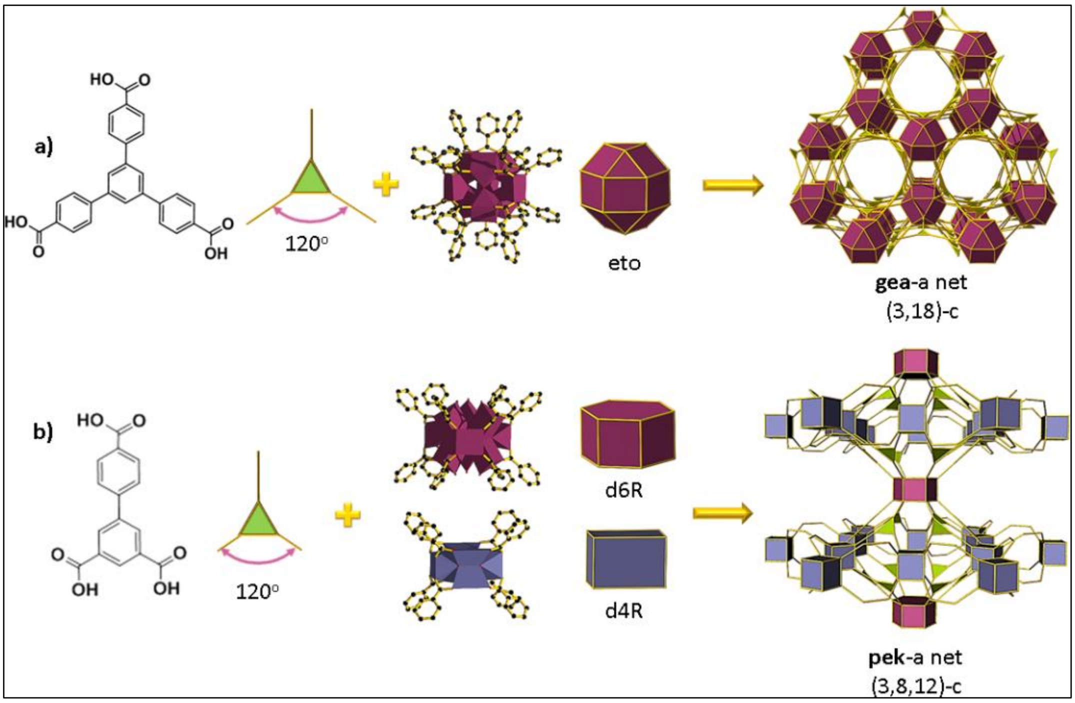

Figure 4.2 Examples of bifunctional trigonal ligands that were previously used by our group to construct novel highly-connected RE-MBBs and are closely related to the ligands used in this study. Figure adapted with permission from Alezi et al., 2015.[2c]

In the first part of this chapter, we report the occurrence of an unprecedented RE octadecanuclear cluster (composed of 18 RE metal ions) as a 2-P MOF building block. Initially, the reaction between $Y(NO_3)_3$ and PDDB with the addition of 2-FBA led to the formation of Y-**hxl**-MOF based on the novel highly-connected cluster. This highly-stable porous framework is based on 2-P layers packed together to form a 3-P framework through forces, including hydrogen bonding, π–π stacking of benzene rings and Van der Waals forces (i.e., supramolecular chemistry).[7]

Under similar reaction conditions, while excluding the modulator, a nonporous 3-P MOF based on RE dinuclear paddlewheel and dimeric clusters (Y-**nbo**-MOF) was created.

In the second part of the chapter, a novel RE octanuclear cluster is described as a 3-P MOF building block. Here, $Y(NO_3)_3$ was reacted with PTPDC in the presence of 2-FBA to produce Y-**tfz**-MOF-1, which is a pillared 3-P MOF based on the unprecedented octanuclear cluster (composed of 8 RE metal ions) and have the rare **tfz** topology. Another structurally-related compound is synthesized using a mixed-ligands approach[8] where the extended ligands, PTPDC and PDDB, are mixed in a ratio of 2:1 and are added to $Y(NO_3)_3$ in the presence of 2-FBA to produce Y-**tfz**-MOF-2. In this 3-P MOF, PTPDC and the *in situ*-formed RE-MBBs are coordinated to form 2-P SBLs and PDDB act as the pillars.

In the last part of this chapter, we go on to show the importance of using the modulator in the reaction to assist in forming the larger RE-MBBs and to deviate from their dominant building units, which are the infinite inorganic chains. Here, PIP, a shorter version of PTPDC, is used resulting in the synthesis of Y-**tfz**-MOF-3. This is a 3-P MOF that is also based on an RE octanuclear cluster but, because of the steric hindrance effect of the shorter ligand, a new structure was formed where the octanuclear cluster was split into two tetranuclear clusters connected through *in situ*-formed formate ligands. Similar reaction conditions were used while eliminating the modulator resulted in the formation of Y-**swk**-MOF that was based on RE-infinite rod-shaped SBUs.

The prepared frameworks were fully characterized with regards to their structural, gas sorption and magnetic properties (for the polynuclear Ln-based MOFs) and were additionally studied to establish structure-property relationships that explain the effects of using different ligands and constructing larger RE clusters on tuning a variety of the materials’ properties.

4.3. Materials and methods

All chemicals mentioned in this work were used as received from Fisher Scientific, Sigma-Aldrich or Acros without any further purification or modification. For details on ligands syntheses, devices and software, in addition to theoretical background with respect to selected subjects, please refer to Chapter 2.

4.4. Experimental section part I: Highly-stable undulant RE-MOF featuring an unprecedented octadecanuclear metal cluster

4.4.1. Synthesis and characterization

4.4.1.1. Synthesis of Y-hxl-MOF

In a 20-mL scintillation vial, a solution containing $Y(NO_3)_3.6H_2O$ (18.38 mg, 0.048 mmol), PDDB (5 mg, 0.016 mmol), DMF (4 mL), 0.75 mL water and 0.1 mL 4 M 2-FBA was prepared and heated to 105 °C over the course of 1 day. Clear polyhedral crystals of Y-**hxl**-MOF were collected, purified by repeated washing with DMF and air dried. The as-synthesized crystals were determined to be insoluble in water and common organic solvents.

4.4.1.2. Activation of Y-hxl-MOF

An approximately 50-mg sample of the as-synthesized Y-**hxl**-MOF was washed with DMF several times (3-5x) over a period of 24 h. The sample was then subjected to solvent exchange by adding around 20 mL of CH_3CN and refreshing 3-5 times daily for 7 days. Before gas sorption experiments, the sample was placed into a 6 mm large bulb glass sorption cell and dried carefully with flowing N_2 after removing the excess surface solvent with a syringe. The sample was then placed under dynamic vacuum at 150 °C for 12 h and then backfilled with N_2 prior to the sorption experiments.

4.4.1.3. Synthesis of Dy-hxl-MOF

In a 20-mL scintillation vial, a solution containing $Dy(NO_3)_3.5H_2O$ (21.05 mg, 0.048 mmol), PDDB (5 mg, 0.016 mmol), DMF (4.5 mL), 0.75 mL water and 0.1 mL 4 M 2-FBA was prepared and heated to 105 °C for 3 days. Clear polyhedral crystals were collected, purified by repeated washing with DMF and air dried.

4.4.1.4. Synthesis of Y-nbo-MOF

In a 20-mL scintillation vial, a solution containing $Y(NO_3)_3.6H_2O$ (18.38 mg, 0.048 mmol), PDDB (5 mg, 0.016 mmol), DMF (2 mL), 1 mL C_2H_5OH and 0.1 mL 4.4 M HNO_3 in DMF was prepared and heated to 105 °C for 1 day. Clear hexagonal crystals were collected and air dried. The as-synthesized crystals were purified through repeated washing with DMF and were determined to be insoluble in water and common organic solvents.

4.4.1.5. Activation of Y-nbo-MOF

An approximately 50-mg sample of the as-synthesized Y-**nbo**-MOF was washed with DMF several times over a period of 24 h. The sample was then subjected to solvent exchange by adding around 20 mL of CH_3OH and refreshing 3-5 times daily for 7 days. Before gas sorption experiments, the sample was placed into a 6 mm large bulb glass sorption cell and dried carefully with flowing N_2 after removing the excess surface solvent with a syringe. The sample was then placed under dynamic vacuum and screened for optimum activation temperature at RT, 85, 105 and 120 °C (increasing at a rate of 1 °C/min). It was then held for 12 h at each temperature, cooled to RT and then backfilled with N_2 prior to the sorption experiments at each activation temperature.

4.4.2. Results and discussion

4.4.2.1. **Y-**hxl**-MOF**

In the presence of 2-FBA as the modulator, a solvothermal reaction between $Y(NO_3)_3$, PDDB (Figure 4.3 a) in DMF and water yielded transparent polyhedral crystals of Y-**hxl**-MOF that were formulated, based on SCXRD studies, as $|(DMA)_2|[Y_{18}(\mu_3\text{-}OH)_{24}(\mu_3\text{-}O)_4(O_2C\text{-})_{24}(H_2O)_{12}].(solv)_x$. Y-**hxl**-MOF crystallizes in the rhombohedral *R*-3*m* space group with cell parameters of a = b = 22.7664 Å, c = 54.206 Å, α = β = 90°, γ = 120° and V = 24331.4 $Å^3$.

In the crystal structure of Y-**hxl**-MOF, there were three crystallographically-independent yttrium ions, where each had an eight-coordination (8-c) environment and were noted as Y1, Y2 and Y3. Among them, Y1 was surrounded by two oxygen atoms from two distinct carboxylates of PDDB ligands, five μ_3-OH groups and one μ_3-O group. Y2 was surrounded by two oxygen atoms from two distinct carboxylates of the ligands, four μ_3-OH and one μ_3-O groups, leaving the eighth coordination site occupied by a terminal water molecule. Finally, Y3 was coordinated by four oxygen atoms from four distinct carboxylates of the ligands, three μ_3-OH groups and one water molecule, altogether completing the eighth coordination site. These yttrium ions (six of each type, i.e., Y1, Y2 and Y3) were bridged together through μ_3-OH, μ_3-O groups and carboxylate moieties to generate two nonanuclear clusters, further connected by 6 μ_3-OH groups to produce an unprecedented octadecanuclear yttrium cluster, $[Y_{18}(\mu_3\text{-OH})_{24}(\mu_3\text{-O})_4(O_2C\text{-})_{24}]$ (Figure 4.3 b). Each octadecanuclear-based MBB was bridged to its six neighboring MBBs through 24 angular PDDB ligands creating a 2-P undulant network (Figure 4.3 c) that can be simplified and analyzed topologically using TOPOS[9] software as **hxl** layers.

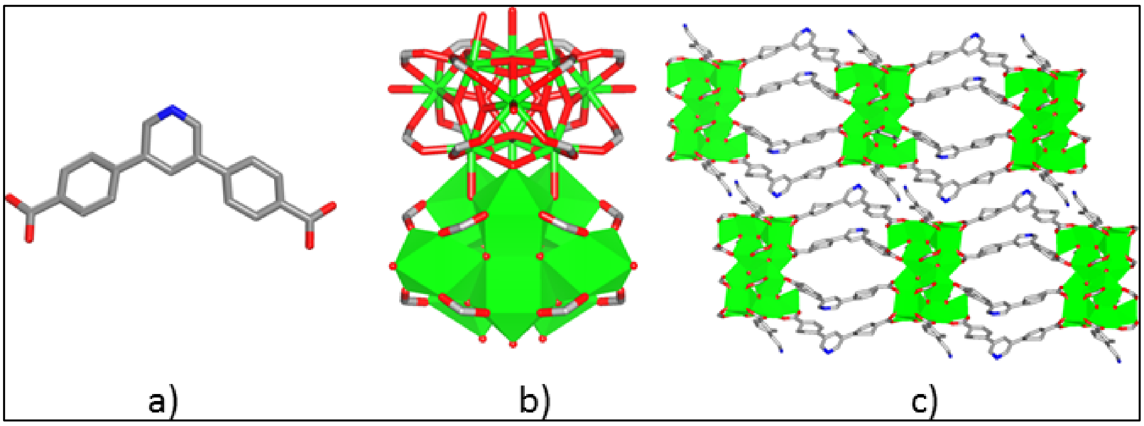

Figure 4.3 (a) PDDB, (b) the novel RE octadecanuclear cluster formed with the aid of 2-FBA and (c) two stacked 2-P layers of Y-**hxl**-MOF. C = gray, O = red, N = blue, Y = green; Hydrogen atoms and solvent molecules are omitted for clarity.

In this structure, the nitrogen donor moieties of PDDB are pointing toward the RE polynuclear clusters, but the length of the ligand and steric hindrance could be obstructing their coordination (Figure 4.4).

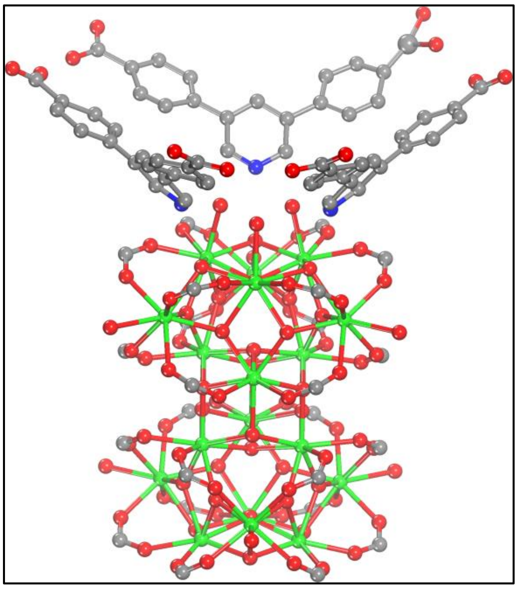

Figure 4.4 The relationship between one octadecanuclear RE-MBB in Y-**hxl**-MOF and the nitrogen donor moiety of PDDB. C = gray, O = red, N = blue, Y = green.

Therefore, the 2-P layers were packed together in a staggered fashion and led to the formation of a 3-P structure through strong hydrogen bonding (2.7 Å - close to that of covalent bonds), π–π stacking of benzene rings,[10] and Van der Waals forces (i.e., supramolecular chemistry)[7] having 2-D channels along the *a*- and *b*-axes with an aperture size of (~ 4.1 x 15.8 Å).[11] The corresponding solvent-accessible free volume of Y-**hxl**-MOF was estimated from the X-ray crystal structure to be 41% using MS software, whereas the theoretical PV was put forth to be 0.42 cm^3/g.

The phase purity of the bulk crystalline material for Y-**hxl**-MOF was confirmed by similarities between the calculated and as-synthesized PXRD patterns (Figure 4.5). In addition, Y-**hxl**-MOF not only demonstrated robust stability in common organic solvents (Figure 4.6), but also conducive air (Figure 4.7) and water stability (Figure 4.8). Furthermore, the layered framework showed high thermal stability under vacuum up to 400 °C (Figure 4.9). These properties are important parameters for potential practical deployment of porous MOF materials.

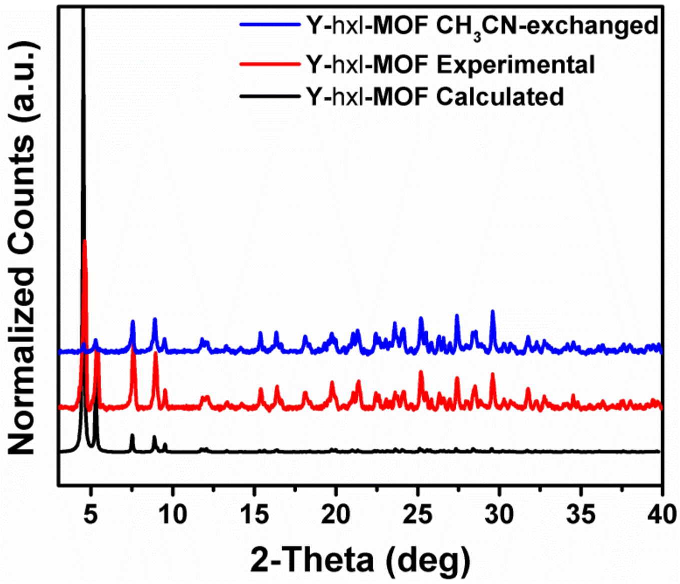

Figure 4.5 Experimental and calculated PXRD patterns of Y-**hxl**-MOF that indicate the purity of the as-synthesized bulk material and the stability of the CH_3CN-exchanged samples.

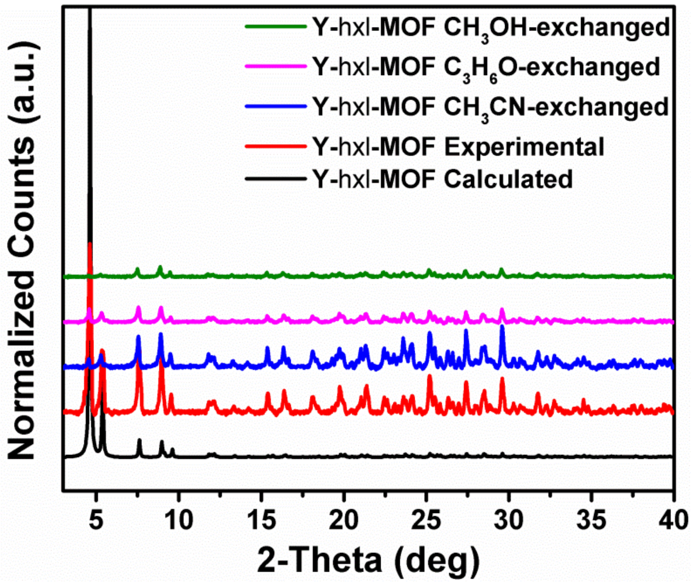

Figure 4.6 PXRD patterns of calculated Y-**hxl**-MOF, experimental and exchanged with different solvents indicating the stability of solvent-exchanged samples.

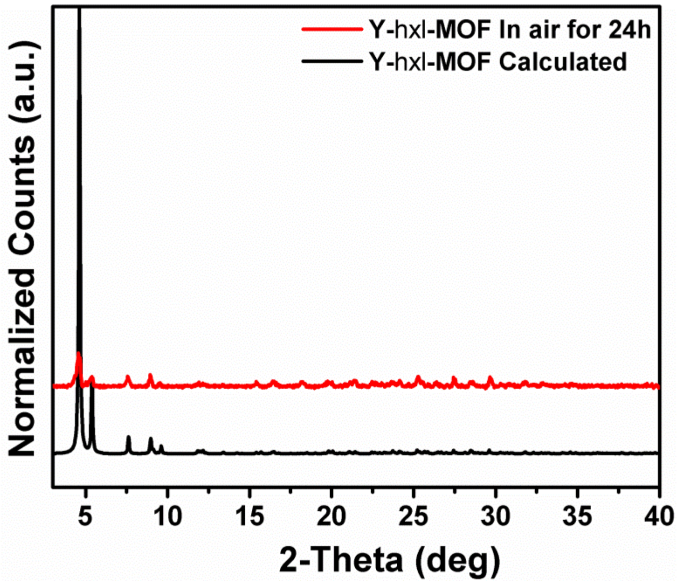

Figure 4.7 Calculated and experimental PXRD patterns of Y-**hxl**-MOF subjected to air, indicating its stability.

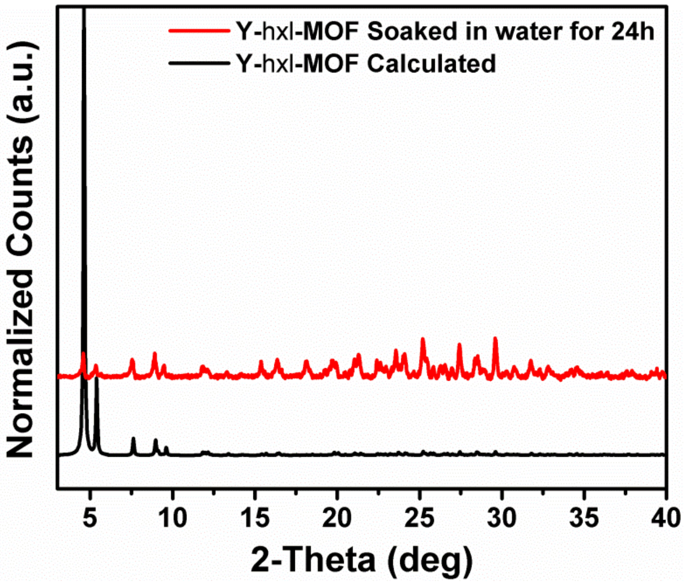

Figure 4.8 Calculated and experimental PXRD patterns of Y-**hxl**-MOF subjected to water, indicating its stability in aqueous media.

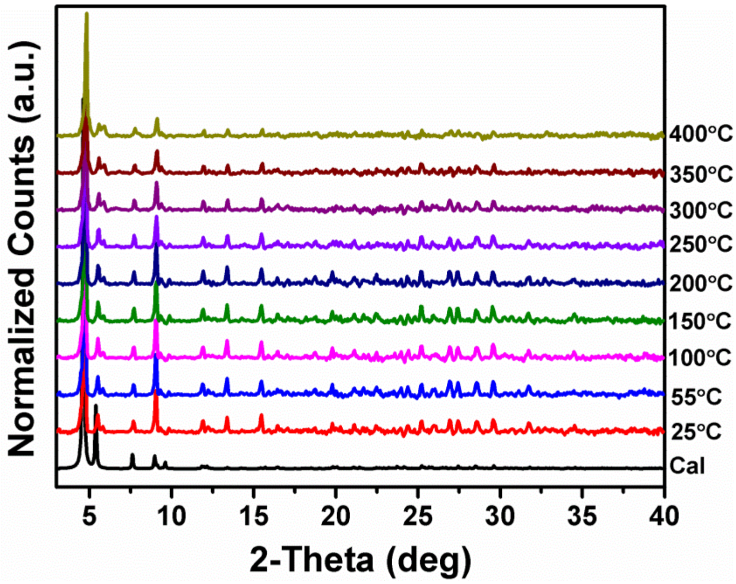

Figure 4.9 VT-PXRD of Y-**hxl**-MOF indicative of its high thermal stability under vacuum up to 400 °C.

To investigate the thermal stability of Y-**hxl**-MOF, TGA was performed on DMF-washed and CH_3CN-exchanged samples under a N_2 atmosphere. The tests were carried out between RT and 700 °C at an increasing heating rate of 20 °C/min in high resolution dynamic mode. The TGA plots of this compound indicated its thermal stability for up to 500 °C (Figure 4.10).

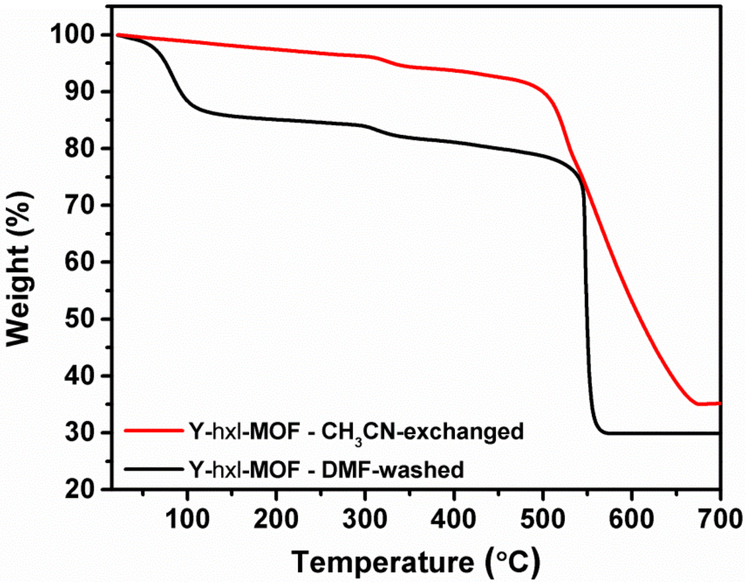

Figure 4.10 TGA plots showing the high thermal stability of Y-**hxl**-MOF at more than 500 °C.

To determine the actual porosity of the framework and subsequently assess its prospective application for gas storage and separation, gas sorption experiments were performed and isotherms were collected using several probe molecules at varying temperatures and pressures. These studies showed that CH_3CN-exchanged Y-**hxl**-MOF exhibits a fully reversible Type I Ar and N_2 isotherms (Figure 4.11), characteristics of permanently microporous materials. The apparent SA_{BET} and total free PV for Y-**hxl**-MOF were estimated to be 782 m^2/g and 0.38 cm^3/g, respectively.

This modest porosity was an expected result with regards to the formation of the large RE polynuclear clusters that affected the maximum gas uptake of the framework.

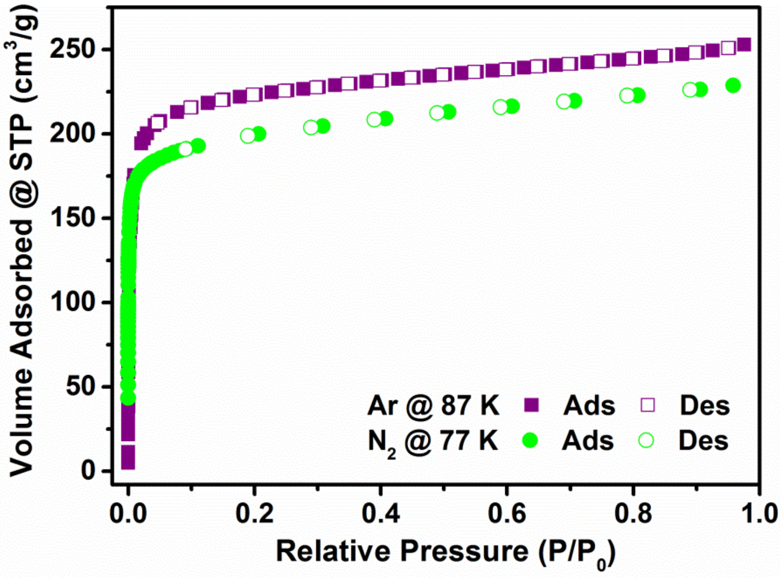

Figure 4.11 N_2 and Ar adsorption isotherms for Y-**hxl**-MOF at 77 and 87 K, respectively.

Encouraged by the framework’s robust stability and permanent porosity, further H_2 and CO_2 adsorption experiments were conducted. The H_2 adsorption uptake was assessed to be 1.02 wt% at 760 Torr and 77 K, while the Q_{st} for H_2 was determined and estimated to be 7.9 kJ/mol at zero coverage for Y-**hxl**-MOF (Figure 4.12).

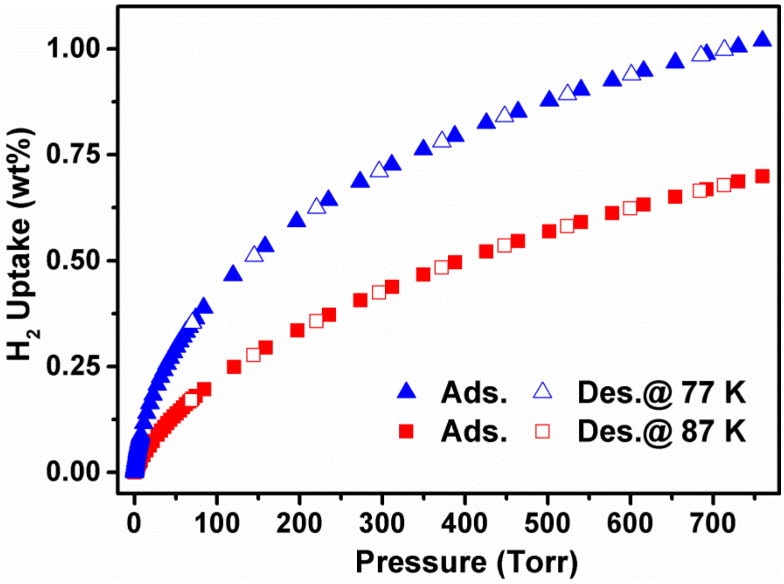

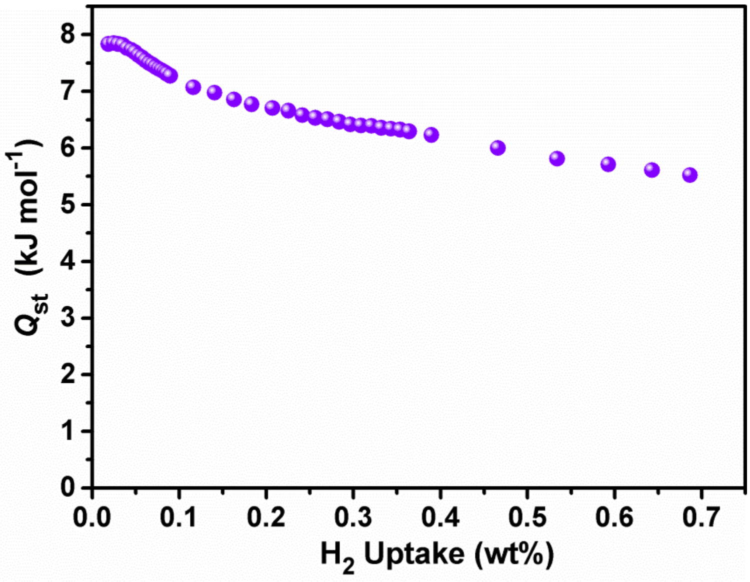

Figure 4.12 LP H_2 sorption isotherms at 77 and 87 K for Y-**hxl**-MOF and their corresponding Q_{st}.

Likewise, CO_2 adsorption experiments were carried out at various temperatures. The maximum uptake was observed to be 2.1 mmol/g at 273 K and 760 Torr. Indeed, the Q_{st} for CO_2 calculated from the corresponding variable temperature adsorption isotherms was 22.9 kJ/mol for Y-**hxl**-MOF at zero coverage (Figure 4.13). This value is nearly constant as CO_2 loading increases (i.e., 22.9 to 20.9 kJ/mol), indicative of homogenous binding sites over the full range of gas loading.[12]

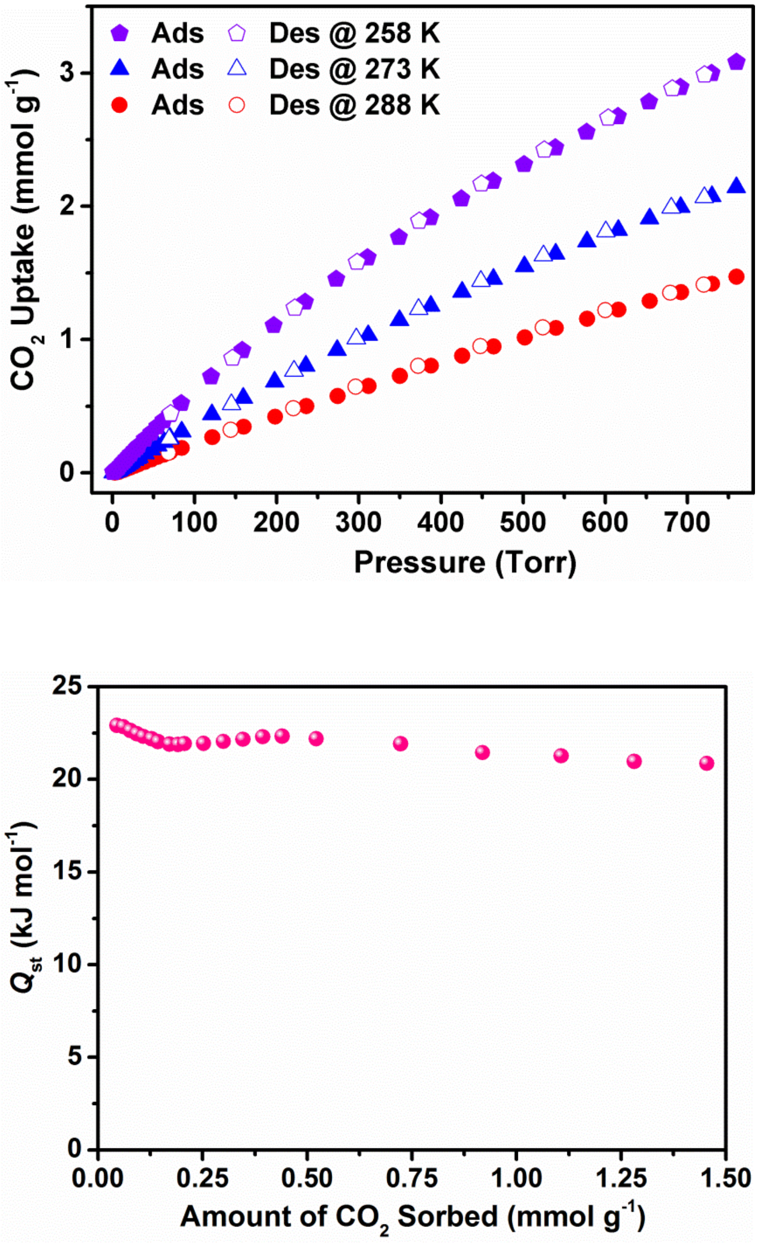

Figure 4.13 Y-**hxl**-MOF variable temperature CO_2 adsorption isotherms collected at 258, 273 and 288 K and their corresponding Q_{st}.

Considering the high-nuclearity of the RE cluster of Y-**hxl**-MOF, its corresponding Dy analog (Dy-**hxl**-MOF) was also prepared using comparable reaction conditions to examine its magnetic properties.[13] The phase purity of the prepared compound was validated by the similarities between calculated Y-**hxl**-MOF PXRD patterns and those of experimental Dy-**hxl**-MOF (Figure 4.14).

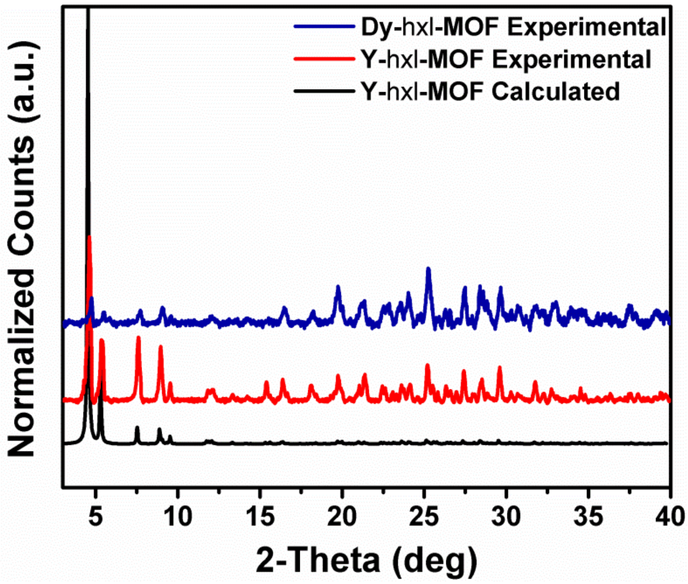

Figure 4.14 Phase purity of Dy-**hxl**-MOF indicated by the similarities between its PXRD pattern and its isostructure, Y-**hxl**-MOF, calculated and experimental ones.

The magnetic properties of this isostructure were measured with a superconducting quantum interference device (see Chapter 2). Therefore, to obtain the intrinsic magnetic properties of Dy-**hxl**-MOF, the low-field magnetization (χ) was measured as a function of temperature (T) in the range of 1.8-300 K under a magnetic field of 100 Oe with the ZFC and FC processes (Figure 4.15).[14] In the whole temperature range, ZFC and FC curves overlapped perfectly, suggesting a paramagnetic property in nature.

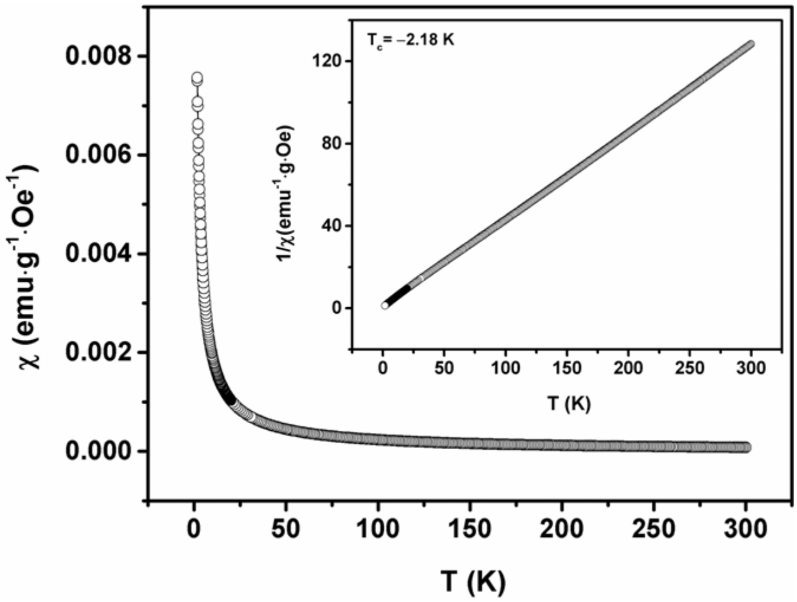

Figure 4.15 Temperature-dependent magnetic susceptibility of Dy-**hxl**-MOF with an applied field H = 100 Oe. Inset yields the $\frac{1}{\chi}$ - T curve.

A close examination reveals that these curves can be perfectly described by Curie-Weiss law of the magnetic susceptibility of the material with a small, negative intercept, T_c, that is equal to – 2.18 K (Figure 4.15 inset). These results showed that there existed a weak, antiferromagnetic-like interaction among the Dy clusters.

The field-dependent magnetization was measured in the temperature range 1.8-30 K. Figure 4.16 inset provides magnetization (*M*) as a function of applied field (H = 0 – 70 kOe) measured at different temperatures. The *M-H* curves show superparamagnetism at low temperatures.

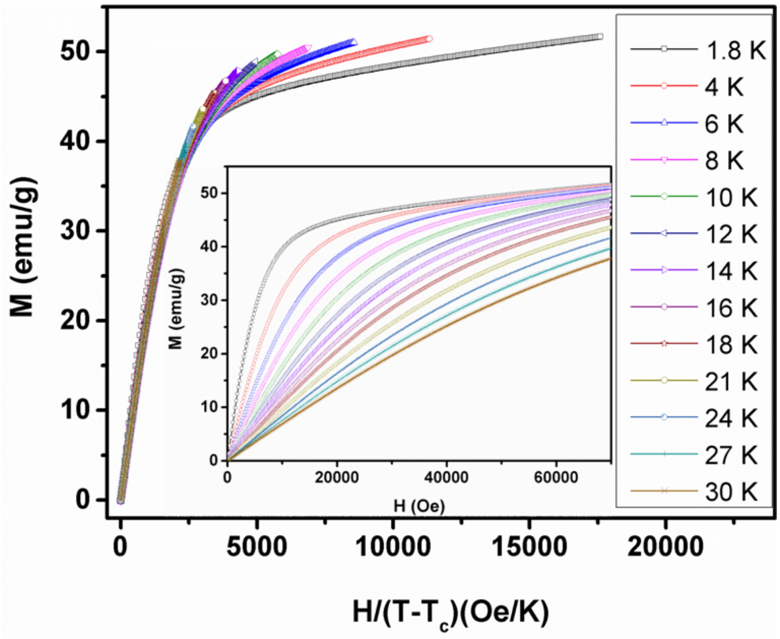

Figure 4.16 Magnetization, M, versus $H/(T - T_c)$ at a temperature range from 1.8-30 K. Inset provides the field-dependent magnetization measured from 1.8-30 K.

If all the Dy clusters in this material have the same energy barrier and magnetic moment, the M - H curves can be described by a modified Langevin function given that the field H is low enough and T is sufficiently high.

Figure 4.16 supplies the relationship, $M(H,T) - H/(T - T_c)$, for the temperature range, 1.8-30 K. All the curves overlapped with each other at lower fields, this approving the uniformity of the energy barrier and magnetic moments in Dy clusters.

The effective magnetic moment could be calculated by the modified Langevin function using the low field magnetization, the molecular formula and molecular mass of the compounds. The calculated effective magnetic moment per molecule that contains 18 Dy ions was 78 μ_B, which is smaller than the 18 individual Dy ions. This alludes to the fact that there is antiferromagnetic ordering among the Dy ions. In general, the detailed magnetic ordering needs further investigation to discern the possible application of this material as a cryogenic magnetic refrigerant with a magnetocaloric effect.[15]

4.4.2.2. Y-nbo-MOF

To confirm the necessity of using the modulator (2-FBA) to form RE polynuclear clusters, the reaction conditions that allowed the formation of Y-**hex**-MOF were modified by eliminating the modulator entirely. In this case, a totally new 3-P MOF composed of linked dimers and dinuclear paddlewheel Y-MBBs was formed, confirming the importance of employing a modulator to form large RE-MBBs, such as the octadecanuclear cluster in Y-**hex**-MOF.

With this, a solvothermal reaction between $Y(NO_3)_3$ and PDDB (Figure 4.17 a) in DMF yielded transparent hexagonal crystals of Y-**nbo**-MOF. This framework crystallizes in the tetragonal space group, *I* 4/*m*, with cell parameters of a = b = 16.4131 Å, c = 32.918 Å and α = β = γ = 90° and V = 8867.8 $Å^3$. In Y-**nbo**-MOF, there are two crystallographically-independent yttrium ions, and among them, Y1 was surrounded by six oxygen atoms from six different ligands while Y2 was coordinated by four oxygen atoms from four independent ligands, one oxygen atom from the μ_2-oxo and one water molecule completing the sixth coordination site. Interestingly, Y1 and Y2 generate dinuclear paddlewheel and dimeric MBBs, respectively. The two types of MBBs are arranged in an alternative fashion that leads to the formation of metal cluster-based layers (Figure 4.17 b) that are pillared through the ligand and result in a 3-P network (Figure 4.17 c) with no nitrogen involvement within the connectivity. The structural/topological analysis of the resulting crystal structure revealed that Y-**nbo**-MOF is a MOF with **nbo** topology.

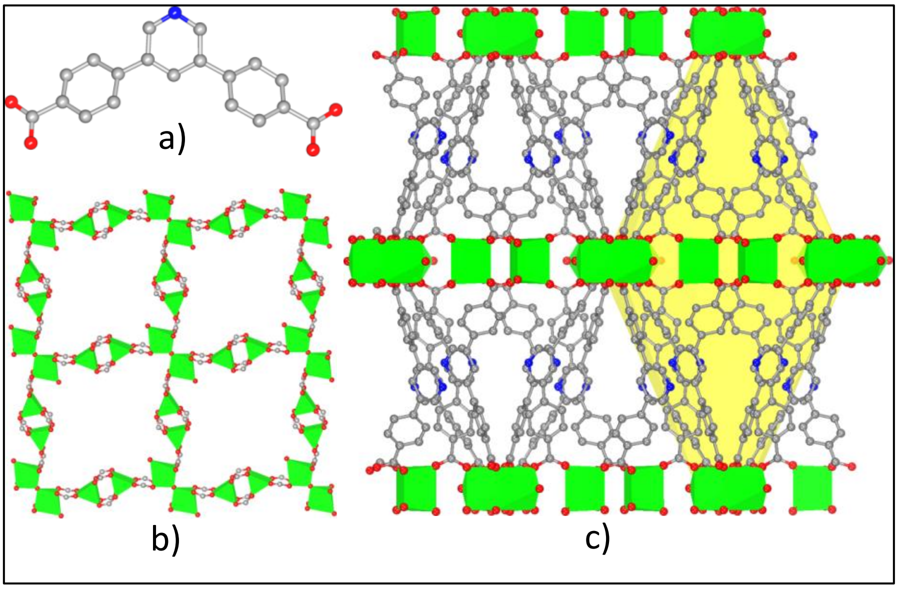

Figure 4.17 (a) PDDB, (b) the dinuclear paddlewheel and dimeric RE-MBBs forming cluster based layers and (c) Y-**nbo**-MOF where PDDB acts as pillars with no nitrogen involvement within the connectivity. C = gray, O = red, N = blue, Y = green; Hydrogen atoms and solvent molecules are omitted for clarity.

In Y-**nbo**-MOF, spindle-like cages with very small windows are formed (Figure 4.17 c). Sorption experiments demonstrated that this compound is nonporous to an assortment of gases, including N_2, Ar, H_2 and CO_2, which could be attributed to its limited window aperture and/or the entrapment of row material inside the cages.

The phase purity of the bulk crystalline Y-**nbo**-MOF was verified by similarities between the calculated and as-synthesized PXRD patterns (Figure 4.18). Additionally, the framework showed distinct stability in various organic solvents, air (Figure 4.19) and water (Figure 4.20).

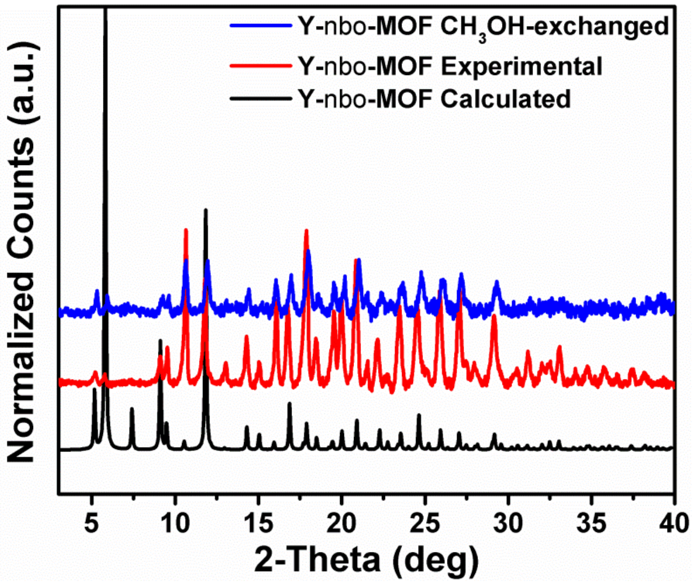

Figure 4.18 Phase purity and stability in CH$_3$OH of Y-**nbo**-MOF indicated by the similarities between the calculated and experimental PXRD.

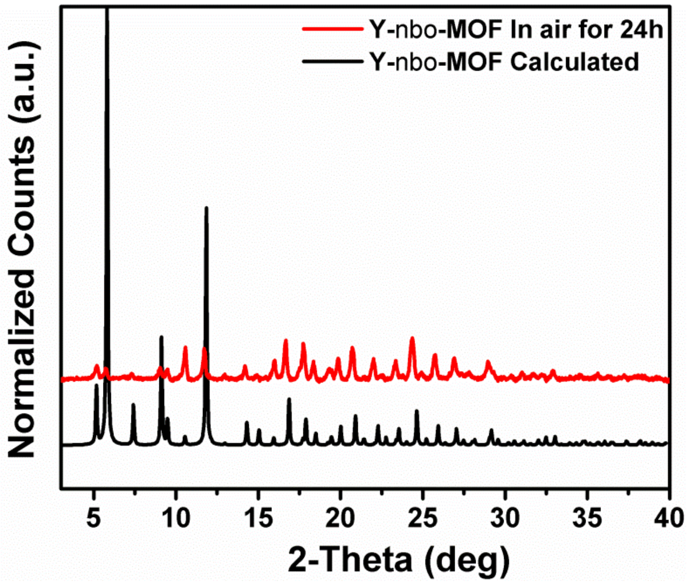

Figure 4.19 PXRD patterns of Y-**nbo**-MOF exposed to air for 24 h indicating its stability in air.

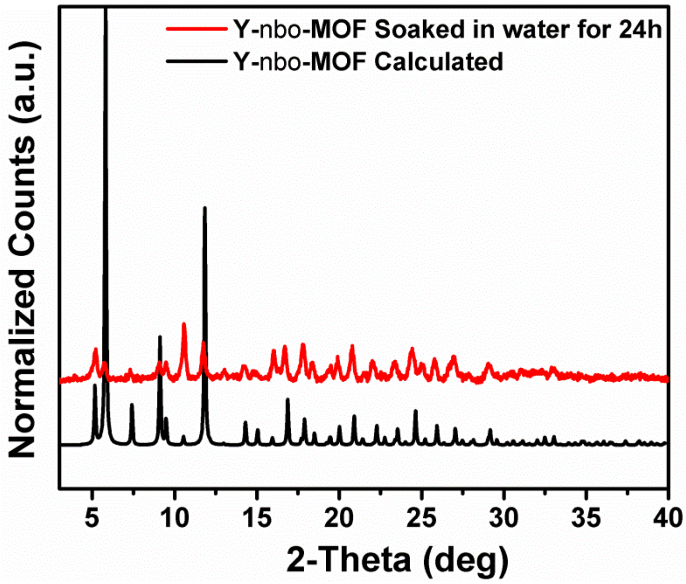

Figure 4.20 PXRD patterns of Y-**nbo**-MOF soaked in water for 24 h indicating its stability in water.

To investigate the thermal stability of Y-**nbo**-MOF, TGA was performed on DMF-washed samples under a N_2 atmosphere. The test was performed between RT and 700 °C at an increasing heating rate of 20 °C/min in high resolution dynamic mode. The TGA plots of this compound indicated its thermal stability up to 400 °C (Figure 4.21).

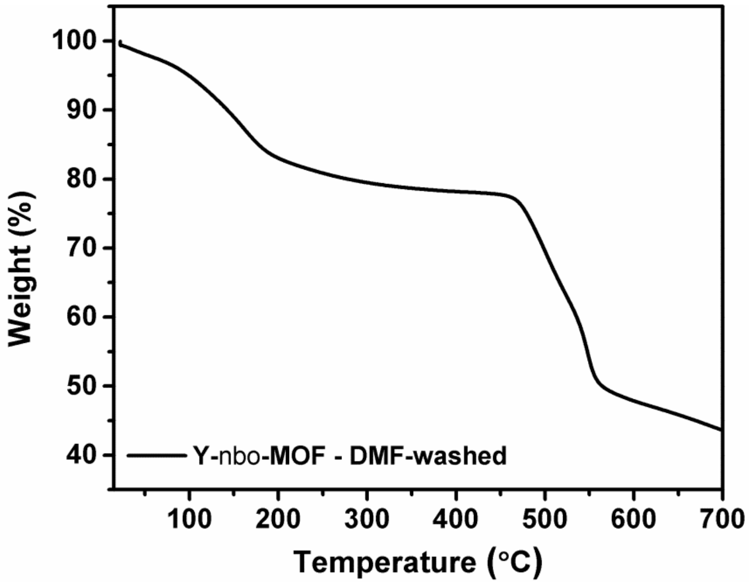

Figure 4.21 TGA plots demonstrating the high thermal stability of Y-**nbo**-MOF up to 400 °C.

4.4.3. Summary and conclusions

In summary, through the addition of a fluorinated modulator to the reaction between $Y(NO_3)_3$ and PDDB, we were able to synthesize Y-**hxl**-MOF, a highly-stable porous 2-P MOF that is based on the novel highly-connected RE octadecanuclear cluster. This MOF exhibited low to moderate gas uptake capacity, possibly a consequence of the presence of the large RE-MBBs. With similar reaction conditions and excluding the modulator, the formation of Y-**nbo**-MOF, a 3-P MOF that is based on the known RE dinuclear paddlewheel and dimeric clusters, was observed. Even though this framework has spindle-like large cages, the sorption assays showed that it was nonporous to gases like N_2, Ar, H_2 and CO_2 because of its limited window aperture or the presence of entrapped row materials.

4.5. Experimental section part II: Mixed-ligands approach to constructing a new 3-P MOF featuring an unprecedented octanuclear RE-MBB and the rare tfz topology

4.5.1. Introduction

In this section, as a continuation of the work described in Part I of this chapter, the ability to isolate new structures and network topologies by subtly changing the geometry of the ligand was utilized. Consequently, the length-to-width ratio of PDDB was adjusted to produce PTPDC (Figure 4.22).

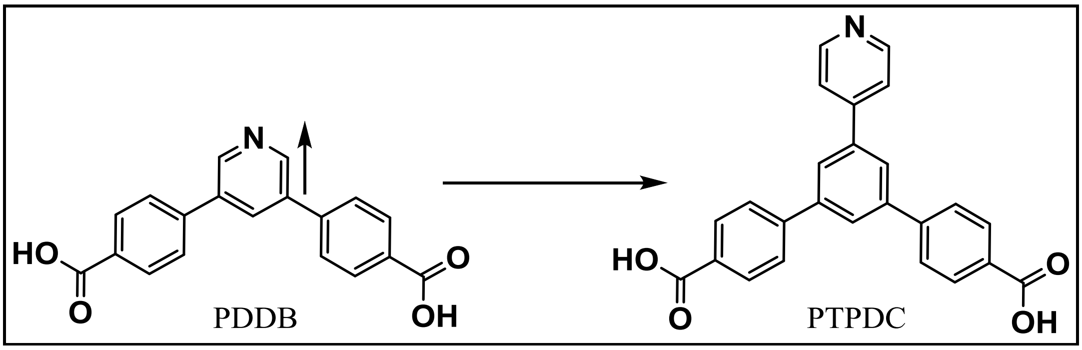

Figure 4.22 A scheme portraying the relationship between PDDB and PTPDC (indicated by an arrow).

Making use of reaction conditions similar to that of Y-**hxl**-MOF while substituting PDDB with PTPDC was anticipated to aid nitrogen coordination to the RE octadecanuclear clusters of the 2-P MOF and assist the formation of a 3-P framework based on covalent bonding rather than supramolecular chemistry. This idea can be understood by reviewing Figure 4.4, which shows how nitrogen donor moieties of PDDB in Y-**hxl**-MOF point toward the clusters, though the length of the ligand and steric hindrance could be restricting their coordination.

Furthermore, ligand expansion can assist forming new MOFs with interesting properties and help compare the behavior of PTPDC (Figure 4.23 a), containing a nitrogen donor moiety, with that of BTB (Figure 4.23 b), used to prepare **gea**-MOF (Chapter 1).[6]

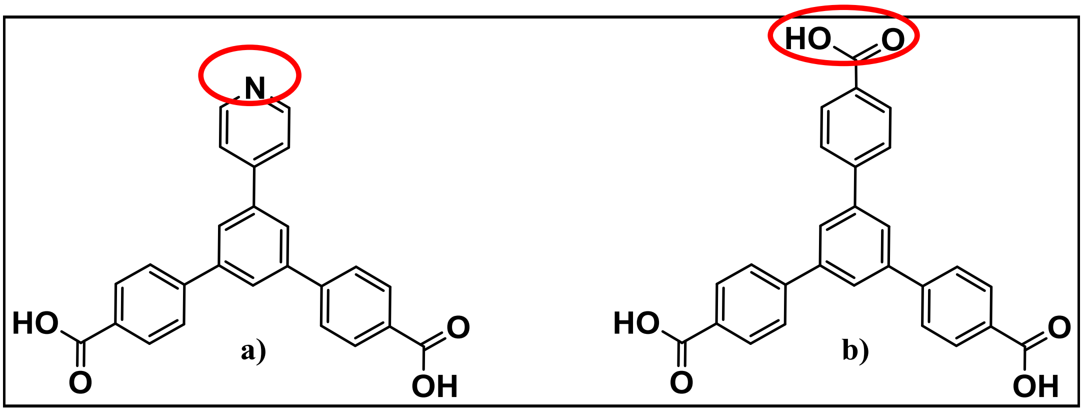

Figure 4.23 The structure of (a) PTPDC compared to (b) the tricarboxylate ligand used to construct **gea**-MOF.

Unfortunately, many trials to identify the reaction conditions required constructing a 3-P MOF related to Y-**hex**-MOF were unsuccessful. In addition, many of these trials led to the formation of Y-**tfz**-MOF-1.

Y-**tfz**-MOF-1 was a new pillared 3-P MOF founded upon a novel octanuclear RE-MBB, but it forced facing a number of challenges in both SC and synchrotron data collection. Therefore, the mixed-ligands approach[8] was employed, and PTPDC and PDDB were mixed in a ratio of 2:1 in the presence of 2-FBA to form the isoreticular Y-**tfz**-MOF-2. In this structure, strictly pillaring PTPDC in Y-**tfz**-MOF-1 was replaced with its shorter counterpart (PDDB), facilitating a reduction in structure distortion. Both structures were synthesized and fully characterized, and the magnetic properties of the Dy and Tb analogues of Y-**tfz**-MOF-2 were evaluated.

4.5.2. Synthesis and characterization

4.5.2.1. Synthesis of Y-tfz-MOF-1

In a 20-mL scintillation vial, a solution containing $Y(NO_3)_3.6H_2O$ (14.6 mg, 0.038 mmol), PTPDC (5 mg, 0.013 mmol), 2 mL DMF, 0.5 mL water and 0.1 mL 4 M 2-FBA was prepared and heated to 105 °C for 3 days. In this reaction, the ratio between the RE metal salt and ligand was equal to 3:1 and that of 2-FBA to the RE metal salt was equal to 10:1. Sheet-like crystals of Y-**tfz**-MOF-1 were collected and purified by repeated washing with DMF.

4.5.2.2. Activation of Y-tfz-MOF-1

A 40-mg sample of the as-synthesized MOF was washed with DMF 3-5 times over a period of 24 h. The sample was then subjected to solvent exchange by adding approximately 20 mL of CH_3OH and refreshing it 3-5 times daily for 7 days. Before gas sorption experiments, the sample was placed into a 6 mm large bulb glass sorption cell and dried carefully with flowing N_2 after removing the excess surface solvent with a syringe. Next, the sample was placed under a dynamic vacuum and screened for optimum activation temperature at RT, 55, 85, 105 and 120 °C (increasing at a rate of 1 °C/min), held for 12 h at each temperature, cooled to RT and then backfilled with N_2 prior to the sorption experiments at each activation temperature.

A second activation method was also employed, which involved activation using a SC-CO_2 dryer.[16] In this method, roughly 50 mg of DMF-washed samples were first rinsed very briefly with CH_3OH to remove surface DMF and then transferred to the SC-CO_2 dryer chamber that was cooled to -7 °C followed by becoming pressurized through injecting CO_2. The sample was soaked in liquid CO_2 with frequent purging for two days to replace any solvent. The temperature and pressure were then raised above the CO_2 critical point, i.e., 31 °C and 74 bar, respectively, and the sample was kept in SC-CO_2 for 1 day. Bleeding was executed slowly over a period of approximately 6 h and the sample became completely dry. Before LP gas sorption experiments, the sample was transferred to a 6 mm large bulb sorption cell under a N_2 environment (in a glove box) and then subjected to dynamic vacuum. It was then screened for optimum activation temperature at RT, 55, 85 and 105 °C (increasing at a rate of 1 °C/min), held for 12 h at each temperature, cooled to RT then backfilled with N_2 prior to each sorption experiment series.

4.5.2.3. Synthesis of Y-tfz-MOF-2

In a 20-mL scintillation vial, a solution containing $Y(NO_3)_3.6H_2O$ (14.6 mg, 0.038 mmol), PTPDC (3.33 mg, 0.008 mmol), PDDB (1.28 mg, 0.004 mmol), 4 mL DMF, 0.75 mL water and 0.1 mL 4 M 2-FBA was prepared and heated to 105 °C for 3 days. Colorless sheet-like crystals of Y-**ftz**-MOF-2 were collected and purified by repeated washing with DMF. In Y-**ftz**-MOF-2 preparation, the ratio between RE metal salt to that of PTPDC was equal to 4.875:1, whereas the ratio between PTPDC and PDDB was equal to 2:1 and that of 2-FBA to RE metal salt was equal to 10:1.

4.5.2.4. Activation of Y-tfz-MOF-2

This was performed on a 20-mg DMF-washed sample using SC-CO_2 activation following the same procedure detailed in Section 4.5.2.2. Before the LP gas sorption experiments, the sample was transferred to a 6 mm large bulb sorption cell under a N_2 environment (in a glove box) and then subjected to dynamic vacuum at RT for 12 h.

4.5.2.5. **Synthesis of Tb-**tfz**-MOF-2**

In a 20-mL scintillation vial, a solution containing $Tb(NO_3)_3.5H_2O$ (16.53 mg, 0.038 mmol), PTPDC (3 mg, 0.008 mmol), PDDB (1.28 mg, 0.004 mmol), 4 mL DMF, 0.75 mL water and 0.1 mL 4 M 2-FBA was prepared and heated to 105 °C for 3 days. Diamond sheet-like crystals of Tb-**tfz**-MOF-2 were collected and purified by repeated washing with DMF.

4.5.2.6. **Synthesis of Dy-**tfz**-MOF-2**

In a 20-mL scintillation vial, a solution containing $Dy(NO_3)_3.5H_2O$ (16.67 mg, 0.038 mmol), PTPDC (3 mg, 0.008 mmol), PDDB (1.28 mg, 0.004 mmol), 4 mL DMF, 0.75 mL water and 0.1 mL 4 M 2-FBA was prepared and heated to 105 °C for 3 days. Diamond sheet-like crystals of Dy-**tfz**-MOF-2 were collected and purified by continual washing with DMF.

4.5.3. Results and discussion

4.5.3.1. **Y-**tfz**-MOF-1**

In the presence of 2-FBA as a modulator, a solvothermal reaction between $Y(NO_3)_3$, PTPDC (Figure 4.24 a) in DMF and water yielded transparent sheet-like crystals of Y-**tfz**-MOF-1. The weak crystal diffraction and synchrotron experimental results, along with substandard SCXRD data collected from different samples, were insufficient to completely solve the structure, but were adequate to demonstrate that it was a new pillared MOF based on a novel RE octanuclear cluster (Figure 4.24 b). These studies revealed that this framework crystallizes in the monoclinic $P2_1/c$ space group with cell parameters of $a = 44.45$, $b = 32.62$, $c = 19.83$ and $\alpha = \beta = \gamma = 90°$.

In this structure, the ligand underwent two types of connectivity modes - the first is through both the carboxylate groups and nitrogen donor moieties (Figure 4.24 c), forming 2-P layers (Figure 4.24 d), while the second was via the carboxylate moieties exclusively (Figure 4.24 e), the result being pillaring of the 2-P layers into 3-P MOF with one-dimensional (1-D) channels of which the free nitrogen donor pointed towards. In addition to the presence of solvent molecules, these expanded ligands pointing into the channels formed high electron densities and were heavily disordered, making it difficult to completely solve the structure.

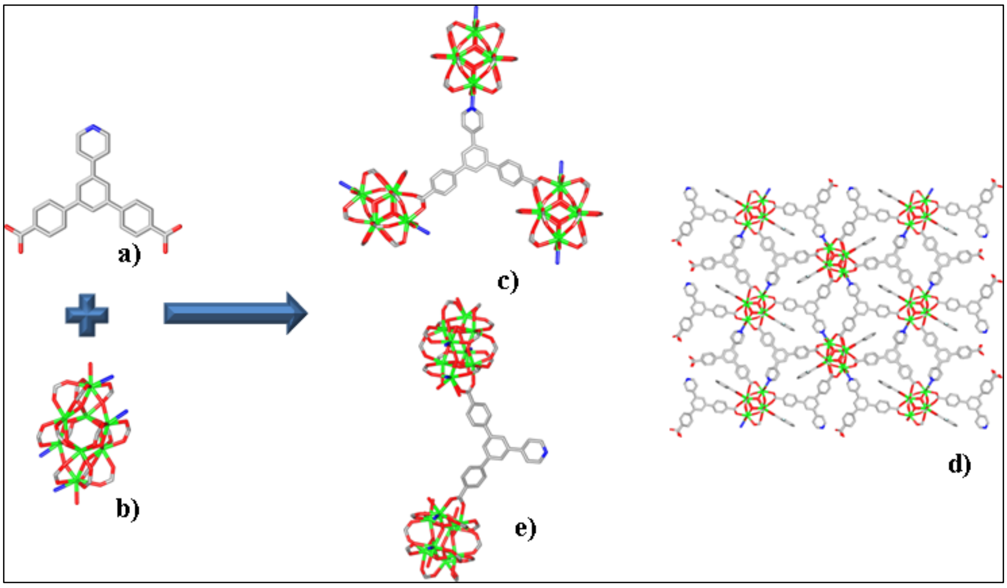

Figure 4.24 (a) PTPDC, (b) the novel RE octanuclear cluster, (c and e) the coordination modes of PTPDC and (d) the crystal structure of Y-**tfz**-MOF-1 showing one 2-P layer. C = gray, O = red, N = blue, Y = green; H atoms are omitted for clarity.

Even though the crystal structure was not wholly solved, various characterization tests were performed. Therefore, PXRD data on the as-synthesized bulk crystalline materials were collected and compared to that calculated from the available SC structure (Figure 4.25). Furthermore, the stability tests demonstrated that Y-**tfz**-MOF-

1 was not stable in $CHCl_3$; in addition, a reduction in crystallinity occurred as evident by the disappearance, reduction of intensity and widening of certain peaks in the PXRD patterns when tested after SC-CO_2 activation in CH_3OH, C_2H_5OH, C_3H_6O and CH_3CN (Figure 4.25). Moreover, the compound exhibited similar behavior when tested in air (Figure 4.26) and had a high degree of sensitivity to water.

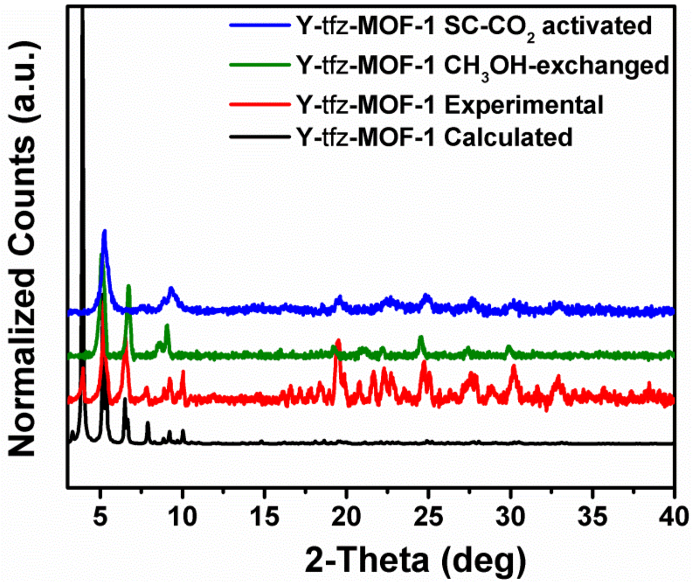

Figure 4.25 PXRD patterns of Y-**tfz**-MOF-1; calculated, experimental, CH_3OH-exchanged and SC-CO_2-activated samples.

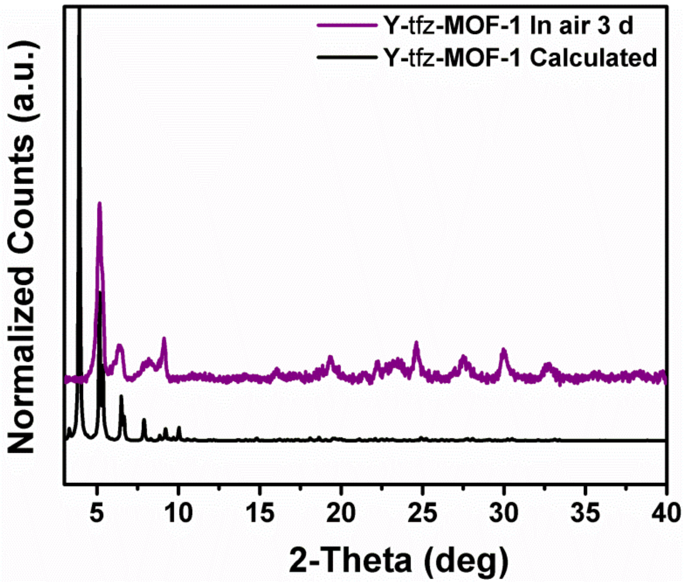

Figure 4.26 Calculated and following air exposure PXRD patterns of Y-**tfz**-MOF-1.

To investigate the thermal stability of Y-**tfz**-MOF-1, TGA was performed on DMF-washed and CH_3OH-exchanged samples under a N_2 atmosphere. The tests were carried out between RT and 700 °C at an increasing heating rate of 20 °C/min in high resolution dynamic mode. The TGA plots of the compound indicated its thermal stability up to 450 °C (Figure 4.27).

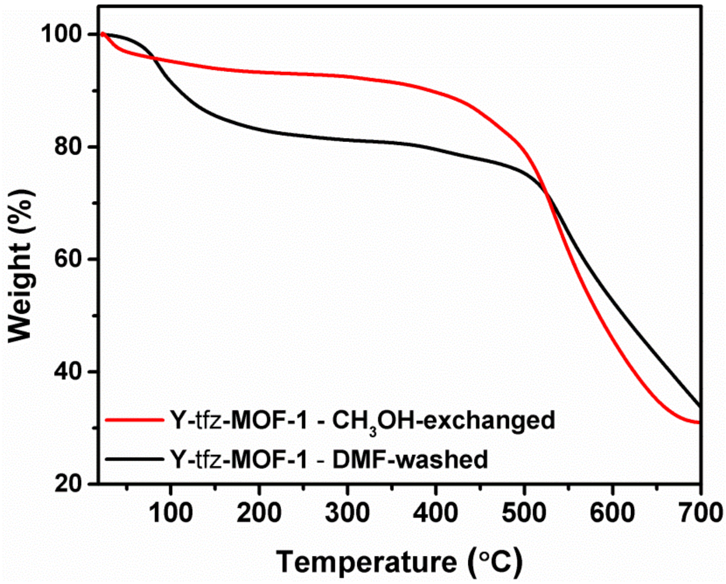

Figure 4.27 TGA plots of DMF-washed and CH_3OH-exchanged Y-**tfz**-MOF-1 samples suggested its thermal stability up to 450 °C.

Additionally, to determine the actual porosity and gas uptake capacity of the framework, gas sorption experiments were conducted. They used both CH_3OH-exchanged and SC-CO_2-activated samples. In both cases, N_2 uptake was very poor with SA_{BET} values being only 3.74 and 88.9 m^2/g and experimental PV only 0.03 and 0.07 cm^3/g for CH_3OH-exchanged and SC-CO_2-activated samples, respectively (Figure 4.28).

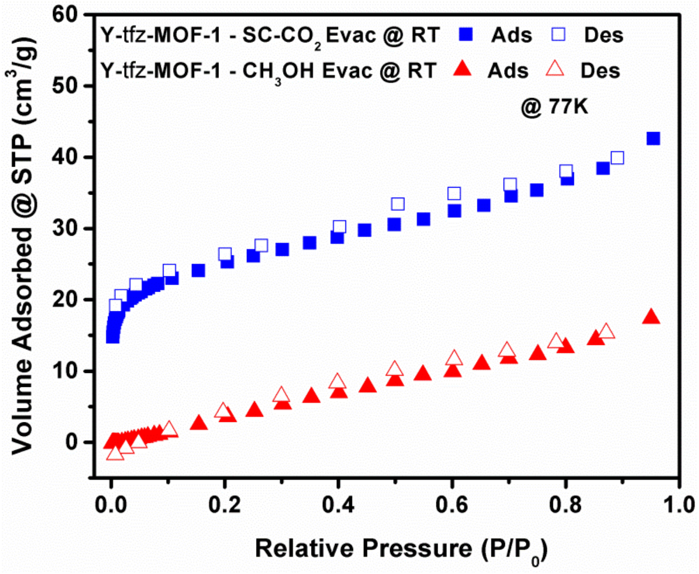

Figure 4.28 Comparing N_2 sorption isotherms of Y-**tfz**-MOF-1 at 77 K utilizing two activation methods.

The reduction in porosity of Y-**tfz**-MOF-1 owes to the partial collapse of the extended framework under vacuum and upon solvent removal.[17] This can be credited to the monodentate mode of nitrogen coordination to metal clusters with a relatively flexible geometry, leading to the formation of a less robust framework (Figure 4.29).[17b, 18]

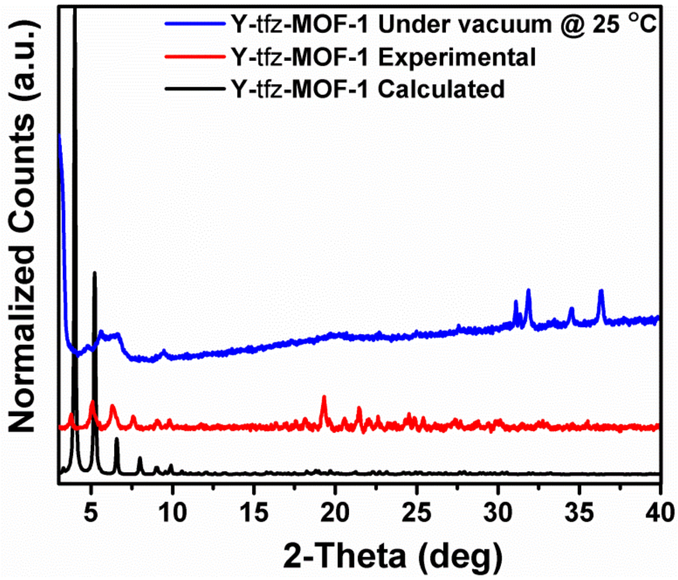

Figure 4.29 PXRD of DMF-washed Y-**tfz**-MOF-1 under vacuum at 25 °C compared to the calculated pattern from the SC structure and the experimental one at 25 °C with no vacuum applied.

At this point, the mixed-ligands approach was employed where PTPDC was mixed with its shorter version, PDDB. The two ligands were mixed in a 2:1 ratio that would allow PDDB to act as the pillaring ligand in order to increase the stability of the structure, reduce disorder in the channels and permit better quality SC data. This mixed-ligands approach resulted in the formation of Y-**tfz**-MOF-2.

4.5.3.2. **Y-**tfz**-MOF-2**

A solvothermal reaction between $Y(NO_3)_3$ and a mixture of PTPDC (Figure 4.30 a) and PDDB (Figure 4.30 b) in a ratio of 2:1 in DMF and water in the presence of 2-FBA was placed at 105 °C to yield colorless sheet-like crystals of Y-**tfz**-MOF-2.

The framework formulated, confirmed by SCXRD studies, was $|(DMA)_2|[Y_8(\mu_3\text{-}OH)_8(2\text{-}FBA)_2(DMF)_4(PTPDC)_4(PDDB)_2].(solv)_x$ and the as-synthesized sample was purified through repeated washing with fresh DMF.

Y-**tfz**-MOF-2 crystallizes in the primitive orthorhombic *Pnma* space group that has cell parameters of a = 19.697, b = 44.173, c = 33.656, $\alpha = \beta = \gamma = 90°$ and V = 29283.4 Å^3. In the crystal structure of Y-**tfz**-MOF-2, there are three crystallographically-independent yttrium ions, Y1 having an 8-c environment and Y2 and Y3 both possessing different 7-c environments. Y1 was surrounded by four oxygen atoms from four distinct carboxylates of two PTPDC and two PDDB. In addition, Y1 was also coordinated to one nitrogen atom from PTPDC, one DMF and two μ_3-OH groups. Y2 was surrounded by three oxygen atoms from three distinct ligands (two from PTPDC and one from PDDB), one 2-FBA and three μ_3-OH groups. Finally, Y3 was coordinated to two oxygen atoms from two distinct PTPDC, one nitrogen atom from a third PTPDC, one DMF molecule and three μ_3-OH group. These yttrium ions (two Y1-type, four Y2-type and two Y3-type) are bridged together through μ_3-OH groups and carboxylate moieties to generate an unprecedented octanuclear yttrium cluster (Figure 4.30 c). Each octanuclear cluster is coordinated to two 2-FBA and four DMF molecules and capped with 16 ligands, among which, twelve (four PDDB and eight PTPDC) were coordinated through their carboxylate groups and four PTPDC were coordinated through their nitrogen atoms.

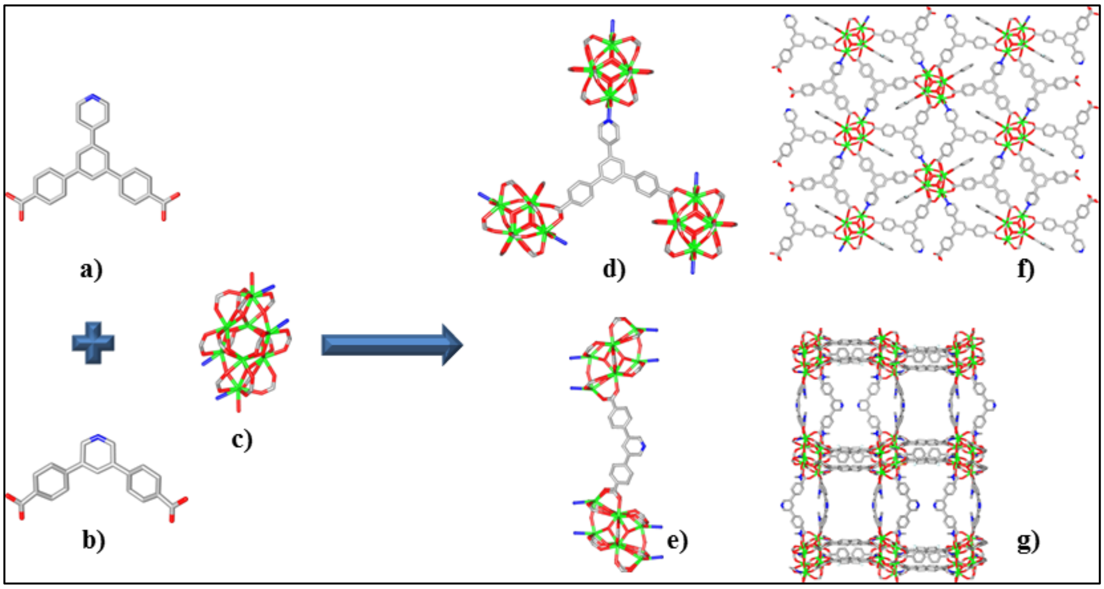

Figure 4.30 (a) PTPDC, (b) PDDB, (c) the novel RE octanuclear cluster, (d) PTPDC connectivity, (e) PDDB connectivity, (f) one 2-P **kgd** layer and (g) the pillared Y-**tfz**-MOF-2 crystal structure showing the entrapped 1-D channels. C = gray, O = red, N = blue, Y = green; Hydrogen atoms and solvent molecules are omitted for clarity.

In this structure, 2-P **kgd** layers (Figure 4.30 f) were formed by the coordination of PTPDC to different clusters through all of its functional groups (Figure 4.30 d). However, PDDB acts as the pillars of these layers through its carboxylate groups, with no nitrogen involvement in coordination, (Figure 4.30 e) to form a 3-P MOF that entraps large 1-D channels along the a-axes with an aperture size of (12 x 8.7 Å) (Figure 4.30 g). The corresponding solvent-accessible free volume of Y-**tfz**-MOF-2 was estimated from the X-ray crystal structure using MS software to be 65%.

The theoretical ratio between PTPDC:PDDB calculated from the SC structure was found to be 3:1. This ratio was confirmed experimentally on multiple Y-**tfz**-MOF-2 samples (from different batches) where approximately 20 mg of oven-dried samples (65 °C) were digested using deuterated HCl and studied with ^{1}H NMR. The experimental ratio between the two ligands was consistently seen to be 2.8:1, agreeing with the theoretical value.

Y-**tfz**-MOF-2 can be simplified and analyzed topologically as a (3,8)-connected structure with **tfz**-d topology. This topology is very rare among MOFs (RCSR database)[19] and it is based on the pillaring of the 2-P hexagonal **kgd** net, which is a (3,6)-connected structure that contains four-membered rings (Figure 4.31).[20]

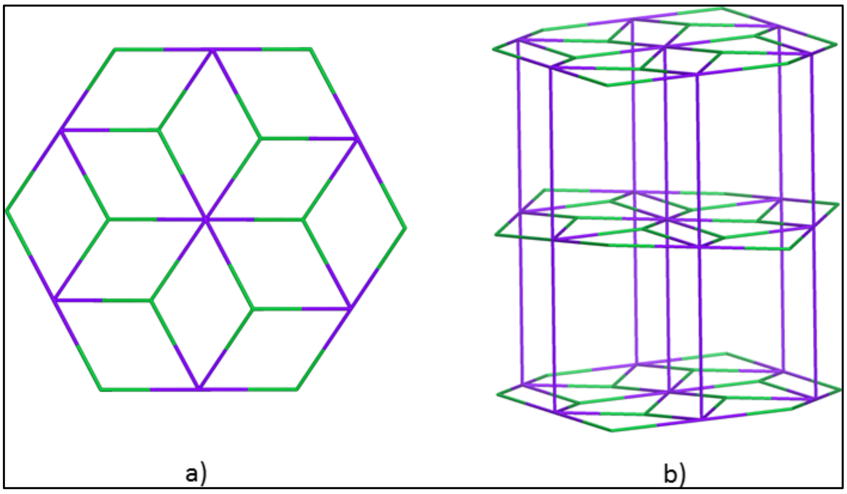

Figure 4.31 (a) Schematic representation of one 2-P hexagonal **kgd** net and (b) the pillaring of these layers to produce Y-**tfz**-MOF-2 with **tfz** topology.

The phase purity of the bulk crystalline material of Y-**tfz**-MOF-2 was confirmed by the similarities between the PXRD patterns of the calculated and DMF-washed samples (Figure 4.32). In addition, Y-**tfz**-MOF-2 did not exhibit stability in common organic solvents (e.g., CH_3OH, C_2H_5OH, CH_3CN and C_3H_6O), nor water or air. Furthermore, the PXRD pattern of the bulk crystalline material of Y-**tfz**-MOF-1 was compared to Y-**tfz**-MOF-2 via PXRD and matched, suggesting the two structures were isoreticular (Figure 4.33).

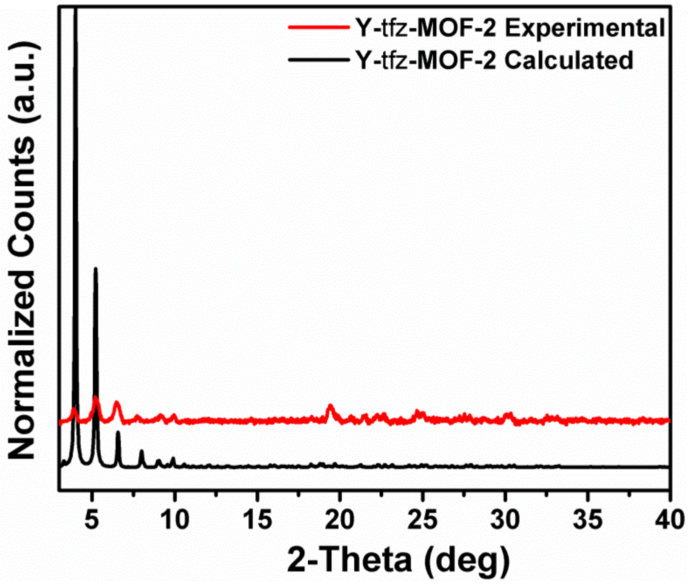

Figure 4.32 Experimental and calculated PXRD patterns of Y-**tfz**-MOF-2 indicating the purity of the as-synthesized samples.

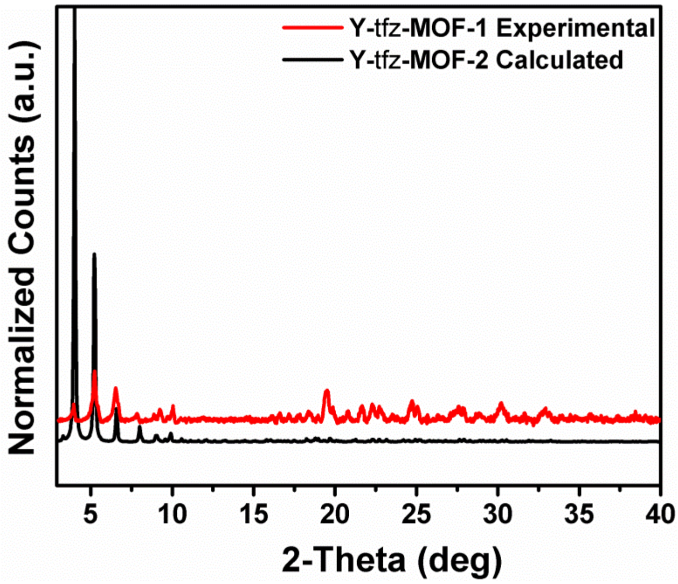

Figure 4.33 Experimental PXRD patterns of Y-**tfz**-MOF-1 compared to the calculated Y-**tfz**-MOF-2, indicating that the two structures are isoreticular.

In order to investigate the thermal stability of Y-**tfz**-MOF-2, TGA was performed on DMF-washed samples under a N_2 atmosphere. The tests were carried out between RT and 700 °C at an increasing heating rate of 20 °C/min in high resolution dynamic mode. The TGA plots of this compound indicated its thermal stability for up to 450 °C (Figure 4.34).

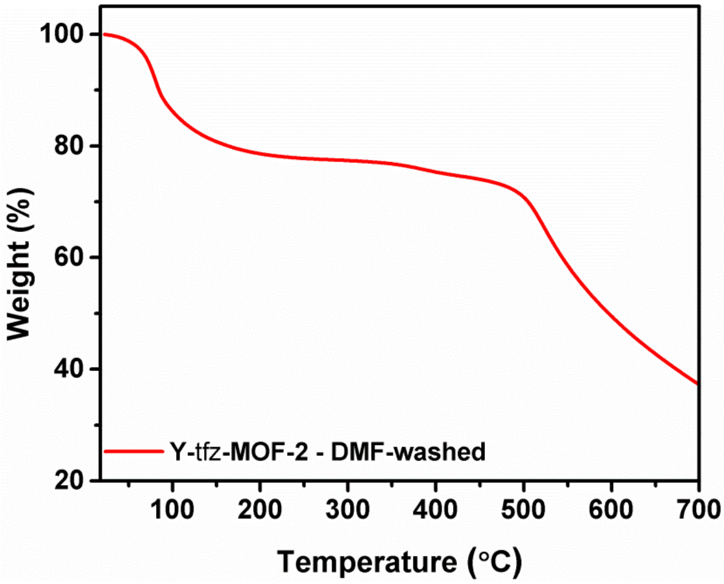

Figure 4.34 TGA plot of DMF-washed Y-**tfz**-MOF-2 indicating its thermal stability up to 450 °C.

In comparison to Y-**tfz**-MOF-1, N_2 sorption isotherms at 77 K of SC-CO_2-activated Y-**tfz**-MOF-2 (Figure 4.35) showed a SA_{BET} of 323.45 m^2/g and an increase in the experimental PV to 0.28 cm^3/g. These values are dramatically lower than the theoretical ones estimated from the crystallographic data (PV of 0.88 cm^3/g). This could be because of the partial collapse of the extended framework upon guest removal under vacuum (Figure 4.36), rendering low gas uptake capacity toward N_2.[17b, 18]

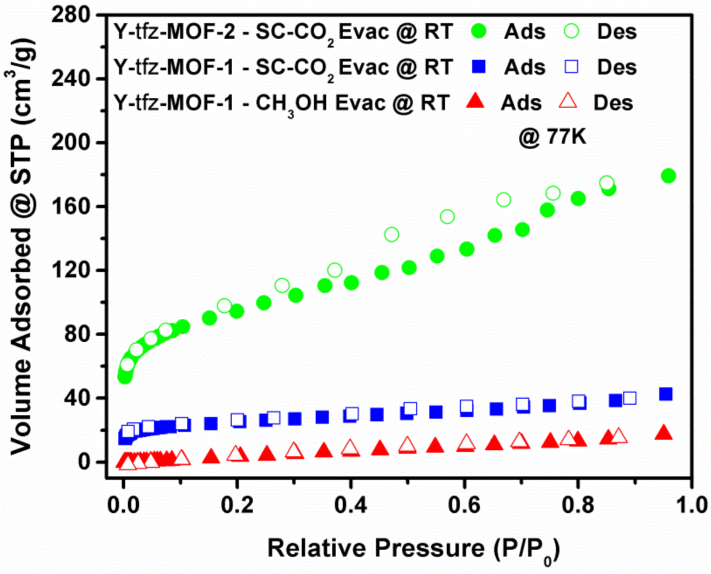

Figure 4.35 N_2 sorption isotherms of Y-**tfz**-MOF-1 utilizing different activation methods compared to that of Y-**tfz**-MOF-2 activated with SC-CO_2.

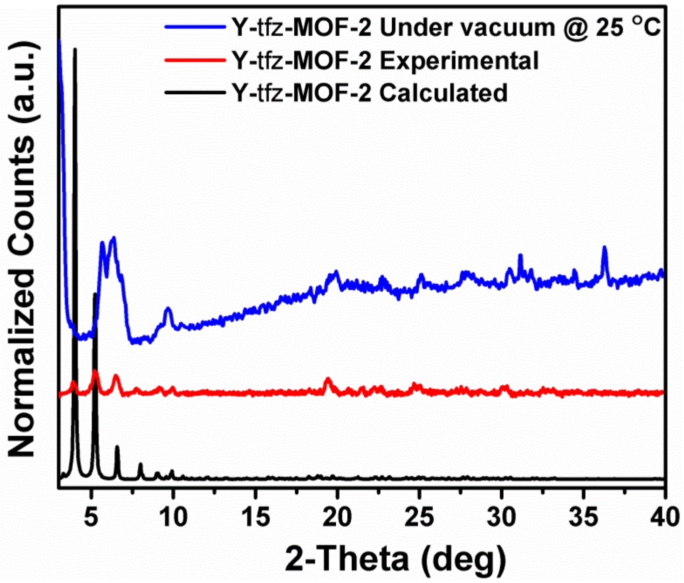

Figure 4.36 PXRD of DMF-washed Y-**tfz**-MOF-2 under vacuum at 25 °C compared to the calculated and experimental patterns at 25 °C with no vacuum applied.

Considering the high-nuclearity of the RE cluster of Y-**tfz**-MOF-2, its corresponding Tb (Tb-**tfz**-MOF-2) and Dy (Dy-**tfz**-MOF-2) analogues were also prepared to examine their magnetic properties.[21]

The phase purity of the prepared compounds was confirmed by the similarities between calculated Y-**tfz**-MOF-2 PXRD patterns and those of the experimental Tb-**tfz**-MOF-2 and Dy-**tfz**-MOF-2 samples (Figure 4.37).

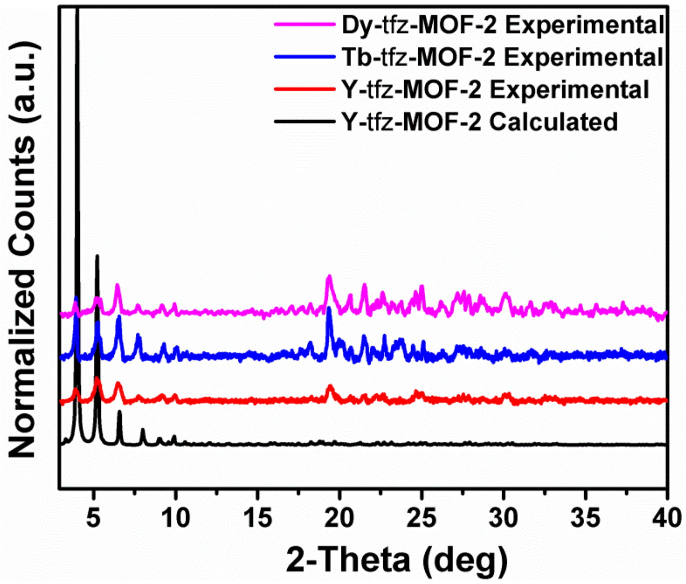

Figure 4.37 Phase purity of Tb-**tfz**-MOF-2 and Dy-**tfz**-MOF-2 indicated by the similarities between their experimental PXRD patterns and those calculated and experimental with Y-**tfz**-MOF-2.

The magnetic properties of these isostructures were measured with a superconducting quantum interference device. Therefore, to obtain the intrinsic magnetic properties of the compounds (see Chapter 2), the low-field magnetization **(**χ**)** was measured as a function of temperature (T) in the range of 1.8-300 K under a magnetic field of 100 Oe with the ZFC and FC processes (Figure 4.38 and Figure 4.39 for Tb-**tfz**-MOF-2 and Dy-**tfz**-MOF-2, respectively). For both compounds, the ZFC and FC curves overlapped perfectly within the entire temperature range, suggesting paramagnetic property in nature.

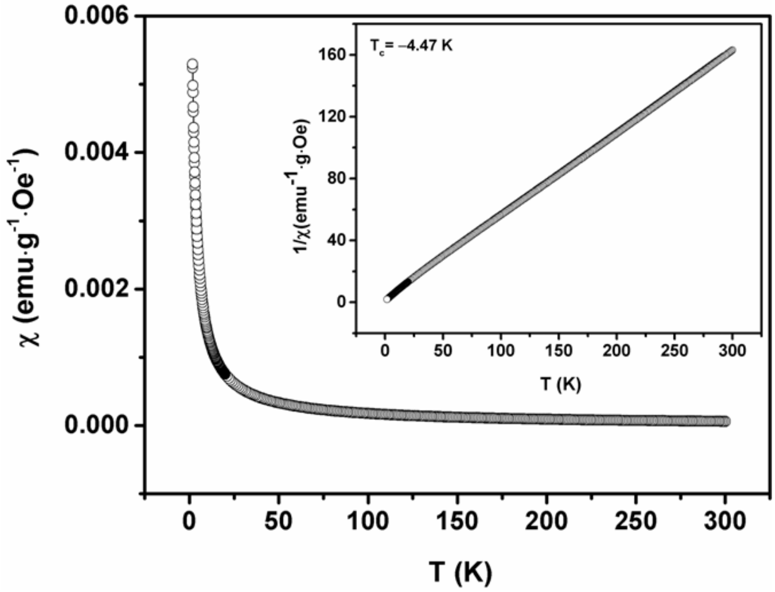

Figure 4.38 Temperature-dependent susceptibility of Tb-**tfz**-MOF-2 with applied field *H* = 100 Oe. Inset provides the $\frac{1}{\chi} - T$ curve.

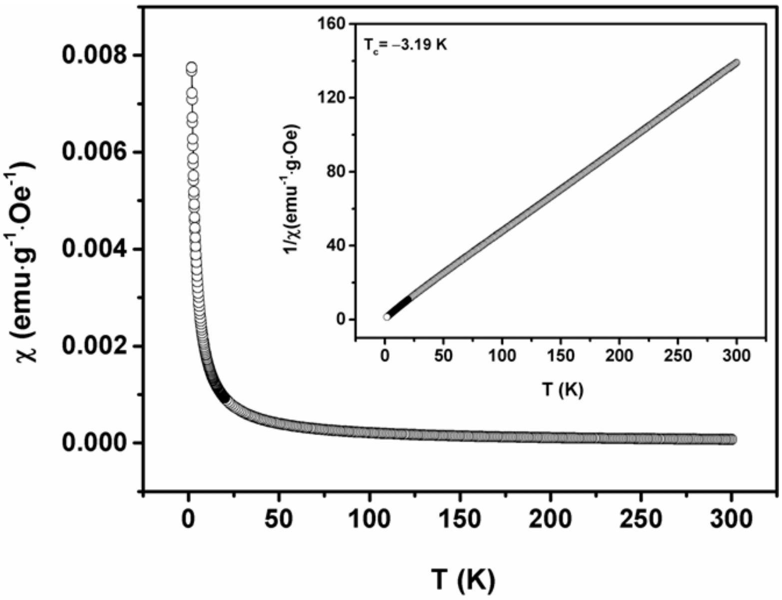

Figure 4.39 Temperature-dependent susceptibility of Dy-**tfz**-MOF-2 with applied field $H = 100$ Oe. Inset provides the $\frac{1}{\chi} - \boldsymbol{T}$ curve.

Close examination reveals that these curves can be perfectly described by the Curie-Weiss law of magnetic susceptibility of the material with a small, negative intercept, T_c, that is equal to – 4.47 and – 3.19 K for the Tb and Dy isostructures, respectively (Figure 4.38 and Figure 4.39 insets). This indicates that there exists a weak, antiferromagnetic-like interaction among the lanthanide clusters.

The field-dependent magnetization was measured in the temperature range of 1.8-30 K. Figure 4.40 and Figure 4.41 insets, for Tb and Dy isostructures, respectively, provide the magnetization (*M*) as a function of applied field (H = 0 to $7{*}10^4$ Oe) measured at varying temperatures. The *M*–*H* curves exhibit superparamagnetism at low temperatures.

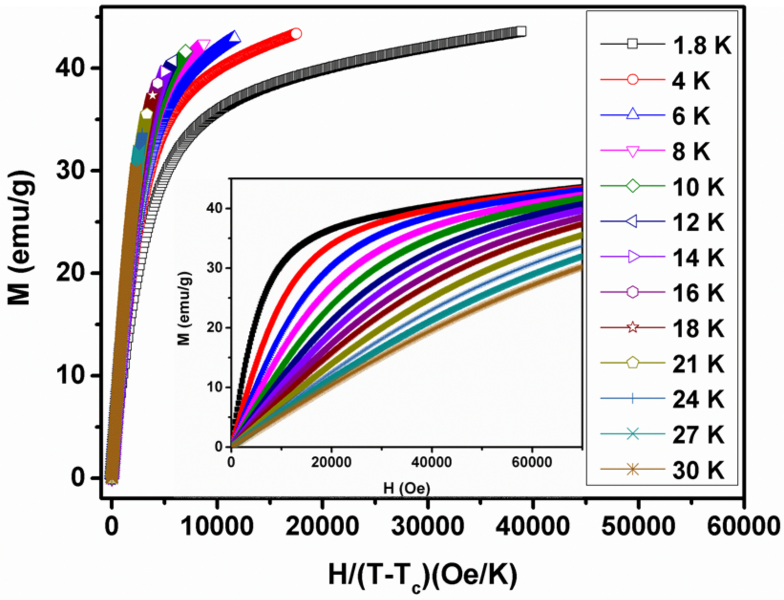

Figure 4.40 Tb-**tfz**-MOF-2 magnetization M versus $\boldsymbol{H/(T-T_c)}$ at temperature range from 1.8-30 K. Inset gives the field-dependent magnetization measured from 1.8-30 K.

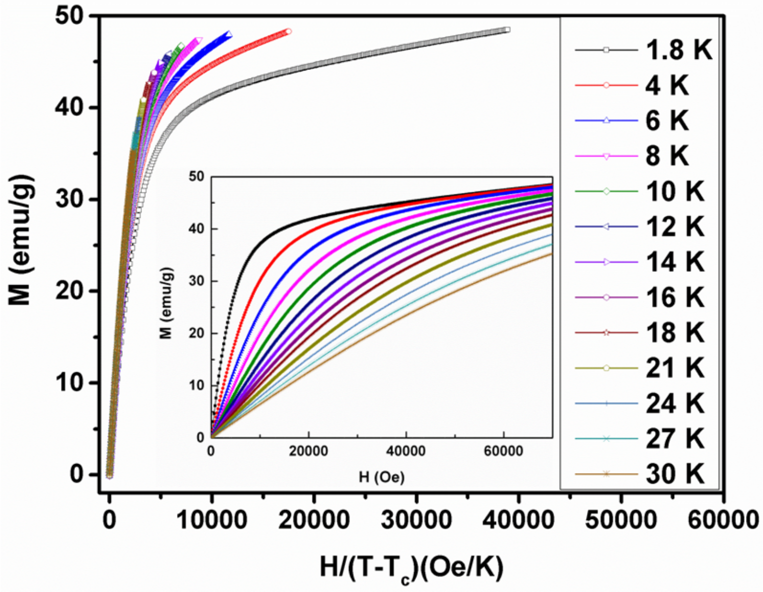

Figure 4.41 Dy-**tfz**-MOF-2 magnetization, M, versus $\boldsymbol{H/(T-T_c)}$ at a temperature range of 1.8-30 K. Inset provides the field-dependent magnetization measured from 1.8-30 K.

If all the lanthanide clusters in these materials have the same energy barrier and magnetic moment, the M–H curves may be described by the Langevin function given that the field, H, is adequately low and T is suitably high.

Figure 4.40 and Figure 4.41 details the relationship, $M(H,T) - H/(T - T_c)$, for the temperature range of 1.8-30 K. All the curves overlap with each other at lower fields, validating the uniformity of the energy barrier and magnetic moments in the lanthanide clusters of both compounds. In general, additional investigation is necessary to study the possible application of these isostructures as cryogenic magnetic refrigerants with a magnetocaloric effect.

4.5.4. Summary and conclusions

In this series of experiments, by replacing one of the carboxylate groups in BTB, the tricarboxylate ligand that was employed to construct **gea**-MOF-1, with a nitrogen atom from the pyridine moiety, we were able to build a new framework based on a novel RE polynuclear cluster.

In summary, through the addition of a fluorinated modulator to the reaction between $Y(NO_3)_3$ and PTPDC, we were able to synthesize a 3-P MOF, Y-**tfz**-MOF-1, based on a novel octanuclear RE-MBB and possessing the very rare **tfz** topology. Notably, this framework was not stable upon guest solvent molecules removal. Therefore, in an effort to increase the stability of the produced MOF, a mixed-ligands approach was utilized where PTPDC and its shorter version, PDDB, were mixed in the presence of the fluorinated modulator to produce, as expected, the isoreticular structure, Y-**tfz**-MOF-2. This structure demonstrated little improvement in overall framework stability; consequently, the Dy and Tb analogues of this RE polynuclear-based structure were synthesized and assessed for their magnetic properties.

4.6. Experimental section part III: A new 3-P MOF featuring an unprecedented RE double tetranuclear (octanuclear) cluster and rare tfz topology

4.6.1. Introduction

Herein, a continuation of the work presented in Experimental Sections Part I and II of this chapter is covered. This was a part of our group's ongoing exploration of various metals and functional ligands with the aim of discovering new modular RE-MBBs that are polynuclear and highly connected.

Therefore, as previously mentioned, the fact that it is possible to isolate new frameworks and network topologies by subtly modifying the geometry of the ligand was utilized. As a consequence, the length-to-width ratio of PTPDC was adjusted to produce PIP (Figure 4.42).

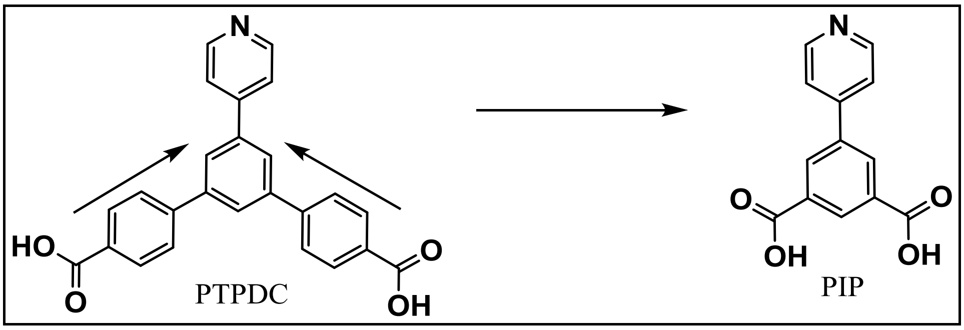

Figure 4.42 A schematic representation of the relationship between PTPDC from the previous section of this chapter and PIP introduced here (indicated by arrows).

This modification of the organic building block facilitated forming new MOFs with interesting properties and aided the comparison of the behavior of PIP (Figure 4.43 a) that contains a nitrogen donor moiety with that of biphenyl-3,4',5-tricarboxylic acid (Figure 4.43 b) used to construct **pek**-MOF (Chapter 1).[2c]

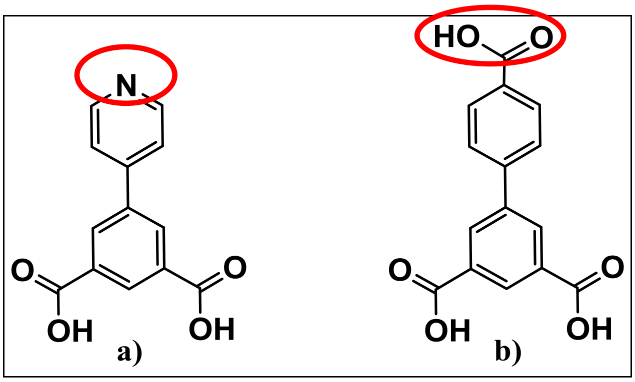

Figure 4.43 The structure of (a) PIP compared to that of (b) the tricarboxylate ligand used to construct **pek**-MOF.

Subsequently, Y-**tfz**-MOF-3, a new 3-P framework based on a novel RE polynuclear cluster, one that can be viewed either as one octanuclear cluster or as double tetranuclear clusters that are connected by formate, was constructed.

Under similar reaction conditions, though not including 2-FBA, a 3-P MOF based on the infinite rod-shaped RE SBUs (Y-**swk**-MOF-2) was built. Furthermore, another related MOF, Y-**swk**-MOF-1, was also prepared by replacing PIP with PMIP (Figure 4.44).

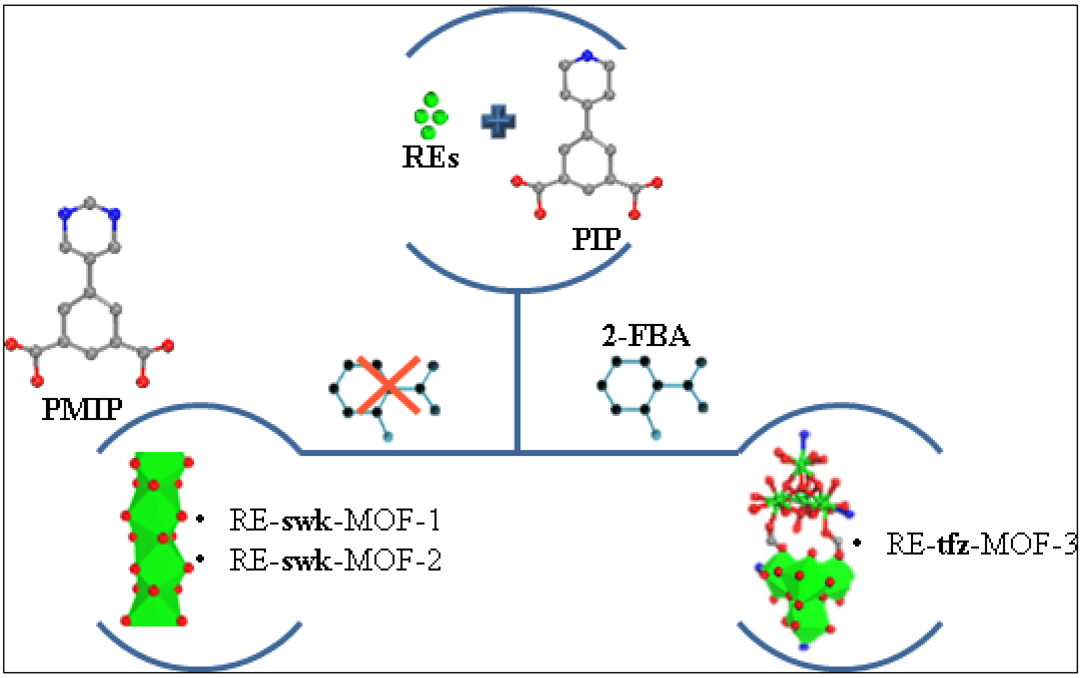

Figure 4.44 Summary of the work presented in this portion of the chapter describing the types of RE-MBBs constructed when using PIP with/without 2-FBA. PMIP was also employed to construct the isoreticular MOF based on the rod-shaped RE SBUs.

All prepared frameworks were synthesized and fully characterized, and the magnetic properties of the Dy and Tb analogues of Y-**tfz**-MOF-3 were evaluated.

4.6.2. Synthesis and characterization

4.6.2.1. Synthesis of Y-tfz-MOF-3

In a 20-mL scintillation vial, a solution containing $Y(NO_3)_3.6H_2O$ (22.98 mg, 0.06 mmol), PIP (5 mg, 0.02 mmol), DMF (2 mL), 1.5 mL water and 0.1 mL 4 M 2-FBA was prepared and heated to 105 °C for 3.5 days. Clear sheet-like crystals of Y-**tfz**-MOF-3 were collected and purified by repeated washing with DMF. The as-synthesized crystals were determined to be insoluble in water and common organic solvents. In the preparation of Y-**tfz**-MOF-3, the ratio of metal-to-ligand was equal to 3:1 and that of 2-FBA to the metal was equal to 6.7:1.

4.6.2.2. Synthesis of Tb-tfz-MOF-3

In a 20-mL scintillation vial, a solution containing $Tb(NO_3)_3.5H_2O$ (26.1 mg, 0.06 mmol), PIP (5 mg, 0.02 mmol), DMF (2 mL), 1.2 mL water and 0.1 mL 4 M 2-FBA was prepared and heated to 105 °C for 1 day. Clusters of crystals of Tb-**tfz**-MOF-3 were collected and purified by repeated washing with DMF. The as-synthesized crystals were determined to be insoluble in water and common organic solvents.

4.6.2.3. Synthesis of Dy-tfz-MOF-3

In a 20-mL scintillation vial, a solution containing $Dy(NO_3)_3.5H_2O$ (26.32 mg, 0.06 mmol), PIP (5 mg, 0.02 mmol), DMF (2 mL), 1.2 mL water and 0.1 mL 4 M 2-FBA was prepared and heated to 105 °C for 1 day. Clusters of crystals of Dy-**tfz**-MOF-3 were collected and purified by repeated washing with DMF. The as-synthesized crystals were determined to be insoluble in water and common organic solvents.

4.6.2.4. Activation of Y-tfz-MOF-3

An approximately 50-mg sample of the as-synthesized Y-**tfz**-MOF-3 was washed with DMF several times over a period of 24 h. The sample was then subjected to solvent exchange by adding roughly 20 mL of CH_3CN and refreshing it for 3-5 times daily for 7 days. Before the gas sorption experiments, the sample was placed into a 6 mm large bulb glass sorption cell and dried carefully with flowing N_2 after removing the excess surface solvent with a syringe. The sample was then placed under dynamic vacuum and screened for optimum activation temperature at RT, 55 and 85 °C (increasing at a rate of 1 °C/min), held for 12 h at each temperature, cooled to RT and then backfilled with N_2 prior to separate sorption experiments at individual heating temperatures. Other activation trials were performed with various organic solvents, such as C_2H_5OH, and followed the same activation procedure.

4.6.2.5. Synthesis of Y-swk-MOF-1

In a 20-mL scintillation vial, a solution containing $Y(NO_3)_3.6H_2O$ (15.32 mg, 0.04 mmol), PMIP (5 mg, 0.02 mmol), DMF (1.5 mL) and 0.03 mL 4.4 M HNO_3 in DMF was prepared and heated to 105 °C for 37 h to yield transparent spherical crystals of Y-**swk**-MOF-1. The as-synthesized crystals were collected and purified through repeated washing with DMF. These crystals were determined to be insoluble in water and common organic solvents. In Y-**swk**-MOF-1 preparation, the ratio of metal-to-ligand was 2:1 and no modulator was included.

4.6.2.6. Synthesis of Tb-swk-MOF-1

In a microwave tube, a solution containing $Tb(NO_3)_3.5H_2O$ (18.9 mg, 0.0435 mmol), PMIP (21.23 mg, 0.087 mmol), DMF (1 mL), 1.5 mL C_2H_5OH and 0.05 mL 4.4 M HNO_3 in DMF was prepared and heated to 115 °C for 37 h. The formed clear needle-like crystals of Tb-**swk**-MOF-1 were collected and purified by repeated washing with DMF. The as-synthesized crystals were determined to be insoluble in water and common organic solvents. In the preparation of Tb-**swk**-MOF-1, the ratio of metal-to-ligand was 1:2 and no modulator was used.

4.6.2.7. Activation of Y-swk-MOF-1 and Tb-swk-MOF-1

Approximately 50-mg samples of the as-synthesized compounds were washed with DMF a number of times over a period of 24 h. The samples were then subjected to solvent exchange by adding roughly 20 mL of CH_3CN and CH_3OH to the Y-**swk**-MOF-1 and Tb-**swk**-MOF-1 samples, respectively, and refreshing them several times daily for 6-7 days. Before gas sorption experiments, the samples were placed into 6 mm large bulb glass sorption cells and dried carefully with flowing N_2 after removing the excess surface solvent with a syringe. The samples were then placed under dynamic vacuum and heated to 55 and 105 °C for Y-**swk**-MOF-1 and Tb-**swk**-MOF-1 samples, respectively (increasing at a rate of 1 °C/min), held for 12 h, cooled to RT then backfilled with N_2 prior to sorption experiments. Additional activation methods were also implemented for Y-**swk**-MOF-1, like exchange with other solvents.

4.6.2.8. Synthesis of Y-swk-MOF-2

In a 20-mL scintillation vial, a solution containing $Y(NO_3)_3.6H_2O$ (22.98 mg, 0.06 mmol), PIP (5 mg, 0.02 mmol), DMF (2 mL), 1.25 mL water and 0.05 4.4 M HNO_3 in DMF was prepared and heated to 105 °C for 27 h. Clusters of microcrystals of Y-**swk**-MOF-2 were collected and purified by repeated washing with DMF. The as-synthesized crystals were determined to contain impurities, and various trials were not successful in obtaining pure phase.

4.6.2.9. Synthesis of Tb-swk-MOF-2

In a microwave tube, a solution containing $Tb(NO_3)_3.5H_2O$ (18.9 mg, 0.0435 mmol), PIP (21.16 mg, 0.087 mmol), 1 mL DMF, 1.5 mL C_2H_5OH and 0.05 mL 4.4 M HNO_3 in DMF was prepared and heated to 115 °C for 37 h. The formed transparent spherical crystals of Tb-**swk**-MOF-2 were collected and purified by repeated washing with DMF. The as-synthesized crystals were determined to be insoluble in water and common organic solvents. In the preparation of Tb-**swk**-MOF-2, the ratio of metal-to-ligand was 1:2 and no modulator was included.

4.6.2.10. Activation of Tb-swk-MOF-2

An approximately 50-mg sample of the as-synthesized Tb-**swk**-MOF-2 was washed with DMF several times over a period of 24 h. The sample was then subjected to solvent exchange by adding roughly 20 mL of CH_3OH and refreshing it 3-5 times daily for 6 days. Before the gas sorption experiments, the sample was placed into a 6 mm large bulb glass sorption cell and dried carefully with flowing N_2 after removing the excess surface solvent with a syringe. The sample was then placed under dynamic vacuum and screened for optimum activation temperature at RT and 85 °C (increasing at a rate of 1 °C/min), held for 12 h, cooled to RT then backfilled with N_2 prior to sorption experiments at individual heating temperatures. Other activation trials were performed with various organic solvents, such as CH_3CN, the same procedure described earlier was followed.

4.6.3. Results and discussion

4.6.3.1. Y-tfz-MOF-3

In the presence of the modulator, 2-FBA, a solvothermal reaction between $Y(NO_3)_3$, PIP in DMF and water yielded transparent sheet-like crystals of Y-**tfz**-MOF-3 that were formulated and validated by SCXRD, as $Y_4O_4(CO_2)$(2-FBA)$(H_2O)_7$(DMF)(DMA). Y-**tfz**-MOF-3 crystallizes in the primitive monoclinic

$P2_1/C$ space group with cell parameters of a = 11.45, b = 22 Å, c = 26 Å and $\alpha = \gamma = 90°$, $\beta = 112.7°$ and V= 6076.44 $Å^3$.

In the crystal structure of Y-**tfz**-MOF-3, there are four crystallographically-independent yttrium ions where each has an 8-c environment and are noted as Y1, Y2, Y3 and Y4. Among them, Y1 is surrounded by three oxygen atoms from three distinct carboxylates of PIP ligands, three μ_3-oxo groups, one nitrogen atom from PIP and one *in situ*-generated formate ligand. Y2 is surrounded by two oxygen atoms from two distinct carboxylates of PIP ligands, three μ_3-oxo groups, one formate ligand and one 2-FBA molecule, leaving the eighth coordination site occupied by a terminal water molecule. Additionally, Y3 is coordinated by three oxygen atoms from three distinct carboxylates of PIP ligands, three μ_3-oxo groups, one nitrogen atom from the ligand and a water molecule completing the eighth coordination site. Finally, Y4 is coordinated to three oxygen atoms from three different ligands, three μ_3-oxo groups, one water and one DMF molecules. These yttrium ions are bridged together through μ_3-oxo groups and carboxylate moieties to generate distorted cubic tetranuclear RE metal clusters (i.e., 8 corners, 4 oxygen and 4 Y). Each tetranuclear cluster is connected to an adjacent one through two *in situ*-generated formate ligands that altogether form a novel RE octanuclear (i.e., double tetranuclear) cluster (Figure 4.45 b).

Each octanuclear cluster is connected to its neighboring clusters through 16 ligands producing a dense 3-P MOF. In other words, each tetranuclear cluster is capped with eight ligands, two of which coordinate through their nitrogen donor moiety and the other six are connected through their carboxylate moieties leaving their nitrogen moiety free and pointing toward a small 1-D channel.

In fact, Y-**tfz**-MOF-3 is a very dense structure that has small 1-D channels along the *b*-axes with an aperture size of 3.4 x 4 Å (Figure 4.45 d). Another type of channel that passes through the a-axis is where the free nitrogen moiety of the ligand is pointing and almost splitting the space into two areas, and the diameter of the largest sphere that can fit within each half is 3.2 Å (Figure 4.45 c).

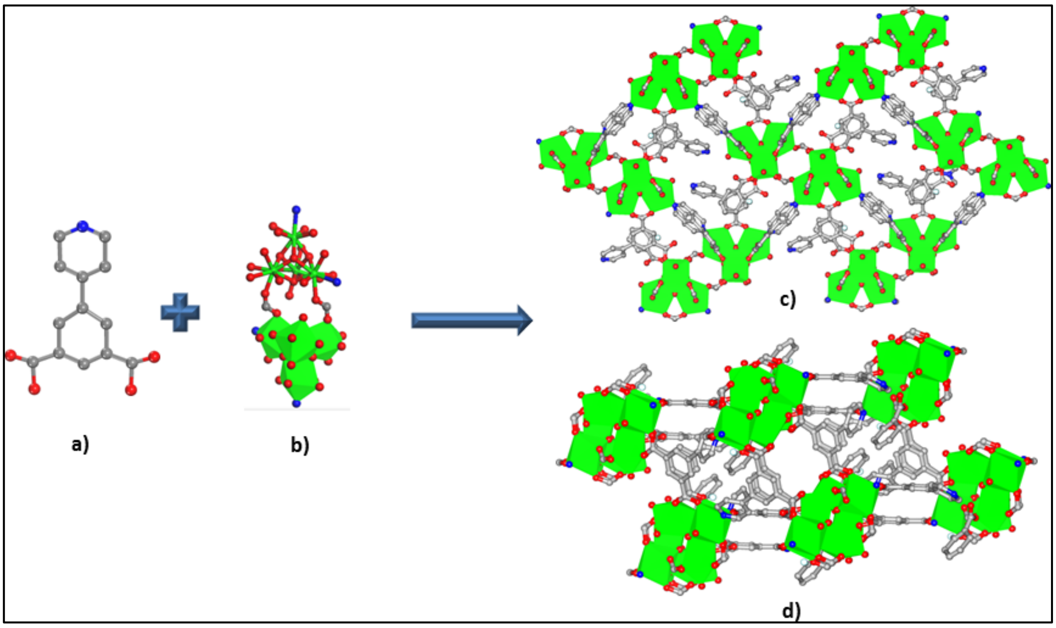

Figure 4.45 (a) PIP, (b) two RE tetranuclear clusters connected with two formate ligands to construct the novel octanuclear cluster, (c) crystal structure of Y-**tfz**-MOF-3 viewed along the a-axis and (d) along b-axis. C = gray, O = red, N = blue, Y = green; Hydrogen atoms and solvent molecules are omitted for clarity.

Topologically, when the structure is simplified and analyzed considering the RE-MBB as a double-tetranuclear cluster, the structure may be viewed as a (3,8)-c MOF with infrequently occurring **tfz**-d topology based on **kgd** 2-P pillared layers (Figure 4.46). Equivalently, when looking at the clusters as octanuclear, the structure can be considered a (3,16)-c MOF with novel topology.

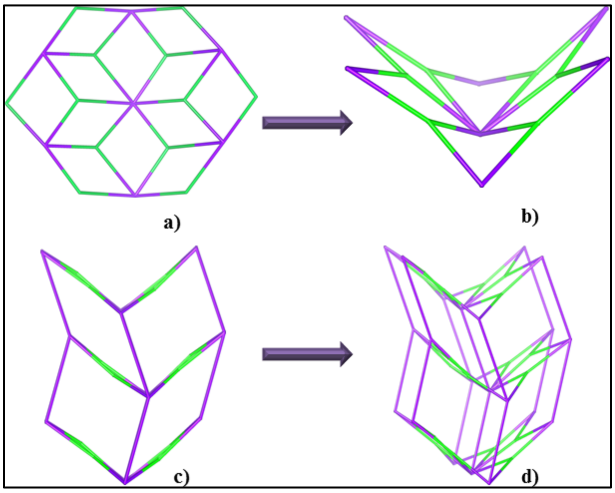

Figure 4.46 (a) Schematic representation of one 2-P hexagonal **kgd** net, top view and (b) side view, (c) the pillaring of these layers to produce Y-**tfz**-MOF-3 with **tfz** topology, side view and (d) the rotated view.

The phase purity of the bulk crystalline materials for Y-**tfz**-MOF-3 was confirmed by similarities between the calculated and as-synthesized PXRD patterns (Figure 4.47). In addition, it must be noted that this compound not only exhibits robust stability in common organic solvents (i.e., CH_3OH, C_2H_5OH, CH_3CN and C_3H_6O, etc.), but favorable air, water and thermal stabilities (Figure 4.48), important parameters for potential practical deployment of porous MOFs material.

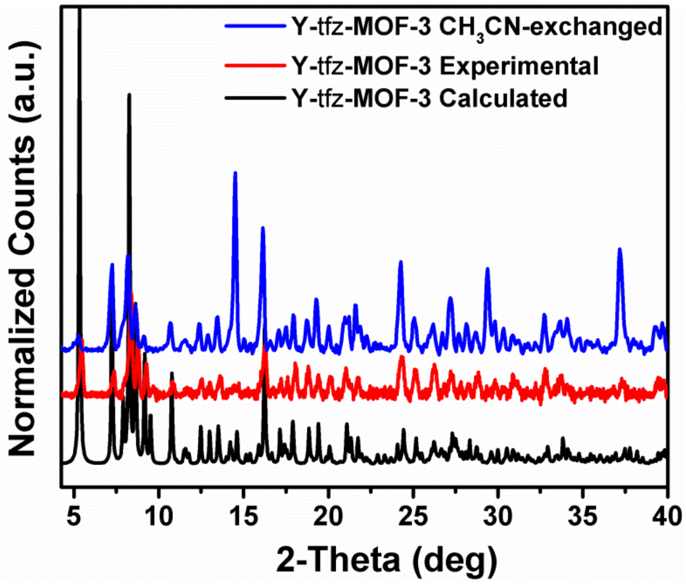

Figure 4.47 Phase purity and stability in CH$_3$CN-exchanged of Y-**tfz**-MOF-3 as indicated by the similarities between the calculated and experimental PXRD.

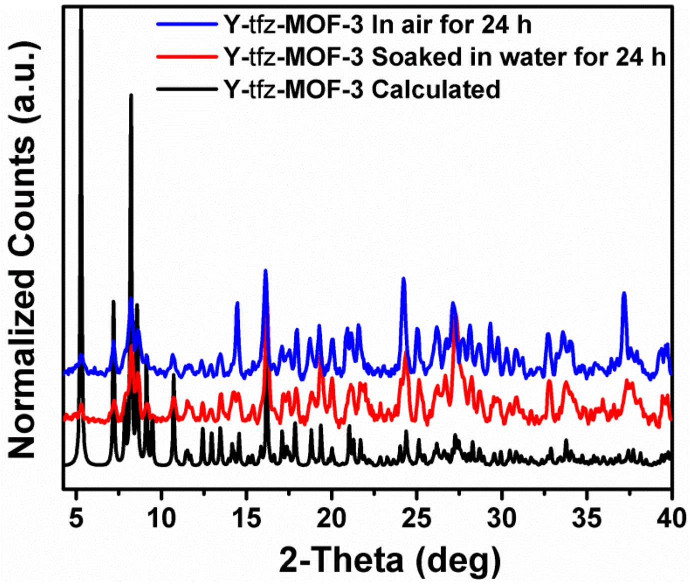

Figure 4.48 PXRD patterns of Y-**tfz**-MOF-3 exposed to air and soaked in water for 24 h that suggests its stability.

To investigate the thermal stability of Y-**tfz**-MOF-3, TGA was performed on DMF-washed and CH_3CN-exchanged samples under a N_2 atmosphere. The tests were carried out between RT and 700 °C at an increasing heating rate of 20 °C/min in high resolution dynamic mode. The TGA plots of Y-**tfz**-MOF-3 suggest its thermal stability at more than 500 °C (Figure 4.49).

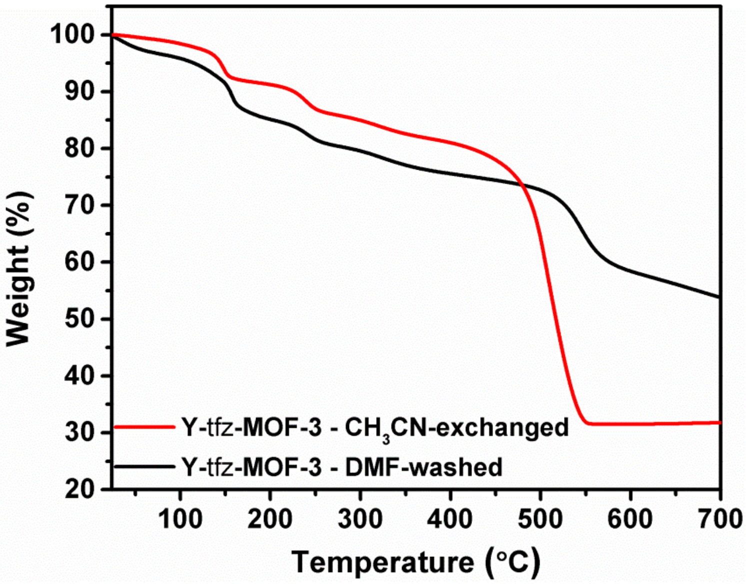

Figure 4.49 TGA plots demonstrating the high thermal stability of Y-**tfz**-MOF-3 at more than 500 °C.

The corresponding solvent-accessible free volume of Y-**tfz**-MOF-3 was estimated from the X-ray SC structure using MS software to be 34%. In addition, the theoretical PV of the structure was estimated to be 0.24 cm^3/g. These low values are because of the presence of bulk RE multinuclear clusters and because the structure is very dense.

After differential activation screening attempts using N_2 at 77 K, samples exchanged with CH_3CN and subjected to vacuum at RT showed the best uptake. Nevertheless, no Type I sorption isotherms, typical for microporous materials, were observed (Figure 4.50). In addition, Y-**tfz**-MOF-3 exhibited a small degree of porosity that did not reach the calculated values where the experimental PV and SA_{BET} were observed to be 0.12 cm^3/g and 48 m^2/g, respectively. This could be attributed to improper activation, the presence of impurities and/or the presence of excess modulator trapped in the small cavities.

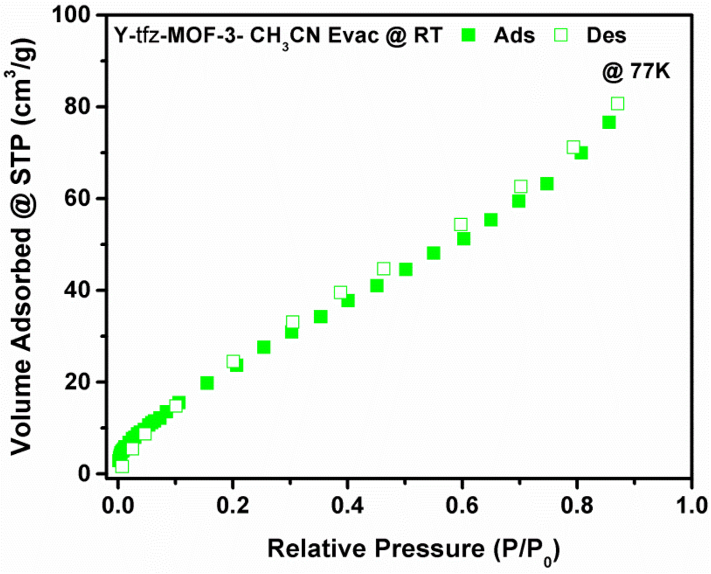

Figure 4.50 N_2-sorption isotherms of Y-**tfz**-MOF-3 exchanged with CH_3CN and evacuated at RT.

Considering that Y-**tfz**-MOF-3 is based on RE polynuclear clusters, Dy and Tb isostructures were prepared and their primary magnetic properties were investigated. The phase purity of the prepared compounds was confirmed by the similarities between the calculated Y-**tfz**-MOF-3 PXRD patterns and those of experimental Tb-**tfz**-MOF-3 and Dy-**tfz**-MOF-3 (Figure 4.51).

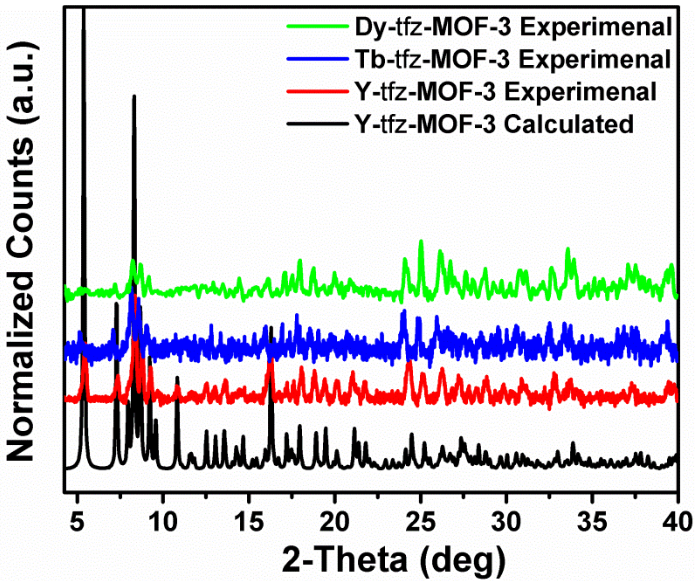

Figure 4.51 Phase purity of Tb-**tfz**-MOF-3 and Dy-**tfz**-MOF-3 as indicated by the similarities between their experimental PXRD patterns and those calculated for Y-**tfz**-MOF-3.

The magnetic properties of these isostructures were measured by a superconducting quantum interference device. Therefore, to evaluate the intrinsic magnetic properties of Tb-**tfz**-MOF-3 and Dy-**tfz**-MOF-3 (see Chapter 2), low-field magnetization was measured as a function of temperature in the range of 1.8-300 K under a magnetic field of 100 Oe with the ZFC and FC processes (Figure 4.52 and Figure 4.53 for Tb and Dy isostructures, respectively). For both compounds, the ZFC and FC curves overlapped perfectly within the entire temperature range, indicating paramagnetism.

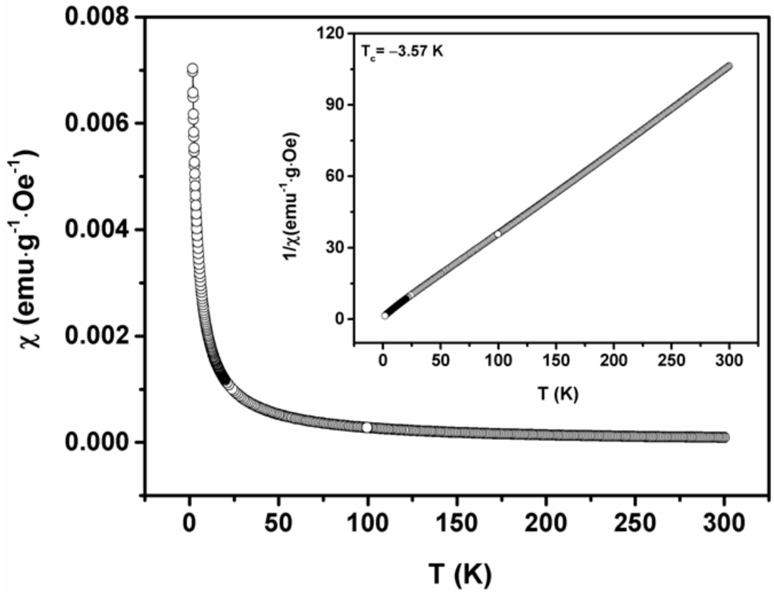

Figure 4.52 Temperature-dependent susceptibility of Tb-**tfz**-MOF-3 with applied field *H* = 100 Oe. Inset provides the $\frac{1}{\chi} - \boldsymbol{T}$ curve.

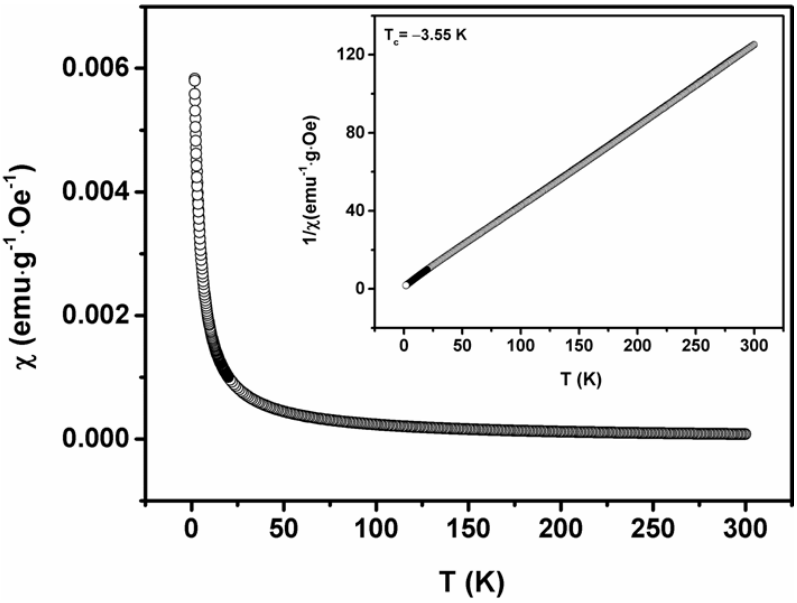

Figure 4.53 Temperature-dependent susceptibility of Dy-**tfz**-MOF-3 with applied field *H* = 100 Oe. Inset provides the $\frac{1}{\chi} - \boldsymbol{T}$ curve.

Close examination reveals that these curves can be perfectly described by the Curie-Weiss law of magnetic susceptibility of the material with a small, negative intercept, T_c, that is equal to – 3.57 and – 3.55 K for the Tb and Dy isostructures, respectively (Figure 4.52 and Figure 4.53 insets). This suggests that there exists a weak, antiferromagnetic-like interaction among the lanthanide clusters.

The field-dependent magnetization was measured in a temperature range of 1.8-30 K. Figure 4.54 and Figure 4.55 insets, for Tb and Dy isostructures, respectively, provide the magnetization (*M*) as a function of applied field (H = 0 to $7*10^4$ Oe) measured at various temperatures. The *M-H* curves exhibit superparamagnetism at low temperatures.

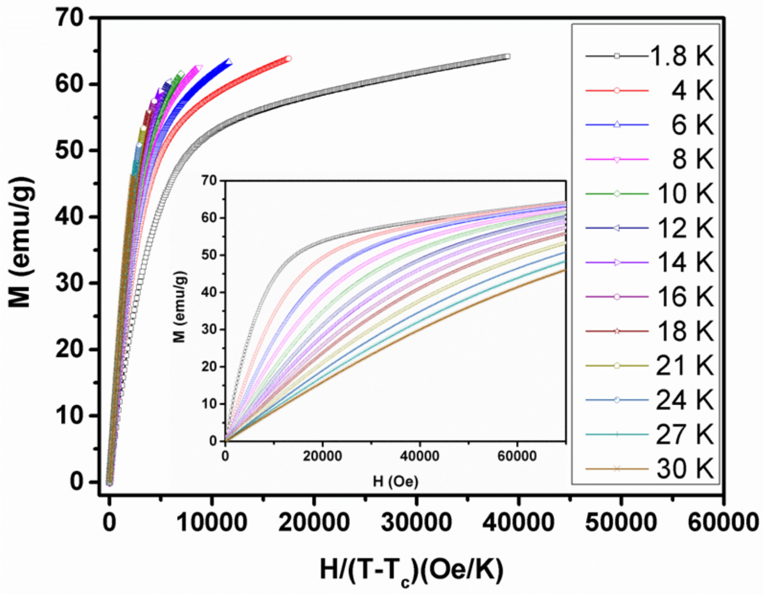

Figure 4.54 Tb-**tfz**-MOF-3 magnetization, *M*, versus $\boldsymbol{H/(T-T_c)}$ at a temperature range from 1.8-30 K. Inset provides the field-dependent magnetization measured from 1.8-30 K.

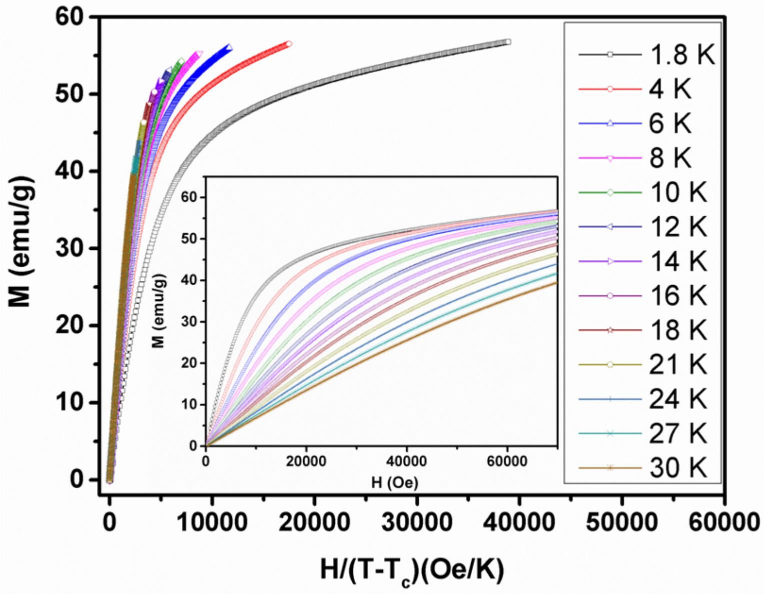

Figure 4.55 Dy-**tfz**-MOF-3 magnetization, *M*, versus $\boldsymbol{H/(T-T_c)}$ at a temperature range from 1.8-30 K. Inset provides the field-dependent magnetization measured from 1.8-30 K.

If all the lanthanide clusters in this material had the same energy barrier and magnetic moment, the *M*–*H* curves could be described by the modified Langevin function given that the field, *H*, is sufficiently low and *T* is high enough. Figure 4.54 and Figure 4.55 describe the relationship, $M(H,T) - H/(T-T_c)$, for the temperature range of 1.8-30 K. All the curves overlapped with each other at lower fields, validating the uniformity of energy barrier and magnetic moments in lanthanide clusters. In general, further inquiry is warranted to study the possible application of these isostructures as cryogenic magnetic refrigerants with a magnetocaloric effect.

4.6.3.2. Y-swk-MOF-1 and its isostructures/isoreticular structures

To emphasize the necessity of using a modulator (2-FBA) in forming new RE polynuclear clusters, PMIP and PIP were used with RE metal salts utilizing different reaction conditions but eliminating the modulator. In this case, new 3-P MOFs were prepared which were isoreticular to each other and composed of the dominant RE SBUs, the 1-D rod-shaped inorganic infinite chains,[22] connected through the carboxylate groups of the ligand. This confirms the importance of using a modulator in forming new large RE clusters and avoiding the default SBUs.

Thus, a solvothermal reaction between $Y(NO_3)_3$ and PMIP (Figure 4.56 b) in DMF yielded spherical crystals of Y-**swk**-MOF-1. Other reaction conditions were also employed, such as different M:L ratios while eliminating the modulator, and it was seen that the same products were produced.

Similarly, the isostructure, Tb-**swk**-MOF-1, as well as the isoreticular structures, Y-**swk**-MOF-2 and Tb-**swk**-MOF-2, with which PIP (Figure 4.56 a) was used, were also synthesized.

X-ray SC structure analysis revealed that Y-**swk**-MOF-1 crystallizes in the hexagonal space group, $P6_3CM$, with cell parameters of $a = b = 16.27$ Å, $c = 7.38$ Å and $\alpha = \beta = 90°$, $\gamma = 120°$ and $V = 1692$ Å^3, forming a 3-P MOF with 1-D channels.

In the crystal structure of Y-**swk**-MOF-1, each metal ion is coordinated to nine oxygen atoms from six different ligands to form octahedral SBUs. These SBUs are face-shared and linked together by metal oxygen bonds to forms rod-shaped metal oxide SBUs (Figure 4.56 c). Further, these SBUs are assembled in a hexagonal form (with respect to each other) and are linked together by the ligands, altogether leading to the formation of irregular hexagonally-packed cylindrical 1-D channels that pass along the c-axis (Figure 4.56 d).

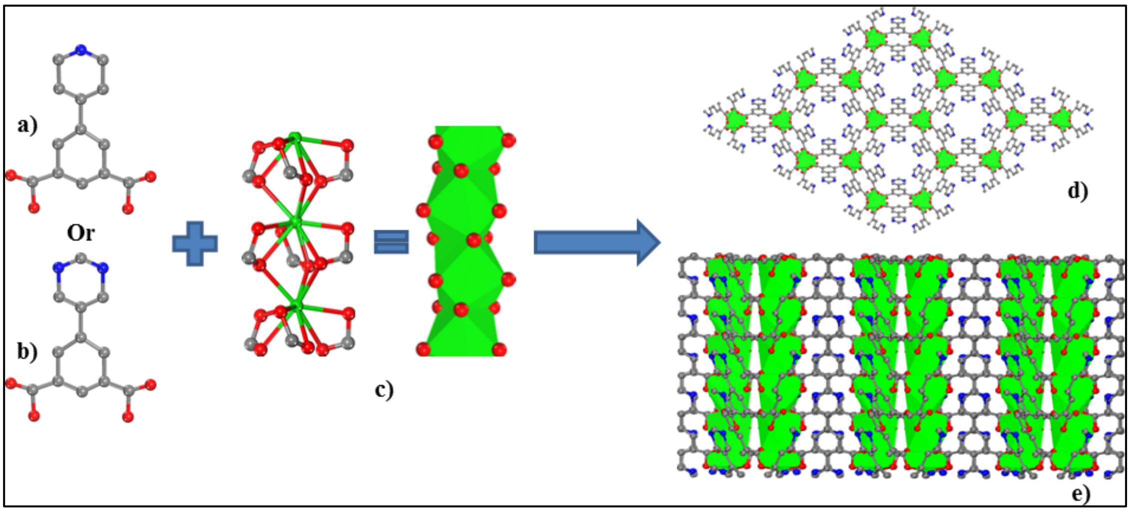

Figure 4.56 (a) PIP, (b) PMIP, (c) rod-shaped RE SBU, (c) Y-**swk**-MOF-1 viewed along the c-axis and (d) along the b-axis. C = gray, N = blue and O = red and Y = green. Hydrogen atoms and solvent molecules are omitted for clarity.

These small channels pass through the c-axis and measures ~ 4.1 Å in diameter (Figure 4.57). It is worth mentioning that the nitrogen donor moieties of the ligands (pyrimidine and pyridine in PMIP and PIP, respectively, in the isoreticular structures) freely pointed towards the center of these channels and were not involved in the coordination of the structure (Figure 4.57 d).

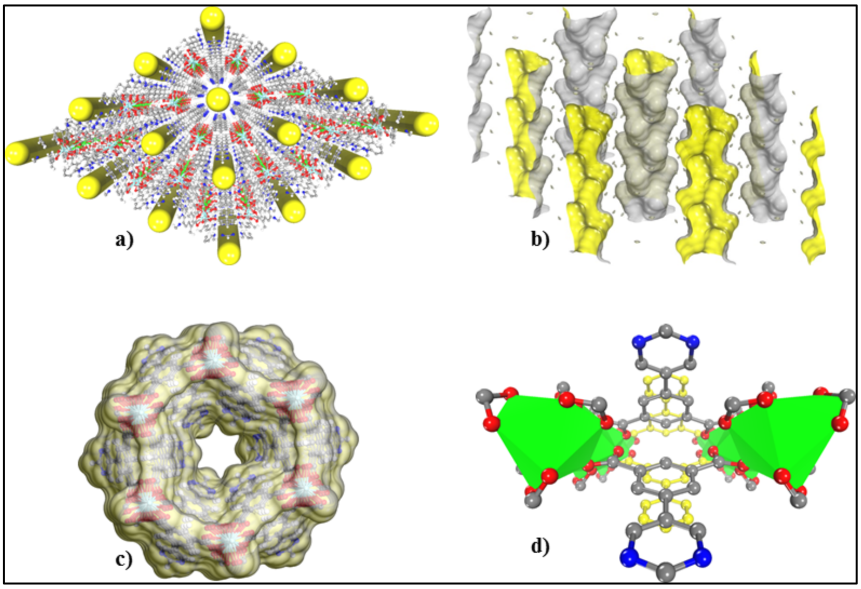

Figure 4.57 The 1-D channels of Y-**swk**-MOF-1: (a) overhead view (represented as yellow cylinders), (b) side view, (c) free space in one channel and (d) the free nitrogen moieties of the ligands pointing toward the channels. C = gray, O = red, N = blue, Y = green; Hydrogen atoms and solvent molecules are omitted for clarity.

Topological analysis uncovered that Y-**swk**-MOF-1 is a MOF with the unusual **swk** topology (Figure 4.58).[23]

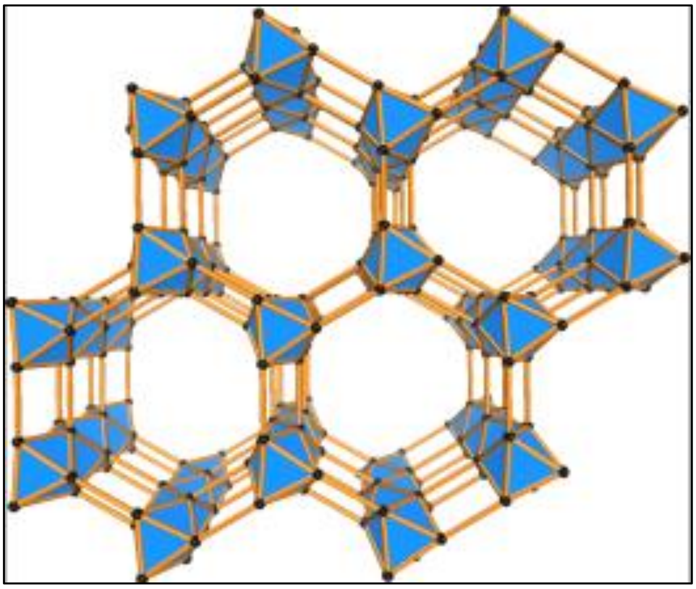

Figure 4.58 Schematic representation of Y-**swk**-MOF-1 topology.

The evident similarities between the calculated and experimental PXRD patterns were used to confirm the phase purity of the bulk crystalline materials of Y-**swk**-MOF-1 (Figure 4.59).

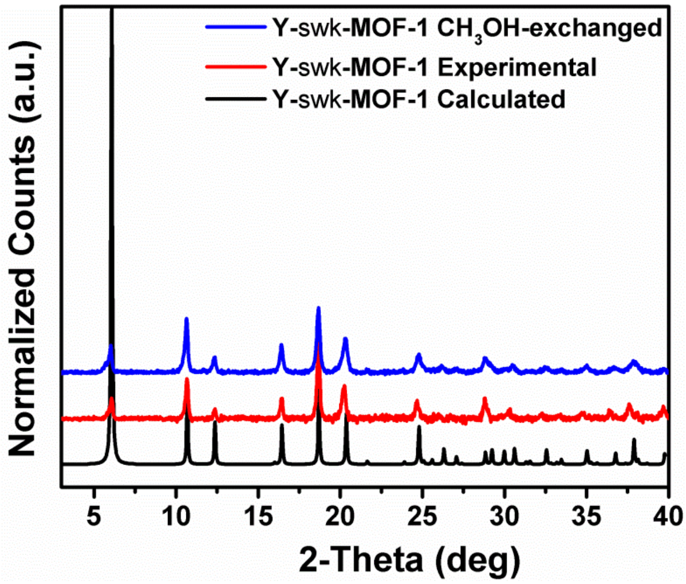

Figure 4.59 Experimental and calculated PXRD patterns of Y-**swk**-MOF-1, indicating the purity of the as-synthesized bulk material and the stability of the CH_3OH-exchanged samples.

It is noteworthy that the crystals of Tb-**swk**-MOF-1, Y-**swk**-MOF-2 and Tb-**swk**-MOF-2 exhibited weak diffraction with the SC diffractometer; therefore, their crystal structure determination was fruitless, though their PXRD patterns were identical to those of Y-**swk**-MOF-1, indicating that these compounds are isostructures or isoreticular structures (Figure 4.60 and Figure 4.61). In addition, all frameworks exhibited high stability in an assortment of organic solvents, air (Figure 4.62) and water (Figure 4.63).

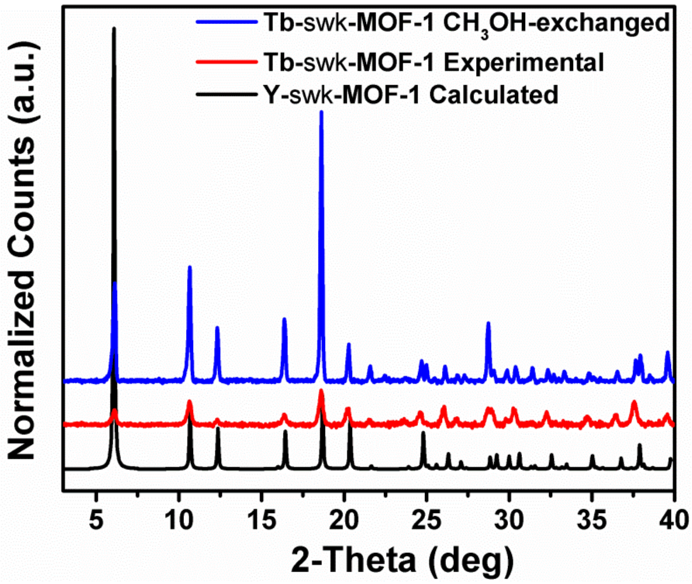

Figure 4.60 PXRD spectra of the as-synthesized and CH_3OH-exchanged Tb-**swk**-MOF-1 compared to Y-**swk**-MOF-1 calculated from the SC experiments indicating that the two are isostructures.

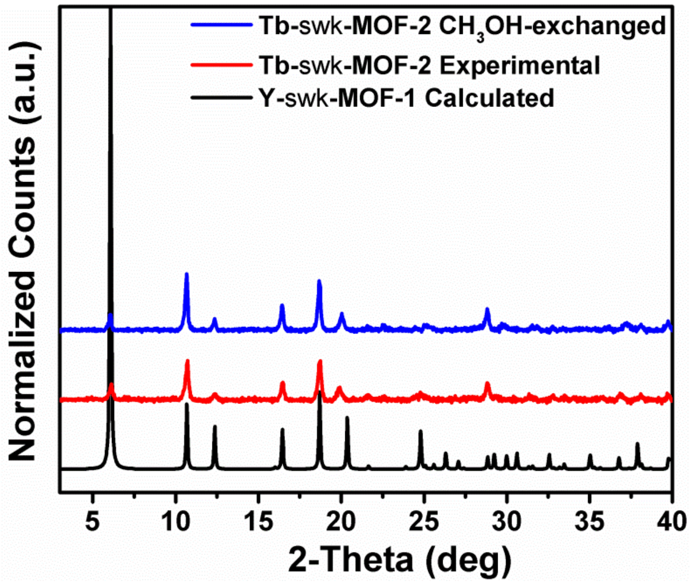

Figure 4.61 PXRD spectra of as-synthesized and CH_3OH-exchanged Tb-**swk**-MOF-2 compared to Y-**swk**-MOF-1 calculated from the SC experiments indicating that the two are isoreticular structures.

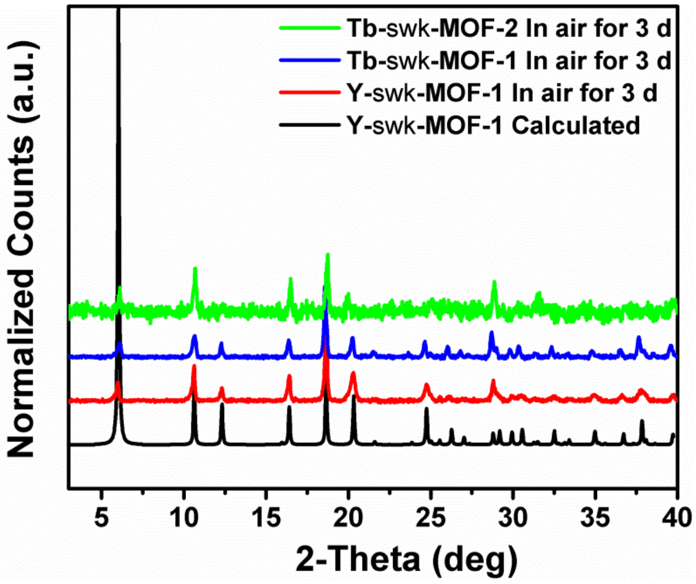

Figure 4.62 PXRD pattern calculated for Y-**swk**-MOF-1 from the SC structure compared to the experimental PXRD patterns of Y-**swk**-MOF-1, Tb-**swk**-MOF-1 and Tb-**swk**-MOF-2 when subjected to air.

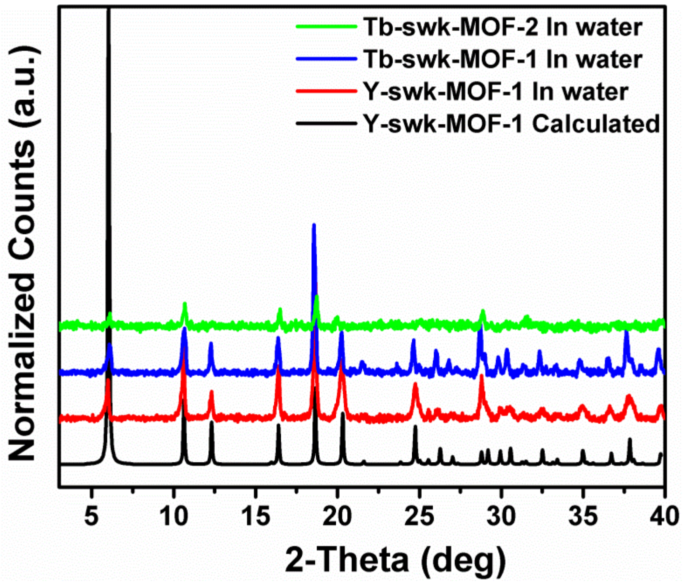

Figure 4.63 PXRD pattern calculated for Y-**swk**-MOF-1 from the SC structure compared to the experimental PXRD patterns of Y-**swk**-MOF-1, Tb-**swk**-MOF-1 and Tb-**swk**-MOF-2 when soaked in water.

To probe the thermal stability of Y-**swk**-MOF-1, TGA was performed on DMF-washed and CH_3OH-exchanged samples under a N_2 atmosphere. The tests were carried out between RT and 700 °C at an increasing heating rate of 20 °C/min in high resolution dynamic mode. The TGA plots of Y-**swk**-MOF-1 suggest its thermal stability at more than 500 °C (Figure 4.64).

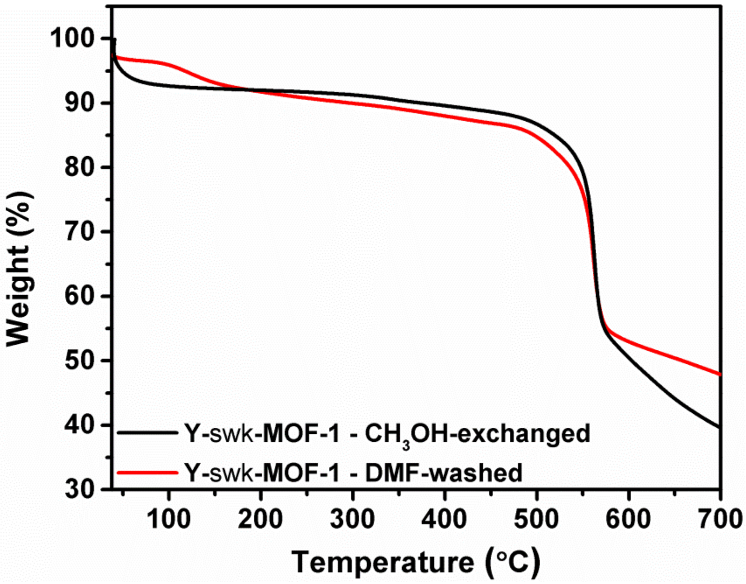

Figure 4.64 TGA plots of Y-**swk**-MOF-1; DMF-washed and CH_3OH-exchanged indicating its thermal stability at up to 500 °C.

Similarly, under the same conditions, TGA of Tb-**swk**-MOF-1 and Tb-**swk**-MOF-2 were performed and their high thermal stability at more than 500 °C was exhibited.

The total potential solvent-accessible volume for the as-synthesized Y-**swk**-MOF-1 was estimated to be 13% from the X-ray SC structure using MS software. Besides this, the PV_{Theo} of the structure was estimated to be 0.07 cm^3/g.

To determine the actual porosity and gas uptake capacity of the framework, gas sorption experiments were performed. Sorption assessments were conducted with CH_3CN-exchanged Y-**swk**-MOF-1, which showed a classic Type I isotherm with a small step (Figure 4.65). The experimental PV and SA$_{BET}$ values were estimated to be 0.17 cm^3/g and 285.5 m^2/g, respectively.

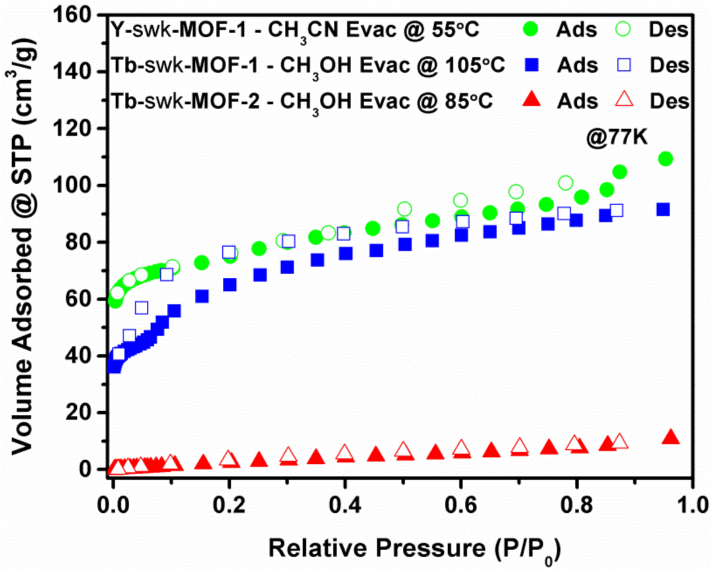

Figure 4.65 N_2 sorption isotherms comparison of Y-**swk**-MOF-1 activated using CH_3CN with Tb-**swk**-MOF-1 and Tb-**swk**-MOF-2 activated by CH_3OH.

Likewise, sorption experiments were performed on CH_3OH-exchanged Tb-**swk**-MOF-1, which also showed a Type I isotherm with a step (Figure 4.65). The experimental PV and SA$_{BET}$ values were estimated to be 0.14 cm^3/g and 185.6 m^2/g, respectively. The high experimental sorption values for both samples, when compared to theoretical values, could be ascribed to imperfection in the crystal structure. Finally, CH_3OH-exchanged Tb-**swk**-MOF-2 propped N_2 as nonporous (Figure 4.65).

Unfortunately, various trials to improve the quality of the prepared crystals were unsuccessful, and further optimization of the synthesis and activation conditions remains to be investigated.

4.6.4. Summary and conclusions

As seen in this section, by replacing one of the carboxylate groups in biphenyl-3,4',5-tricarboxylic acid, the tricarboxylate ligand used to construct the **pek**-MOF, with a nitrogen atom, we were able to build a new framework based on a novel RE polynuclear cluster.

In summary, through the addition of 2-FBA as a modulator to the reaction between $Y(NO_3)_3$ and PIP, we were able to synthesize a 3-P MOF based on a novel RE octanuclear (double tetranuclear) cluster with the very rare **tfz** topology. This framework is very dense and exhibited low gas uptake. Therefore, Tb and Dy analogues of this RE polynuclear structure were synthesized and studied for their magnetic properties.

On the other hand, by using similar reaction conditions but without adding the fluorinated modulator, new 3-P MOFs based on the default rod-like RE SBU and the uncommon **swk** topology were prepared. This showed the importance of using a fluorinated modulator to aid the formation of RE polynuclear clusters.

4.7. General conclusions

Overall, in this chapter, we report the successful synthesis of new highly-connected MOFs that are based on various, unprecedented RE-MBBs, namely the RE octadecanuclear, octanuclear and double tetranuclear clusters. Therefore, through systematic studies on reacting RE metal salts with hetero-functional ligands while using 2-FBA as a modulator, we were able to identify the reaction conditions required for the *in situ* generation of the unprecedented MBBs and their corresponding MOFs.

We also provide support for the importance of the presence of 2-FBA to form these novel polynuclear RE-MBBs. This was demonstrated through the use of the same reaction conditions that formed these MOFs while leaving out the modulator. As expected, only MOFs based on the dominant RE infinite-chain MBBs or dinuclear clusters were formed.

The ligands in the study were angular and contain, in addition to carboxylate groups, nitrogen donor moieties in order to investigate the influence of their presence on the construction, connectivity and stability of the newly prepared MOFs. It was found that nitrogen atoms are not always involved in the coordination of the frameworks, and whenever they are, they coordinate to the metal in a monodentate fashion with a relatively flexible geometry, bringing about formation of frameworks that are less stable upon guest solvent molecules removal. Therefore, the frameworks underwent partial or complete collapse as evidenced by low or a complete lack of porosity.

Furthermore, the fact that it is possible to isolate new frameworks and network topologies by subtly changing the geometry of the ligand, e.g., adjusting its length-to-width ratio, was indeed made use of.

The reaction conditions that previously allowed the construction of **fcu**-MOFs were used with PDDB as the ligand to construct a novel RE octadecanuclear cluster and form a stable 2-P Y-**hxl**-MOF. Moreover, the employment of an extended ligand, PTPDC, resulted in the formation of the second highly-connected RE octanuclear clusters and their assembly to form pillared 3-P MOFs with the rare **tfz** topology. Likewise, the effect of using a shorter version of the PTPDC ligand was also evaluated by using PIP, and the building of the RE double tetranuclear cluster closely related to the octanuclear MBB was observed.

4.8. REFERENCES

1. (a) Eddaoudi, M.; Moler, D. B.; Li, H.; Chen, B.; Reineke, T. M.; O'Keeffe, M.; Yaghi, O. M., *Accts. Chem. Res.* **2001,** *34*, 319-330.(b) Liu, Y.; Kravtsov, V.; Larsen, R.; Eddaoudi, M., *Chem. Commun.* **2006**, 1488-1490.

2. (a) Roy, S.; Chakraborty, A.; Maji, T. K., *Coordin. Chem. Rev.* **2014,** *273*, 139-164.(b) Devic, T.; Serre, C.; Audebrand, N.; Marrot, J.; Ferey, G., *J. Am. Chem. Soc.* **2005,** *127*, 12788-12789.(c) Alezi, D.; Peedikakkal, A. M.; Weselinski, L. J.; Guillerm, V.; Belmabkhout, Y.; Cairns, A. J.; Chen, Z.; Wojtas, L.; Eddaoudi, M., *J. Am. Chem. Soc.* **2015,** *137*, 5421-5430.(d) Park, Y. K.; Choi, S. B.; Kim, H.; Kim, K.; Won, B. H.; Choi, K.; Choi, J. S.; Ahn, W. S.; Won, N.; Kim, S.; Jung, D. H.; Choi, S. H.; Kim, G. H.; Cha, S. S.; Jhon, Y. H.; Yang, J. K.; Kim, J., *Angew. Chem. Int. Ed. Engl.* **2007,** *46*, 8230-8233.(e) Luo, J. H.; Xu, H. W.; Liu, Y.; Zhao, Y. S.; Daemen, L. L.; Brown, C.; Timofeeva, T. V.; Ma, S. Q.; Zhou, H. C., *J. Am. Chem. Soc.* **2008,** *130*, 9626.

3. Xue, D. X.; Cairns, A. J.; Belmabkhout, Y.; Wojtas, L.; Liu, Y.; Alkordi, M. H.; Eddaoudi, M., *J. Am. Chem. Soc.* **2013,** *135*, 7660-7667.

4. Luebke, R.; Belmabkhout, Y.; Weselinski, L. J.; Cairns, A. J.; Alkordi, M.; Norton, G.; Wojtas, L.; Adil, K.; Eddaoudi, M., *Chem. Sci.* **2015,** *6*, 4095-4102.

5. Jansze, S. M.; Cecot, G.; Wise, M. D.; Zhurov, K. O.; Ronson, T. K.; Castilla, A. M.; Finelli, A.; Pattison, P.; Solari, E.; Scopelliti, R.; Zelinskii, G. E.; Vologzhanina, A. V.; Voloshin, Y. Z.; Nitschke, J. R.; Severin, K., *J. Am. Chem. Soc.* **2016,** *138*, 2046-2054.

6. Guillerm, V.; Weselinski, L.; Belmabkhout, Y.; Cairns, A. J.; D'Elia, V.; Wojtas, L.; Adil, K.; Eddaoudi, M., *Nat. Chem.* **2014,** *6*, 673-680.

7. (a) Wang, C. C.; Sheu, G. B.; Ke, S. Y.; Shin, C. Y.; Cheng, Y. J.; Chen, Y. T.; Cho, C. H.; Ho, M. L.; Chen, W. T.; Liao, R. H.; Lee, G. H.; Sheu, H. S., *CrystEngComm* **2015,** *17*, 1264-1272.(b) Thomas-Gipson, J.; Perez-Aguirre, R.; Beobide, G.; Castillo, O.; Luque, A.; Perez-Yanez, S.; Roman, P., *Cryst. Growth Des.* **2015,** *15*, 975-983.

8. (a) Yin, Z.; Zhou, Y. L.; Zeng, M. H.; Kurmoo, M., *Dalton Trans.* **2015,** *44*, 5258-5275.(b) Zhang, X. Q.; Gao, Y. F.; Liu, H. T.; Liu, Z. L., *CrystEngComm* **2015,** *17*, 6037-6043.(c) Haldar, R.; Maji, T. K., *CrystEngComm* **2013,** *15*, 9276-9295.

9. (a) Blatov, V. A.; Shevchenko, A. P.; Serezhkin, V. N., *J. Appl. Crystallogr.* **2000,** *33*, 1193.(b) Blatov, V. A., *Struct. Chem.* **2012,** *23*, 955-963.

10. Gándara, F.; Fortes-Revilla, C.; Snejko, N.; Gutiérrez-Puebla, E.; Iglesias, M.; Angeles Monge, M., *Inorg. Chem.* **2006,** *45*, 9680-9687.

11. Zhang, X. T.; Sun, D.; Li, B.; Fan, L. M.; Li, B.; Wei, P. H., *Cryst. Growth Des.* **2012,** *12*, 3845-3848.

12. Xue, D. X.; Belmabkhout, Y.; Shekhah, O.; Jiang, H.; Adil, K.; Cairns, A. J.; Eddaoudi, M., *J. Am. Chem. Soc.* **2015,** *137*, 5034-5040.

13. (a) Dey, C.; Kundu, T.; Biswal, B. P.; Mallick, A.; Banerjee, R., *Acta Crystallogr. Sect. B-Struct. Sci.* **2014,** *70*, 3-10.(b) Lin, Z. J.; Xu, B.; Liu, T. F.; Cao, M. N.; Lu, J. A.; Cao, R., *Eur. J. Inorg. Chem.* **2010**, 3842-3849.(c) Nayak, S.; Nayek, H. P.; Pietzonka, C.; Novitchi, G.; Dehnen, S., *J. Molec. Struct.* **2011,** *1004*, 82-87.

14. Guo, F.-S.; Chen, Y.-C.; Liu, J.-L.; Leng, J.-D.; Meng, Z.-S.; Vrabel, P.; Orendáč, M.; Tong, M.-L., *Chem. Commun.* **2012,** *48*, 12219-12221.

15. (a) Lorusso, G.; Sharples, J. W.; Palacios, E.; Roubeau, O.; Brechin, E. K.; Sessoli, R.; Rossin, A.; Tuna, F.; McInnes, E. J.; Collison, D., *Adv. Mater.* **2013,** *25*, 4653-4656.(b) Biswas, S.; Jena, H. S.; Adhikary, A.; Konar, S., *Inorg. Chem.* **2014,** *53*, 3926-3928.

16. (a) Farha, O. K.; Hupp, J. T., *Accts. Chem. Res.* **2010,** *43*, 1166-1175.(b) Farha, O. K.; Eryazici, I.; Jeong, N. C.; Hauser, B. G.; Wilmer, C. E.; Sarjeant, A. A.; Snurr, R. Q.; Nguyen, S. T.; Yazaydin, A. O.; Hupp, J. T., *J. Am. Chem. Soc.* **2012,** *134*, 15016-15021.

17. (a) Luebke, R.; Eubank, J. F.; Cairns, A. J.; Belmabkhout, Y.; Wojtas, L.; Eddaoudi, M., *Chem. Commun.* **2012,** *48*, 1455-1457.(b) Luebke, R. Metal-Organic Frameworks: Building Block Design Strategies for the Synthesis of MOFs. King Abdullah University of Science and Technology, Thuwal, Kingdom of Saudi Arabia, **2014**.

18. Alkordi, M. H.; Eddaoudi, M., Zeolitelike Metal–Organic Frameworks (ZMOFs): Design, Structure, and Properties. In *Supramol. Chem.*, John Wiley & Sons, Ltd: **2012**.

19. (a) O’Keeffe, M., Reticular Chemistry Structure Resource, http://rcsr.anu.edu.au/.(b) O'Keeffe, M.; Peskov, M. A.; Ramsden, S. J.; Yaghi, O. M., *Accts. Chem. Res.* **2008,** *41*, 1782-1789.

20. (a) Guillerm, V.; Kim, D.; Eubank, J. F.; Luebke, R.; Liu, X.; Adil, K.; Lah, M. S.; Eddaoudi, M., *Chem. Soc. Rev.* **2014,** *43*, 6141-6172.(b) Garibay, S. J.; Stork, J. R.; Wang, Z. Q.; Cohen, S. M.; Telfer, S. G., *Chem. Commun.* **2007**, 4881-4883.

21. (a) Chandrasekhar, V.; Das, S.; Dey, A.; Hossain, S.; Sutter, J. P., *Inorg. Chem.* **2013,** *52*, 11956-11965.(b) Das, S.; Hossain, S.; Dey, A.; Biswas, S.; Sutter, J. P.; Chandrasekhar, V., *Inorg. Chem.* **2014,** *53*, 5020-5028.

22. Rosi, N. L.; Kim, J.; Eddaoudi, M.; Chen, B.; O'Keeffe, M.; Yaghi, O. M., *J. Am. Chem. Soc.* **2005,** *127*, 1504-1518.

23. (a) Li, M.; Li, D.; O'Keeffe, M.; Yaghi, O. M., *Chem. Rev.* **2014,** *114*, 1343-1370.(b) O'Keeffe, M.; Yaghi, O. M., *Chem. Rev.* **2012,** *112*, 675-702.

Chapter 5: Evaluation of Selected MOFs as Drug Delivery Vehicles

5.1. Abstract

In this chapter, the ability of MOFs to be utilized as drug delivery vehicles was assessed. Therefore, two different MOFs, In **rho**-ZMOF and Cu **rht**-MOF-7, were specifically studied as potential drug delivery carriers.

As a consequence of its anionic nature and ion exchange ability, the potential use of In **rho**-ZMOF as a delivery system for the cationic antiarrhythmic drug, Proc, was examined. This framework demonstrated its ability to store the drug through electrostatic interactions. In addition, it showed cation-triggered controlled release of the drug over a longer period, which would overcome the need for frequent drug administration (every 3-4 h).

Moreover, because of the large cages of the neutrally-charged Cu **rht**-MOF-7, it was chosen to be looked at as a potential drug delivery carrier for IBU, a neutral NSAID. The amount of drug that ended up being loaded into the framework was observed to be low, most likely because of the size of the windows of the framework cages that allow drug molecules to enter in only one orientation, causing diffusion restriction.

5.2. General introduction

As a result of the unique properties and outstanding performance demonstrated by MOFs to store and controllably release various API,[1] it was important to explore and further study the possibility to utilize MOFs in the area of medicine.[2] Consequently, two MOFs that are porous and known for their high water stability were investigated for their potential use in this area.

The first framework is the anionic In **rho**-ZMOF, evaluated as a potential carrier for the cationic antiarrhythmic drug, Proc. This framework belongs to the ZMOF class; therefore, it combines the advantages of both MOFs and zeolites.[3] For example, it has homogeneously sized and shaped extra-large tunable cavities with ion exchange capability.[3-4]

It is worth mentioning that, even though the toxicity of indium-based compounds is well known, the unique features of this framework encouraged, as a proof-of-concept, its assessment as a drug delivery carrier. This is especially true as this study was initiated in 2011, a time where very few MOFs were being assessed for their potential in drug delivery. In addition, the framework can be incorporated into topically-applied systems, such as transdermal patches, where only the API passes into the body.

The second MOF of interest is Cu **rht**-MOF-7,[5] a neutral porous framework with large cavities investigated as a carrier for the neutrally-charged NSAID, IBU.

5.3. Materials and methods

All chemicals mentioned in the work were used as received from Fisher Scientific, Sigma-Aldrich or Acros without any purification or modification. The purity of Proc and IBU was verified by their ^{1}H NMR spectra. For details about methods, devices and software used, please refer to Chapter 2.

5.4. Experimental section part I: Evaluation of an anionic MOF as a delivery vehicle for a cationic drug

5.4.1. Introduction

In **rho**-ZMOF (Figure 5.1 a) is a 3-P framework that possesses accessible α-cages with extra-large cavities (diameter ~ 18.2 Å) and windows (~ 8.6 Å). Here, the accessible free volume corresponds to around 56% with apparent SA_{Lang} of 1067 m^2/g.[6] Each unit cell of In **rho**-ZMOF contains 48 In metal ions and 96 ligands (H_3ImDC) to form an anionic framework with an overall formula of $([In_{48}(HImDC)_{96}]^{48-})_n$. The negative charge of the as-synthesized framework is balanced by dimethylammonium (DMA^+) counter-ions that are the product of DMF dissociation during framework synthesis. Therefore, this framework has an ion exchange potential where the DMA^+ cations can be exchanged with other cationic moieties, like acridine orange,[6] Na^+, Mg^{2+} or other metal cations.[3, 7]

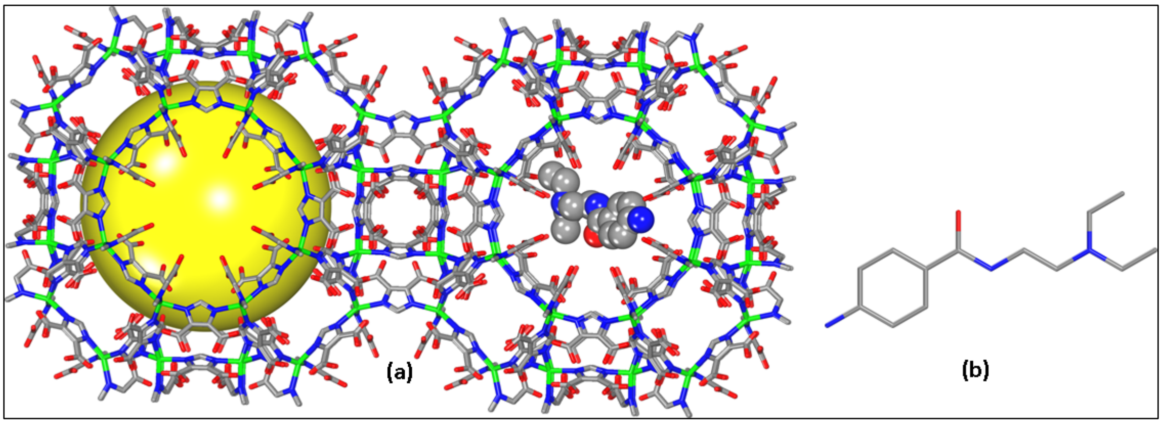

Figure 5.1 (a) A fragment of In **rho**-ZMOF showing one Proc molecule inside the cage; (b) Proc structure. Yellow sphere represents the largest sphere that would fit in the cavities without touching the van der Waals atoms of the framework. In = green, C = gray, N = blue and O = red. Hydrogen atoms and solvent molecules omitted for clarity.

These properties make In **rho**-ZMOF attractive as a delivery vehicle for Proc (Figure 5.1 b), a cationic[8] antiarrhythmic drug with a short half-life and needing to be administered every 3-4 h.[9] Proc is available as a hygroscopic crystalline powder that is very soluble in water. The incorporation of Proc, with a maximum diameter of~6.1 Å, inside the framework is accomplished through cation exchange. The favorable electrostatic interaction is anticipated to provide controlled release of the drug and prevents its leaching upon administration. Loaded Proc is expected to be released from the pores of the framework in a controlled manner as a result of cation exchange with the exogenous cations supplied by biological buffers (e.g., PBS) or biological fluids. Of note is that, to date, different systems have been studied as Proc controlled-release formulations, including polymeric, hydrogel and composite systems.[10]

5.4.2. Procedures

5.4.2.1. Synthesis of In rho-ZMOF

The original reported (In-ImDC) **rho**-ZMOF preparation conditions were modified.[6] Here, H_3ImDC (0.014 g, 0.087 mmol), $In(NO_3)_3.2H_2O$ (0.015 g, 0.0435 mmol), DMF (1.5 mL) and C_2H_5OH (0.5 mL) were added to a 20-mL scintillation vial, which was sealed and heated at 85 °C for 48 h. The colorless polyhedral crystals were collected, washed with DMF, exchanged with C_2H_5OH for 2 days and dried in a Büchner funnel for 24 h. At this stage, the framework had a formula of $|(DMA^+)_{48}|[In_{48}(HImDC)_{96}]$.

5.4.2.2. Stability of In rho-ZMOF in Proc loading and release solvents

The stability of In **rho**-ZMOF in Nanopure or DI water (18.2 mΩ) as the drug loading solvent and in 0.1 M PBS (pH 7.4) as the drug release solvent were evaluated by soaking the framework in the different solvents for up to 12 days. In addition, the framework stability after both drying and complete drug loading was investigated by using PXRD to assess the crystallinity of the framework following different treatments.

5.4.2.3. Drug loading experiment

Proc loading into the framework was achieved through ion exchange where drug cations replace the extra-framework DMA^+ ions that balance the framework charge. This was accomplished with two methods; the first was to exchange DMA^+ ions with Na^+, followed by exchanging Na^+ ions with Proc cations. Conversely, the second method involved exchanging DMA^+ ions directly with drug cations.

More specifically, the first method was performed by placing 90 mg of C_2H_5OH-exchanged and dried In **rho**-ZMOF crystals (n = 3) into 2 mL of 0.2 M $NaNO_3$ solution (0.68 g in a solution of 32 mL of C_2H_5OH and 8 mL of water). This solution was frequently decanted and replaced with 2 mL of fresh solution over a period of 24 h to form Na@**rho**-ZMOF. This is the amount of time needed for complete framework cation exchange (15-24 h).[6] Na@**rho**-ZMOF crystals were then collected, washed three times with C_2H_5OH, dried in an oven at 85 °C for 15 min and weighed. The dried crystals were next placed in 2 mL of 0.1 M Proc solution in DI water, which was frequently decanted and replaced over a period of 24 h. This led to the exchange of some Na^+ in the framework with Proc cations, producing drug loaded In **rho**-ZMOF (Na/Proc@**rho**-ZMOF).

With regards to the second drug loading method, 90 mg of C_2H_5OH-exchanged In **rho**-ZMOF crystals that were dried overnight in a Büchner funnel (n = 3) were added to a 25-mL conical flask and soaked in 5 mL of 0.1 M solution of Proc HCl in DI water. The mixture was next placed in a shaking water bath and subjected to bidimensional shaking at 50 rpm and 25 °C. After 10 min, the solution was totally removed (with the aid of centrifugation) and replaced with 5 mL of fresh loading solution. After another 10 min, the solution was decanted and replaced with 5 mL loading solution in which the crystals were kept for 24 h while repeating the process frequently. After the drug loading was complete, the loaded crystals (Proc@**rho**-ZMOF) were collected, washed with C_2H_5OH several times and dried. Here, the total amount of drug consumed by the framework was measured by UV-Vis spectroscopy and was equal to the sum of the amount of drug consumed during each step.

5.4.2.4. Determination of the amount of Proc loaded into In rho-ZMOF

5.4.2.4.1. ICP-OES

Here, 30 mg of Na@**rho**-ZMOF and Na/Proc@**rho**-ZMOF samples (n = 2) were digested using 2 mL of concentrated nitric acid to produce a clear solution. Then, 20 mL of Nanopure water was added and the solution filtered through a 0.45 µm syringe filter, transferred to special ICP tube and the volume was completed to 45 mL with Nanopure water.

5.4.2.4.2. AAS

Different samples were prepared for AAS as follows: specific weights of Na@**rho**-ZMOF and Na/Proc@**rho**-ZMOF samples (n = 2) were placed in conical flasks to which 10 mL of concentrated HCl acid were added. The mixtures were left for few minutes then 10 mL of DI water was added and sonication ensued. The solutions were next transferred into 250 mL volumetric flasks and the volume completed with DI water.

Serial dilutions of Na^+ in Nanopure water were prepared with commercially available atomic absorption standard solution having a concentration of 2 ppm to construct calibration curves of the following concentrations: 0.3, 0.6, 1, 1.5 and 2 ppm. Quality control solutions were prepared with 1 ppm and 2 ppm concentrations.

Similarly, serial dilutions of In^+ in Nanopure water were also prepared with commercially available atomic absorption standard solution having a 20 ppm concentration to construct calibration curves of the following concentrations: 2.5, 5, 10, 15 and 20 ppm. Quality control solutions with 10 ppm and 20 ppm concentrations were prepared to verify analysis accuracy.

5.4.2.4.3. FT-IR

Drug loading into the framework was indicated by comparing the spectra of parent MOF samples, loaded ones and that of the pure drug.

5.4.2.4.4. EA of C, N and H

EA of C, N and H contents of the loaded framework was performed to estimate the amount of drug loaded.

5.4.2.4.5. TGA

TGA was performed on loaded framework samples under a N_2 atmosphere. The tests were carried out between RT and 700 °C at an increasing heating rate of 5 °C/min in high resolution dynamic mode. For comparison, TGA of the original In **rho**-ZMOF samples exchanged with C_2H_5OH were collected under the same conditions.

5.4.2.4.6. Drug contents determination by mechanical destruction of the framework

Drug contents were estimated by grinding 10 mg of loaded crystals (n = 3) into a very fine powder using a mortar and a pestle and then adding 20 mL of 0.1 M PBS. The mixture was placed in a shaking water bath at 100 rpm and 37 °C for 2 days, and then subjected to sonication for 15 min. The resultant suspension was filtered through a 0.45 µm syringe filter, diluted with 0.1 M PBS and the amount of drug was quantified using HPLC.

5.4.2.4.7. HPLC assay and calibration curves of Proc in PBS

The mobile phase consisting of a mixture of 90:10 (v/v) 50 mM KH_2PO_4 (adjusted with HCl to pH 3.5) to CH_3CN, was freshly prepared on the day of analysis, filtered through 0.45 µm membrane filter and degassed.[11] The column used was a ZORBAX Eclipse XDB-C18 reverse-phase column (5 µm, 4.6 x 150 mm). The operating temperature was 30 °C; the flow rate was 1 mL/min and the injected volume was 10 µL. The column effluent was monitored continuously with UV detection at λ_{max} = 278 nm. Proc concentration was calculated with a previously constructed calibration curve of Proc in PBS (prepared and assayed on the same day of analysis). A stock solution of Proc (1 mg/mL) in 0.1 M PBS was initially prepared followed by the preparation of diluted standard solutions in the following concentrations: 5, 10, 20, 50 and 100 µg/mL. The different solutions were analyzed with HPLC and calibration curves were created as the integrated area as a function of the concentration.

5.4.2.4.8. UV-VIS spectrophotometric assay and calibration curves of Proc in Nanopure water

As described earlier, throughout the drug loading experiment using method 2 to prepare Proc@**rho**-ZMOF (Section 5.4.2.3), the amount of drug uptake by the framework was measured with UV-Vis spectroscopy. Here, the maximum absorbance wavelength of Proc was determined by performing a UV scan of the Proc solution with a concentration of 10 µg/mL in Nanopure water. Serial dilutions were prepared from a solution of 1 mg/mL concentration of Proc in DI water to construct calibration curves of the following concentrations: 5, 10, 15 and 18 µg/mL. Proc calibration standards were measured at λ_{max} = 278 nm (n = 3) on the day of analysis and the data were represented as mean ± SD.

5.4.2.5. *In vitro* Proc release studies

In a typical *in vitro* drug release experiment, 10 mg of loaded crystals were placed in 5 mL of 0.1 M PBS (pH = 7.4) in stoppered 25-mL conical flasks (n = 2). The experiment was performed under sink condition, and the flasks were shaken in a thermostat-controlled horizontal shaker at 37 ± 0.5 °C and 100 rpm. At predetermined time intervals (20, 30, 60 min, 2, 3, 4, 5, 6, 12, 24 h, 2, 3, 4 and 5 days), 300 µL from the release media samples was withdrawn with a syringe for analysis and replaced with an equal volume of fresh pre-warmed media. Extracted samples were diluted with PBS (100 µL + 650 µL), filtered through a 0.45 µm syringe filters and analyzed for Proc contents with HPLC. The amount of released drug at each time interval was calculated using the same-day constructed calibration curve of Proc in PBS.

To confirm that drug release was facilitated by buffer cations, a control experiment was performed under the same conditions with Nanopure water as the release media and the extracted samples diluted with water (100 µL + 400 µL).

The Hayton and Chen equation[12] was employed to correct the concentration of released Proc in each sample because of the dilution effects of adding fresh release media.

5.4.3. Results and discussion

As stated before, as a proof-of-principle of the potential application of different MOFs as drug delivery vehicles, the ability of In **rho**-ZMOF to store and controllably release Proc was explored. This framework is a representative example of anionic ZMOFs with exceptional properties and ion exchange potential.

Theoretically, because one unit cell of In **rho**-ZMOF has 48 anions that are balanced by 48 DMA^+ cations in the as-synthesized compound,[13] these ions can be exchanged with 48 molecules carrying a single positive charge or 24 doubly-protonated ones. In addition, using MS software, the total unit cell volume of the framework was estimated to be 29970.7 Å^3 with an accessible free volume of 17186 Å^3.

Alternatively, the volume of one Proc molecule can be estimated using the same software to be roughly 368 Å^3. Therefore, one In **rho**-ZMOF unit cell can hold up to 46 Proc molecules, each having a single positive charge (Figure 5.2 a).[8, 14] However, this would cause high molecular packing of the drug inside the cages; therefore, it was assumed that each drug molecule is doubly protonated (Figure 5.2 b),[8] which in turn would lead to the assumption that each unit cell of the framework can hold up to 23 Proc molecules. This value can be translated into a 30% (wt/wt) of drug loading (i.e., up to 0.3 g/g material).

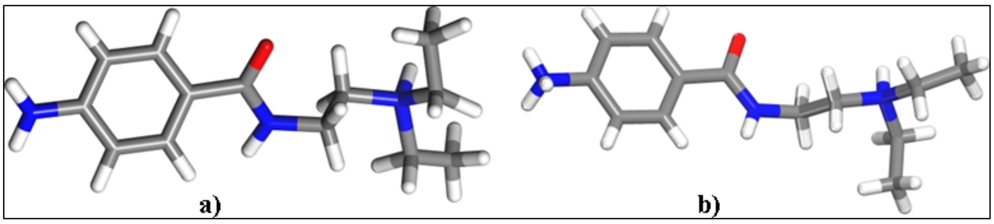

Figure 5.2 The structure of (a) protonated and (b) doubly-protonated Proc molecules.

Experimentally, the framework was prepared and the polyhedral crystals were collected, washed with DMF, exchanged with C_2H_5OH and dried in a Büchner funnel. The crystals were then loaded with the drug to form either Na/Proc@**rho**-ZMOF or Proc@**rho**-ZMOF, depending on the method of drug loading employed. The amount of Proc loaded into the frameworks was estimated to be approximately 0.23 g/g material with various techniques that included ICP, AAS, EA, TGA, HPLC and UV-Vis spectroscopy. In addition, the drug release profile was followed.

5.4.3.1. Stability of In rho-ZMOF

The stability and structural integrity of the framework are crucial because its degradation would affect the drug release rate from the pores. Therefore, PXRD of In **rho**-ZMOF (Figure 5.3) showed high stability subsequent to drying and in DI water. Furthermore, Proc loading into the pores did not influence the crystallinity of the framework. This was confirmed by the agreement between the PXRD patterns of the as-synthesized and treated samples.

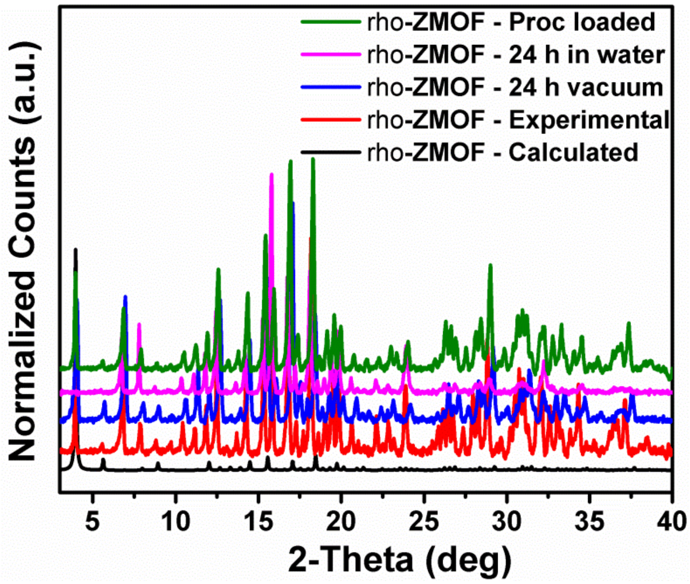

Figure 5.3 In **rho**-ZMOF calculated PXRD pattern compared to the as-synthesized, vacuum dried, in DI water and after complete drug loading patterns.

5.4.3.2. Determination of the amount of Proc loaded using ICP-OES and AAS

The ICP-OES and AAS experiments performed on both Na@**rho**-ZMOF and Na/Proc@**rho**-ZMOF samples (n = 2) exhibited that after drug loading, the In:Na ratio was reduced from approximately 1:1.046 to 1:0.6 in the two samples, respectively. Therefore, about 45% of the Na^+ ions were exchanged with drug cations.

Following our assumption that each drug molecule is doubly protonated, this can be translated to a drug loaded amount of roughly 0.23 g/g material.

5.4.3.3. FT-IR

The IR peaks of the loaded sample of In **rho**-ZMOF showed a combination of unshifted principle peaks of Proc (Figure 5.4).

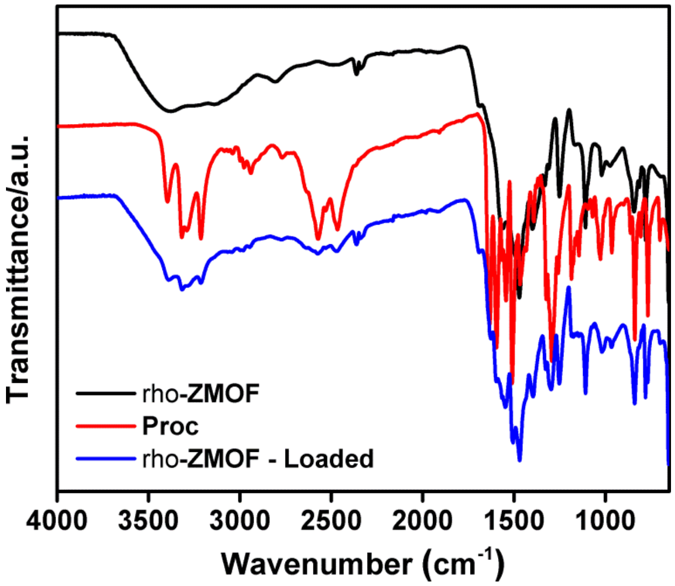

Figure 5.4 IR spectroscopy of In **rho**-ZMOF before and after Proc loading compared to pure Proc spectrum.

5.4.3.4. EA of C, N and H

EA was performed on both Na@**rho**-ZMOF and Na/Proc@**rho**-ZMOF samples and the results are listed in Table 5.1.

Table 5.1 EA data of Na@**rho**-ZMOF and Na/Proc@**rho**-ZMOF.

	C%		H%		N%	
	Calc.	**Found**	**Calc.**	**Found**	**Calc.**	**Found**
Na@**rho**-ZMOF	21.6	21.4	2.91	2.51	10.1	9.8
Na/Proc@**rho**-ZMOF	29.07	29.04	3.7	3.54	11.65	11.3

Here, the calculated formula of Na@**rho**-ZMOF was found to be $In_{48}(L)_{96}Na_{50.4}(C_2H_5OH)_{0.048}(H_2O)_{288}$, where the solvents represented 19.5% of the total weight. On the other hand, the calculated formula of Na/Proc@**rho**-ZMOF could be expressed as $In_{48}(L)_{96}(Proc)_{18.24}Na_{29.76}(C_2H_5OH)_{0.48}(H_2O)_{240}$, with solvent contents of 14.7% and the amount of loaded drug at approximately 0.2 g/g material.

5.4.3.5. TGA

Reviewing the TGA of Na/Proc@**rho**-ZMOF (Figure 5.5), two major weight loss steps were observed. The first was because of the evaporation of solvent molecules and was estimated to be 15%, which is very close to the experimental value found with EA. However, the second step was based on drug molecules departing from the pores followed by framework degradation. This method underestimates the amount of drug in the framework as it is complicated to distinguish the weight loss from the drug and the framework decomposition.[2] This is true because the temperature of the framework destruction (300-400 °C) is very close to that of Proc departure, which also depends on the ionic interaction with the framework.[1] Therefore, the approximate amount of the drug loaded was found to be just 0.15 g/g.

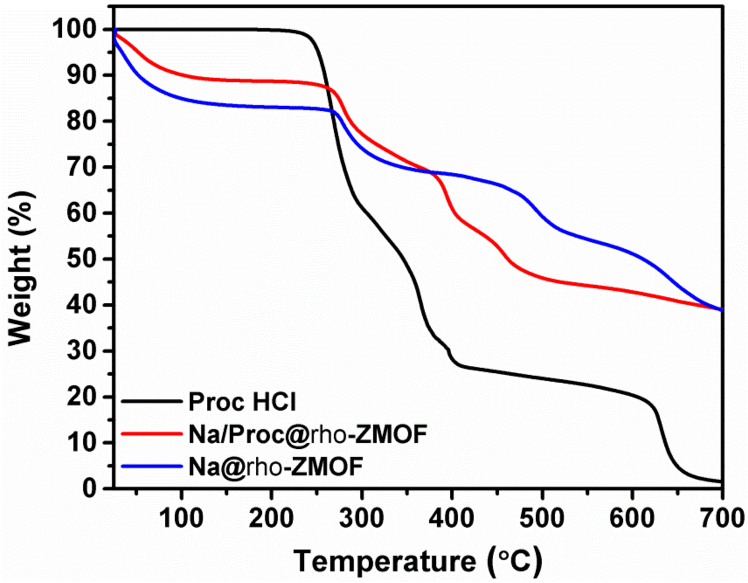

Figure 5.5 TGA plot of Proc, Na@**rho**-ZMOF and Na/Proc@**rho**-ZMOF.

5.4.3.6. Drug contents determination by mechanical destruction of the framework

In this experiment, mechanical destruction of the crystals was performed by subjecting the sample to grinding, shaking and sonication with the aid of cation-triggering using PBS. The amount of drug loaded was measured with HPLC and found to be 0.21 g/g material. It is interesting to note that the addition of concentrated acid to completely digest the crystals, which is the typical way to perform this kind of experiment, was avoided to prevent procainamide degradation.[15] In addition, we believe that the mechanical destruction of the framework in the presence of PBS would completely release all entrapped drug molecules.

5.4.3.7. HPLC assay and calibration curve of Proc in PBS

HPLC was made use of to measure the amount of drug found or released in PBS in terms of both drug contents and the drug release experiments, respectively. Here, solutions of as-purchased Proc showed one peak that was observed at a retention time of 3.642 min (Figure 5.6).

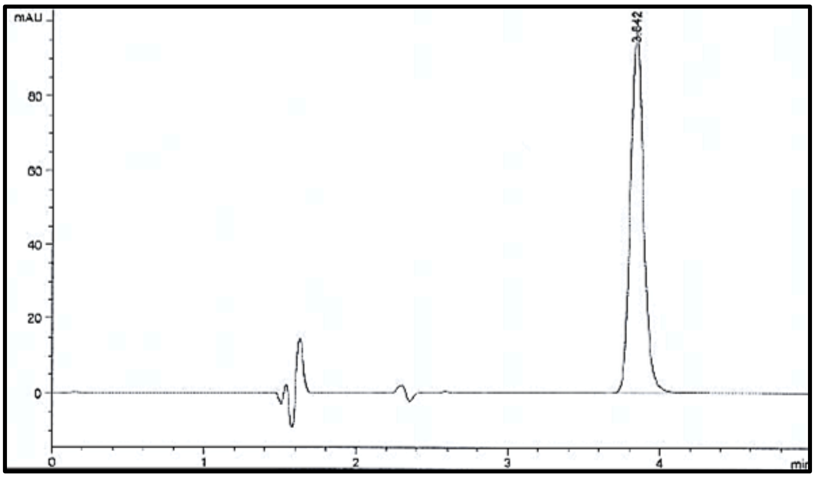

Figure 5.6 An example of a HPLC chromatogram of Proc at PBS in a concentration of 50 µg/mL.

The Proc standard calibration curve in PBS was linear over the calibration range of 5-100 µg/mL with $R^2 = 1$. Calibration curve data were plotted as the mean of 3 runs and were represented as the integrated area as a function of concentration in µg/mL (Figure 5.7).

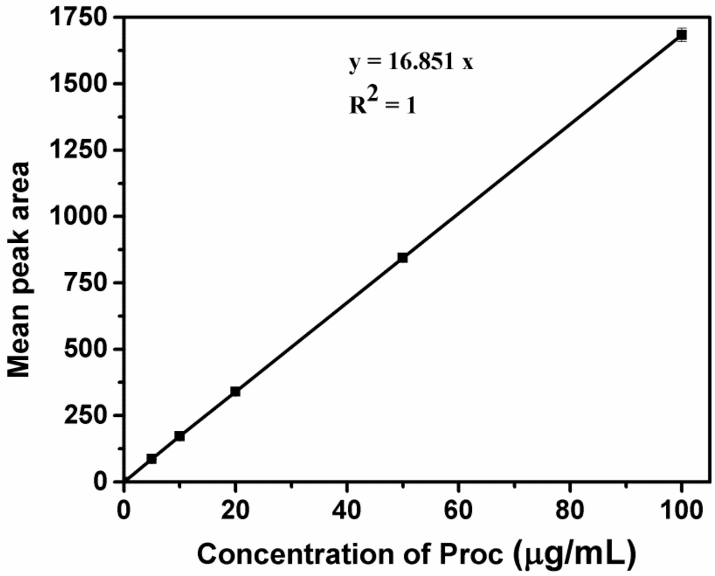

Figure 5.7 HPLC standard calibration curve of Proc in 0.1 M PBS (pH = 7.4) (n = 3).

5.4.3.8. UV-VIS spectrophotometric assay and calibration curves of Proc in Nanopure water

During the drug loading experiment, the amount of drug loaded into Proc@**rho**-ZMOF was estimated with UV-Vis spectroscopy where:

The total amount of drug consumed by the framework =

∑ (amount of drug in original solution – amount remaining at each time interval).

Spectrophotometric UV wavelength scanning of the Proc solution with a concentration of 10 µg/mL of DI water had a maximum absorbance at λ_{max}= 278 nm (Figure 5.8). Proc standard calibration curves were constructed with different dilutions that indicated a linear relationship (R^2 = 0.9977) between absorbance and Proc concentration passing through the origin and obeying Beer-Lambert's law (Figure 5.9).

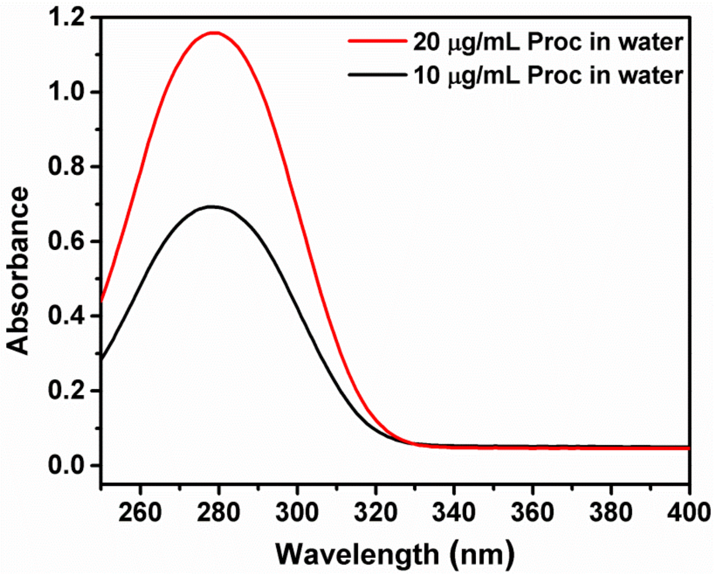

Figure 5.8 An example of UV-Vis spectra of Proc in Nanopure water at concentrations of 10 and 20 μg/mL.

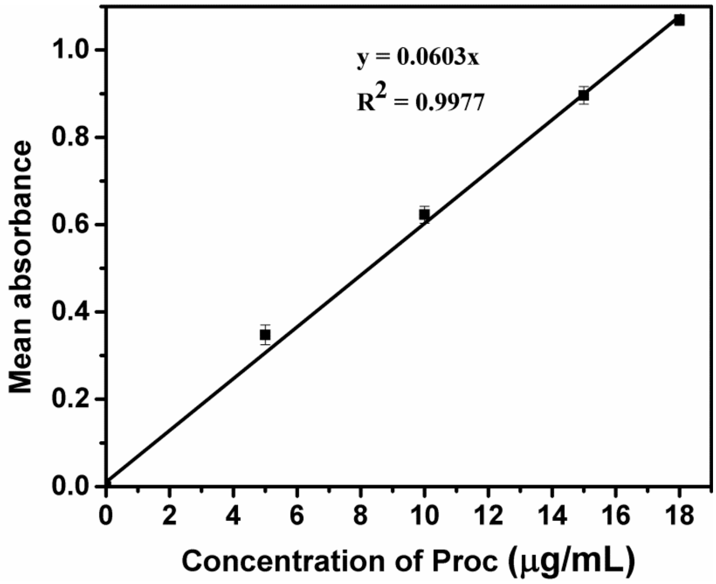

Figure 5.9 UV-Vis standard calibration curve of Proc in Nanopure water at 278 nm (n = 3).

The amount of Proc loaded into In **rho**-ZMOF was found to be 0.49 g/g, which is an overestimated value that can be attributed to the amount of drug bound to the external surfaces of the framework.

5.4.3.9. *In vitro* Proc release studies

The *in vitro* drug release profile provides valuable information about the efficiency of the drug delivery system being studied. Therefore, under the current release experiment design, sink condition was ensured throughout the trial. This was achieved with the knowledge that Proc is freely soluble in the release media (0.1 M PBS with pH of 7.4) and by avoiding the maximum concentration of Proc released exceeding 15% of the saturation solubility of the drug in that media. The amount of drug released was assayed with HPLC.

During a typical cation-triggered drug release experiment, steady drug release was observed over a period of 30 h, and complete release was reached after 48 h (Figure 5.10). Compared to the control experiment, in which Nanopure water was used as the release media, higher amounts of drug were released in PBS at a relatively faster rate (90% (wt/wt) in 11 h). This can be credited to the mediated release by the buffer cations. On the other hand, when Nanopure water was used as the release media, drug release was only 20% (wt/wt) at 11 h, and the maximum amount of drug released in this experiment was only approximately 51% at around 96 h (Figure 5.10). The amount of drug released during the control experiment represents drug molecules associated with the outer surface of the framework.

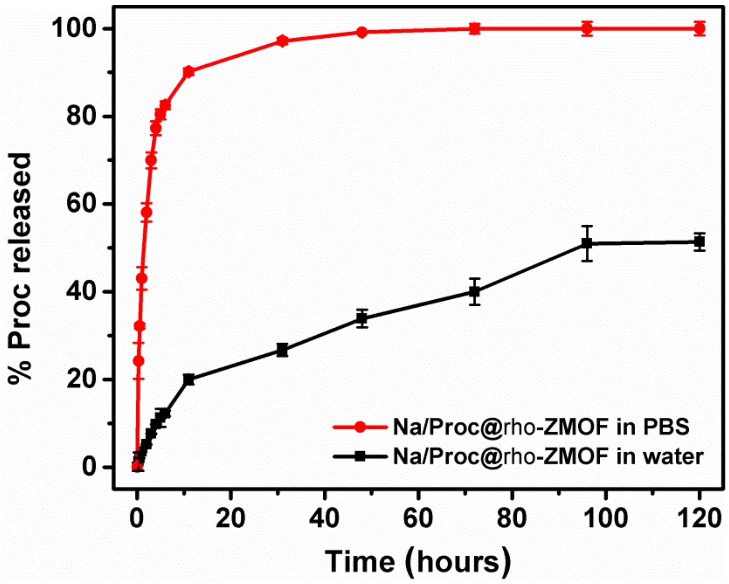

Figure 5.10 Proc release profile from In **rho**-ZMOF.

5.4.4. Summary and conclusions

The use of MOFs in biomedical applications is a new area that is still under development. Therefore, this work was performed as a proof-of-concept for the ability of MOFs to be employed in the field of medicine. Consequently, because of its anionic nature and ion exchange ability, In **rho**-ZMOF was chosen to be studied as a drug delivery system for the cationic antiarrhythmic drug, Proc. In fact, this framework demonstrated its ability to store and controllably releases the drug over a period of more than 11 h, overcoming the need for frequent administration (every 3-4 h). Drug release from the framework was triggered by the various biological buffer cations. Finally, taking into account the Proc content obtained by a number of techniques (Table 5.2), ICP-EOS and AAS may be considered the most reliable.

Table 5.2 Estimated amount of Proc loaded into In **rho**-ZMOF.

Method	**ICP-OES**	**AAS**	**EA**	**MOF destruction (HPLC)**	**TGA**	**Drug loading (UV-Vis)**
Amount of Proc loaded g/g	0.23	0.23	0.2	0.21	0.15	0.49
Notes	Most reliable				Under estimated	Over-estimated

5.5. Experimental section part II: Evaluation of a neutral MOF as a delivery vehicle for a neutral drug

5.5.1. Introduction

Cu **rht**-MOF-7 (Figure 5.11) is a neutral framework that possesses three large accessible cages with inner diameters of 10.4, 17.8 and 15.7 Å. These cages have windows of 6.4 Å and 6.8 Å in size. The potential accessible free volume corresponds to 70% with an apparent SA_{Lang} of 2170 m^2/g.[5] These properties make Cu **rht**-MOF-7 an attractive delivery vehicle for IBU, which is a neutrally charged NSAID used previously throughout the literature because of its structure (Figure 5.11), molecular dimensions (6 * 10.3 Å) and its effective volume of about 200 $Å^3$.[2, 16] The molecular weight of IBU is 206.28 mole/g, its melting point is 80 °C, and it comes as a stable white crystalline powder that is very soluble in C_2H_5OH.

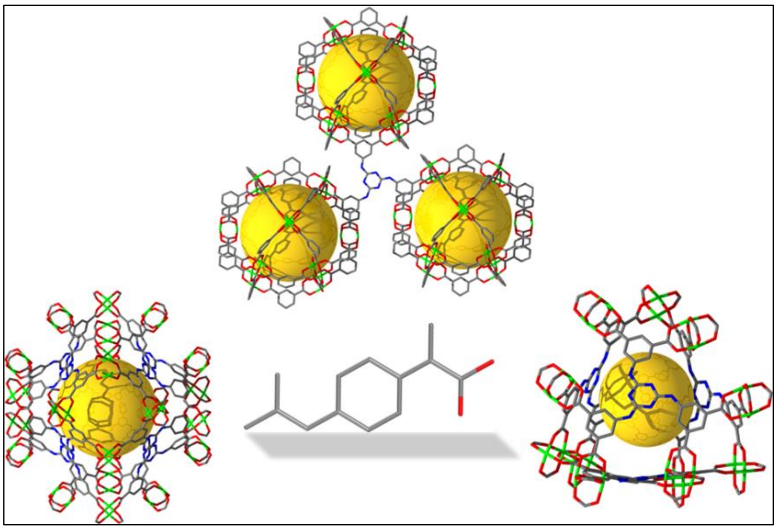

Figure 5.11 Representation of IBU molecule and selected fragments from the SC structure of Cu **rht**-MOF-7 exhibiting its different cages. Cu = green, C = gray, N = blue and O = red. Hydrogen atoms and solvent molecules have been omitted for clarity. Yellow spheres represent the largest sphere that would fit in the cavities without touching the van der Waals atoms of the framework.

5.5.2. Procedures

5.5.2.1. Synthesis of Cu rht-MOF-7

Cu **rht**-MOF-7 crystals were prepared as previously reported.[5] Here, 5,5',5''-(s-Triazine-2,4,6-triyltriimino)triisophthalate hexasodium (18 mg, 0.024 mmol), $Cu(BF_4)_2.2.5H_2O$ (20.0 mg, 0.071 mmol), DMF (2 mL), and 0.6 mL of 3 M HNO_3 in DMF were added respectively to a 20-mL scintillation vial, which was sealed and heated to 65 °C for 7 days. The green polyhedral crystals were collected, washed several times with DMF, exchanged with C_2H_5OH for 2 days and then dried in an oven at 85 °C for 30 min.

5.5.2.2. Stability of Cu rht-MOF-7 in drug loading and release solvents

Based on the fact that Cu **rht**-MOF-7 stability in different solvents and water is known,[5] its stability after both drying and drug loading was assessed. This was performed with PXRD to assess the crystallinity of the framework after different treatments.

5.5.2.3. Drug loading procedure

IBU uptake by Cu **rht**-MOF-7 was followed by ^{1}H NMR using a Bruker 500MHz SB liquid NMR spectrometer. Here, two different solutions were prepared. The first had a concentration of 0.097 M of IBU in CD_4O (30 mg/1.5 mL) and the second had a concentration of 0.0097 M TBAB in CD_4O (4.8 mg/1.5 mL) as an IS. The ^{1}H NMR spectra of 600 µL of each solution were recorded separately, and then the two solutions were mixed and the mixture ^{1}H NMR spectrum was also recorded. The ratio between IBU and the IS (the relative integral) in this spectrum was set as the initial experimental ratio. A 10-mg sample of Cu **rht**-MOF-7 crystals that was exchanged with C_2H_5OH and dried in an oven at 85 °C was added to the mixture in a screw-capped NMR tube, and an ^{1}H NMR spectrum was collected at each time interval. Sampling times were divided as follows: 5 min after mixing the crystals with the drug loading solution followed by various readings every 10 min for up to 18 h, and then one reading every 24 h.

5.5.2.4. Determination of IBU content in Cu rht-MOF-7

The amount of drug loaded into the framework was confirmed with various techniques, including TGA, EA and ^{1}H NMR, during the loading experiments and after complete digestion of the loaded samples.

5.5.2.5. TGA

To determine the amount of loaded IBU in Cu **rht**-MOF-7 crystals, TGA was performed on 10 mg of loaded samples under a N_2 atmosphere. The tests were carried out between RT and 700 °C at an increasing heating rate of 5 °C/min in high resolution dynamic mode. For comparison, TGA of the original framework samples exchanged with C_2H_5OH were collected under the same conditions.

5.5.2.6. EA

EA of C, N and H contents of the loaded framework was performed to determine the amount of drug loaded.

5.5.2.7. ^{1}H NMR spectroscopy of digested samples

IBU-loaded Cu **rht**-MOF-7 crystals were completely digested by mixing 1 mL D_2O and a half pellet of NaOH with 3 mg of the loaded crystals. This mixture was sonicated till all crystals were digested, filtered using a 0.45 µm syringe filter and the ^{1}H NMR spectrum acquired. Here, the ratio between the drug and the ligand was an indication of drug uptake and could be used to estimate the amount of drug loaded. This result was compared to the ^{1}H-NMR spectrum of pure crystalline IBU, which confirmed IBU inclusion into the framework.

5.5.2.8. Drug release study

IBU release from Cu **rht**-MOF-7 was followed by ^{1}H NMR with a Bruker 500MHz SB liquid NMR spectrometer with TBAB as an IS and NS as the release media. Therefore, a solution of 0.015 M TBAB in D_2O (4.7 mg/1 mL) was prepared. A 10 µL-sample of this solution was diluted with 990 µL of D_2O and 0.009 g of NaCl was added. A 0.5 mL of this solution was utilized as the release media and added in a screw-capped NMR tube to 10 mg of previously loaded crystals that were washed once with CD_4O and dried. The release experiment was kept at 37 °C throughout its duration in the NMR spectrometer, and a ^1H NMR spectrum was recorded at each time interval. Spectra acquiring time was divided as follows: 5 min after mixing the crystals with the drug release solution, and then every 10 min for up to 18 h followed by one reading every 24 h.

5.5.3. Results and discussion

Arising from the exceptional properties of the neutrally-charged Cu **rht**-MOF-7, it was of interest to explore its capacity to store and controllably release IBU. Therefore, the framework was prepared following the previously reported procedure and the green polyhedral crystals were collected, washed with DMF, exchanged with C_2H_5OH and dried.

5.5.3.1. **Stability of Cu** rht**-MOF-7**

The PXRD of Cu-**rht**-MOF-7 demonstrated its high stability after vacuum drying, and it maintained its crystallinity following drug loading (Figure 5.12).

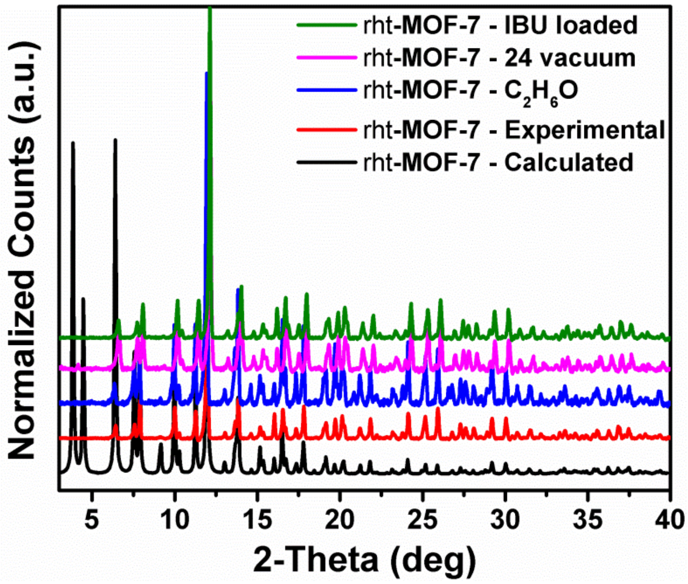

Figure 5.12 Cu-**rht**-MOF-7 calculated PXRD patterns compared to those of the framework after vacuum drying and complete drug loading.

5.5.3.2. Determination of the amount of IBU loaded using ^{1}H NMR

IBU loading into the dehydrated framework was followed by acquiring, at preset time intervals, the ^{1}H NMR spectra of a solution containing the drug, IS and the framework (Figure 5.13). The change in the ratio between IBU and the IS was used to calculate the actual amount of drug that diffused into the framework. It is worth noting that all recorded ^{1}H NMR spectra had a robust signal-to-noise ratio with no overlapping between the chemical shifts of different components.

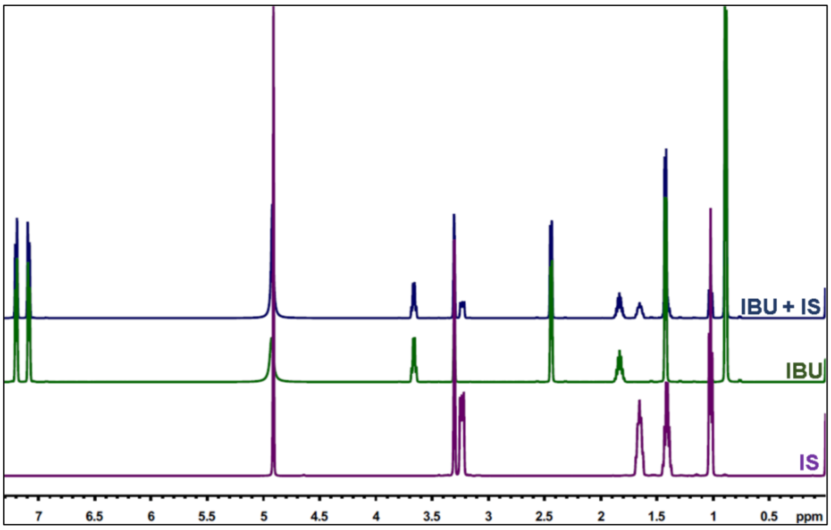

Figure 5.13 Representative ^{1}H NMR spectra showing chemical shifts of the IS, IBU and a mixture thereof.

Even though high drug loading was expected because of the large cages and high accessible free volume of the framework, drug loading experiments showed a maximum of only 4.4% (0.044 g/g) after one day of loading (Figure 5.14). This could be attributed to the size of windows of different cages of the framework (6.4 and 6.8 Å) that allowed IBU molecules (6 * 10.3 Å) to diffuse into the cages in a specific orientation and drug diffusion hindering.

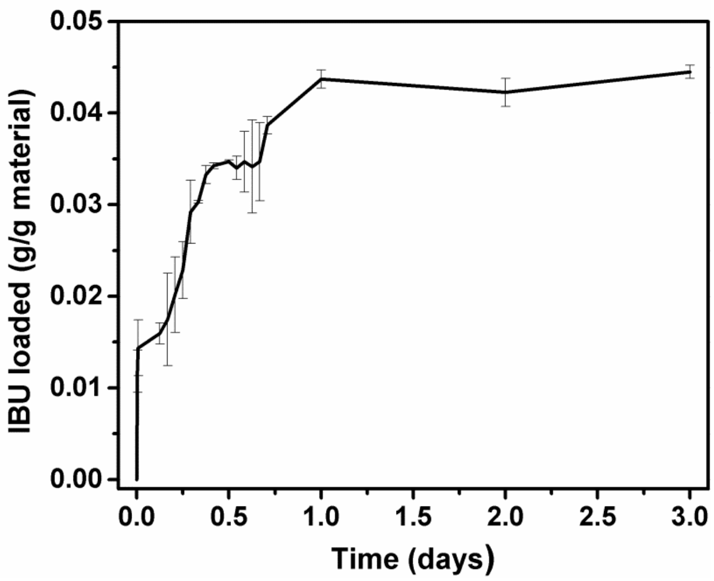

Figure 5.14 IBU loading profile into Cu **rht**-MOF-7

5.5.3.3. TGA

Looking at the TGA of the IBU-loaded framework (Figure 5.15), the first weight loss was observed within the 25-100 °C range, and it was because of the departure of C_2H_5OH and water molecules from the framework. The second step began at 204 °C, and it was the result of the exodus of IBU followed by the destruction of the framework. Interestingly, free IBU sample sublimates at roughly 120 °C, but when incorporated into the porous material, the strength of the interactions with the framework affected its departure temperature. Therefore, it was difficult to accurately estimate the amount of loaded drug using TGA because the temperature of framework destruction (277 °C) was very close to that of IBU departure. Therefore, the amount of loaded IBU was estimated to be only 3.1% through considering the weight loss between 200 and 350 °C. Nevertheless, residual drug may depart from the framework at higher temperatures and cause an underestimation of the amount of loaded drug.[2]

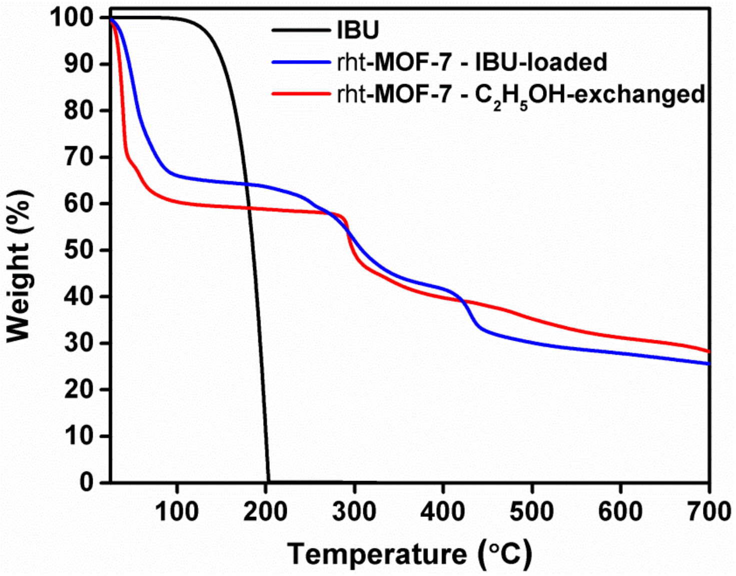

Figure 5.15 TGA of IBU and Cu **rht**-MOF-7 before and after IBU loading.

5.5.3.4. EA of C, N and H

EA was performed on both IBU loaded and parent framework samples and the results are described in Table 5.3.

Table 5.3 EA data of IBU loaded and C_2H_5OH-exchanged Cu **rht**-MOF-7.

	C%		H%		N%	
	Calc.	Found	Calc.	Found	Calc.	Found
C_2H_5OH-exchanged **rht**-MOF-7	28.66	29.09	5.54	6.23	5.75	5.65
IBU loaded **rht**-MOF-7	38.05	38.11	4.62	4.64	7.26	7.23

Here, the calculated formula of C_2H_5OH-exchanged Cu **rht**-MOF-7 was found to be $Cu_3(L)(H_2O)_{26.4}(C_2H_5OH)_{4.5}$, where solvents represented 46% of the total weight and is in agreement with the TGA findings. Conversely, the calculated formula of IBU-loaded Cu **rht**-MOF-7 can be expressed as $Cu_3(L)(IBU)_{0.29}(H_2O)_{5.4}(CH_3OH)_{6.5}$, showing solvent contents at approximately 30% and drug loading of roughly 4.6%.

5.5.3.5. Drug contents determination by complete framework destruction

A sample of loaded Cu **rht**-MOF-7 was completely digested, and its ^{1}H NMR spectrum was acquired (Figure 5.16). The ligand-to-IBU ratio was found to be 1:0.29, which is in line with the EA results.

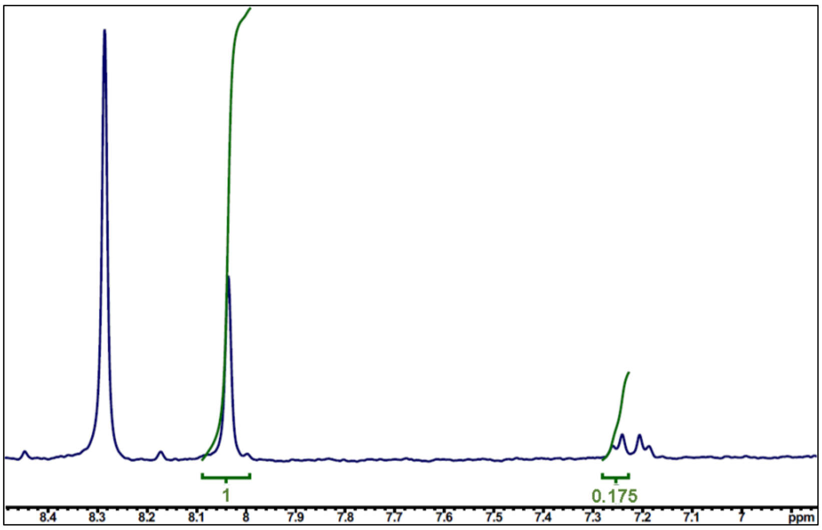

Figure 5.16 Representative ^{1}H NMR spectrum of digested IBU-loaded Cu **rht**-MOF-7 sample showing the chemical shifts and ratio between the ligand and IBU.

5.5.3.6. *In vitro* IBU release studies

Drug release profile experiments using ^{1}H NMR spectroscopy exhibited poor signal-to-noise ratio because the amount of loaded IBU was very low.

5.5.4. Summary and conclusions

As a result of the large cages of the neutrally-charged Cu **rht**-MOF-7, it was selected to be evaluated as a potential drug delivery carrier for IBU, a neutrally-charged

NSAID. Even though IBU diffusion into this framework was expected to be high, it was found that drug loading reached a maximum of just 4.4%. This low drug loading capacity could be attributed to the size of the windows of the different framework cages (6.4 and 6.8 Å) that allowed IBU molecules (6 * 10.3 Å) to enter the cages strictly in a specific orientation and leading to restricted drug diffusion. Table 5.4 summarizes the estimated amount of IBU-loaded into Cu **rht**-MOF-7 with different techniques.

Table 5.4 Estimated amount of IBU loaded into Cu **rht**-MOF-7 using different quantification techniques.

Method	**EA**	**MOF destruction**	**TGA**	**Drug loading**
%IBU loaded	4.6	4.6	3.1	4.4
Notes			Underestimated	

5.6. REFERENCES

1. An, J.; Geib, S. J.; Rosi, N. L., *J. Am. Chem. Soc.* **2009,** *131*, 8376-8377.

2. Horcajada, P.; Serre, C.; Vallet-Regi, M.; Sebban, M.; Taulelle, F.; Ferey, G., *Angew. Chem. Int. Ed. Engl.* **2006,** *45*, 5974-5978.

3. Eddaoudi, M.; Sava, D. F.; Eubank, J. F.; Adil, K.; Guillerm, V., *Chem. Soc. Rev.* **2015,** *44*, 228-249.

4. Alkordi, M. H.; Eddaoudi, M., Zeolitelike Metal–Organic Frameworks (ZMOFs): Design, Structure, and Properties. In *Supramol. Chem.*, John Wiley & Sons, Ltd: **2012**.

5. Luebke, R.; Eubank, J. F.; Cairns, A. J.; Belmabkhout, Y.; Wojtas, L.; Eddaoudi, M., *Chem. Commun.* **2012,** *48*, 1455-1457.

6. Liu, Y.; Kravtsov, V.; Larsen, R.; Eddaoudi, M., *Chem. Commun.* **2006**, 1488-1490.

7. Nouar, F.; Eckert, J.; Eubank, J. F.; Forster, P.; Eddaoudi, M., *J. Am. Chem. Soc.* **2009,** *131*, 2864-2870.

8. Janik, A.; Bukowska, M.; Jamrozy, K.; Stadnicka, K., *Struct. Chem.* **2009,** *20*, 699-707.

9. Yang, B. B.; Abel, R. B.; Uprichard, A. C.; Smithers, J. A.; Forgue, S. T., *J. Clin. Pharmacol.* **1996,** *36*, 623-633.

10. (a) Sintov, A.; Levy, R. J., *Int. J. Pharm.* **1997,** *146*, 55-62.(b) Kerin, N. Z.; Meengs, W. L.; Timmis, G. C.; Salerno, D.; Haber, H. E.; Singer, R. M.; Switzer, D.; Zoble, R.; Carlson, M.; Weidler, D.; Raghavan, P.; Schwartz, K.; Somberg, J. C.; Kereiakes, D.; Ellenbogen, K. A., *Cardiovasc. Drug. Ther.* **1997,** *11*, 169-175.(c) Ananthoji, R.; Eubank, J. F.; Nouar, F.; Mouttaki, H.; Eddaoudi, M.; Harmon, J. P., *J. Mat. Chem.* **2011,** *21*, 9587-9594.

11. Ricker, R., *Procainamides and Metabolites on ZORBAX XDB-C8*. Agilent Technologies, Inc.: **2002**.

12. Hayton, W. L.; Chen, T., *J. Pharm. Sci.* **1982,** *71*, 820-821.

13. Sava, D. F.; Kravtsov, V.; Nouar, F.; Wojtas, L.; Eubank, J. F.; Eddaoudi, M., *J. Am. Chem. Soc.* **2008,** *130*, 3768-3770.

14. Peeters, O. M.; Blaton, N. M.; Deranter, C. J.; Denisoff, O.; Molle, L., *Cryst. Struct. Commun.* **1980,** *9*, 851-856.

15. Marcus, A. D.; Taraszka, A. J., *J. Am. Pharm. Assoc.* **1957,** *46*, 28-31.

16. (a) Kuppler, R. J.; Timmons, D. J.; Fang, Q.-R.; Li, J.-R.; Makal, T. A.; Young, M. D.; Yuan, D.; Zhao, D.; Zhuang, W.; Zhou, H.-C., *Coordin. Chem. Rev.* **2009,** *253*, 3042-3066.(b) Asefa, T.; Otuonye, A. N.; Wang, G.; Blair, E. A.; Vathyam, R.; Denton, K., *Adsorption* **2009,** *15*, 287-299.(c) Wang, G.; Otuonye, A. N.; Blair, E. A.; Denton, K.; Tao, Z. M.; Asefa, T., *J. Solid State Chem.* **2009,** *182*, 1649-1660.(d) Zhu, Y. F.; Shi, J. L.; Li, Y. S.; Chen, H. R.; Shen, W. H.; Dong, X. P., *Micropor. Mesopor. Mat.* **2005,** *85*, 75-81.

Chapter 6: Conclusions and Future Outlook

The synthesis of materials with specific properties for targeted applications is an ongoing challenge in materials chemistry. One of the most interesting classes of solid-state materials that have been recently introduced with the potential to address this issue is the class of MOFs with their hybrid organic-inorganic nature. The interest in them is rapidly increasing because of MOFs unique properties and their tunable chemistry that offers a degree of control over the resulting materials. It is worth noting that when mixing the organic and inorganic moieties during MOFs synthesis, the most simple “default” structures are expected to be synthesized. Therefore, new design strategies have been introduced to enable the synthesis of more complex MOFs with targeted topologies and permitting the modification of their properties to target specific applications. The use of these techniques is advisable to prevent the random unpredicted outcomes as was the case when MOFs were first introduced.

In this work, two important newly introduced design strategies were implemented with the goal of exploring these pathways and synthesizing new targeted MOF materials. These two strategies are the supermolecular building layers (SBLs) and the molecular building blocks (MBBs) approaches, which depend on the assembly of *in situ*-formed predetermined building blocks to construct the new materials. All prepared novel MOF materials and their isostructures or isoreticular structures were characterized and investigated for different targeted applications, such as gas storage and separation.

The first part of the work presented in this dissertation (Chapter 3) addressed the rational design of various MOFs with predicted topologies and tunable cavities utilizing the SBLs approach. At this point, as an extension of our group previous work, different novel 3-P MOFs were created by pillaring pre-targeted edge-transitive 2-P SBLs implementing the newly introduced ligand-to-axial (L-A) pillaring strategy.

The effect of expanding confined spaces (isoreticular chemistry) by using an extended isophthalic acid-based trigonal hetero-functional ligand (5’-(pyridin-4-yl)-[1,1’:3’,1’’-terphenyl]-4,4’’-dicarboxylic acid (PTPDC)), along with Zn nitrate salt, was examined. Here, Zn-**pyr**-MOF was synthesized upon the L-A pillaring of the *in situ*-formed 2-P square lattice (**sql)** layers. The resulting 3-P MOF with **pyr** topology was predicted as it is one of the “default” topologies that may result when combining the geometrically octahedral 6-c metal clusters and the geometrically trigonal 3-c organic ligands. This framework experienced partial collapse after both conventional and SC-CO_2 activation, demonstrated in the form of low gas uptake capacity.

Further experimental work targeting a more stable MOF using the single-crystal-to-single-crystal transmetalation resulted in the formation of Cu(e)-**pyr**-MOF in which~ 75% of Zn ions were exchanged with Cu ions. This isostructure showed improved gas uptake capacity after SC-CO_2 activation but did not reach to the expected theoretical values.

Therefore, direct synthesis of a Cu analogue was targeted by using PTPDC and Cu nitrate salt to construct Cu-**pyr**-MOF. This isostructure exhibited high porosity with ultra-high SA among the highest values that have been reported to date for any porous material. Furthermore, the framework showed potential for applications to separate CO_2 from N_2 and CH_4.

Additionally, when using a shorter ligand (5-(pyrimidin-5-yl)isophthalic acid (PMIP)) while combining the same geometric entities (the 6-c octahedral metal clusters and the 3-c trigonal ligand), 2-P **kgm** layers were formed and pillared into a 3-P MOF with

eea topology. Here, the ligand contained an additional functionalization site that was not intended for involvement with the coordination to assess the ability to fine-tune the properties of prepared MOFs while preserving their underlying network topology. Interestingly, by mixing PMIP with both Cu nitrate and Cu halide salt (Cu(X), where X is Cl, Br or I), we were able to construct three isostructural MOFs, which are Cl-, Br- and I-**eea**-MOF, respectively. The only difference among these isostructures lies in the type of halide ion coordinated to the tetrahedral Cu^+ MBB that was formed at the additional functionalization site of the ligand.

In this specific case, no significant difference was observed in the behavior of the three isostructures toward various gases. However, it was anticipated that this additional functionalization site could be further employed to introduce other moieties that mostly affected material behavior. For example, Cu^+ in the tetrahedral MBB can be exchanged with Ag^+ ions, which may bestow different yet interesting properties to the prepared MOFs. In addition, a framework suitable for gas storage applications can be targeted with an analogous ligand that is expanded by extending the isophthalic acid moiety as well as adding an alkyne linkage in the "arm" of the ligand at the 5th position. This leads to the construction of an isoreticular MOF that is anticipated to have, in addition to the additional functionalization site, a high SA.

Finally, six-connected axial-to-axial (6-c A-A) pillaring of 2-P **kgm** layers was utilized to construct two isoreticular MOFs with the rare **lon** topology and enabled the modification of their properties without altering the underlying network topology. Therefore, the effect of tetrazolate (the organic ligand) modification on the structure-function relationship of the ester-bearing Cu-**lon**-MOF and the totally decarboxylated Cu(H)-**lon**-MOF isoreticular structure was exemplified in the case of adsorption of different single and mixed gases. Generally, it was found that the complete decarboxylation of ester groups in the organic building block led to drastic enhancement of various gas adsorption uptakes.

The results presented from this part of the work demonstrate the power of using the newly introduced SBLs approach to construct 3-P MOFs with targeted topologies, their interesting properties and the ability to modify these properties according to requirements.

Further, this approach can be widely implemented, especially with the availability of a number of pillaring techniques, such as the axial-to-axial (A–A) and ligand-to-ligand (L–L), in addition to the L-A pillaring that was used in this work. These techniques depend on the geometry and nature of the different organic and inorganic components that will result in the formation of pre-programmed SBLs. Additionally; the SBLs design strategy enables control over the SBLs pores by expansion and/or decoration, resulting in the production of MOFs with predicted topologies and tunable cavities. Therefore, there are no limits when constructing predesigned MOFs for targeted applications as one can fine-tune their properties as necessary.

In the second part of this work (Chapter 4), the MBBs approach was utilized, using rare earth (RE) metal ions, 2-flourobenzoic acid (2-FBA), as a reaction modulator, and different angular polytopic hetero-functional ligands containing carboxylate and nitrogen moieties. Moreover, the fact that it is possible to isolate new frameworks and network topologies by subtly modifying the geometry of the ligand, e.g., adjusting its length-to-width ratio, led to this also being examined. The goals were to synthesize MOFs based on novel highly-connected polynuclear RE-MBBs and explore the diverse coordination modes and possible geometries. These discovered highly-connected nets could be further utilized to design new MOFs and aid the predictability of structural outcomes.

Therefore, the reaction conditions that formerly allowed the isolation of **fcu**-MOFs, now, in the presence of the angular bi-functional ligand 4,4’-(pyridine-3,5-diyl)dibenzoic acid (PDDB), permitted the introduction, for the first time, of a highly connected RE octadecanuclear MBB and the formation of the novel and highly stable 2-P Y-**hxl**-MOF. Using similar reaction conditions without adding 2-FBA led to the production of Y-**nbo**-MOF, a nonporous 3-P MOF based on the known RE dinuclear paddlewheel and dimeric clusters. Afterwards, the reaction between an extended ligand, PTPDC, and Y nitrate salt with the aid of a fluorinated modulator resulted in the formation of a second novel and highly-connected RE octanuclear MBBs and their assembly to form Y-**tfz**-MOF-1, a pillared 3-P MOF with the quite infrequent **tfz** topology. This framework exhibited low stability upon solvent guest molecules removal. Therefore, to increase the stability of the produced MOF, a mixed-ligands approach was utilized where PTPDC and its shorter version, PDDB, were mixed in the presence of 2-FBA to produce, as expected, the isoreticular structure, Y-**tfz**-MOF-2. Unfortunately, this MOF only possessed a slightly enhanced stability; thus, Dy and Tb analogues of this RE polynuclear-based structure were synthesized and studied for their magnetic properties. With this, future investigations using other shorter ligands as the pillars may prove beneficial for increasing the stability of the compound and, consequently, increase its gas uptake.

Furthermore, through the addition of 2-FBA to the reaction between Y nitrate salt and 5-(pyridin-4-yl)isophthalic (PIP), a shorter version of PTPDC, we were able to synthesize a new 3-P MOF that was based on the novel RE double-tetranuclear cluster with **tfz** topology, Y-**tfz**-MOF-3. This framework was very dense and demonstrated very limited porosity; therefore, Tb and Dy analogues of this RE polynuclear-based structure were synthesized and assessed for their magnetic properties.

Alternatively, when utilizing PIP and its analogue with a pyrimidine moiety, PMIP, under similar reaction conditions while also eliminating the modulator; two new 3-P MOFs were synthesized. These MOFs were Y-**swk**-MOF-1 and Y-**swk**-MOF-2 and are based on the default rod-like RE secondary building unit (SBU) with the uncommon **swk** topology.

In general, the experiments presented in Chapter 4 resulted in identifying the appropriate reaction conditions amenable to reliable consistent *in situ* formation of the unprecedented double tetranuclear, octanuclear and octadecanuclear RE-MBBs and consequently the synthesis of their corresponding MOFs. This was accomplished through systematic exploration of the use of RE metal salts in combination with hetero-functional ligands in the presence of 2-FBA as a reaction modulator. After isolating these reaction conditions, the RCSR database and its mathematical and structural data may be employed to predict the possible structural outcomes when using other organic ligands having the required functionalities and geometry, i.e., help in designing new MOFs and aid in predicting the topological outcomes.

In addition, the importance of using 2-FBA as a modulator for the formation of the polynuclear RE-MBBs and preventing the formation of the default RE-MBBs was shown through maintaining the same reaction conditions that led to the formation of these MOFs while leaving out the modulator. Here, and just as expected, only MOFs based on the dominant RE infinite-chain MBBs or dinuclear clusters were created. In addition, It was observed that nitrogen atoms are not always involved in the coordination of the framework, and whenever they are, they coordinate to the metal in a monodentate manner with a relatively flexible geometry, leading to the formation of frameworks that are less stable upon guest solvent molecules removal. Therefore, the frameworks underwent partial or complete collapse and consequently exhibited low or a complete lack of porosity. Finally, structures and gas sorption behavior of prepared MOFs were evaluated to establish structure-property relationships that elucidate the effect of using different ligands on tuning various properties of the prepared compounds. For selected MOFs, magnetic properties were investigated.

The aforementioned experiments presented in Chapter 3 and 4 represent examples of how SBLs and MBBs design methods can be followed to develop and fine-tune new materials targeted for specific applications, including, but not limited to, gas storage/separation, chemical sensing, catalysis and drug delivery.

The last portion of this dissertation (Chapter 5) dealt with evaluating a couple of known MOFs as potential drug delivery vehicles. Here, selected MOFs that were previously prepared by our group, namely the anionic In **rho**-ZMOF and the neutral Cu **rht**-MOF-7, were evaluated as potential drug delivery vehicles for the cationic Proc and the neutrally charged IBU, respectively. It is noteworthy that, even though In is known for its toxicity, the investigation of these MOFs was a proof-of-concept as the study was conducted at a time when MOFs were newly introduced as drug delivery carriers. Since then, and during the course of the past few years, MOFs have been proven to be suitable candidates for drug delivery applications. However, further research is still needed to understand the full potential of MOFs as drug delivery vehicles.

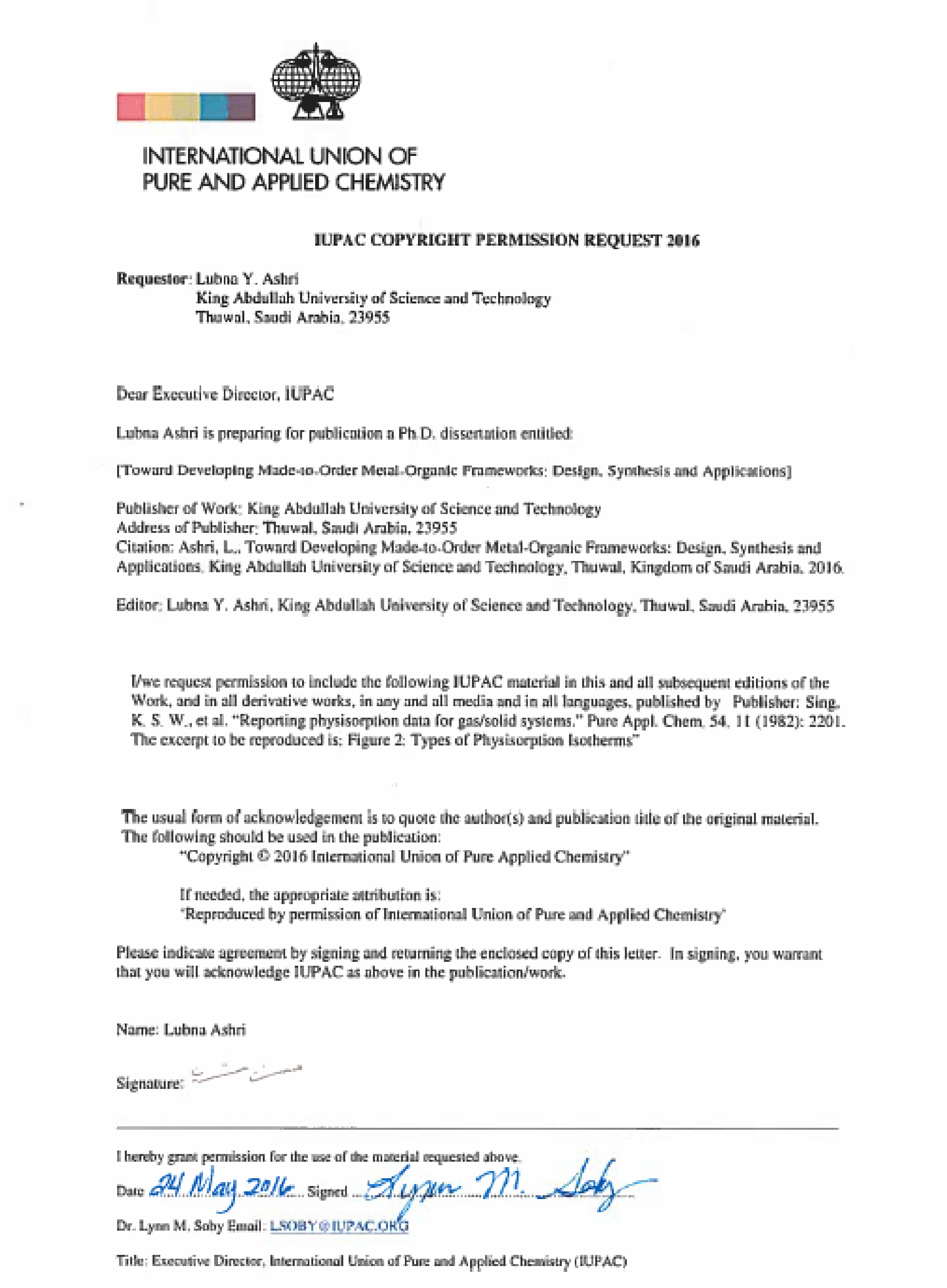

INTERNATIONAL UNION OF
PURE AND APPLIED CHEMISTRY

IUPAC COPYRIGHT PERMISSION REQUEST 2016

Requestor: Lubna Y. Ashri
King Abdullah University of Science and Technology
Thuwal, Saudi Arabia, 23955

Dear Executive Director, IUPAC

Lubna Ashri is preparing for publication a Ph.D. dissertation entitled:

[Toward Developing Made-to-Order Metal-Organic Frameworks: Design, Synthesis and Applications]

Publisher of Work: King Abdullah University of Science and Technology
Address of Publisher: Thuwal, Saudi Arabia, 23955
Citation: Ashri, L., Toward Developing Made-to-Order Metal-Organic Frameworks: Design, Synthesis and Applications. King Abdullah University of Science and Technology, Thuwal, Kingdom of Saudi Arabia, 2016.

Editor: Lubna Y. Ashri, King Abdullah University of Science and Technology, Thuwal, Saudi Arabia, 23955

I/we request permission to include the following IUPAC material in this and all subsequent editions of the Work, and in all derivative works, in any and all media and in all languages, published by Publisher: Sing, K. S. W., et al. "Reporting physisorption data for gas/solid systems." Pure Appl. Chem. 54, 11 (1982): 2201. The excerpt to be reproduced is: Figure 2: Types of Physisorption Isotherms"

The usual form of acknowledgement is to quote the author(s) and publication title of the original material. The following should be used in the publication:

"Copyright © 2016 International Union of Pure Applied Chemistry"

If needed, the appropriate attribution is:
'Reproduced by permission of International Union of Pure and Applied Chemistry'

Please indicate agreement by signing and returning the enclosed copy of this letter. In signing, you warrant that you will acknowledge IUPAC as above in the publication/work.

Name: Lubna Ashri

Signature:

I hereby grant permission for the use of the material requested above.

Date 24 May 2016 Signed Lynn M. Soby

Dr. Lynn M. Soby Email: LSOBY@IUPAC.ORG

Title: Executive Director, International Union of Pure and Applied Chemistry (IUPAC)